UNIVERSITÀ DEGLI STUDI DI ROMA "TOR VERGATA"

FACOLTA' DI INGEGNERIA MECCANICA

DOTTORATO DI RICERCA IN

PROGETTAZIONE DEI SISTEMI MECCANICI

DOCTORAL PROGRAM IN DESIGN OF MECHANICAL SYSTEMS

CICLO DEL CORSO DI DOTTORATO

XXII

Titolo della tesi

DYNAMIC ANALYSIS OF RAILWAY SYSTEMS USING COMPUTATIONALLY EFFICIENT WHEEL-RAIL CONTACT MODELS

Nome e Cognome del dottorando

MICHELANGELO BOZZONE

A.A. 2009/2010

Docente Guida/Tutor: *Prof.* PIETRO SALVINI

Coordinatore: *Prof.* CARLO BRUTTI

A B S T R A C T

The present thesis describes an investigation on the railway system motion like a wheel-set, a bogie or a wagon.
Through the search of equilibrium configurations, the positions of contact points between rails and wheels are first located. The detection methods allow also the definition of the normal vectors to rail and wheel surfaces and the principal curvatures at contact points. To reduce computing time the results are stored in a lookup table that can be used for dynamic analysis of wheel-sets, bogie or wagon.

A dynamic analysis has been performed on a bogie composed of two wheel-sets and a frame. The bogie frame is joined to the wheel-sets by means of a primary suspension system, acting on the three principal directions, *i.e.* longitudinal, transverse and vertical.

The bogie moves along rails following its variable path. In particular, the dynamic analysis investigates the bogie behaviour in both straight and curved paths, with or without an initial perturbation and a super-elevation angle. Imposing an initial transverse disturbance, the hunting motion is observed and the critical speed value estimated.

The contact characteristics have been determined by means of the lookup table. In order to minimize cpu-time, a new method for the interpolation of the lookup table entries has been developed. Finally, two different methods for the integration of the differential equations have been tested and comparisons with the results obtained by Simpack-rail multibody software are discussed.
The railway systems have been analyzed in proximity of their critical conditions both in straight and curved tracks.
The critical speed is estimated through the rise up of hunting motion. The critical speed, the contact forces in the critical conditions and the derailment limits are determined under different load conditions and track paths; two methods are used for its determination. The influence of the longitudinal suspension stiffness of the primary and secondary suspension systems on the critical conditions of the bogie and wagon are deduced for straight and curved track type.

C O N T E N T S

Part one

C H A P T E R 1 - FOUNDAMENTAL ELEMENTS IN RAILWAY ANALYSIS

C H A P T E R 2 - THE CMS DEVELOPED MODELS

C H A P T E R 3 - THE ROLLING-CONTACT THEORIES

Part two

C H A P T E R 6 - THE BOGIE DYNAMIC

C H A P T E R 7 - THE WAGON DYNAMIC

L I S T O F F I G U R E S

Part one

C H A P T E R 1 - FOUNDAMENTAL ELEMENTS IN RAILWAY ANALYSIS

C H A P T E R 2 - THE CMS DEVELOPED MODELS

C H A P T E R 3 - THE ROLLING-CONTACT THEORIES

C H A P T E R 4 - THE STABILITY OF THE MOTION

Part two

C H A P T E R 5 - THE CONTACT CHARACTERISTICS

C H A P T E R 6 - THE BOGIE DYNAMIC

C H A P T E R 7 - THE WAGON DYNAMIC

C H A P T E R 8 – NUMERICAL RESULTS

L I S T O F T A B L E S

Part one

C H A P T E R 1 - FOUNDAMENTAL ELEMENTS IN RAILWAY ANALYSIS

C H A P T E R 2 - THE CMS DEVELOPED MODELS

C H A P T E R 3 - THE ROLLING-CONTACT THEORIES

Part two

C H A P T E R 5 - THE CONTACT CHARACTERISTICS

C H A P T E R 6 - THE BOGIE DYNAMIC

Part one

C H A P T E R I

FOUNDAMENTAL ELEMENTS IN RAILWAY ANALYSIS

1.1 - Historical considerations on the development of the railway

The birth of railway is not known with precision. The use of the iron rails goes back to the middle of 1700 together with the invention of the first steam machine. In 1803 the first public railway of the world was inaugurated: the *Surrey Iron Railway* used only for the food transportation. Various tests with one horse have been done on this line, at the end of which one horse was able to carry a convoy of 55 t with 50 people on board.

Richard Trevithick created the first locomotive and he deposited its patent in 1800. Four years later its locomotive was able to carry a cargo for 15 km of railway but he didn't develop its creation. In 1814 *George Stephenson* built his first locomotive and some years later he convinces the responsibles of *the Stockton-Darlington's* railway to introduce its locomotive on their line. In 1823 the English law authorized the company for the people transport.

Finally on 27 September 1825 George Stephenson drives a steam locomotive between Stockton and Shildon, a part of the 34 km of the Stockton-Darlington line, drawing a cargo of 69 t including 6 wagons of coal and 21 wagons with wooden bench and 600 passengers. He named this steam-machine *Locomotion* and it was able to move until 24 km/h and it furnished the name to this machine. Today this day is considered the birth-day of the railway transportation and its creator was obviously George Stephenson. Figure 1.1 shows the Locomotion while Figure 1.2 its creator, George Stephenson. Table 1.1 reports some characteristics of the Locomotion.

Figure 1.1
The Locomotion

Figure 1.2
George Stephenson (1781-1848)

Gauge	**1435 mm**
Maximum boiler pressure	$1.76\ kg/cm^2$
Power wheel diameter	**1219 mm**
Mean velocity	$6\ km/h$
Weight	**6 t**

Table 1.1
Principal *Locomotion* characteristics

At this time the city of Manchester and the harbour of Liverpool were at the beginning of their industrial revolution with many textile farms that import a great quantity of cotton from the America. It was calculated that the time necessary to travel the canal between Liverpool and Manchester, 50 km long, was longer than the time required to cross the Atlantic ocean and the railway appeared the better solution to resolve this problem; in 1829 a competition was published for the building of the best locomotive with an award of 500 pound.

The characteristics that this machine should had was:

- low weight, less than 6 t;
- move at 16 km/h with a load of 20 t.

On 6 October 1829 *George and Robert Stephenson* won the competition with their *Rocket* locomotive that can be considered the first modern steam locomotive equipped with all the principal mechanisms of the modern machines.

The competition included besides the building of a new locomotive also the construction of a railway line between Liverpool and Manchester and this line was the first important railway

of the story. In fact, on 15 September 1830 the line Liverpool-Manchester was inaugurated and with this event began the railway age.

In the first year of operation the line transported more than ten time the usual number of passengers and already in 1843 the railway was long 3274 km and in 1855 the lengh increases to 13315 km.

After the *Rocket*, the *Robert Stephenson & Co*. built some other locomotives, like the *Northumbian*, the *Planet* that drew a train of 80 t, the *Samson* and in 1833 the *Patentee*, covered with a patent. This new machine opened the development of the railway transportation in all the countries of Europe included Italy. In this occasion the gauge adopted by Stephenson, 1435 mm, was adopted in all countries even if in some cases other locomotive builder chose a different gauge, as *Isambard Kingdon*, head of the *Great Western Railway*, who adopted in 1835 a larger gauge, 7 foot equal to 2134 mm, and he built the railway London-Bristol.

But since the costs for the railway adjustments for the different gauges were too expensive, as near the switches and in proximity of the stations where one could find also three different gauges, the British Government promulgated the famous *Gauge Act* that fixed the *Stephenson gauge* as the universal gauge to use in all railway lines and except in some cases, all of these was conformed.

The development of the railway transportation in the rest of the world was very different depending from the various countries. In Italy the first railway was the *Naples-Portici* line inaugurated on 3 October 1839 with a Patentee locomotive named *Vesuvio* and produced by *Longridge & Starbuck*. This locomotive transported King Ferdinando for a distance of 7.5 Km. The design and the capitals was French while the builder was *Armand Bayard de la Vingtrie*. In 1840 was built the first Italian plant for the construction and reparation of the locomotives: the *Pietrarsa plants*. After *the two Sicilies kingdom*, it was the turn of the *Lombardo-Veneto state* that built in 1840 the *Milan-Monza* railway and in 1842 was the time of the *Padua-Mestre* railway. In 1844 the *grand duchy of Tuscany* built the *Pisa-Leghorn* line. In 1848 the *Sardegna kingdom* built the Turin-Moncalieri line 8 km long and in 1853 the first important *Turin-Genoa* line with its tunnel long 3255 m under the Giovi crossing. In 1861, the year of birth of the Italy kingdom, the situation was the following: 101 km of railway in the *Pontificial state*, 305 km in the grand duchy of Tuscany, 187 km in the two Sicilies kingdom, the line *Piacenza-Bologna* (1859) and the *Bologna-Rimini-Ancona* line (1861).

During the first world war the railway transportation had a fundamental importance: in three years more than 15 million of men and twenty million of tons of materials and ammunitions were transported with a mean of 270 trains at day. During the fascism age there was a large development of the railway transportation in Italy (*Rome-Naples* line in 1927 and *Bologna-Florence* line in 1934).

1.2 - The railway track

The track is one of the most important element in the railway study. Its principal function is to operate as a guide for all the wheel-sets of the train and to support all the loads transmitted from the wheels to the rails and to damper the vibration generated during the motion.

The form of the track can be rectilinear or curvilinear, with or without inclination. The radius of curvature of the track depends from the railway importance and from the maximum velocity of the train. For modern high speed trains, moving with velocity higher than 250 km/h, the minimum allowed radius is very large, generally about 4000 – 5000 m; for mountain track, where the inclination is higher than $30‰$, the minimum allowed radius is about 250 m. In particular cases, for example in the urban transports, the radius can be also 60 m. In the cases in which the gauge is lower than the standard one, the minimum allowed radius is reduced. Obviously every railway has a maximum admissible train velocity depending from its minimum radius and its maximum inclination.

The values of the minimum allowed radius $R_{\min}$ and the maximum allowed inclination $i_{\max}$ adopted in Italy are reported in table 1.2 by respect to the maximum admissible velocity $V_{\max}$.

$i_{\max}$ $(‰)$	$R_{\min}$ (m)	$V_{\max}$ (Km/h)
30	250	74
25	410	95
20	550	110
16	650	120
13	750	128
11	840	135
8	900	140
<6	>1000	<150

Table 1.2
Relation among the maximum allowed inclination, the minimum allowed radius and the maximum admissible velocity on a curved track.

1.3 - The track system

The generic railway line can be distinguished in two subsystems: the superstructure or track and the subgrade.

The first subsystem includes the rails, the sleepers and the track supports, while the second one includes the base and the formation layer.

The rails support the load and guide the train wheels; the sleepers distribute the loads applied and keep the rails at constant distance; the ballast also distributes the load, damps the train vibration and ensures a fast drainage of the rainwater.

Figure 1.3 show a scheme of the superstructure and the subgrade.

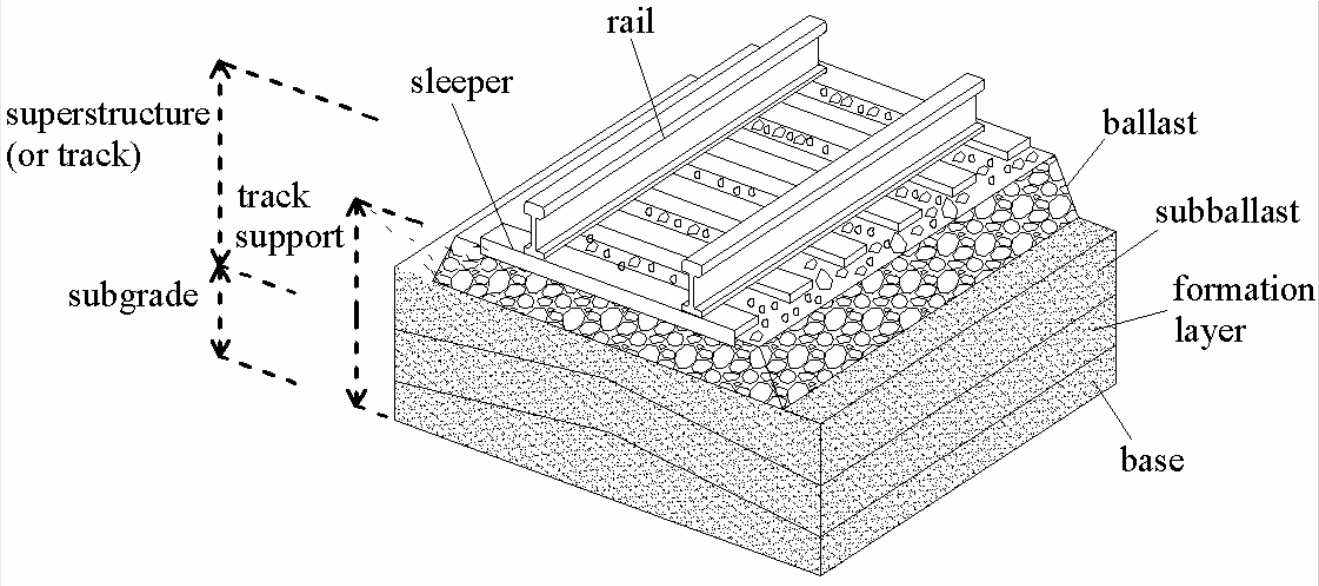

Figure 1.3
Scheme of a conventional track structure

1.4 – The rails

The rails are the supporting parts with which the wheels are in contact. They are steel made and must resist to the heavy vertical and transverse loads transmitted by the wheels. They are assimilated to a continuous beams put on distributed supports. The transverse section is like a double “T” to guaranties the maximum inertia moment with the same area. The principal parts of the rails are: the *head*, that is in contact with the wheels, the *foot* that is connected with the sleepers and the *web* that connects together the head and the foot.

The rails are classified as function of the weight of a piece long 1 m.; for example the type *UNI 60* have a weight of 60 kg per linear meter.

Today all the dimensions are standardized. In Italy the types more used are: *UNI 21, UNI 27, UNI 30, UNI 36, UNI 46, UNI 50, UNI 60* ; the last one is also named *UIC 60* and it is the most used in the new constructions and in the renovation of the old ones. This rail type are produced in two different lengths: 36 and 48 m.

Generally the rails are inner tilted with a cone angle (mostly 1/20): the inclination increases the stability during the motion and permits the wheel-set to remain centred by respect to the track axis; moreover the cone angle compensates the absence of the differential between the two wheels in curve where they have the same angular velocity because rigidly mounted on the wheel-set axle; the wheel tread has a cone angle, generally equal to the rail one.

The distance between the two rails is named *gauge*. Different types of gauges exist depending from the country. The most used is the *standard gauge* defined as the distance between the inner sides of the rails, measured 14 mm below the rolling plane. Tracks with different gauge exist and it varies from 0.6 m to 1.676 m; some examples are the following:

- the mentioned *standard gauge*, equal to 1.435 m with a maximum permissible range of +10 mm and -3 mm;
- the *broad gauge*, equal to 1.524 m (Russia) and 1.672 m (Spain) adopted mainly for political reason to prevent the movement of foreign trains into the national railway;
- the *metric gauge*, equal to 1.000 m or 1.067 m;
- the *reduced gauge*, equal to 0.95 m used in many European railways. The adoption of a reduced gauge permits to economize on the railway building, especially in the mountain line where the railway construction is more difficult and expensive than in the plain, because of the presence of many curves and tunnels.

Generally where the track is curved the gauge is increased to facilitate the circulation of the wagons without bogies, having the wheel-sets mounted with large distance. The gauge expansion depends from the track radius: in Italy the expansion is applied where the radius is less than 484 m and it is 5 mm; the maximum expansion applicable is 30 mm used where the radius is less than 300 m. In every cases the expansion is applied on the inner rail and the transition between the rectilinear to the curvilinear gauges is gradually made (1 mm for each meter of track where $V_{\max} \geq 70\,{}^{Km}\!/_{h}$ and 2 mm/m where $V_{\max} < 70\,{}^{Km}\!/_{h}$).

Figure 1.4 shows the transverse sections of three types of rails: the first, named *Vignola* (by its inventor *Charles Vignolas*) is the most used in the railroads while the second and third types are used in the urban transport; the last type is used in the curve.

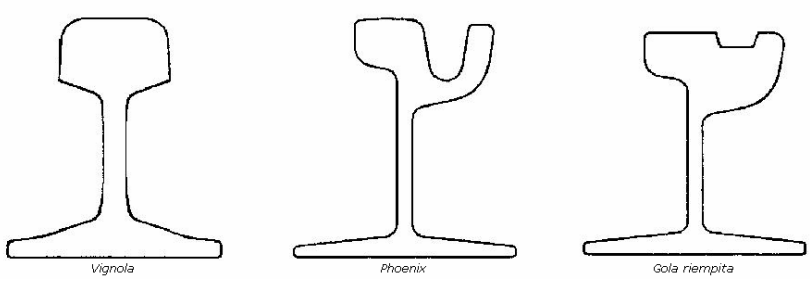

Figure 1.4

Transverse sections of rails

1.5 - The sleepers

The sleepers are the transverse elements mounted orthogonally to the track axis. They have the function to connect the two rails in such manner that their distance remains constant during the time and to transmit the load from the rails to the supports. Generally the sleepers are in wood made or in reinforced concrete, in some cases also in steel, and they can be created in monobloc or bibloc forms. The dimensions depend from the track characteristics (i.e the gauge) and the train type; in every cases they are standardized. They can be made by different wood types: oak, English oak, Scot pine and they can be mounted naturally or soaked with a particular antiseptic. In Italy the dimensions and the treatments are regulated by the *UNI 7407*.

The concrete sleeper type has generally the monobloc form, made with prestressed concrete and reinforced with high resistance steel bars. This type are used for the new constructions and for the old ones renovation. In some cases, for instance in the underground sides, the sleepers can be absent because the rails are directly fixed to the floor by means of particular elastic connections.

The distance between the sleepers depends from the track importance: in Italy there exist three categories: *principal lines*, *medium importance lines* - used for wheel-set loaded at maximum with 16 t - and *secondary lines*; the sleeper distances are respectively 0.6 m, 0.666 m and 0.75 m.

1.6 - The track support

Usually the track rests on ballast but there are some cases in which the support is formed by a concrete slab. In the first case the support is flexible while in the second case it is inflexible. The slab track is used in some networks as in the. Japanese and German ones and in tunnels because it has a smaller cross-section and hence a cheaper maintenance. However the ballast type is preferred for its higher flexibility and transverse resistance, especially for high speed lines.

1.7 - The wheel-and-axle-set

The wheel-and-axle-set is the principal component of every railway system. It is formed by the wheel-set and the bushes; the wheel-set is composed by two wheels and an axle joined together to form a single mechanical part and it is the only non suspended part of the train. The wheel oneself is formed by two parts: the disc and the tread. The disc is directly mounted on the axle to form a unique block and the tread is joined on the disc at high temperature.
At the external extremity of the tread there is the flange that has the function to stabilize the wheel-set during the motion and maintains it on the railway.
At the extremity of the wheel-set there are two spindles where are mounted the bushes; this extremities sustain the carriage through the suspension system. On the wheel-set axle are mounted the brake disks that furnish a wide surfaces for the brake shoes and they are furnished by wings to increase the heat transfer.
Figure 1.5 shows a wheel-set and its principal parts.

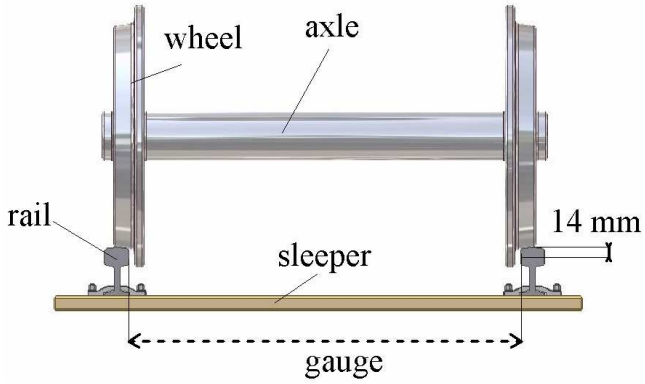

Figure 1.5
The wheel-set and its principal parts

CHAPTER 2

THE CMS DEVELOPED MODELS

2.1 - INTRODUCTION

The acronym CMS means “Commercial Multibody Software” . This software used for the creation of the railway models used to validate first and to compare then the code developed in Matlab environment aimed to analyze the railway systems. The CMS models regard the following systems:

- bogie with two wheel-sets;
- wagon with two bogies;
- the buffers-coupler system;
- train formed by two wagons.

2.2 – THE BOGIE MODEL

The bogie developed in CMS environment is formed by two wheel-sets, one frame and the primary suspension system. The suspension system connects the frame with the wheel-sets; it has the function to transmit the loads from the frame to the wheel-sets and to damp the mass motion. It acts along the three principal directions, that is the longitudinal, the transverse and the vertical ones and it is formed by 12 elements: 6 elastic and 6 viscous. Table 2.1 reports the principal mechanical and inertial characteristics of the primary suspension system while Figure 2.1 shows the CMS bogie model with the suspension system.

Wheel-set mass	1595 Kg	Longitudinal spring stiffness	10^6 N/m
Bogie frame mass	2469 Kg	Transverse spring stiffness	$2 \cdot 10^7$ N/m
Wheel profile	S1002	Vertical spring stiffness	$1.5 \cdot 10^6$ N/m
Rail profile	UIC60	Longitudinal viscous coefficient	$2.49 \cdot 10^3$ Ns/m
Wheel-set distance	2.5 m	Transverse viscous coefficient	$1.11 \cdot 10^4$ Ns/m
Wheel radius	0.457 m	Vertical viscous coefficient	$3.04 \cdot 10^3$ Ns/m
Rail gauge	1.360 m	Vertical length at rest	0.5 m
Inclination rail angle	1/20	Longitudinal length at rest	0.75 m
Transverse length at rest	0.3 m	Frame I_{xx}	1130 kgm^2
Wheelset I_{xx}	935 kgm^2	Frame I_{yy}	1140 kgm^2
Wheelset I_{yy}	174 kgm^2	Frame I_{zz}	2142 kgm^2
Wheelset I_{zz}	935 kgm^2		

Table 2.1
Masses, main dimensions and features of the bogie components.

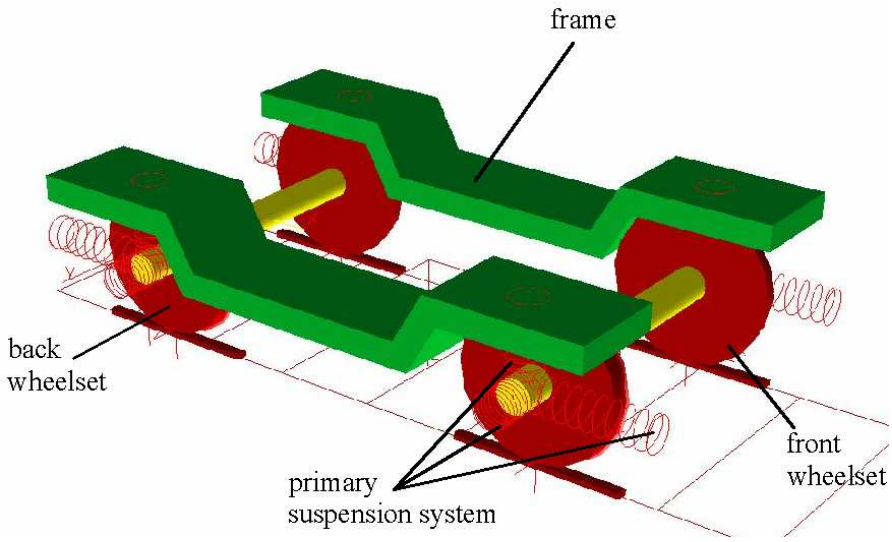

Figure 2.1
The CMS bogie model with the primary suspension system

2.3– THE WAGON MODEL

The CMS wagon model is formed by two bogies, one car body and the secondary suspension system. As for the bogie, the secondary suspension system transmits the loads from the car body to the bogies and damps the mass oscillations. It is formed by 6 elastic elements and 6 viscous ones that act along the longitudinal, transverse and vertical directions. Figure 2.2 shows the CMS wagon model and its suspension system while Table 2.2 reports the principal mechanical and inertial characteristics of the secondary suspension system.

a)

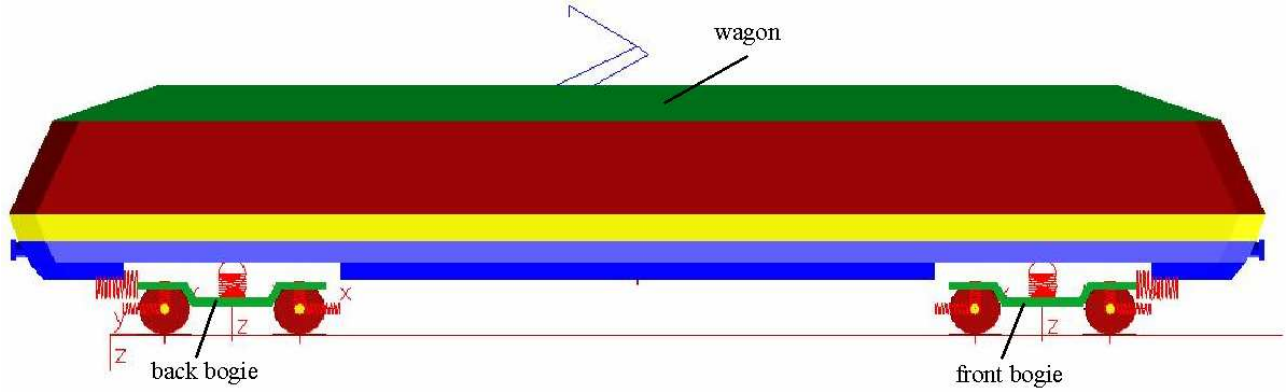

b)

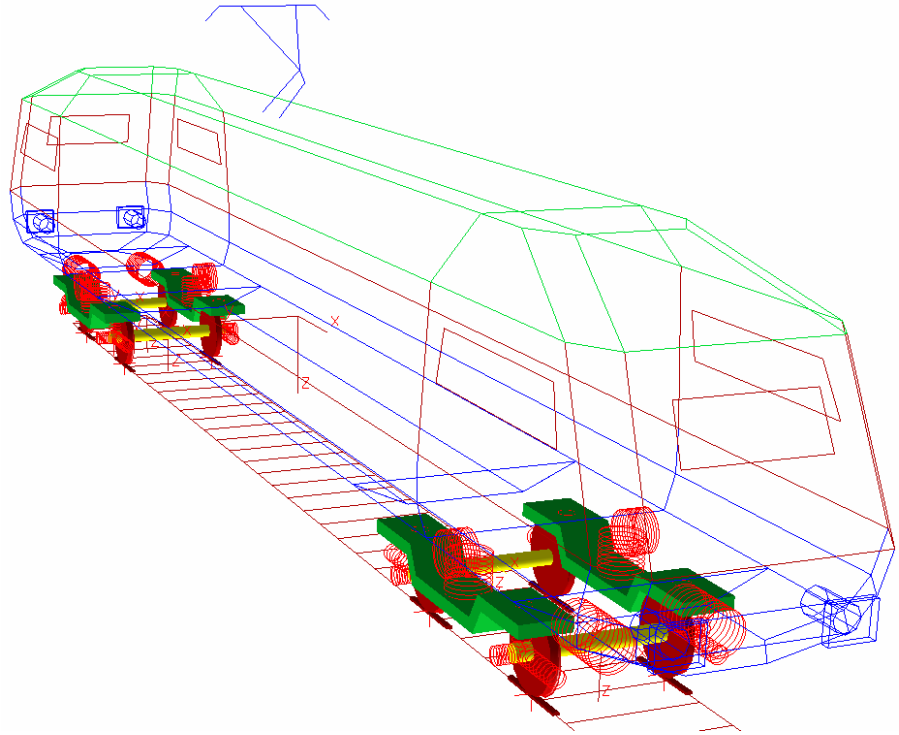

c)

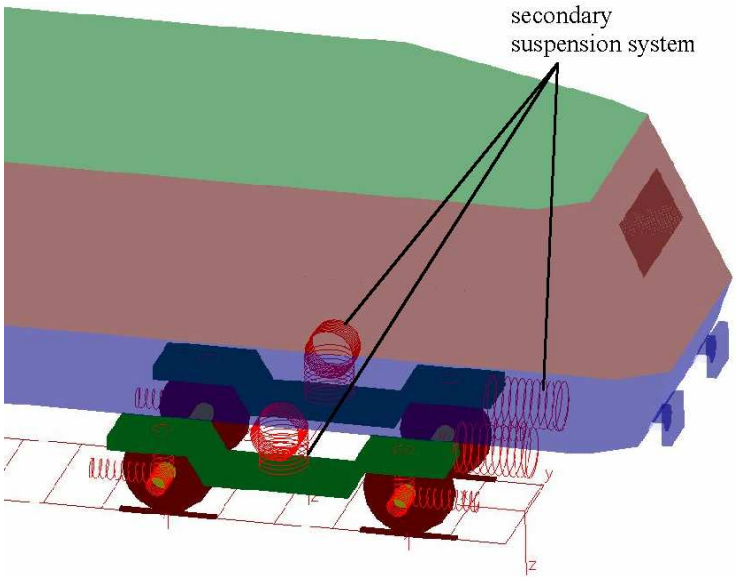

Figure 2.2
The CMS wagon model: a) the wagon with the two bogies; b) , c) particular of the secondary suspension system

Wagon mass	40816 kg	Vertical spring stiffness	$1.5 \cdot 10^5$ N/m
bogie distance	15 m	Longitudinal viscous coefficient	$3 \cdot 10^3$ Ns/m
Wagon I_{xx}	30000 kgm^2	Transverse viscous coefficient	$3 \cdot 10^3$ Ns/m
Wagon I_{yy}	687000 kgm^2	Vertical viscous coefficient	$3 \cdot 10^4$ Ns/m
Wagon I_{zz}	687000 kgm^2	Vertical length at rest	0.5 m
Longitudinal spring stiffness	$8 \cdot 10^6$ N/m	Longitudinal length at rest	0.75 m
Transverse spring stiffness	$5 \cdot 10^6$ N/m	Transverse length at rest	0.3 m

Table 2.2
Principal inertial and mechanical characteristics of the wagon and of the secondary suspension system.

2.4 – THE BUFFERS

The buffers principally carry out two functions:

- they maintain constant the distance between two consecutive wagons or between the locomotive and the first wagon;
- they damp the longitudinal motion between two consecutive wagons.

There are various buffer types with different shapes depending from the convoy category and from the track characteristics as the gauge; they can be single or double. The most used type is the *plate-piston* one, that makes very fast the change of the train configuration. Recently, because of the rapid development of the high-speed trains with fixed configuration, more complex integrated types have been developed, based on pneumatic systems.
The plate-piston buffer is formed by the following parts:

- the piston;
- the cylinder;
- the plate;
- the elastic-viscous elements for the absorption of the loads.

Figure 2.3 shows a scheme of the plate-piston type. In order to make better the response of the buffer during the crash, its elastic element is characterized by an hysteresis behaviour, i.e. it has a variable stiffnesses during the leaving and approach phases and its value depends from the displacement of the piston. Figure 2.4 shows the elastic stiffness of the buffer used in the CMS model in function of the piston displacement when it is in approach and in leaving.

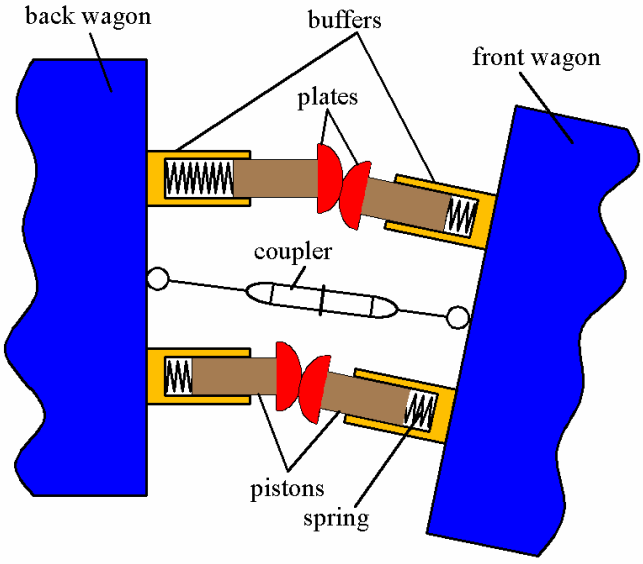

Figure 2.3
The buffer and the coupler systems.

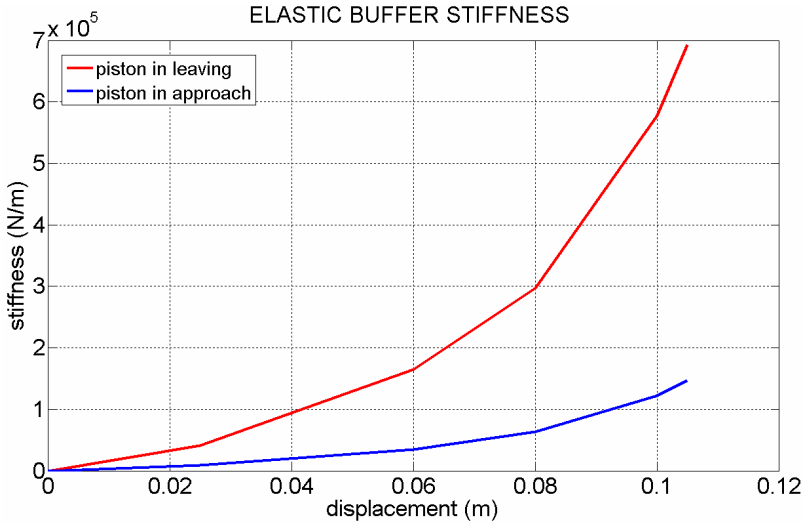

Figure 2.4
The buffer stiffness during the approach and leaving phases.

2.5 – THE COUPLER

The principal function of the coupler is to transfer the draught from the front to the back wagon. Many coupler configurations have been designed but the most used is the *chain* type having at minimum two links, a central threaded element to put it in tension and a hook having different shapes (see Figure 2.3). As the buffers, the coupler is characterized by an hysteresis behaviour with its elastic stiffness function of the displacement, from the phases of the movement of the wagons (in approach or in leaving). Figure 2.5 shows the elastic stiffness of the coupler used in the CMS model in function of the coupler end displacements when it is in approach or in leaving.

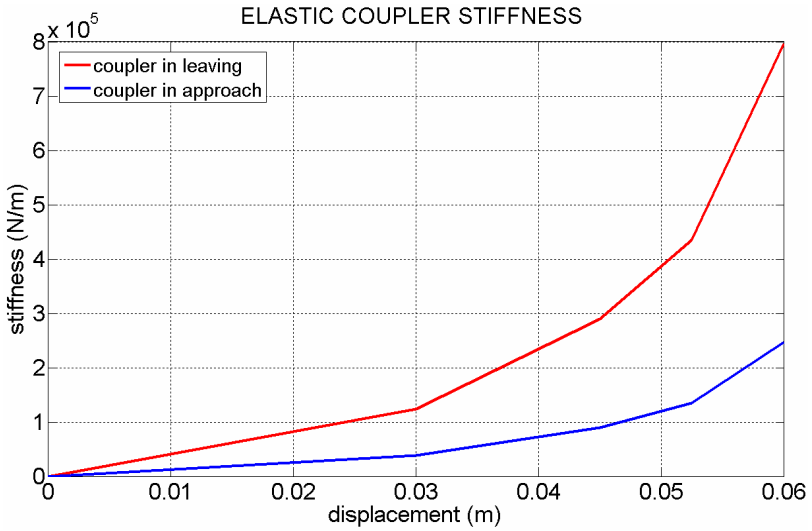

Figure 2.5
The coupler stiffness during the approach and leaving phases.

2.6 – THE CMS BUFFERS-COUPLER MODEL

A CMS buffers-coupler model has been developed in order to permit the linking of two consecutive wagons in the CMS train model; it is formed by the following parts:

- buffer cylinders;
- buffer pistons;
- piston plates;
- a coupler;
- two connecting plates.

The system is assembled in the following mode (see Figure 2.6):
The two cylinder pairs of the buffers are fixed with the respective connecting plates.
The two piston pairs of the buffers are coupled with the respective cylinders through cylindrical connections.
The piston plates are fixed with the buffer pistons.
The coupler is modelled with a piston and a cylinder both coupled through a spherical connections with the two connecting plates.
All the elastic elements are characterized by hysteresis as shown in Figure 2.4 and 2.5.
In order to make the system more realistic, the buffer plates are modelled with a segment of sphere having radius equal to 0.5 m

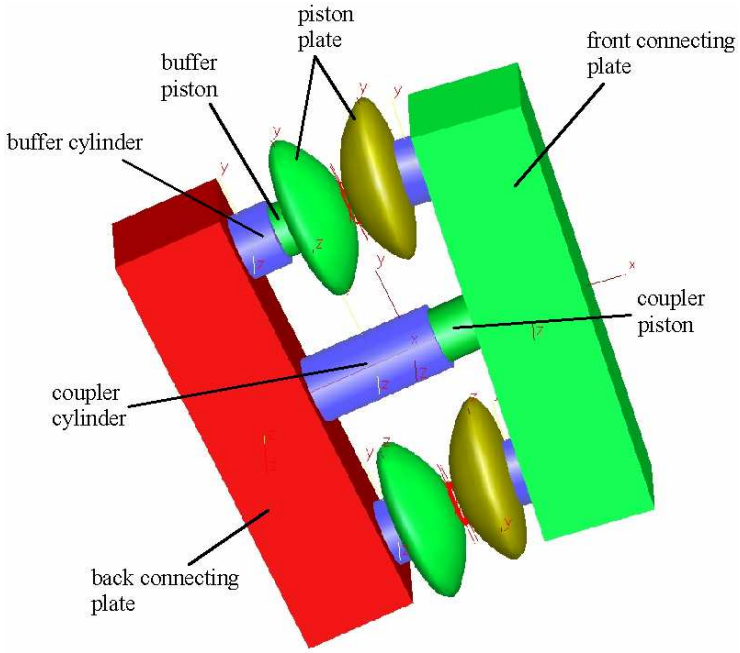

a)

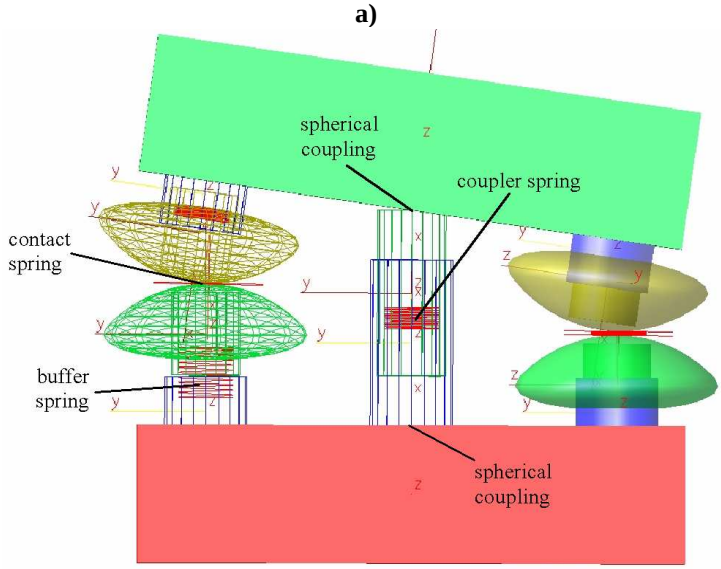

b)

Figure 2.6
Scheme of the buffers-coupler CMS model.

The contact force between two buffer plates can be divided in two components: the normal and the tangential ones. The normal component $\vec{N}$ is directed along the normal versor $\vec{n}$ to the surface in the contact point and its value is proportional to the maximum normal indentation c between the two plates and to the elastic stiffness k_c set equal to $70 \cdot 10^9$ N/m. The expression of $\vec{N}$ is the following:

$$\vec{N} = k_{el} c \vec{n}$$

The tangential component $\vec{T}$ belongs to the tangential plane and it is parallel to the relative velocity between the two bodies in contact and its value is calculated assuming the Coulomb's friction model with the friction coefficient μ set 0.1. The expression of $\vec{T}$ is given by:

$$\vec{T} = -\left|\vec{N}\right|\mu\,\vec{t}$$

where $\vec{t}$ is the versor parallel to the relative velocity of the two plates in the contact point.

Figure 2.7 shows the two components of the contact force between the two buffer plates in contact.

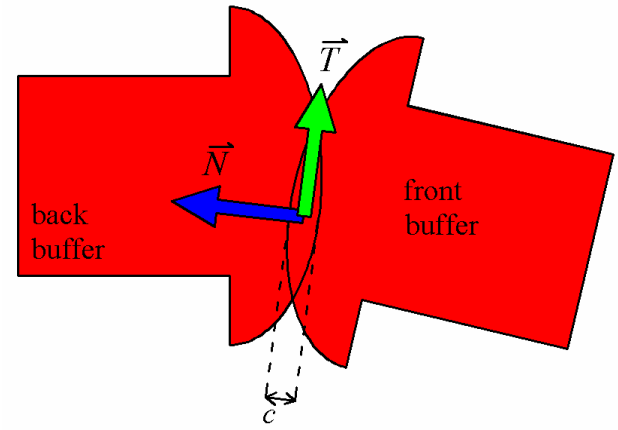

Figure 2.7
The two components of the contact force between the two buffer plates in contact.

2.6.1 – Validation of the CMS model

In order to validate the results achieved with the CMS model, it has been developed a similar model in Matlab environment. The new model is a simplified version of the CMS model; the variations regard the buffer plates that are replaced with two contact springs acting between the buffer pistons. All the remaining parts are unaltered. The motion of the original model (Figure 2.6) and that of the simplified version (Figure 2.8) coincide when the movement of the masses are one-dimensional i.e. it evolves along the symmetry axis. This event occurs when the following conditions are verified:

- the external force is directed along the coupler axis (axis of symmetry);
- the initial kinematical conditions are symmetric respect the coupler axis.

Under these conditions the two systems are equivalent. The scheme of the simplified CMS model is shown in Figure 2.8 while the scheme of the Matlab simplified model is reported in Figure 2.9 where are also showed the simplification due to the symmetry.

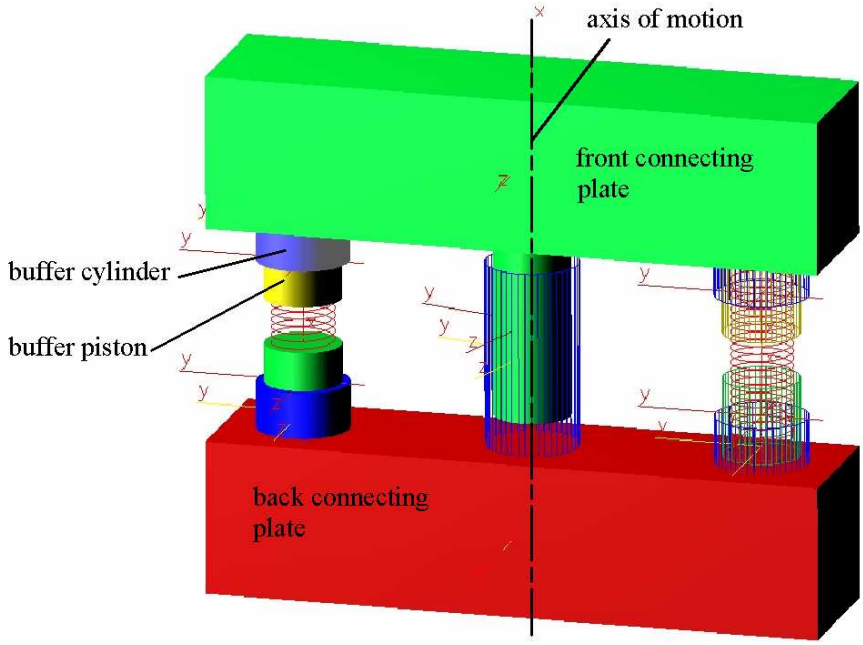

Figure 2.8
The CMS simplified version of the buffers-coupler model.

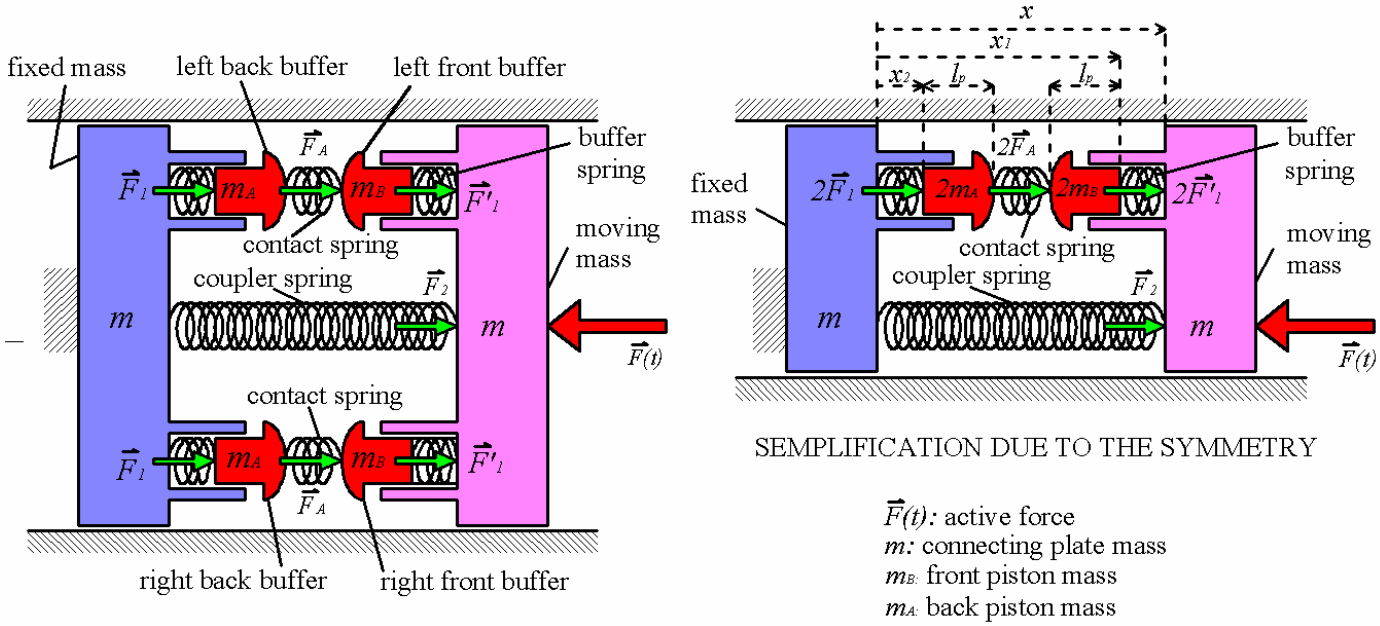

Figure 2.9
The Matlab simplified scheme of the buffers-coupler model.

The masses of the system are the following:

m_A=500 Kg

m_B=500 Kg

m=33000 Kg

During the simulation the active force has the following expression:

$F(t) = Asen(Bt)$
where
$A = 150000\ N$
$B = 50$

The elastic stiffnesses k_c of the contact springs is $200000\ N/m$ The buffer and coupler springs have a hysteresis behaviour; the following figures report the stiffness of the buffers and the coupler springs:

- front buffer: Figure 2.4;
- back buffer: Figure 2.10;
- coupler: Figure 2.5.

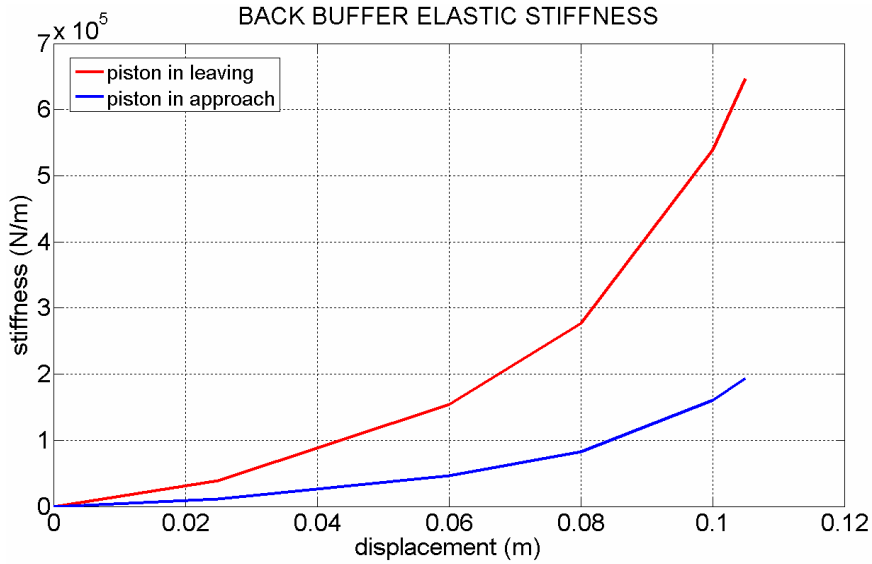

Figure 2.10
The back buffer stiffness during the approach and leaving phases.

The positions of the masses m_A, m_B, m are named respectively x_2, x_1, x and they are measured respect to the fixed mass. The initial conditions are the following:

$x_1(0) = 0.5$ m;
$x_2(0) = 0$ m
$x(0) = 0.5$ m.
$\dot{x}_1(0) = \dot{x}_2(0) = \dot{x}\ (0) = 0.$

the length l_p is equal to 0.25 m. The three masses motion equations are the following:

$$\begin{cases} 2m_A \dfrac{d^2x_2}{dt^2}\vec{i} = 2\vec{F}_1 - 2\vec{F}_A \\ 2m_B \dfrac{d^2x_1}{dt^2}\vec{i} = 2\vec{F}_A + 2\vec{F}_1' \\ m\dfrac{d^2x}{dt^2}\vec{i} = -2\vec{F}_1' + \vec{F}_2 + \vec{F}(t) \end{cases}$$

where the symbols have the following meaning:

$\vec{F}_1$ is the force generated by the back buffer spring on the buffer piston;
$\vec{F}_A$ is the force generated by the contact spring on the front buffer piston;
$\vec{F}_1'$ is the force generated by the front buffer spring on the buffer piston;
$\vec{F}_2$ is the force generated by the spring coupler on the moving mass m.
$\vec{F}(t)$ is the external force acting on the mass m

The values of the elastic forces depend from the mass positions and from the spring elastic characteristics as follow:

$$\begin{cases} \vec{F}_A = k_c\left(x_2 - x_1 + 2\cdot l_p\right)\cdot\vec{i} \\ \vec{F}_1 = f_1\left(x_2, k_1\right)\cdot\vec{i} \\ \vec{F}_1' = f_1'\left(x - x_1, k_1'\right)\cdot\vec{i} \\ \vec{F}_2 = f_2\left(x - l_0, k_2\right)\cdot\vec{i} \\ \vec{F}(t) = F(t)\cdot\vec{i} \end{cases}$$

the symbols have the following meaning:

$\vec{i}$ is the versor parallel to the coupler axis directed from the back to the front buffers;
k_c is the elastic stiffness of the contact spring;
k_1 is the elastic stiffness of the back buffer spring; it depends from the displacement of the mass m_A and from the fact if the mass is in approach or in leaving, as shown in Figure 2.10;
k_1' is the elastic stiffness of the front buffer; it depends from the m_B and m displacements and from the fact if the masses are in approach or in leaving, as shown in Figure 2.4;
k_2 is the elastic stiffness of the coupler; it depends from the displacement of the mass m and from the fact if the mass is in approach or in leaving, as shown in Figure 2.5;
l_0 is the length at rest of the coupler spring, equal to 0.5 m.
The functions f_1, f_1', f_2 define the force values under the following conditions:
$\vec{F}_2$ is null when the coupler is not in tension, that is when $\left(x - l_0\right) \le 0$;
$\vec{F}_A$ is null when the buffers are not in contact, i.e. when $\left(x_2 - x_1 + 2\cdot l_p\right) \le 0$

Figure 2.11 shows the applied active force respect to time while Figures 2.12-2.17 report the comparison of the displacements of the three masses and their velocities obtained by means of the CMS and Matlab models.

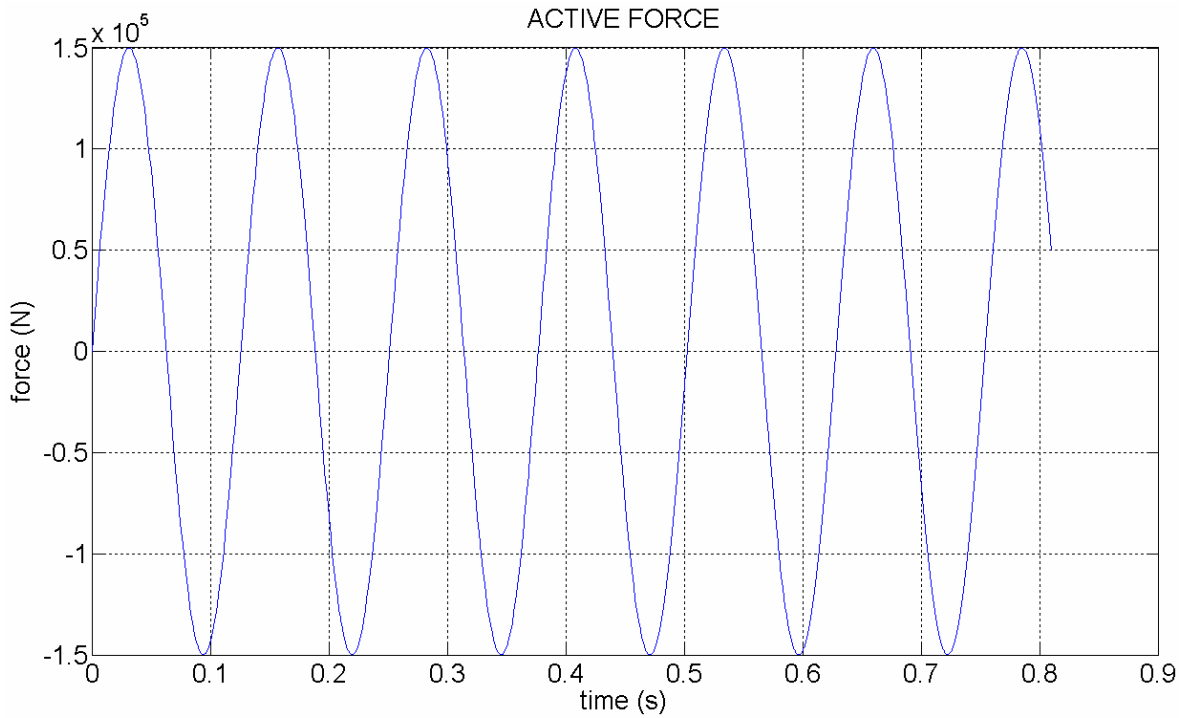

Figure 2.11
Active force respect to time

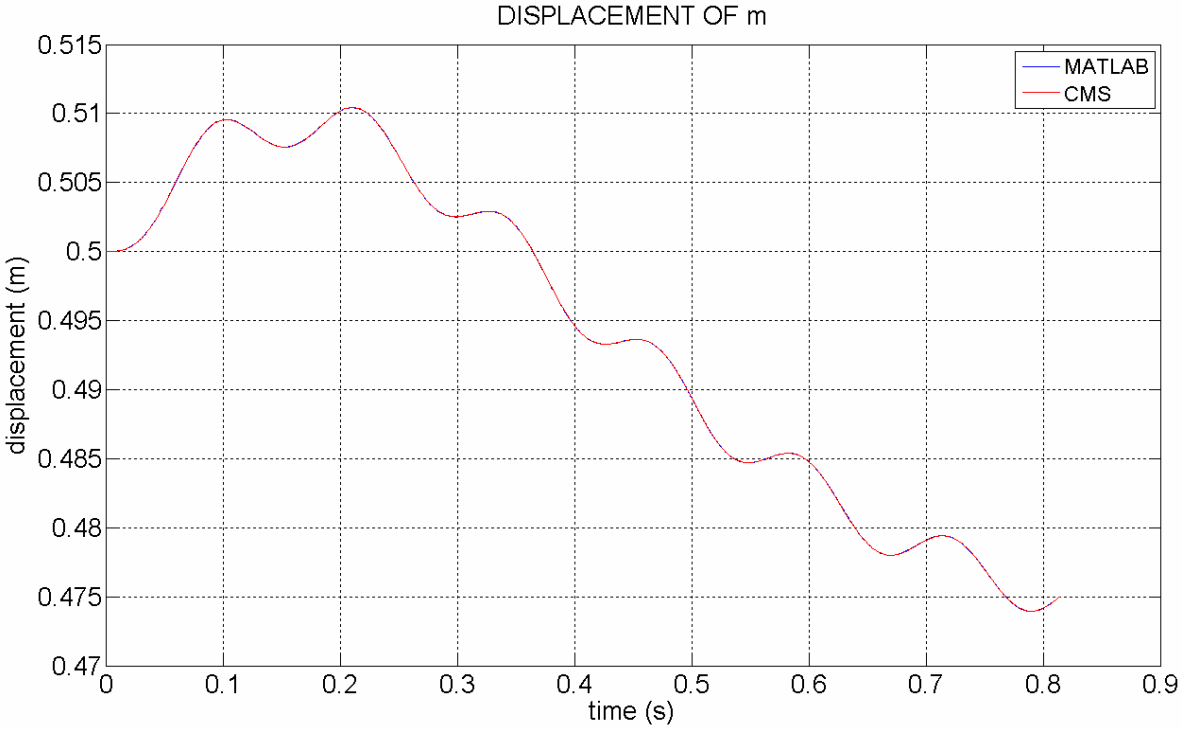

Figure 2.12
Comparison between the displacements of m in the CMS (red curve) and Matlab (blue curve) models.

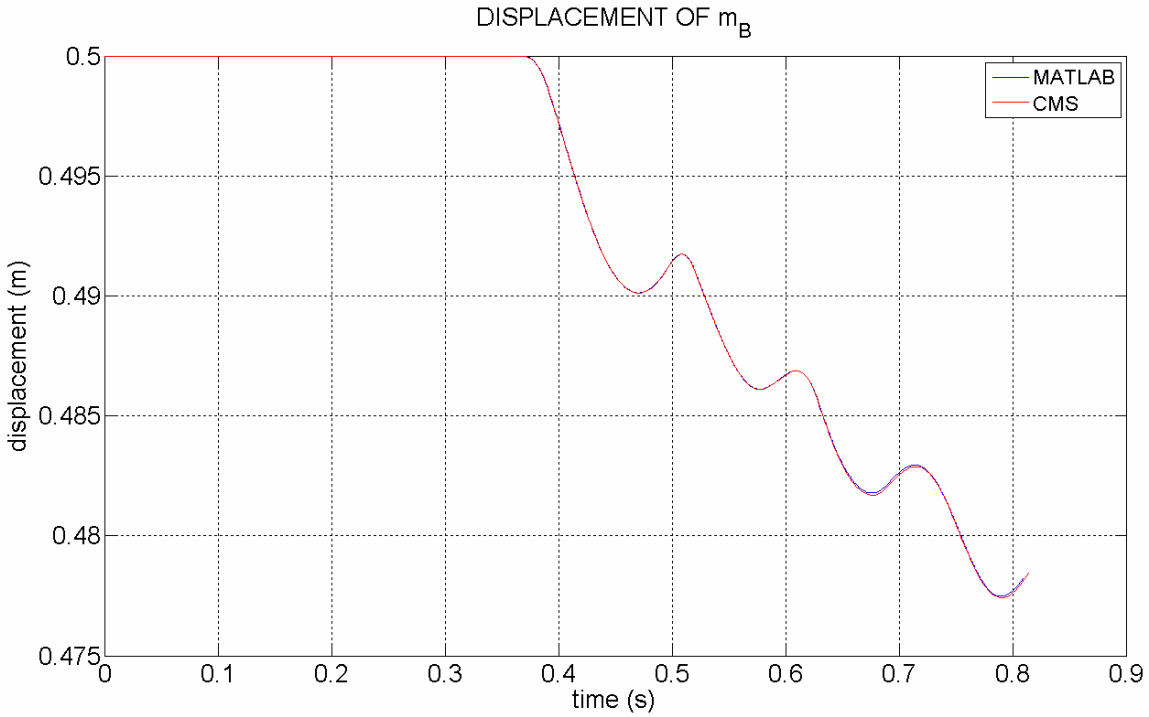

Figure 2.13

Comparison between the displacements of m_B in the CMS (red curve) and Matlab (blue curve) models.

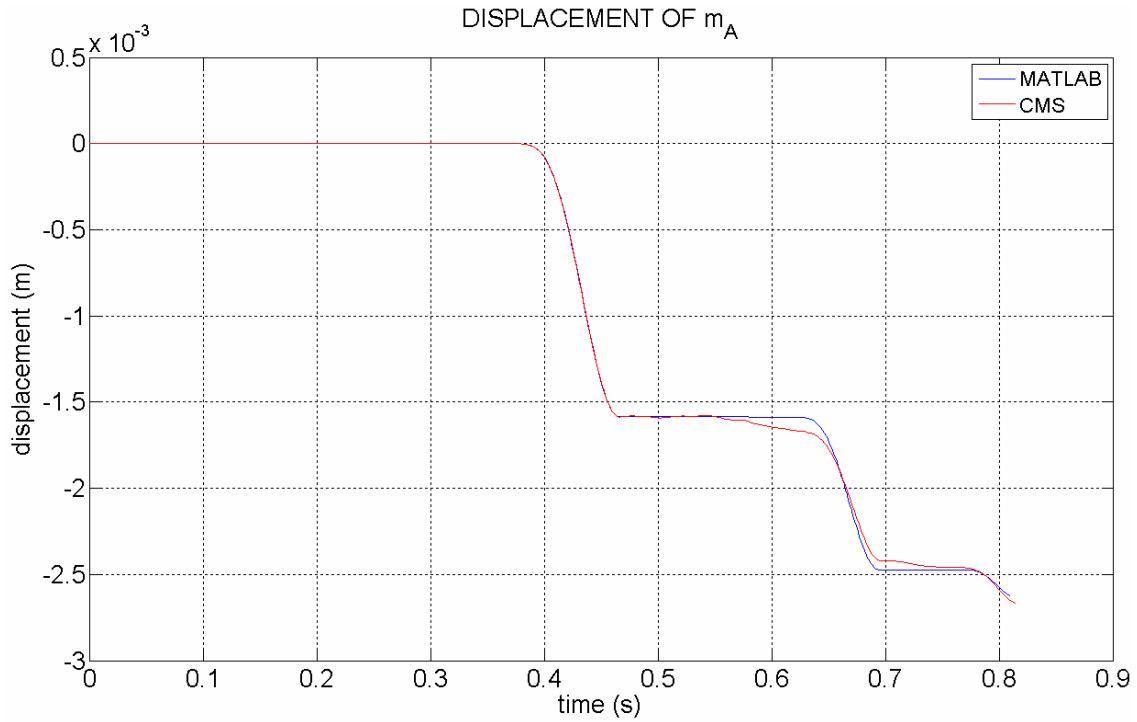

Figure 2.14

Comparison between the displacements of m_A in the CMS (red curve) and Matlab (blue curve) models.

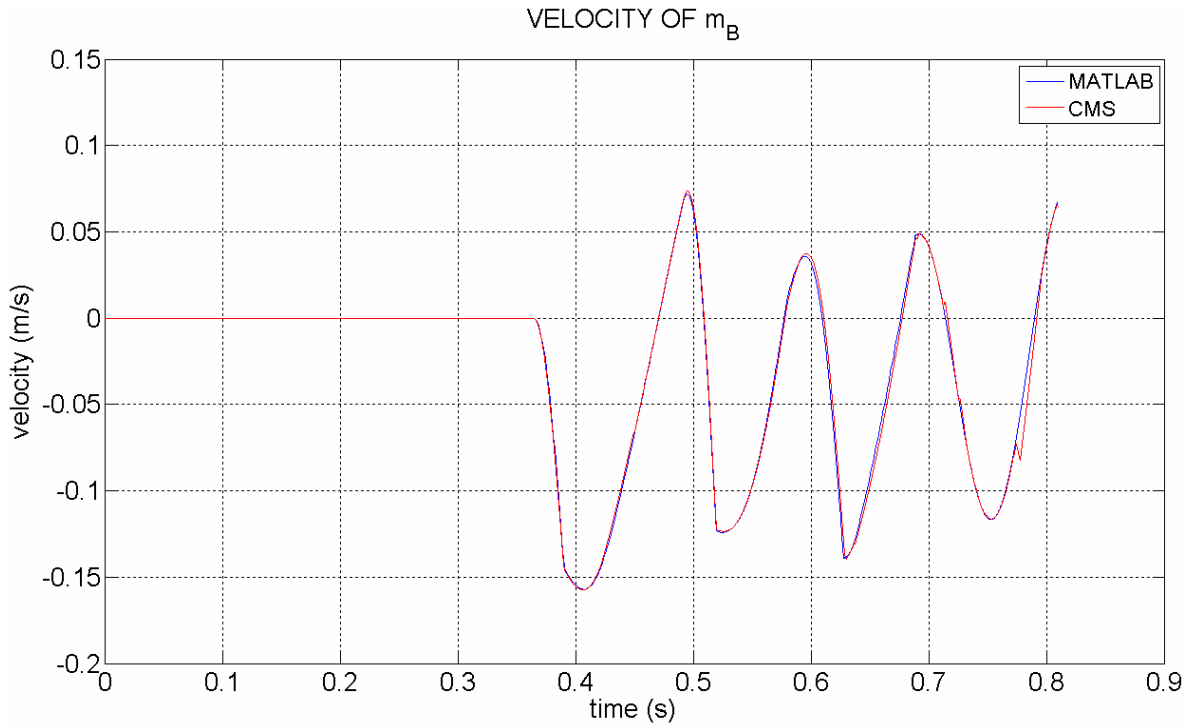

Figure 2.15

Comparison between the velocities of m_B in the CMS (red curve) and Matlab (blue curve) models.

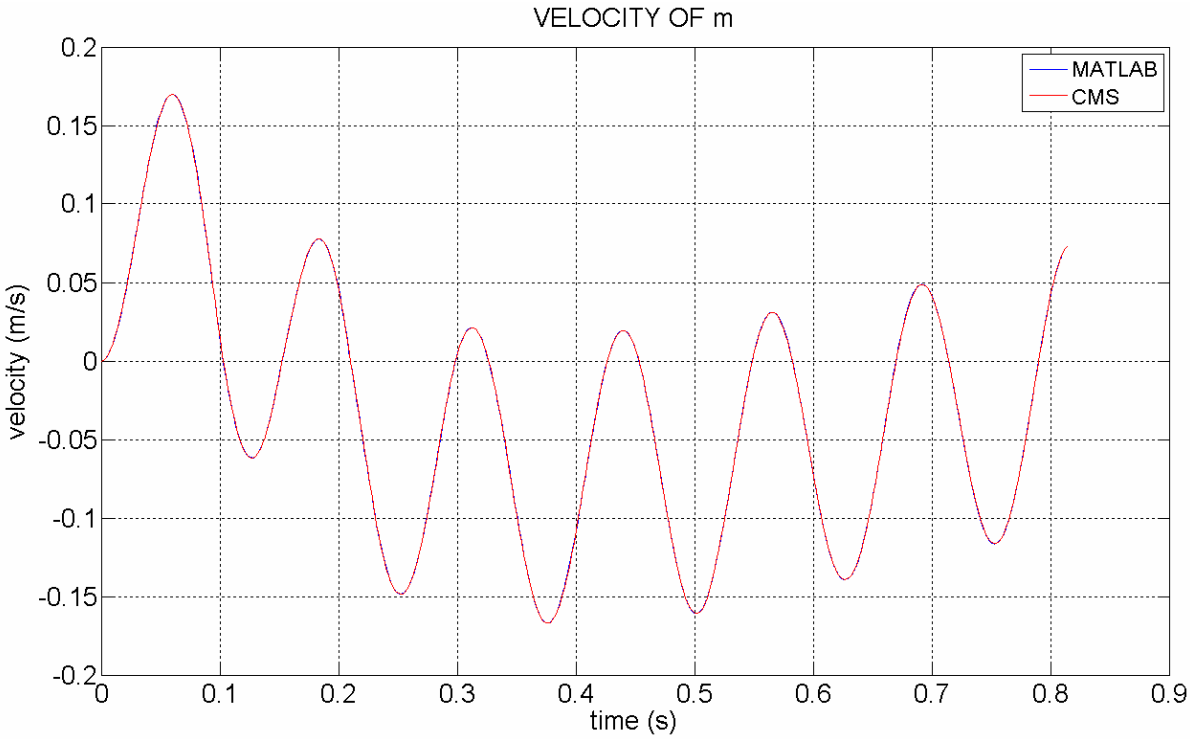

Figure 2.16

Comparison between the velocities of m in the CMS (red curve) and Matlab (blue curve) models.

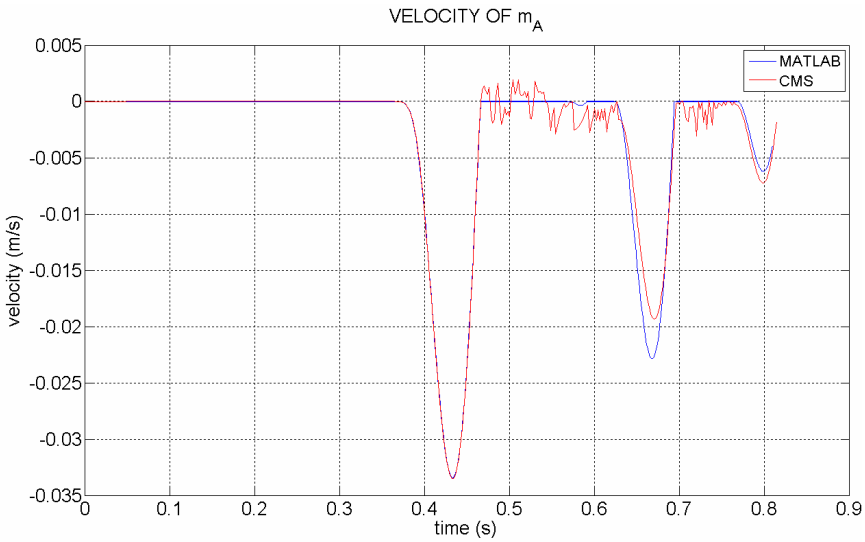

Figure 2.17

Comparison between the velocities of m_A in the CMS (red curve) and Matlab (blue curve) models.

2.7 – THE CMS TRAIN MODEL

The CMS model of the train is formed by two wagons connected together by means of the buffers-coupler system described in paragraph 2.6. The buffers-coupler system is joined with the wagons through the two connecting plates. During the motion the buffer plates crash one against the other and the coupler transmits the draught from the front to the back wagons. The front wagon is put in movement by an engine couple applied to its wheel-sets.

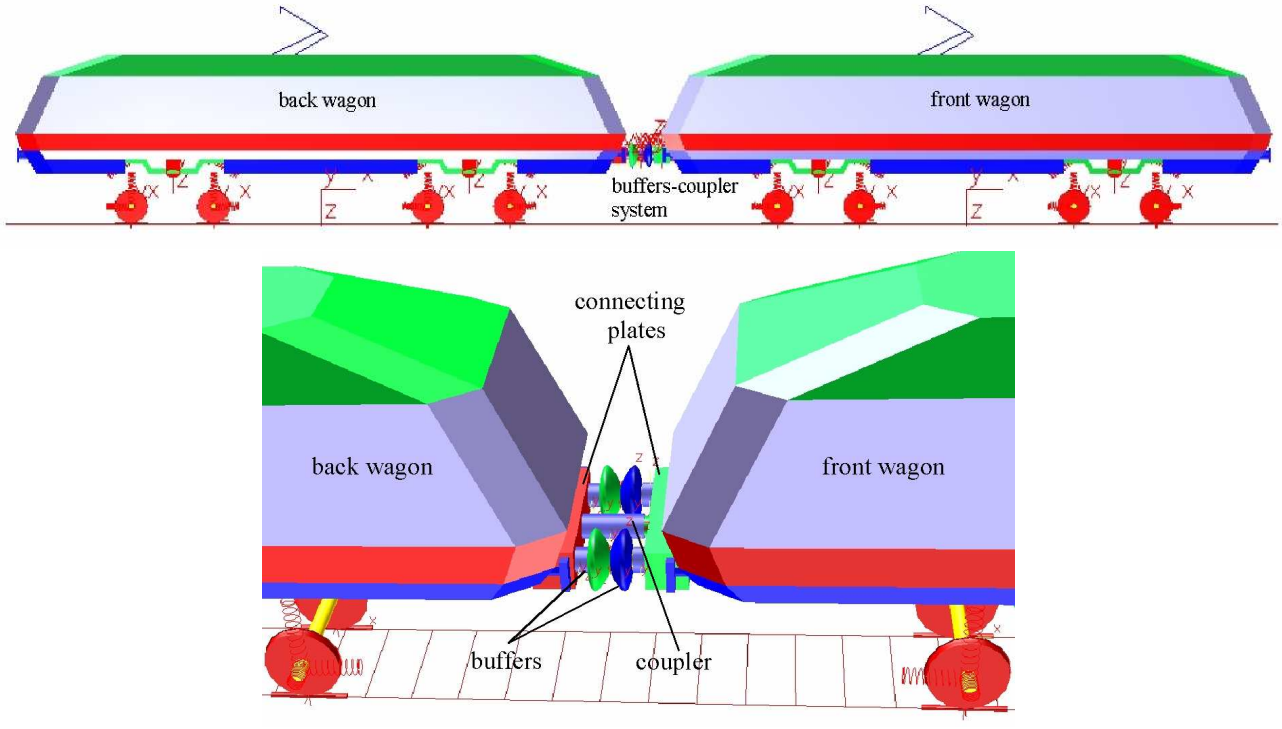

Figure 2.18
The CMS train model

C H A P T E R 3

THE ROLLING-CONTACT THEORIES

3.1 - INTRODUCTION

The determination of the contact forces between the wheel and the rail is one of the fundamental problem in a dynamic analysis of a railway system. Various contact models have been developed. In this chapter a rigid body contact is discussed, with particular reference to the *Hertz's* theory and to the wheel/rail creep forces.

The contact between two bodies can be possible in one point or area, depending from the shape of the two surfaces. In the first case we have a *nonconformal* contact while in the second one a *conformal* contact. When a load is applied on the two bodies in the case of a nonconformal contact, they deform at the contact point to form a contact area that is very small as compared with the dimensions of the bodies.

In 1882, *Heinrich Hertz* presented its contact theory that accounts for the shape of the two bodies in proximity of the contact point. The theory assumes that the contact area is elliptic.

Generally, in wheel-rail interaction the nonconformal model is used, in spite of the wheel and rail surface are significantly different in the region of contact.

Due to the elasticity of the bodies and to the normal forces applied, some points in the contact region may sleep or stick when the two bodies are moved one respect to the other.

The difference between the tangential strains in the adhesion area generates the creepages that are defined considering the kinematic of the two bodies.

The creepages generate the tangential creep forces and the creep spin moment. The creep forces and moment have a significant effect on the stability of a railway system.

The force transmitted between the contact surfaces can be evaluated through different rolling contact theories. For a better understanding, in Figure 3.1 a scheme showing the theories, their relationships and interrelations is drawn. Authors and the period of development are reported too.

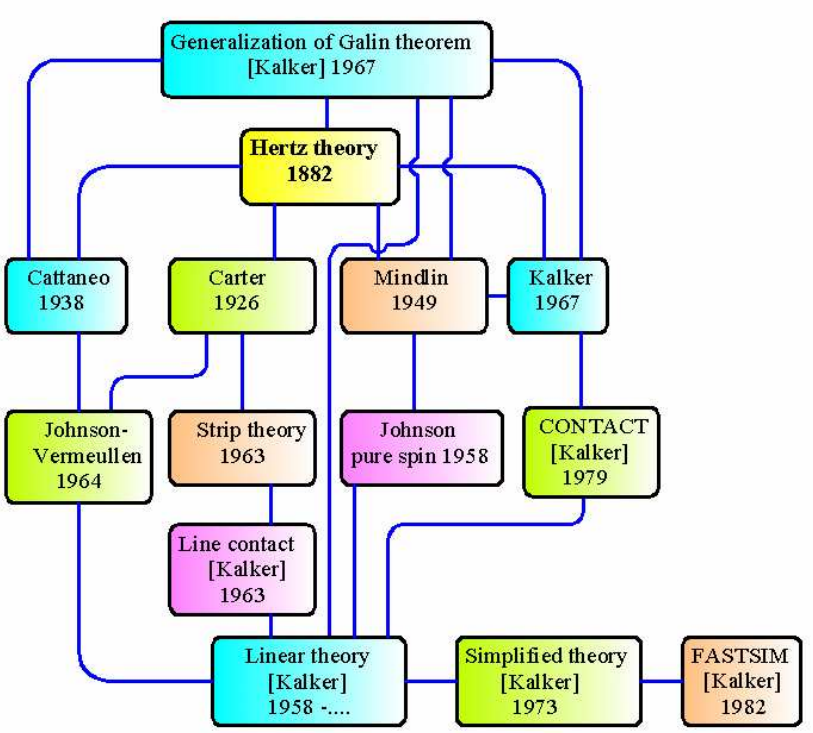

Figure 3.1

Scheme of the various rolling contact theories and relative authors ([2])

In the figure the connecting lines indicate a theoretical link between theories.

The most used theory in multibody softwares is the *Kalker's FASTSIM algorithm* [2]. This algorithm is based on the Kalker simplified theory in which the contact surfaces are replaced by a set of springs. The advantages of the method are simplicity of conception and operational speed. FASTSIM is 1000 times faster than the *Kalker's CONTACT algorithm* which is based on the so called *Kalker exact theory*. However, results accuracy is about 15% lower than experimental evidences.

Polach [27] recently developed a method faster than FASTSIM. This method offers a trade off between calculation time saving and accuracy.

FASTSIM is embodied in commercial multibody softwares such as ADAMS/rail, SIMPACK, MEDYNA, GENSYS, VOCO.

3.2 – THE HERTZ THEORY

In 1882 Hertz (Figure 3.2) presented its contact theory. In this theory the contact area is assumed elliptic and the theory is valid when the dimensions of the contact area are small compared with the dimensions of the two bodies and the relative radii of curvatures.

The general assumptions used in the Hertz's theory can be summarized as follow:

- small deformation of the two bodies in the region of contact under a static compression;
- continuity of the two surfaces;
- the stress resulting from the contact force vanishes at a distance far from the contact;
- the surfaces are frictionless;
- the two bodies are elastic and no plastic deformation occurs in the contact area.

3.2.1 - Geometry and Kinematics

We consider a body *B* and its surface *S* (see Figure 3.3). It is *P* a generic point on *S*. We consider the inner normal versor to *S* in *P* named $\vec{n}$ and a tangent plant *t* to *S* in *P*.

Figure 3.2
Heinrich Rudolf Hertz

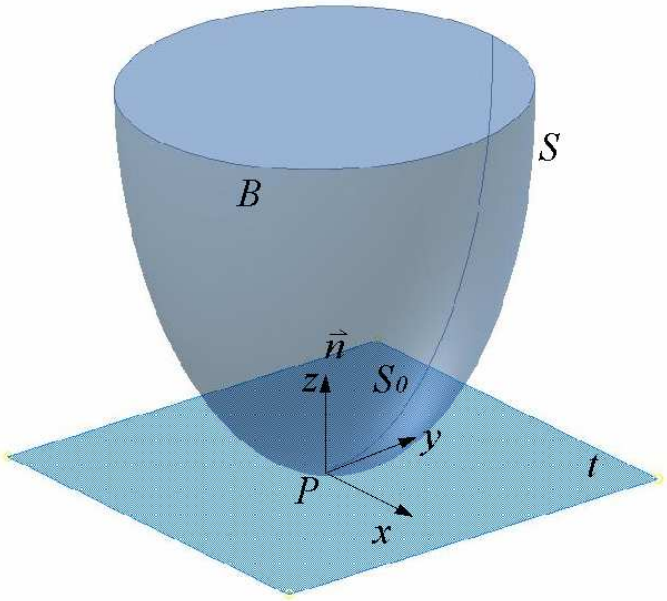

Figure 3.3
The body *B*, its surface *S*, the point *P*, the normal versor $\vec{n}$ and the tangential plane *t*

We consider a reference system S_0 having the axes *x* and *y* on the tangent plane, the origin in *P* and the axis *z* directed as the normal $\vec{n}$.
The surface *S* may be expressed with reference to S_0 with the equation $f(x, y)$.

If we consider only a small interval about the point *P* having coordinate x_0 and y_0, the function $f(x, y)$ may be expressed with a Taylor envelope as follow:

$$f(x,y) = f(x_0,y_0) + f_x(x_0,y_0)(x-x_0) + f_y(x_0,y_0)(y-y_0) + \frac{1}{2} f_{xx}(x_0,y_0)(x-x_0)^2 +$$

$$+ \frac{1}{2} f_{yy}(x_0,y_0)(y-y_0)^2 + f_{xy}(x_0,y_0)(x-x_0)(y-y_0);$$

Where the symbol f_{ij} denote the second order derivative respect to the *i* and *j* variable. Owing to the choice of the reference system and to the tangential plane definition we have:

$f_x(x_0,y_0) = 0;$
$f_y(x_0,y_0) = 0;$
$f(x_0,y_0) = 0.$

With these conditions the equation of the surface becomes:

$$f(x,y) = \frac{1}{2} f_{xx}(x_0,y_0)(x-x_0)^2 + \frac{1}{2} f_{yy}(x_0,y_0)(y-y_0)^2 + f_{xy}(x_0,y_0)(x-x_0)(y-y_0);$$

Until now we have considered a generic reference system S_0; we may consider a particular frame $S_0^{|}$ with the same origin and axis *Z* but rotate by and angle ψ around *Z* so that the term f_{xy} becomes null.

Considering the smallness of the examined interval as the Hertz's theory contemplates and hence the negligibility of the first derivative in the point *P*, we may approximate the second derivative with the surface curvature. In fact for a one variable function $y(x)$, the curvature *C* is given by:

$$C = \frac{1}{R} = \frac{\frac{\partial^2 y}{\partial x^2}}{\left[1 + \left(\frac{\partial y}{\partial x}\right)^2\right]^{3/2}}$$

where *R* is the radius of curvature. If $\frac{\partial y}{\partial x} << 1$ the curvature expression becomes $C = \frac{\partial^2 y}{\partial x^2}$.

Using the curvature approximation, considering that $x_0 = y_0 = 0$ and expressing the equation respect to $S_0^{|}$, $f(x,y)$ becomes:

$$f(X,Y) = \frac{1}{2} C_x X^2 + \frac{1}{2} C_y Y^2$$

Where C_x and C_y are respectively the surface curvatures respect to the *X* and *Y* directions of $S_0^{|}$.

It is possible to demonstrate that with the new choice of the reference system $S_0^{|}$, the curvature C_x and C_y are the principal curvatures of the surface in the point *P*.

At this point we may consider the two surfaces in contact and for every one we may define a reference system like the previous one. We have thus $S_{01}^{|}$ and $S_{02}^{|}$ with the same origin *P* and with the axes Z_1 and Z_2 parallel but having opposite directions. The two axes X_1 and X_2 belonging to the tangent plane are rotate by an angle ω. The two bodies are illustrate in Figure 3.4.

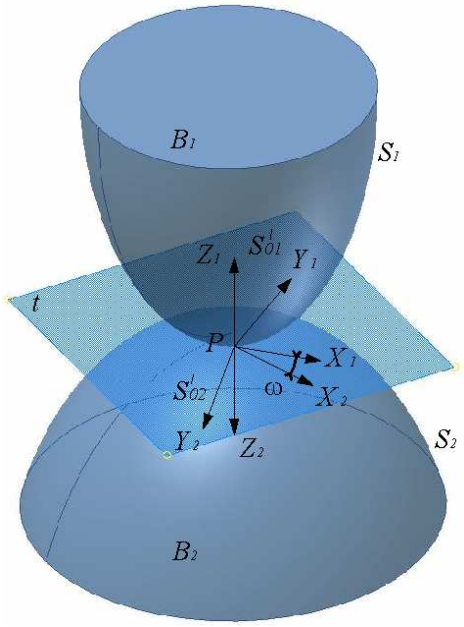

Figure 3.4
The two bodies in contact and the respective reference systems.

For the two bodies we can write the following equations:

$$Z_1 = \frac{1}{2} C_{1x} X_1^{\,2} + \frac{1}{2} C_{1y} Y_1^{\,2}$$

$$Z_2 = \frac{1}{2} C_{2x} X_2^{\,2} + \frac{1}{2} C_{2y} Y_2^{\,2}$$

where Z_1 and Z_2 are the third coordinates respectively of the first and second body, C_{1x} and C_{1y} are respectively the minimum and maximum curvatures of the first body, C_{2x} and C_{2y} are respectively the minimum and maximum curvatures of the second body, X_1 and Y_1 are the two coordinates of the first body on the tangent plane while X_2 and Y_2 are the two coordinates of the second body on the same plane.

If we consider a point *M* on the tangent plane and its normal projection on the two surfaces we have the points M_1 and M_2 respectively on the first and second surfaces. The distance between M_1 and M_2 is defined by:

$$d_{12} = Z_1 + Z_2 = \frac{1}{2}C_{1x}X_1^{\,2} + \frac{1}{2}C_{1y}Y_1^{\,2} + \frac{1}{2}C_{2x}X_2^{\,2} + \frac{1}{2}C_{2y}Y_2^{\,2}$$

In order to simplify the d_{12} expression we may consider a third reference system $S_0^{\parallel}$ having the axes $\overline{X}$ and $\overline{Y}$ on the tangent plane and the axis $\overline{Z}$ parallel to the normal surface and to the axis Z_1. The angle between the axes $\overline{X}$ and X_1 is named φ as shown in Figure 3.5.

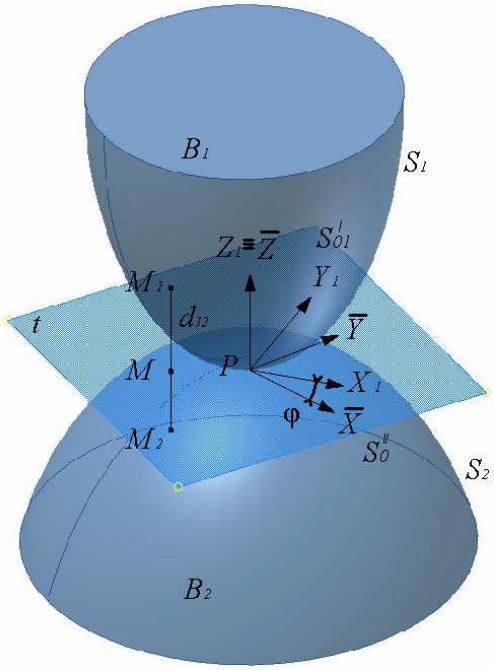

Figure 3.5
The reference systems $S_0^{\parallel}$ and the gap d_{12} between the points M_1 and M_2.

The transformations between $S_0^{\parallel}$ and $S_{01}^{|}$ and between $S_0^{\parallel}$ and $S_{02}^{|}$ may be expressed as follow:

$$X_1 = \overline{X}cos\varphi - \overline{Y}sen\varphi;$$
$$Y_1 = \overline{X}sen\varphi + \overline{Y}cos\varphi;$$
$$X_2 = \overline{X}cos(\omega - \varphi) + \overline{Y}sen(\omega - \varphi);$$
$$Y_2 = -\overline{X}sen(\omega - \varphi) + \overline{Y}cos(\omega - \varphi).$$

Replacing the previous transformations, the d_{12} expression becomes:

$$d_{12} = A\overline{X}^2 + B\overline{Y}^2 + C\overline{X}\overline{Y}$$

where:

$$A = \frac{1}{2}\left[C_{1x}\cos^2\varphi + C_{1y}sen^2\varphi + C_{2x}\cos^2(\omega-\varphi) + C_{2y}sen^2(\omega-\varphi)\right]$$

$$B = \frac{1}{2}\left[C_{1x}sen^2\varphi + C_{1y}\cos^2\varphi + C_{2x}sen^2(\omega-\varphi) + C_{2y}\cos^2(\omega-\varphi)\right]$$

$$C = \frac{1}{2}\left[(C_{1y}-C_{1x})sen2\varphi - (C_{2y}-C_{2x})sen2(\omega-\varphi)\right]$$

If we choose the angle $\varphi = \overline{\varphi}$ defined by the following relation:

$$tan2\overline{\varphi} = \frac{(C_{2y}-C_{2x})sen2\omega}{(C_{1y}-C_{1x})+(C_{2y}-C_{2x})cos2\omega}$$

the expression of d_{12} change into the following:

$$d_{12} = \overline{A}\overline{X}^2 + \overline{B}\overline{Y}^2 \qquad (3.1)$$

In this manner if we fix d_{12}, the points having the same gap belong to an ellipse with equation (3.1).

In order to simplify the treatment, we may introduce the angle τ given by:

$$\cos\tau = \frac{\overline{A}-\overline{B}}{\overline{A}+\overline{B}}$$

where:

$$\overline{A}-\overline{B} = \frac{1}{2}\left[(C_{1x}-C_{1y})\cos 2\overline{\varphi} + (C_{2x}-C_{2y})\cos 2(\omega-\overline{\varphi})\right];$$

$$\overline{A}+\overline{B} = \frac{1}{2}(C_{1x}+C_{1y}+C_{2x}+C_{2y})$$

Taking into account the equality $C = 0$ and after some passages we obtain:

$$\cos\tau = \frac{\overline{A}-\overline{B}}{\overline{A}+\overline{B}} = \frac{\sqrt{(C_{1x}-C_{1y})^2 + (C_{2x}-C_{2y})^2 + 2(C_{1x}-C_{1y})(C_{2x}-C_{2y})\cos 2\omega}}{(C_{1x}+C_{1y}+C_{2x}+C_{2y})}$$

This expression proves that $\cos\tau$ depends only from the geometrical quantities of the two contact bodies.

In order to determine the contact pressure between the two bodies, we must perform the following hypothesis:

a) the total applied force N between the two bodies must be equal to the total normal component of the pressure p in the contact area, that is:

$$N = \iint p\,dxdy \qquad (3.2)$$

b) the displacement at a distance away from the contact region can be neglected;

c) the normal stresses outside the contact region are assumed to be zero;

d) the normal stresses acting on the two bodies are in balance within the contact region;

e) the shear stresses along the surfaces of the bodies are zeros.

These conditions can be satisfied by assuming from the pressure *p* the following quadratic form:

$$p\left(\overline{X},\overline{Y}\right)= p_0\sqrt{1-\left(\frac{\overline{X}}{a}\right)^2-\left(\frac{\overline{X}}{b}\right)^2} \qquad (3.3)$$

Where p_0 is a constant, a and b are respectively the maximum and minimum semi-axes of the contact ellipse. Replacing (3.3) in (3.2) after some passages we have:

$$N=\frac{2}{3}p_0\pi ab$$

and

$$p(\overline{X},\overline{Y})=\frac{3N}{2\pi ab}\sqrt{1-\left(\frac{\overline{X}}{a}\right)^2-\left(\frac{\overline{Y}}{b}\right)^2}$$

The semi-axes a and b have been determined by Hertz as follow:

$$a = m\left(3\pi N\frac{\left(K_1+K_2\right)}{4\left(\overline{A}+\overline{B}\right)}\right)^{1/3}$$

$$b = n\left(3\pi N\frac{\left(K_1+K_2\right)}{4\left(\overline{A}+\overline{B}\right)}\right)^{1/3}$$

where K_1 and K_2 are constant depending from the material properties of the two bodies:

$$K_1=\frac{1-\upsilon_1^2}{\pi E_1}$$

$$K_2=\frac{1-\upsilon_2^2}{\pi E_2}$$

where:

υ_1 and υ_2 are the Poisson module of the two bodies;

E_1 and E_2 are the elasticity module of the two bodies.

The coefficients *m* and *n* are given by Hertz in table 3.1 as function of $\cos\tau$.

$\tau(\deg)$	*m*	*n*	$\tau(\deg)$	*m*	*n*	$\tau(\deg)$	*m*	*n*
0.5	61.4	0.1018	**10**	6.604	0.3112	**60**	1.486	0.717
1	36.89	0.1314	**20**	3.813	0.4125	**65**	1.378	0.759
1.5	27.48	0.1522	**30**	2.731	0.493	**70**	1.284	0.802
2	22.26	0.1691	**35**	2.397	0.530	**75**	1.202	0.846
3	16.5	0.1964	**40**	2.136	0.567	**80**	1.128	0.893
4	13.31	0.2188	**45**	1.926	0.604	**85**	1.061	0.944
6	9.79	0.2552	**50**	1.754	0.641	**90**	1.0	1.0
8	7.86	0.285	**55**	1.611	0.678			

Table 3.1
Hertz coefficients *m* and *n*.

Source : Hertz H - Über die berührung fester elastische Körper und über die Harte, Verhandlungen des Vereins zur Beförderung des Gewerbefleisses, Leipzig, Nov. 1882.

3.3 – THE CREEPAGES

Considering two moving bodies in contact, we can observe two phenomena in the contact region: the *rolling* and the *sliding* motion. In general case the bodies have different linear and angular velocities. The relative angular velocity along the normal to the surface in the contact point is called *spin*, while the relative linear velocity in the contact point is called *sliding*. When rolling occurs without sliding or spin it is called *pure rolling*. Generally when two moving bodies are pressed one against the other by a normal force some points in the contact area slip while other ones may stick. The difference between the tangential strains in the adhesion area are called *creepages*.

To define the creepages between wheel and rail, we consider the wheel-rail relative velocity $\vec{V}_P$ at contact points. The creepages are classified in three different categories according to the directions interested:

longitudinal creepage: $\zeta = \dfrac{\vec{V}_P \cdot \vec{n}_{long}}{\|V_G\|}$

transverse creepage: $\eta = \dfrac{\vec{V}_P \cdot \vec{n}_{trans}}{\|V_G\|}$:

spin creepage: $\varphi = \dfrac{\vec{V}_P \cdot \vec{n}_{norm}}{\|V_G\|}$

where:

$\vec{n}_{long}, \vec{n}_{trans}, \vec{n}_{norm}$ are respectively the longitudinal, transverse and normal versors;

$\left\|\vec{V}_G\right\|$ is the Euclidean norm of the barycenter velocity of the wheel-set.

In Figure 3.6 are represented the wheel-set velocities at barycenter G , at contact point P and the principal contact versors.

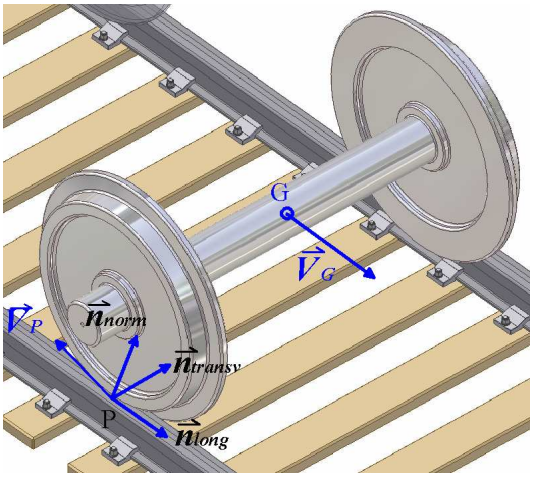

Figure 3.6

Velocity of the wheel-set in the contact point and principal versors

3.4 - WHEEL RAIL CONTACT FORCES

When a wheel moves on the rail the creepages generate tangential forces in the contact region and this fact has a great importance in the steering and stability study of railroad system.

According to the Hertz's theory, the contact area is elliptic and when the wheel and rail are pressed one against the other by a compressive force, they deform and if they move relative to each other, tangential forces develop in the contact region.

In general the contact area is divided in two regions: the *adhesion region* and the *slip region*. In the first region the body particles do not slide relative to each other, while in the second region there is sliding.

Figure 3.7 show the two regions.

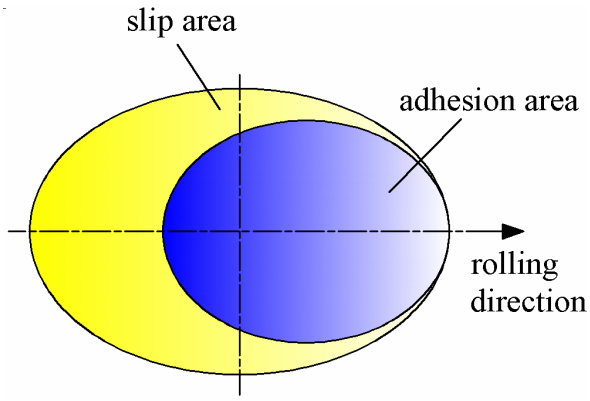

Figure 3.7
The adhesion and slip areas

The creep forces and the spin moment in general depend from the creepages, the extension and shape of the contact area and from the normal force. The relationship between the creepage components - longitudinal, lateral and spin – and the force components – longitudinal and lateral - and the spin moment are governed by the *creep-force law*. It has been developed various creep-force theories in the time; the more accurate and applied today are the following:

- *the Johnson-Vermeullen's theory*
- *the Kalker's linear theory*
- *the Polach's theory*

3.4.1 - Johnson and Vermeullen's Theory

In this theory the contact surfaces between the two rolling bodies is asymmetrically divided in two regions: the slip region and the stick or no-slip or adhesion region (see Figure 3.7). The adhesion area is assumed elliptical and its edge is in contact with the edge of the contact area. The total resulting tangential force is defined as:

$$\frac{\vec{F}}{\mu N} = \begin{cases} \left(\frac{1}{\tau}\right)\left[\left(1-\frac{1}{3}\tau\right)^3 - 1\right]\left(\zeta_0 \vec{i} + \eta_0 \vec{j}\right) & for|\tau| \le 3 \\ -\left(\frac{1}{\tau}\right)\left(\zeta_0 \vec{i} + \eta_0 \vec{j}\right) & for|\tau| > 3 \end{cases}$$

where the symbols have the following meaning:

ζ_0 and η_0 are the normalized longitudinal creepages, defined as:

$$\zeta_0 = \frac{\pi abG\zeta}{\mu N\phi}$$
$$\eta_0 = \frac{\pi abG\eta}{\mu N\psi}$$

N is the normal force component;

ζ and η are respectively the longitudinal and lateral creepages;

G is the modulus of rigidity;

a and b are the semi-axes of the contact ellipse;

μ is the coefficient of friction.

$\tau = \sqrt{\zeta_0^2 + \eta_0^2}$;

$\vec{i}$ and $\vec{j}$ are respectively the longitudinal and lateral versors.

The coefficient ϕ and ψ are function of the complete elliptical integrals B_e, C_e, D_e of argument *e* as follow (ν is the Poisson's ratio):

$$\left.\begin{aligned}\phi &= B_e - \upsilon(D_e - C_e)\\ \psi &= B_e - \upsilon\left(\frac{a}{b}\right)^2 C_e\end{aligned}\right\} \qquad \text{for } a \le b, e = \sqrt{1-\left(\frac{a}{b}\right)^2}$$

$$\left.\begin{aligned}\phi &= \left(\frac{b}{a}\right)[D_e - \upsilon(D_e - C_e)]\\ \psi &= \left(\frac{b}{a}\right)[D_e - \upsilon C_e]\end{aligned}\right\} \qquad \text{for } a > b, e = \sqrt{1-\left(\frac{b}{a}\right)^2}$$

It is important to note that this theory is valid in the case of no spin.

The complete elliptical integrals are given as follows:

$$B_e = \int_0^{\pi/2} \frac{\cos^2 w}{\sqrt{1-e^2\sin^2 w}}\,dw$$

$$C_e = \int_0^{\pi/2} \sin^2 w \cos^2 w \left(1-e^2\sin^2 w\right)^{-\frac{3}{2}} dw$$

$$D_e = \int_0^{\pi/2} \frac{\sin^2 w}{\sqrt{1-e^2\sin^2 w}}\,dw$$

It is clear that the elliptical integrals are related to each other as follows:

$$B_e = D_e - e^2 C_e;$$

$$C_e = \frac{(D_e - B_e)}{e^2}$$

In order to simplify the calculation it is reported the values of the elliptical integrals as function of $g = a/b$ in table 3.2.

g	B_e	C_e	D_e
0	1.0	$-2+\ln(4/g)$	$-1+\ln(4/g)$
0.05	0.9964	2.3973	3.3877
0.1	0.9889	1.7352	2.7067
0.15	0.9794	1.3684	2.3170
0.2	0.9686	1.1239	2.0475
0.25	0.9570	0.9463	1.8442
0.3	0.9451	0.8105	1.6827
0.35	0.9328	0.7036	1.5502
0.4	0.9205	0.6170	1.4388
0.45	0.9081	0.5460	1.3435
0.5	0.8959	0.4863	1.2606
0.55	0.8838	0.4360	1.1879
0.6	0.8719	0.3930	1.1234
0.65	0.8603	0.3555	1.0656
0.7	0.8488	0.3235	1.0138
0.75	0.8376	0.2955	0.9669
0.8	0.8267	0.2706	0.9241
0.85	0.8159	0.2494	0.8851
0.9	0.8055	0.2289	0.8490
0.95	0.7953	0.2123	0.8160
1.0	$\pi/4$	$\pi/16$	$\pi/4$

Table 3.2
Complete elliptical integrals, tabulated in Jahnke-Emde (1943)

3.4.2 – The Kalker's linear theory

Kalker (1967, Figure 3.8) suggested that, for very small creepages, the area of slip is very small and its effect can be neglected; in this manner the adhesion area can be assumed to be equal to the area of contact.

Figure 3.8
Joost Kalker

This theory is based on a linear relationship between the creepage and the tangent force. The tangential components along the longitudinal direction, $\vec{F}_{long}$, along the lateral direction, $\vec{F}_{trans}$, and the moment of spin $\vec{M}_{spin}$ are given by:

$$\vec{F}_{long} = -(c^2 G C_{11} \zeta)\vec{n}_{long}$$
$$\vec{F}_{trans} = -(c^2 G C_{22} \eta + c^3 G C_{23} \varphi)\vec{n}_{trans}$$
$$\vec{M}_{spin} = -(c^3 G C_{32} \eta + c^4 G C_{33} \varphi)\vec{n}_{norm}$$

where:

$$c = \sqrt{ab};$$
$$G = \left(\frac{1}{2}\left(\frac{1}{G_1} + \frac{1}{G_2}\right)\right)^{-1}$$

The symbols have the following meaning:

G_1 and G_2 are the wheel and the rail tangent elasticity modules, respectively;

ζ, η, φ are the longitudinal, lateral and spin creepages of the wheel respect to the rail at the contact point;

$C_{11}, C_{22}, C_{33}, C_{23}, C_{32}$ are the Kalker's coefficients functions of the ratio *a/b* and the Poisson's module;

$\vec{n}_{long}, \vec{n}_{trans,} \vec{n}_{norm}$ are the longitudinal, lateral and normal versors at contact points.

In 1984 Kalker calculated the creepage and spin coefficients when the relative slip is small but the contact area is not necessarily elliptic. This calculations were made with the aid of the program *CONTACT* and the error found was less than 5% respect to the measurements. This fact proves that the Kalker's coefficients are very accurate for the analysis of the wheel/rail problems. In fact nowadays the linear theory is extensively used in railroad vehicle dynamic analysis. The Kalker's coefficients C_{11}, C_{22}, C_{33}, C_{23} and C_{32} are reported in table 3.3. They are function of the ratio *a/b* between the two contact ellipse semi axes and of the Poisson coefficient ν.

		C_{11}			C_{22}			$C_{23}=-C_{32}$			C_{33}		
	g	$\upsilon=0$	$1/4$	$1/2$	$\upsilon=0$	$1/4$	$1/2$	$\upsilon=0$	$1/4$	$1/2$	$\upsilon=0$	$1/4$	$1/2$
$\frac{a}{b}$	$\downarrow 0.0$	$\frac{\pi^2}{4}(1-\nu)$			$\frac{\pi^2}{4}$			$\frac{\pi\sqrt{g}}{3(1-\nu)}\left(1+\nu\left(\frac{1}{2}\Delta+\ln 4-5\right)\right)$			$\frac{\pi^2}{16}(1-\nu)g$		
	0.1	2.51	3.31	4.85	2.51	2.52	2.53	0.334	0.473	0.731	6.42	8.28	11.7
	0.2	2.59	3.37	4.81	2.59	2.63	2.66	0.483	0.603	0.809	3.46	4.27	5.66
	0.3	2.68	3.44	4.80	2.68	2.75	2.81	0.607	0.715	0.889	2.49	2.96	3.72
	0.4	2.78	3.53	4.82	2.78	2.88	2.98	0.720	0.823	0.977	2.02	2.32	2.77
	0.5	2.88	3.62	4.83	2.88	3.01	3.14	0.827	0.929	1.07	1.74	1.93	2.22
	0.6	2.98	3.72	4.91	2.98	3.14	3.31	0.930	1.03	1.18	1.56	1.68	1.86
	0.7	3.09	3.81	4.97	3.09	3.28	3.48	1.03	1.14	1.29	1.43	1.50	1.60
	0.8	3.19	3.91	5.05	3.19	3.41	3.65	1.13	1.25	1.40	1.34	1.37	1.42
	0.9	3.29	4.01	5.12	3.29	3.54	3.82	1.23	1.36	1.51	1.27	1.27	1.27
$\frac{b}{a}$	**1.0**	3.40	4.12	5.20	3.40	3.67	3.98	1.33	1.47	1.63	1.21	1.19	1.16
	0.9	3.51	4.22	5.30	3.51	3.81	4.16	1.44	1.59	1.77	1.16	1.11	1.06
	0.8	3.65	4.36	5.42	3.65	3.99	4.39	1.58	1.75	1.94	1.10	1.04	0.954
	0.7	3.82	4.54	5.58	3.82	4.21	4.67	1.76	1.95	2.18	1.05	0.965	0.852
	0.6	4.06	4.78	5.80	4.06	4.50	5.04	2.01	2.23	2.50	1.01	0.892	0.751
	0.5	4.37	5.10	6.11	4.37	4.90	5.56	2.35	2.62	2.96	0.958	0.819	0.650
	0.4	4.84	5.57	6.57	4.84	5.48	6.31	2.88	3.24	3.70	0.912	0.747	0.549
	0.3	5.57	6.34	7.34	5.57	6.40	7.51	3.79	4.32	5.01	0.868	0.674	0.446
	0.2	6.96	7.78	8.82	6.96	8.14	9.79	5.72	6.63	7.89	0.828	0.601	0.341
	0.1	10.7	11.7	12.9	10.7	12.8	16.0	12.2	14.6	18.0	0.795	0.526	0.228
	$\downarrow 0.0$	$\frac{2\pi}{(\Delta-2\nu)g}\left\{1+\frac{3-\ln 4}{\Delta-2\nu}\right\}$			$\frac{\frac{2\pi}{g}\left\{1+\frac{(1-\nu)(3-\ln 4)}{(1-\nu)\Delta+2\nu}\right\}}{(1-\nu)\Delta+2\nu}$			$\frac{\frac{2\pi}{3g\sqrt{g}}}{((1-\nu)\Delta-2+4\nu)}$			$\frac{\pi}{4}\left\{1-\frac{\nu(\Delta-2)}{(1-\nu)\Delta-2+4\nu}\right\}$		

Table 3.3

The Kalker's coefficients C_{11}, C_{22}, C_{33}, C_{23} and C_{32}; $\Delta=\ln\left(\frac{16}{g^2}\right)$; $g=\min\left(\frac{a}{b},\frac{b}{a}\right)$.

3.4.3 - The Polach nonlinear theory

In 1999 Polach (Figure 3.9) introduced an algorithm for the computation of the wheel/rail creep forces. In this model the shape of the contact area is elliptic. Since in the Hertz theory the maximum stress distribution is equal to σ, the maximum tangential stress at any point is $\tau_{\max} = \mu\sigma$, where μ is the friction coefficient assumed constant in the whole contact area.

In this theory it is assumed that the relative displacement between the bodies in the adhesion area increases linearly from one side A to the other side C, as shown in Figure 3.10. At same time the tangential stress increases linearly with the distance from the leading edge. When the tangential stress reaches the maximum value, sliding takes place.

Figure 3.9
Oldrich Polach

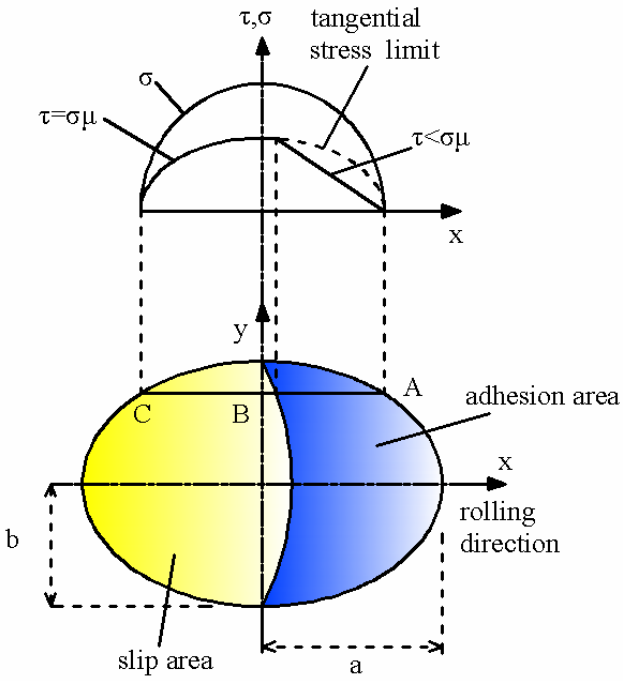

Figure 3.10
Normal and tangential stress distribution according to Polach theory

The tangential force is given by:

$$F_{px} = -\frac{2\mu N}{\pi}\left(\frac{\varepsilon}{1+\varepsilon^2} + \tan^{-1}\varepsilon\right)$$

where the symbols have the following meaning:

N is the normal component of the contact force;

ε is the gradient of the tangential stress in the area of adhesion and it is given by:

$$\varepsilon = \frac{1}{4}\frac{G\pi abC_h}{\mu N}v_c$$

where G is the modulus of rigidity while C_h is a constant depending from the Kalker's coefficients as follows:

$$C_h = \sqrt{\left(C_{11}\frac{\zeta}{\nu}\right)^2 + \left(C_{22}\frac{\eta}{\nu}\right)^2}$$

$$\nu = \sqrt{\zeta^2 + \eta^2}$$

where:

ζ and η are respectively the longitudinal and lateral creepages;

C_{11} and C_{22} are the Kalker's coefficients;

Using the modified lateral creepage that accounts for the effect of spin creepage φ the magnitude of the creepage becomes:

$$\nu_c = \sqrt{\zeta^2 + \eta_c^2}$$

where the modified lateral creepage η_c is given by:

$$\eta_c = \eta \quad \text{if} \quad |\eta + \varphi a| \le |\eta|$$

$$\eta_c = (\eta + \varphi a) \quad \text{if} \quad |\eta + \varphi a| > |\eta|$$

The lateral tangential force that accounts for the effect of the spin is given by:

$$F_{py} = -\frac{9}{16} a\mu NK\left[1 + 6.3\left(1 - e^{-a/b}\right)\right]$$

where K is a constant given by:

$$K = |\varepsilon_y|\left(\frac{\delta^3}{3} - \frac{\delta^2}{2} + \frac{1}{6}\right) - \frac{1}{3}\sqrt{\left(1-\delta^2\right)^3}$$

and δ is given by:

$$\delta = \frac{(\varepsilon_y)^2 - 1}{(\varepsilon_y)^2 + 1}$$

ε_y is the gradient of the tangential stress and it is given by (C_{23} is the Kalker's coefficient):

$$\varepsilon_y = \frac{8}{3}\frac{Gb\sqrt{ab}}{\mu N}\left(\frac{C_{23}\eta_c}{1 + 6.3\left(1 - e^{-a/b}\right)}\right)$$

Finally the creep forces are given as follows:

$$F_x = F_{px}\frac{\zeta}{\nu_c}$$

$$F_y = F_{px}\frac{\eta}{\nu_c} + F_{py}\frac{\varphi}{\nu_c}$$

The Polach theory yields accurate prediction of the tangential contact forces and today it is implemented in some computer code for the dynamic simulation of railway system.

3.5 – THE SURFACE CURVATURES

In order to determine the principal curvatures [11] on the wheel and on the rail at contact points let us consider a generic surface *z=f(x,y)* and a generic point *P(x,y)* on it. The Gauss coefficients are defined as follows:

$$E = 1 + p^2;$$

$$F = pq;$$

$$G = 1 + q^2$$

$$L = \frac{r}{\sqrt{1 + p^2 + q^2}};$$

$$M = \frac{s}{\sqrt{1 + p^2 + q^2}};$$

$$N = \frac{t}{\sqrt{1 + p^2 + q^2}}$$

where the coefficients *p, q, r, s, t* are the first and second partial derivatives of *f(x, y)* evaluated at point *P*;

$$p = \frac{\partial f}{\partial x}; \quad q = \frac{\partial f}{\partial y}; \quad r = \frac{\partial^2 f}{\partial x^2}; \quad s = \frac{\partial^2 f}{\partial x \partial y}; \quad t = \frac{\partial^2 f}{\partial y^2}$$

The Gauss curvature is given by

$$\kappa = C_{\min} C_{\max} = \frac{LN - M^2}{EG - F^2}$$

while the mean curvature is:

$$H = \frac{1}{2}\left(C_{\min} + C_{\max}\right) = \frac{EN - 2FM + GL}{2\left(EG - F^2\right)}$$

Hence, the principal curvatures $C_{\max}$ and $C_{\min}$, namely the maximum and minimum ones, are:

$$C_{\min} = H - \sqrt{H^2 - \kappa};$$

$$C_{\max} = H + \sqrt{H^2 - \kappa}.$$

The two principal directions φ_1 and φ_2 are obtained solving the second order algebraic equation:

$$(FN - GM)\varphi^2 + (EN - GL)\varphi + (EM - FL) = 0$$

Figures 3.11 and 3.12 show the mapping of the minimum and maximum curvatures and the principal directions on the wheel and rail. It is important to observe that the curvature of a generic curve on a surface in a definite point can be positive or negative.

In order to better explain the concept we consider a solid limited by a surface. We consider a curve on the surface and a point *P* on the curve. It is defined the tangent line to the curve in *P* named *t*. The curvature *Cr* of the curve in *P* will be positive if the position of the center of curvature *C* and the solid are to the same part respect to *t*, otherwise it is assumed negative.

Figure 3.13 explains the sign rule used for the curvature.

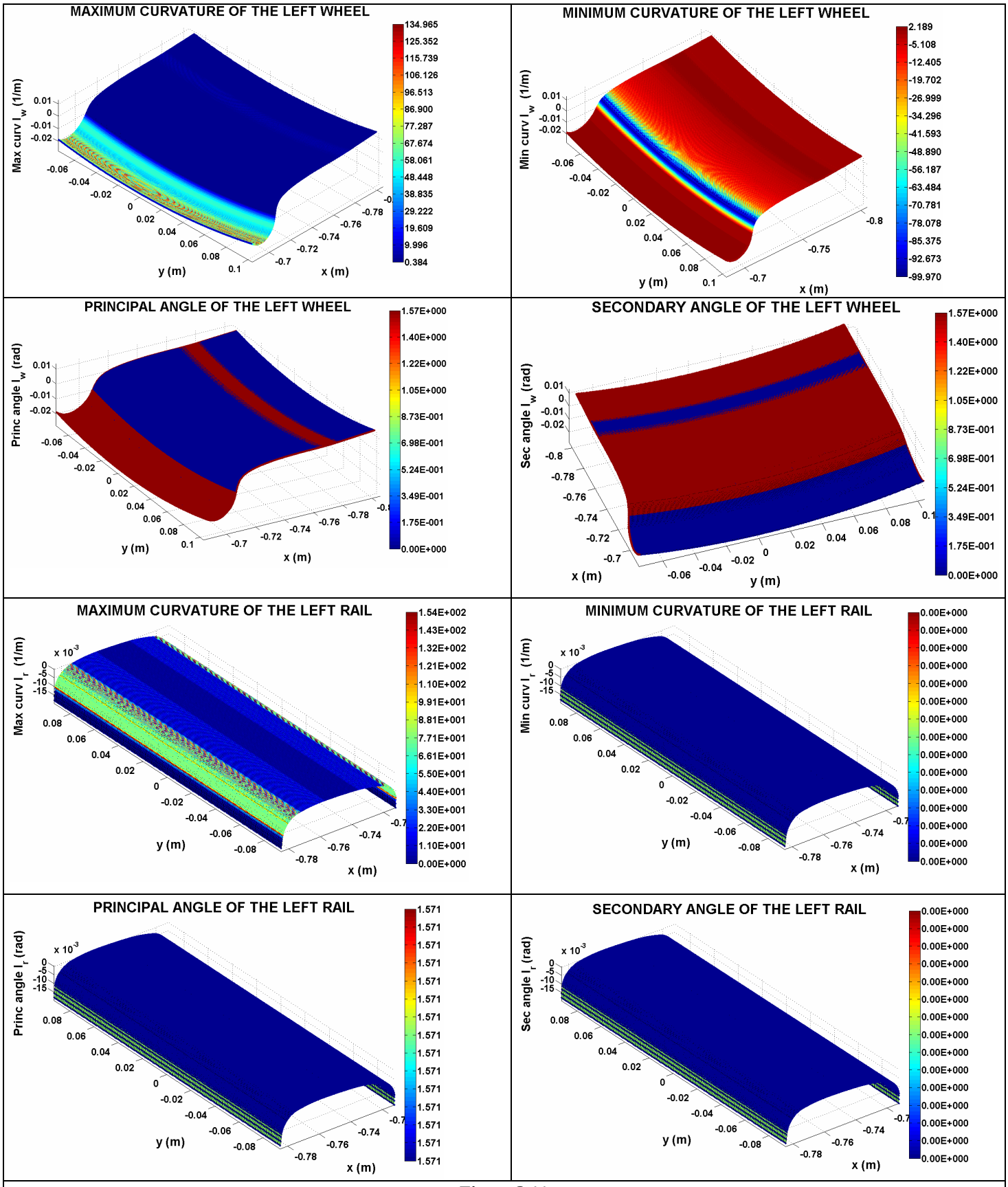

Figure 3.11
The principal curvatures and angles on the left wheel and rail

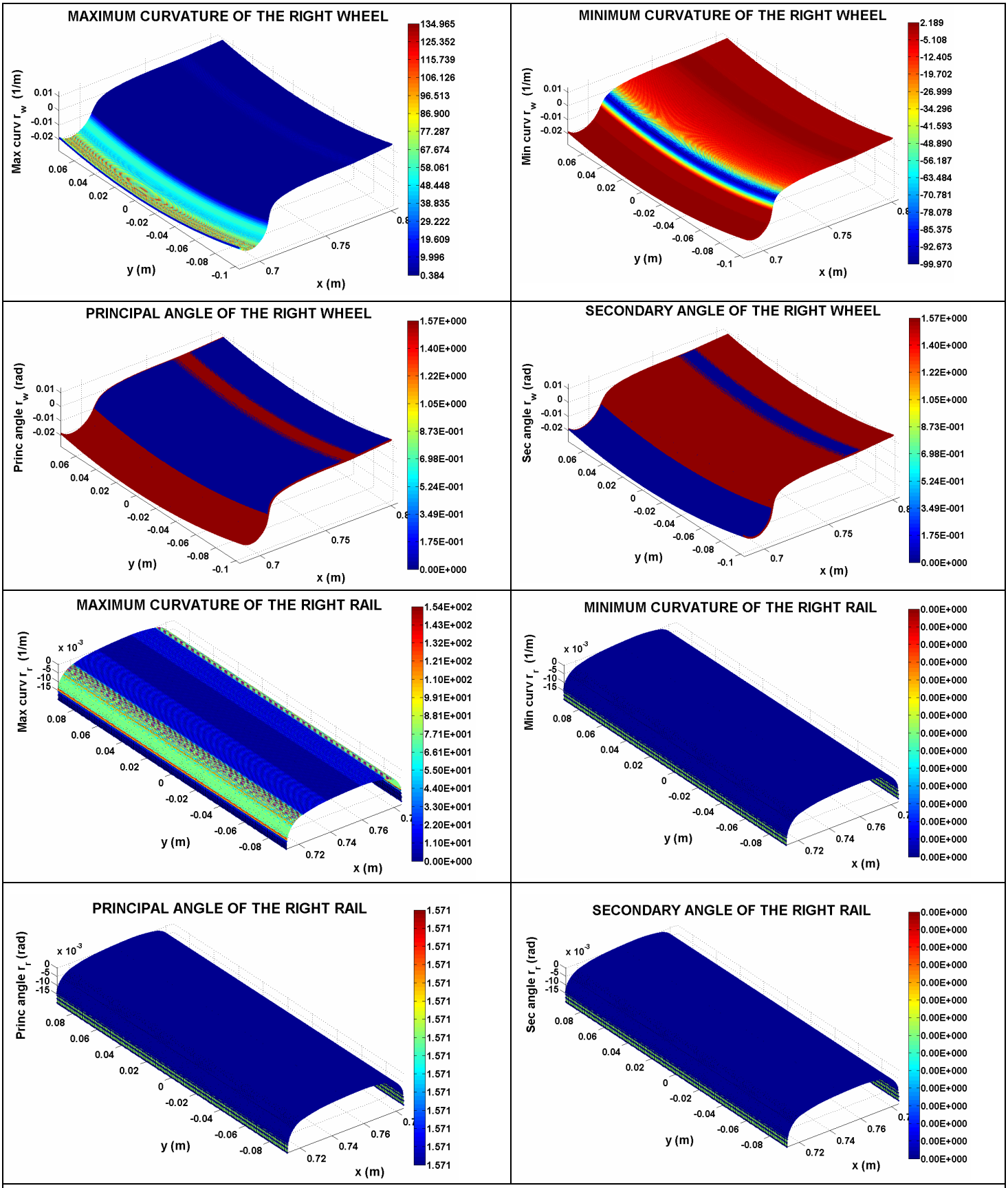

Figure 3.12

The principal curvatures and angles on the right wheel and rail

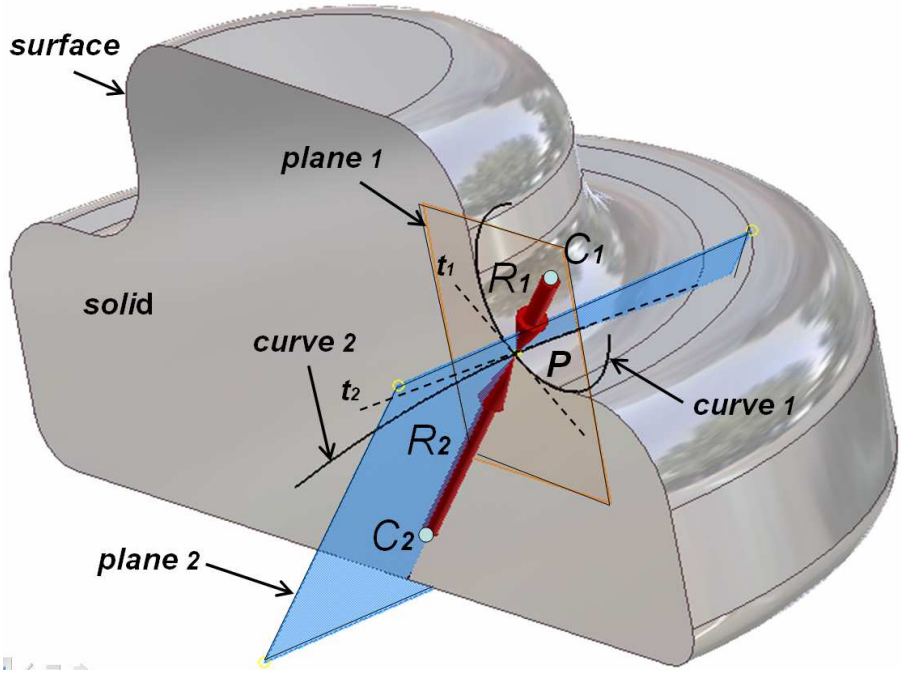

R : radius of curvature

$$\left|Cr_1\right| = \frac{1}{R_1}$$

$$\left|Cr_2\right| = \frac{1}{R_2}$$

$$Cr_1 \le 0$$

$$Cr_2 \ge 0$$

Figure 3.13

The rule used for the determination of the curvature sign

CHAPTER 4

THE STABILITY OF THE MOTION

4.1 - INTRODUCTION

The dynamic analysis of railway systems, like wheel-sets, bogies or trains, in proximity of their critical behaviour, is one the most important analysis for the design of these complex systems. An important role is played by the dimensioning of the primary and secondary suspension systems. In the preliminary design of a bogie the search of the optimum value of the suspension characteristics has a major importance. However, the stiffness and damping of the suspension elements have a different effect on the bogie behaviour in straight or curved paths. Let us consider a standard bogie, like the one depicted in paragraph 6.2, provided with a primary suspension system acting along the three principal directions: vertical, longitudinal and transverse. When considering two opposite variations of the longitudinal stiffness one can observe a variation of the critical speed in straight paths: the critical speed variation maintains the same sign of the stiffness variation. This means that the higher is the longitudinal stiffness the better are the stability characteristics of the bogie. On the contrary, considering the bogie behaviour in curved paths and focusing the attention on the contact forces between wheels and rails, we observe that reduction of these loads are achieved with lower values of the longitudinal stiffness. In conclusions, variations of the longitudinal stiffness causes opposite effects on the bogie when it moves on straight or curved tracks.

This phenomenon is partially explained in Figure 4.1 that reports the two bogie wheel-sets moving in an horizontal plane. When perturbed, the wheel-sets the following configurations (eigenmodes) can be distinguished:

- *Tractive mode*, the two wheel-sets longitudinally move in phase mode;
- *Longitudinal anti-phase mode*, the two wheel-sets longitudinally move in anti-phase mode;
- *Shearing mode*, the two wheel-sets rotate in phase about the vertical axis;
- *Bending (steering) mode*, the two wheel-sets rotate in anti-phase around the vertical axis;

To achieve a self-steering ability in curve associated with a high critical speed, the longitudinal stiffness should be decreased for the bending mode and increased for the shearing mode. To guarantee a proper transmission of the braking and acceleration actions between the wheel-sets and the frame bogie the stiffness must be high in the tractive eigenmode, this condition conflicts with the self-steering of the bogie in curved tracks. For these reasons an optimum value of the longitudinal stiffness does exist, depending on the stability requirements demanded to the railway system. The effective critical speed depends by many variables; one of the most important is the bogie load ratio, defined as the ratio between the vertical load directly applied on the frame bogie and its weight. In curved tracks the radius of curvature also strongly influences the critical speed; some plots have been generated to show the dependence of the bogie critical speed to both the load ratio and the radius of curvature.

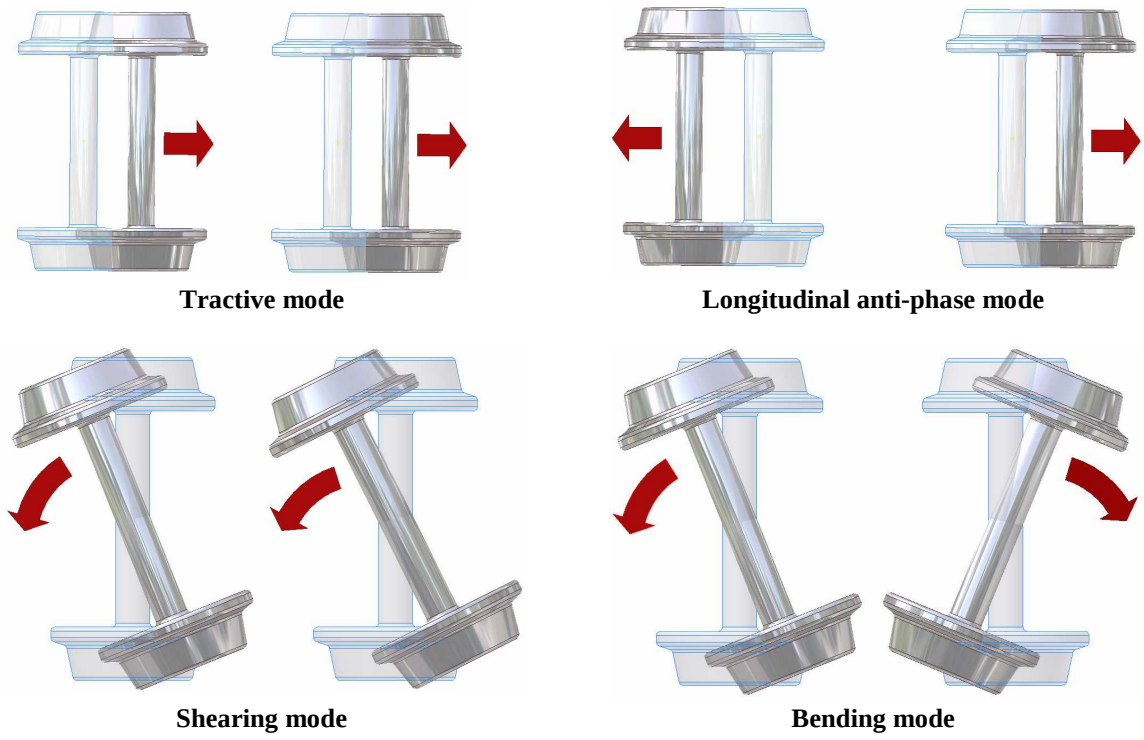

Figure 4.1
The four eigenmodes of a two wheel-sets bogie

An analysis on the influence of the longitudinal stiffnesses of the primary suspension system of the bogie on the critical speed and on the contact forces is reported in chapter 8 respect to the load conditions and the track characteristics.

4.2 - THE CRITICAL SPEED DETERMINATION

The determination of the critical speed can be made with two methods [4, 6, 8, 9, 15, 26] that are both connected with the concept of hunting motion.

4.2.1 – The hunting motion

One of the most important aspect of the motion of a rail-system is the hunting motion.
The hunting motion is defined as the lateral motion of the wheel-set with respect to its centered position. In a simplified model, the wheels are conical, with the largest diameter at the internal extremity, that is in proximity of the inner faces of the rails, as shown in Figure 4.2.

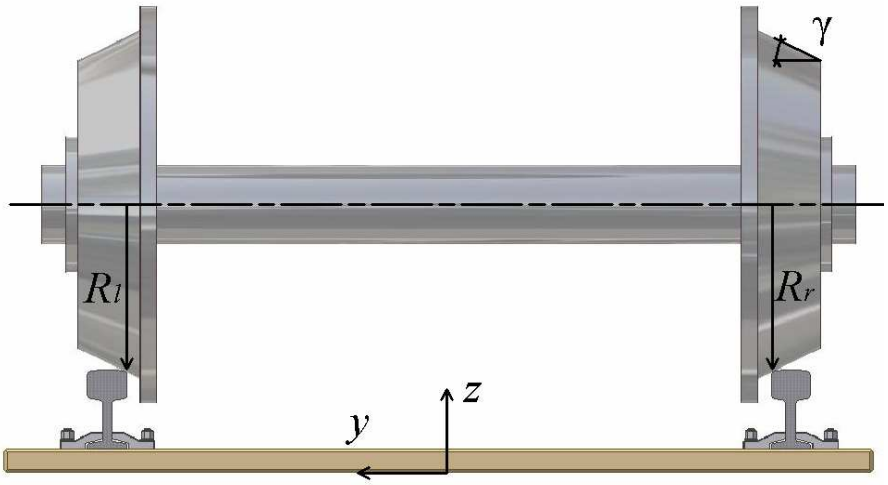

Figure 4.2
The simplified model of a wheel-set having two conical wheels.

To explain the hunting motion the simplified model is used, having two conical wheels and a cone angle named γ as shown in Figure 4.2. The wheel-set is centered respect the two rails and moves with longitudinal velocity named V_{long}. When a perturbation appears the wheel-set begin to move laterally. We assume that when the transverse displacement *y* of the barycentre is not null, the two wheel radii at contact points are R_r and R_l respectively for the right and left wheels. If $y = 0$ the two radii are equal, that is $R_r = R_l = R_0$.
When y is not null, the variations of the two radii in the contact points respect to the centered positions are:

$$\Delta R = y\gamma$$

and the two rolling radii become:

$$R_r = R_0 - y\gamma$$
$$R_l = R_0 + y\gamma$$

If the wheel-set rotates with a constant angular velocity ω, the velocity V_r and V_l respectively of the right and left wheels in proximity of the contact points are:

$$V_r = R_r\omega$$
$$V_l = R_l\omega$$

while the velocity of the barycentre of the wheel-set is given by:

$$V = \frac{(V_r + V_l)}{2} = R_0\omega$$

If we indicate with ψ the yaw angle of the wheel-set, as shown in Figure 4.3, the following expression is valid:

$$\tan\psi = \frac{dy}{dx}$$

and if $\psi << 1$ the approximation $\tan\psi \cong \psi$ is true. The lateral velocity V_y is given by:

$$V_y = \frac{dy}{dt} = \frac{dy}{dx}\frac{dx}{dt} = \psi V_x = \psi V\cos\psi \cong \psi V = \psi R_0\omega \qquad (4.1)$$

where V_x is the longitudinal component of V.

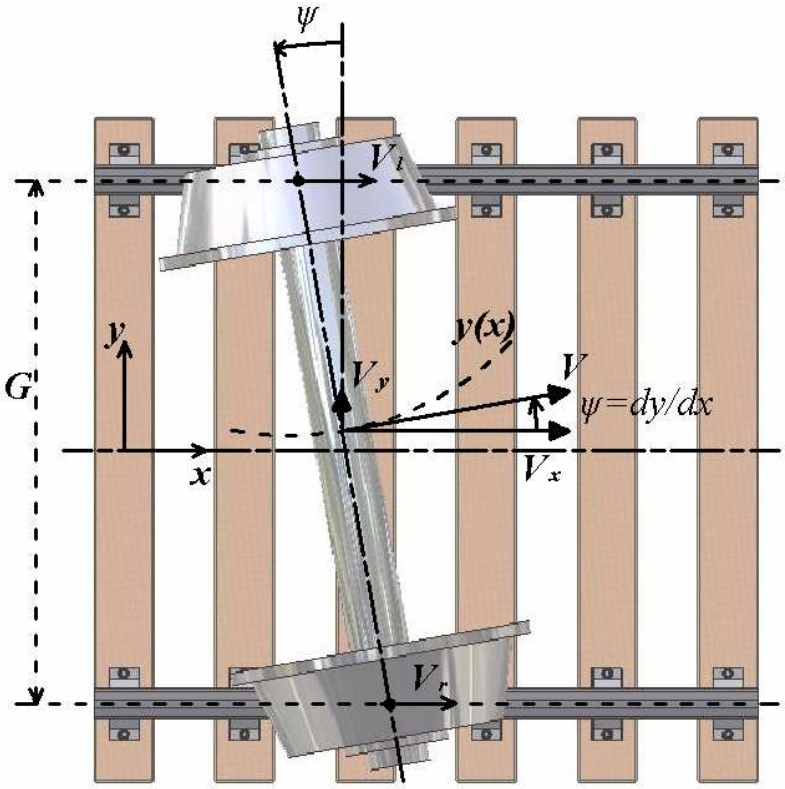

Figure 4.3

The yaw angle ψ and the lateral velocity of the wheel-set.

The rate of change of ψ can be written as:

$$\frac{d\psi}{dt} = \frac{V_r - V_l}{G} = -\frac{2y\omega\gamma}{G} \qquad (4.2)$$

where G is the distance between the two contact points measured orthogonally to the rail axis.

Differentiating equation 4.1 respect to time and substituting the expression of $\frac{d\psi}{dt}$ before determined, we have:

$$\frac{d^2y}{dt^2} + \left(\frac{2R_0\omega^2\gamma}{G}\right)y = 0. \qquad (4.3)$$

This equation describes the lateral motion of the perturbed wheel-set moving with angular velocity ω.

The general solution is given by:

$$y = A\sin(\omega_n t + C)$$

that is a constant amplitude oscillation. The constants A and C depend from the initial conditions. We note that the previous relation is correct if the following relation is true:

$$\frac{2R_0\omega^2\gamma}{G} > 0$$

ω_n is the natural frequency of the undamped system and it is given by:

$$\omega_n = V\sqrt{\frac{2\gamma}{R_0 G}}$$

Clearly the conicity γ must be positive. The oscillation period is given by the known *Klingel's formula*:

$$T = \frac{2\pi}{\omega_n} = \frac{2\pi}{V}\sqrt{\frac{R_0 G}{2\gamma}}$$

When the wheels are cylindrical or in other words the conicity is null, the solution of 4.3 is a straight line and the motion after a perturbation is not oscillatory. In the case of negative conicity the coefficient of *y* is negative and the solution is an exponential one with the lateral displacement increasing continuously with time. Therefore, as these simple kinematic considerations demonstrate, the fundamental characteristics that a wheel-set must posses to guarantee a stable oscillatory solution is to have a positive conicity. These concept are explained in Figure 4.4.

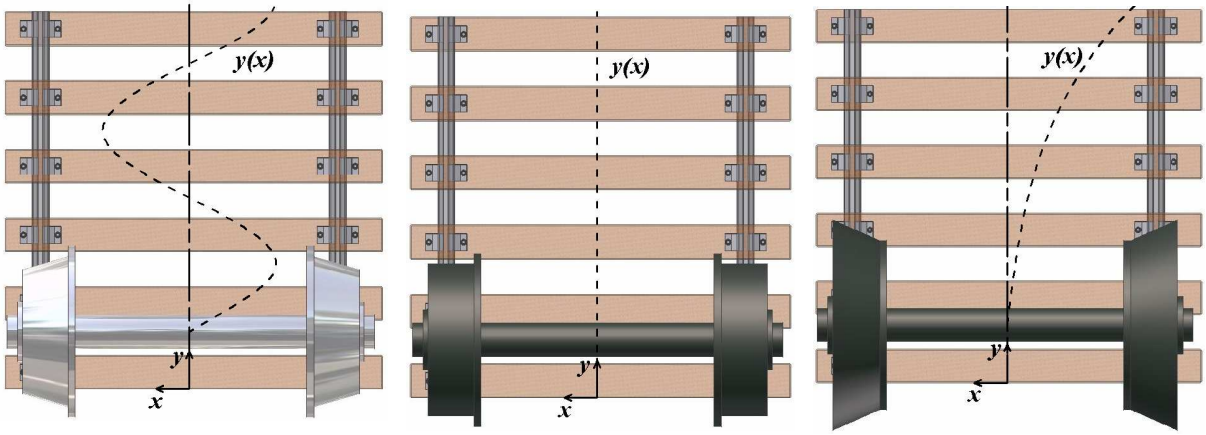

Figure 4.4

The three motion types associated with the conicity values.

It is important to note that the *Klingel's* formula has been derived only with a simple kinematic considerations without considering the effect of any forces. In reality the wheel-set is subjected to the normal and tangential contact forces that influence the oscillatory motion. In fact when the rolling radii are different, also the velocities in the contact points are distinct as the creepages. For these reasons, the tangential forces create a dissymmetrical condition on the wheel-set and generate the oscillatory motion. The oscillation can increase or decrease with time, also with a positive conicity, depending from the initial wheel-set velocity.

From equation 4.1 and 4.2 we can see that the derivative of the yaw angle ψ is null when the lateral displacement *y* is null and this means that ψ is maximum or minimum when *y* is null and vice versa. This implies that there is a phase shift equal to $\pi/2$ between the lateral displacement and the yaw angle.

4.2.2 – Methods for the critical speed determination

We now consider a wheel-set moving on a straight path. If the initial lateral displacement is null and if the motion is unperturbed, the wheel-set remains centered between the two rails. Otherwise, if the conicity is positive and the motion is laterally perturbed, an oscillation appears and it can be damped or undamped, depending from the initial longitudinal velocity.
If the mass oscillations extinguish themselves with time, it means that the longitudinal speed is lower than the critical one otherwise if the oscillations increase then the velocity is greater than the critical velocity.
The previous definition of the critical speed suggests the method for its calculation. One should observe the motion of the bogie at different longitudinal velocities to find the velocity at which the oscillation amplitudes are at least constant with time. The method gives precise results but has the disadvantage of being too time consuming. The second method searches for the critical speed starting from the higher values. The bogie runs with an initial longitudinal velocity higher than the critical speed, an initial perturbation is applied. Because of the friction forces acting on the wheels, the bogie slows down with time when no driving forces are applied. When the speed is higher than the critical one, the hunting oscillations increase with time. The trend reverses when the decreasing velocity overcomes the critical speed. Therefore, in order to determine the critical speed one needs only to detect the velocity value at which the trend changes. This method is faster than the first one, but this is paid to the detriment of accuracy. Figures 4.5a and 4.5b show the plots used by the first method, whereas Figure 4.5c and 4..5d the one used by the second method.

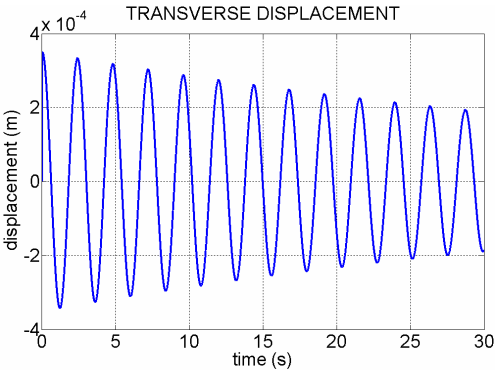

$$V_1 < V_{cr} < V_2$$

$$V_{cr} : \text{critical speed}$$

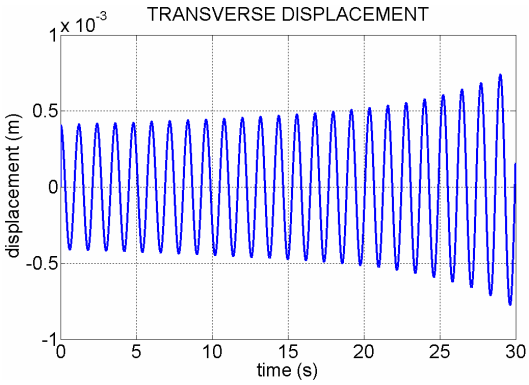

a) Transverse displacement of the wheel-set at stable velocity V_1

b) Transverse displacement of the wheel-set at unstable velocity V_2

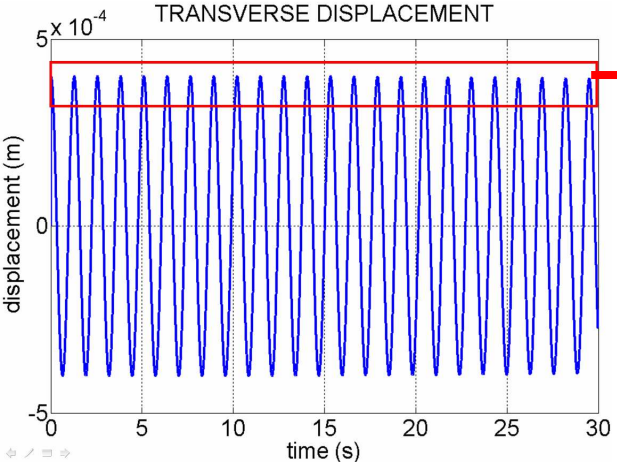

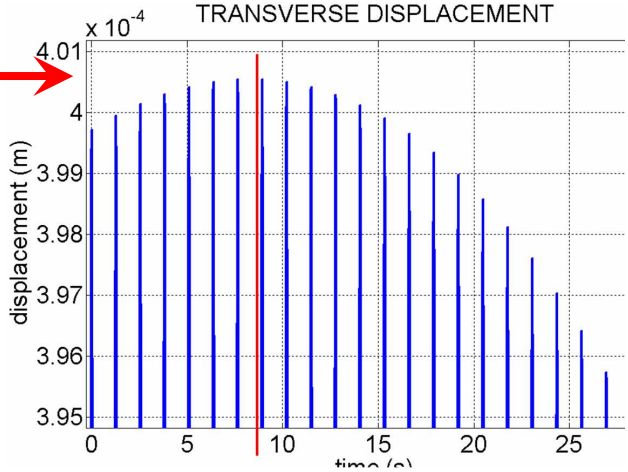

c) Transverse displacement of the wheel-set started at unstable velocity V_2

d) Time in correspondence of which the trend changes and at which the critical speed is defined

Figure 4.5
The two methods used to the determination of the wheel-set critical speed; a) 1st method: transverse displacement in a stable motion ; b) 1st method: transverse displacement in a unstable motion; c) 2st method: transverse displacement in a unstable-stable motion; d) zoom of the graphic c).

Part two

CHAPTER 5

THE CONTACT CHARACTERISTICS

5.1 - INTRODUCTION

The solution of wheel/rail contact problem is required by the dynamic analysis of railways systems. In particular, for each wheel-set it is necessary:

- to define the spatial attitude of the axle in its workspace;
- to locate the actual wheel/rail contact points;
- to compute the value of normal force components generated in the contact between surfaces.

The compilation of a lookup table - where the numeric relationships between coordinates are stored – makes it possible the development of a software dedicated to the dynamic simulation of the wheel-set, of the bogie or of the entire railway convoy. In this way different types of analyses [1-6, 8] can be carried out, such as the determination of wheel-set critical speed and the simulation of contact forces under dynamic conditions.

During dynamic analysis the implemented software solves numerically the equations of motion. At each time step the dependent coordinates, consistent with the contact constraints, are obtained through interpolation from the lookup table.
The advantages of the methods herein presented are:

- reduction of the computation time, since the identification of the contact conditions is obtained by a linear interpolation scheme;
- possibility to extend the simulation over a long time interval;
- capability of a real time simulation with the appropriate hardware;

- possibility to study the dynamics with different wheel-set and rail profiles through the update of the lookup table.

Different methodologies for the investigation on wheel-rail contact are available [8,11-15]. These can be classified into two main groups. The first group searches for the contact points by solving the system of algebraic-differential equations that includes the constraints due to rigid contact between wheels and rails. The second group, to which the methods herein presented belongs, introduces elasticity between the mating surfaces.

In reference [8] the contact points are determined through the concept of *difference surface*, defined as the distance - measured along the normal direction - between the wheel and rail surfaces.

If such *difference surface* presents only positive values, then the rail and the wheel are not in contact. If the *difference surface* shows at least some negative values, then there are one or more contact areas. Contact points are located where the *difference surface* reaches its local minima, with a negative value of the function. Accordingly, at these points the indentation between the contact bodies attains a maximum. This criterion is also used to calculate the contact force components.

In order to calculate the minimum of the difference, the simplex method is iteratively exploited.

The results obtained with this method are compared with those achieved with the *grid method*. This last evaluates the function in a series of points and find the minima comparing all obtained values. The reliability of the *grid method*, depends mainly on the number of points chosen to evaluate the function. Even if the grid method is simple and reliable, it cannot be used for this type of application because of its high computational costs.

In reference [12-14] it is hinted a method alternative to the one based on lookup tables. In particular, the contact characteristics are calculated on-line during the dynamic simulation, considering the sections of the rails and the wheel for each position of the wheel-set on the rails. For each section a group of nodal points is used through interpolation by a spline to mimic the profiles of the contact surfaces. The position of the contact points and directions of normal versors are then calculated. In particular, it is required that the vector joining the contact points, one on the rail and one on the wheel, and the normals through these points, belong to the same straight line. This method allows the on-line change of surface profiles. This feature is useful in case of rail-switch, local gauge and slope variations.

In reference [15-18] two methods for the determination of the contact points are presented: the constraint method and the elastic method, with which the normal forces on the surfaces can be calculated as well.

In the constraint method the contact points on both solids coincide as it is guaranteed by imposing the kinematic contact constraints. In the elastic method the contact points do not, in general, coincide. The contact point on the first body is located inside the volume of the second body when the solids interact each other. In this case, the contact points are selected within the intersecting volume. Points presenting the maximum normal distance are the elected contact points.

In the constraint method, no penetration is allowed between the bodies since it is assumed that the surfaces do not experience any deformation. On the other hand, in the elastic method penetration occurs and this is used to evaluate contact forces. These are null when penetration is absent. Two surface parameters are used to describe the geometry of each of the two surfaces in contact. In the analysis, the contact points are grouped in batches. A batch is a collection of sets of pairs of nodal points on the wheel and rail, respectively. A limit of two contact batches is assumed. The two points (one on the wheel and one on the rail) that lead to the maximum indentation are selected as the points of contact for any given batch. The number of points of contact between the wheel and the rail is assumed to be equal to the number of the contact batches.

All methods share the difficulties of lengthy computing times and of managing great amounts of data. In fact, these analyses usually require many iterations and the matrices containing the surface geometries are huge.

In this paper three new different methods for the compilation of a lookup table, storing precalculated solutions for the wheel/rail contact location, are discussed. According to this point of view, the location of contact points is preliminary established for a given finite set of independent variables. In a dynamic analysis, the values of the dependent variables are obtained through interpolation on previous discrete set of values. Obviously, the accuracy of the interpolation depends on the following factors: the Euclidean distance between two adjacent nodes of the mesh, the local linearized shape of the mesh and the admissible penetrating gap. The numerical tests herein carried out confirm the reliability and the computational efficiency of the method.

5.2 - THE WHEEL-SET/RAILS SYSTEM

The shape profile of the wheels and of the rails section are *S1002* e *UIC60*, respectively. Table 5.1 summarizes the main geometric features of the wheel-set-rails system. Figure 5.1 depicts the axle, the two wheels (wheel-set) and the track considered in this investigation.

Internal gauge	1.360 m
Wheel radius r_w	0.457 m
Rails tilt	1/20

Table 5.1

Main geometric features of the wheel-set-rails system

The wheel-set has six degrees-of-freedom when not constrained. These degrees-of-freedom reduce to two due to the constraints introduced by imposing continuous contact with rails. Thus only two independent variables need to be prescribed to compute the spatial position of the wheel-set.

With reference to Figure 5.2, a fixed and a moving right-hand Cartesian coordinate system are introduced. The fixed inertial coordinate system, denoted by *SRo*, has its origin *O* in the middle of the gauge, the axis Xo tangent to the rails and the *Zo* axis directed upward. The moving coordinate system, denoted by SR_G, has its origin in the centre of mass *G* of the wheel-set, axis Y_G directed along the axis of the axle and the Z_G axis directed upward.

Initially the axes of the fixed and moving coordinate systems are all parallel and the centre of mass *G* is on *Zo* axis at a distance r_w from the origin *O*.

The absolute coordinates of *G* will be denoted x_g, y_g, z_g whereas θ_x, θ_y, θ_z denote the angles between couples of *x*, *y* and *z* axes, respectively.

The displacement y_g and the yaw angle θ_z are assumed as independent variables; therefore, the four dependent variables should be deduced by imposing a continuous physical contact between rails and wheel-set.

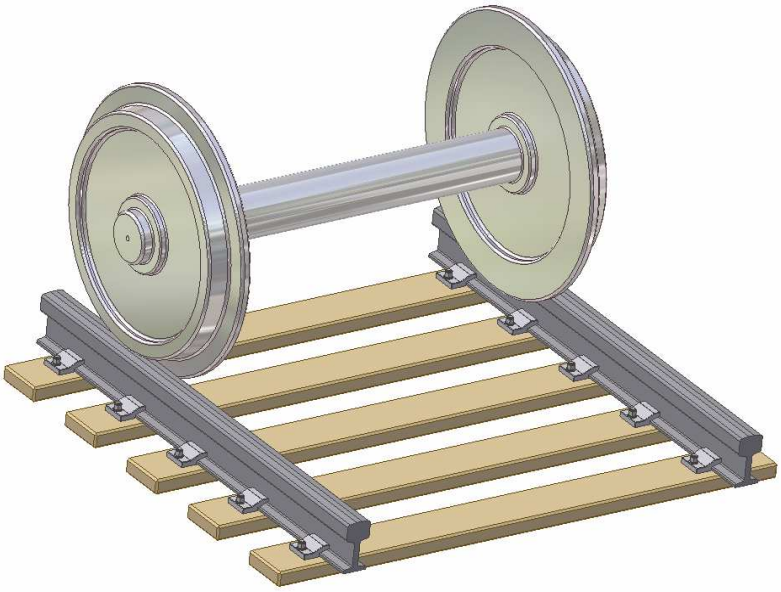

Figure 5.1
Axle, wheels and track: Physical model

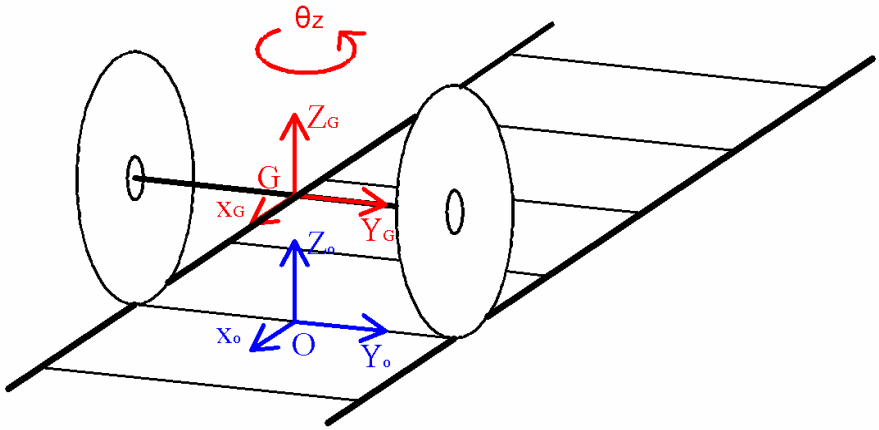

Figure 5.2
Cartesian coordinate systems and independent degrees of freedom of the axle

5.3 - MODEL SETUP

The first modeling step is the acquisition of wheel and rail profiles, as shown in figure 5.3. The surface of the rail is obtained by means of an extrusion of the rail profile along the X_o axis.

The surface of the wheel is generated through a revolution of the wheel profile about Y_G, as shown in figure 5.4.

The two surfaces are meshed. The coarser is the mesh the less is the expected accuracy and the computation time.

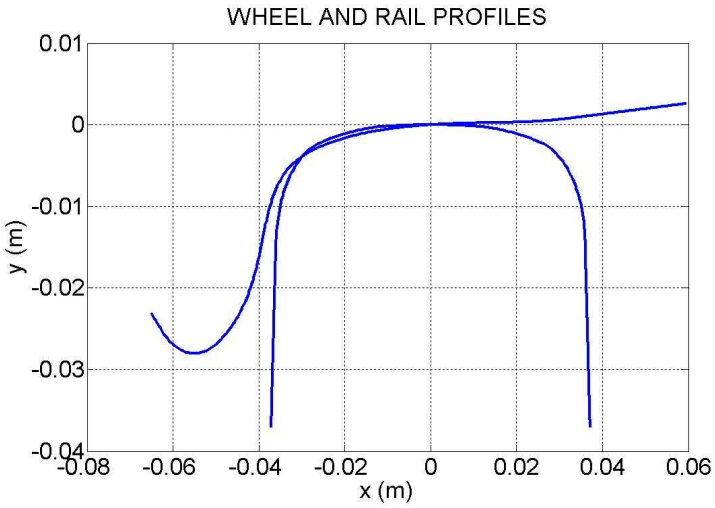

Figure 5.3
Wheel and rail profile shapes

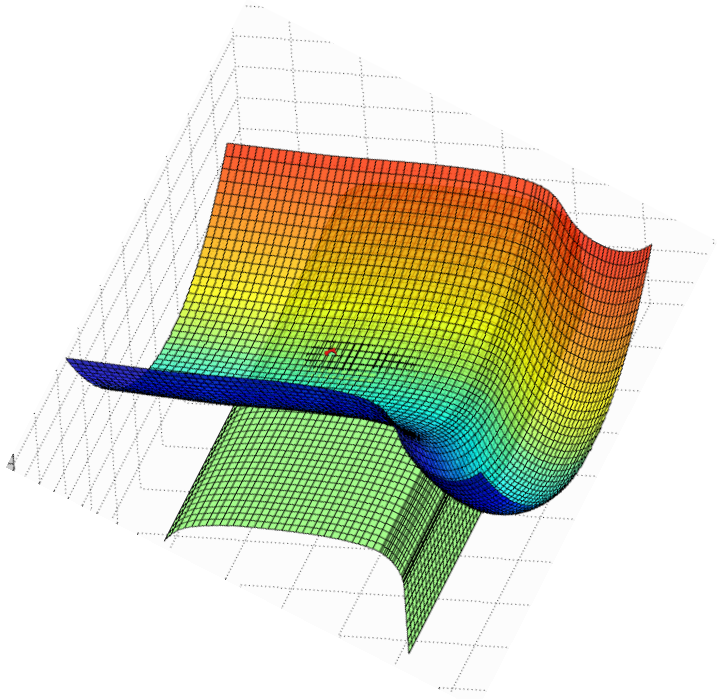

Figure 5.4
Meshes representing the wheel and rail surfaces

In spite to locate contact points, as shown in figure 5.5a, four fictitious spring elements are added to the wheel-set: one for each dependent position variable. The spring ends are attached to *G* and to the ground, respectively. Under static conditions the forces and torques generated by these spring elements and the contact forces must satisfy the following vector equilibrium equations:

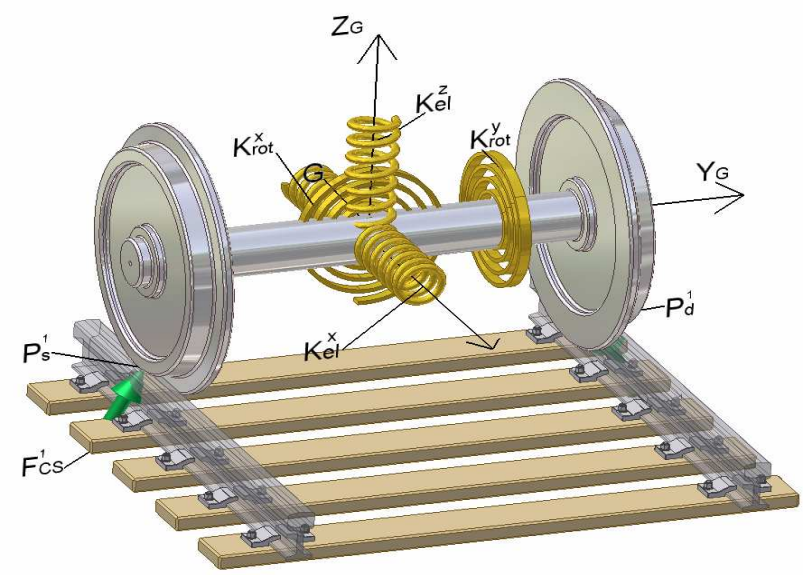

a)

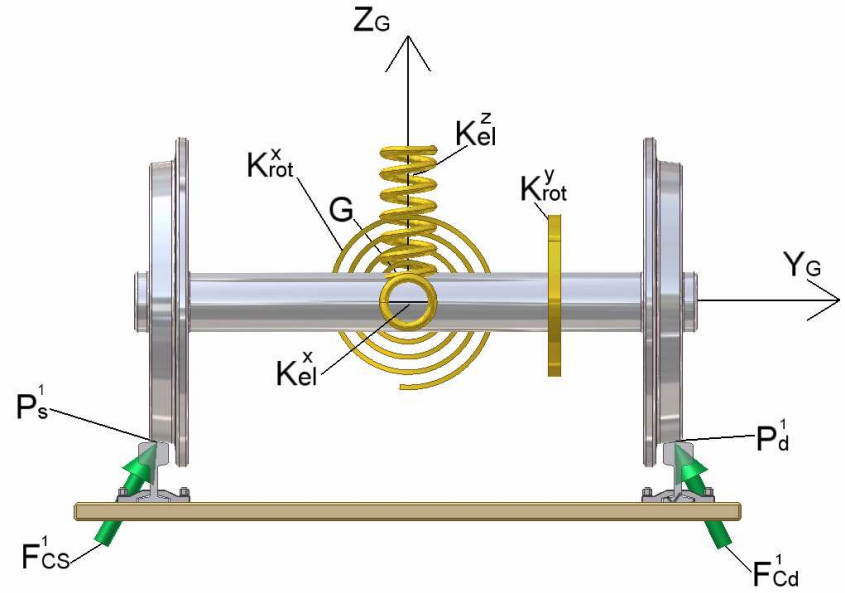

b)

Figure 5.5
Free-body diagram for the static equilibrium of the wheel-set

$$\sum_{i=1,3} k_{el}^{i}\left(x_{Gi}-l_{0i}\right)\vec{N}_{i}+\sum_{h=1}^{n_{CS}}\vec{F}_{cs}^{\,h}+\sum_{g=1}^{n_{CD}}\vec{F}_{cd}^{\,g}=0$$

$$\sum_{i=1,2} k_{rot}^{i}\theta_{i}\vec{N}_{i}+\sum_{h=1}^{n_{CS}}\left(\vec{G}P_{s}^{\,h}\times\vec{F}_{cs}^{\,h}\right)+\sum_{g=1}^{n_{CD}}\left(\vec{G}P_{d}^{\,g}\times\vec{F}_{cd}^{\,g}\right)=0 \qquad (5.1)$$

where:

the upperscript *i* varying from 1 to 3 denotes the *x*, *y*, *z* components;

k_{el}^{i} is the stiffness of the spring acting along the i^{th} axis of *SRo*;

k_{rot}^{i} is the stiffness of the torsional spring which counteracts rotations about the i^{th} axis of *SRo*;

l_{0i} is the undeformed spring length;

n_{CS} and n_{CD} are the number of contact points on left and right wheels, respectively;

$\vec{F}_{cs}^{\,h}$ are the contact forces at the h^{th} contact points on the left wheel;

$\vec{F}_{cd}^{\,g}$ are the contact forces at the g^{th} contact points on the right wheel;

$\vec{G}P_s^h$ are the vectors oriented from G to the h^{th} left point of contact;

$\vec{G}P_d^g$ is the vectors oriented from G to the g^{th} right point of contact;

$\vec{N}_i$ is the versor oriented along the i^{th} axis of *SRo*.

In table 5.2 the spring stiffnesses are summarized.

k_{el}^x	$10^7 \frac{N}{m}$	k_{rot}^x	$5.6 \cdot 10^6 Nm$	l_{0x}	0
k_{el}^z	$10^7 \frac{N}{m}$	k_{rot}^y	$5.6 \cdot 10^6 Nm$	l_{0z}	7 mm

Table 5.2

Stiffnesses and undeformed lengths of the spring elements

5.4 - CONTACT POINTS DETECTION

5.4.1 - The intersecting volume

As shown in the geometry depicted in figure 5.6a, the intersecting volume V_{int} is the one shared by the wheel and rail when they are in contact through a penetration volume between the bodies.

Let us denote by:

S_r and S_b the wheel and rail portions of surface delimited by n_r and n_b nodes, respectively;

$i=3,\ldots, n_r$ and $j=3,\ldots, n_b$ the nodes of the wheel and rail surfaces, respectively;

$\vec{V}_{ij}$ the vector joining the nodes i and j;

$\vec{N}_i$ the normal to surface *Sr* at the i^{th} node, oriented toward the convexity of S_r;

$\vec{N}_j$ the normal to surface S_b at the j^{th} node, oriented toward the convexity of S_b;

The i^{th} node and j^{th} node are included in the intersecting volume only if the following inequalities are simultaneously satisfied:

$\vec{V}_{ij} \cdot \vec{N}_j \geq 0$

$\vec{V}_{ij} \cdot \vec{N}_i \leq 0$

Among the nodes included in the intersecting volume we distinguish those which belong to wheel, or to the surface S_r, and form the intersecting volume V_{int}^r, from those which belong to the rail, or to the surface S_b, and form the volume V_{int}^b. The union of V_{int}^r and V_{int}^b gives the volume V_{int}. Hereinafter, we will focus on the determination of the centre of contact on both surfaces. However, compenetrating volume magnitudes are not really necessary. This is the reason why nodal points coordinates are used to test contact conditions.

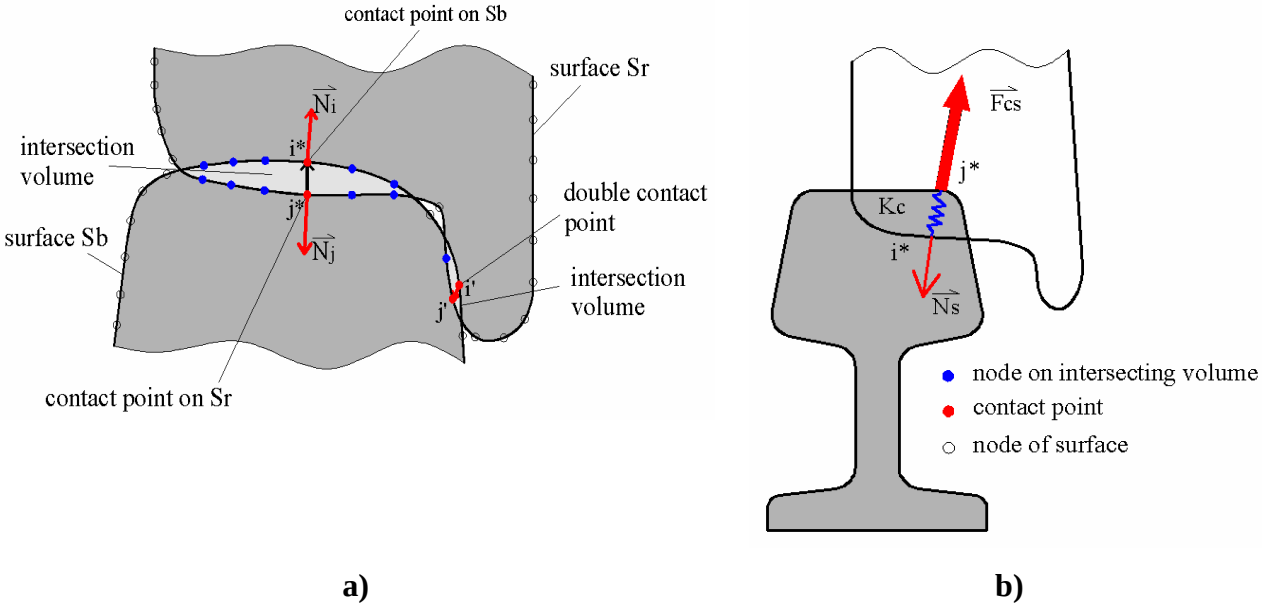

Figure 5.6
a) Wheel/rail intersecting volume in the method of maximum distance; b) elastic model used for the contact force between the wheel and rail.

5.4.2 - The contact points

Three different methods for computing wheel-rail contact points are proposed and discussed. All the methods share the same objective of locating the intersections between V_{int}^b and V_{int}^r.

We named these methods as follows:

- *maximum distance*
- *maximum normal distance*
- *load centre*

5.4.2.1 - Method of the maximum distance

All nodes included in V_{int} are candidate to be contact points between the surfaces. For each node i^* of S_r within V_{int} we find the node j^* of S_b within V_{int} such that the norm of $\vec{V}_{i^*j^*}$ has the minimum value. In this way a correspondence between the set of nodes i^* and the set of nodes j^* is established. The indentation is computed by means of the scalar product

$$C_{i^*j^*} = \vec{V}_{i^*j^*} \cdot \vec{N}_{j^*} \qquad (5.2)$$

Among all the set of nodes i^*, j^* the contact points are those experiencing the maximum value of $C_{i^*j^*}$.

$$C_{\max} = \max\left(C_{i^*j^*}\right)$$

5.4.2.2 - Method of the *maximum normal distance*

This method offers a refinement in the computation of contact point P'_b but needs the election of a reference surface. Here the wheel surface is adopted. The method of maximum distance is initially applied. Then, with reference to the geometry depicted in figure 5.7, the coordinates of the new contact point P'_b on the rail are obtained from:

$$\vec{OP'}_b = \vec{OP}_r + \left(\left(\vec{OP}_b - \vec{OP}_r\right) \cdot \vec{N}_r \right)\vec{N}_r$$

where:

$\vec{OP}_r$ is the position vector of the contact point on the wheel computed with the method of the maximum distance;

$\vec{OP}_b$ is the position vector of the contact point on the rail computed with the method of the maximum distance;

$\vec{N}_r$ is the normal versor to the wheel surface at point P_r.

The maximum indentation $C_{\max}$ is calculated using the formula:

$$C_{\max} = \left(\vec{OP}_b - \vec{OP}_r\right) \cdot \vec{N}_r$$

With this method the accuracy of the computation is less dependent on the surface mesh coarseness. This turns also into an overall speedup. The main limitation of this method is that the contact points on the wheel surface need to be located on the grid nodes.

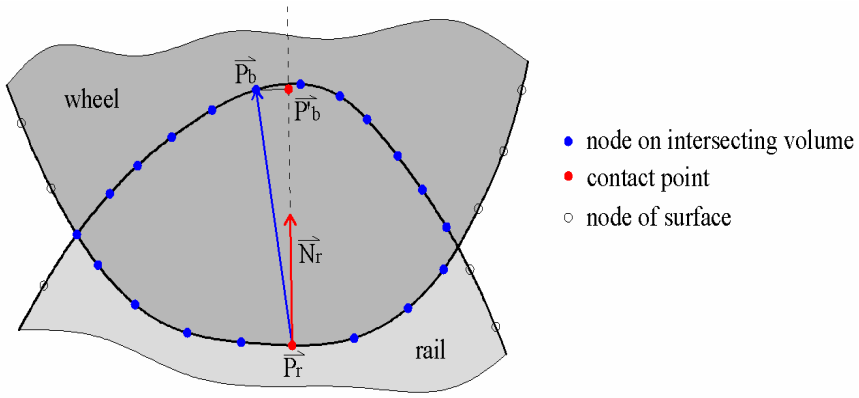

Figure 5.7
Wheel/rail intersecting volume in the method of the maximum normal distance.

5.4.2.3 - Method of the *centre of load*

In this method the volumes of intersection V_{int}^{b} and V_{int}^{r} are separately considered.

The contact points are made coincident with the load centre P_{Gr} and P_{Gb} of the grid nodes on the boundary of V_{int}. Analytically this results into:

$$\vec{OP}_{Gr} = \frac{\sum_{i=1}^{n_r} \vec{OP}_i^{\,r}}{n_r}$$

$$\vec{OP}_{Gb} = \frac{\sum_{j=1}^{n_b} \vec{OP}_j^{\,b}}{n_b}$$

where :

$\vec{OP}_{Gr}$ and $\vec{OP}_{Gb}$ denote the position vectors of the barycentres of the grid nodes on the boundaries of V_{int}^{b} and V_{int}^{r}, respectively;

$\vec{OP}_i^{\,r}$ and $\vec{OP}_j^{\,b}$ denote the position vectors of generic grid nodes on the boundaries of V_{int}^{b} and V_{int}^{r} respectively;

n_r and n_b denote the nodes number of the intersection volumes of the wheel and the rail, respectively.

The maximum indentation $C_{\max}$ is calculated by means of the formula:

$$C_{\max} = \left(O\vec{P}_{Gb} - O\vec{P}_{Gr}\right) \cdot \vec{N}_r$$

Since P_{Gr} does not belong to the wheel surface, the normal versor $\vec{N}_r$ coincides with the normal to the wheel surface passing through P_{Gr}, as shown in figure 5.8.

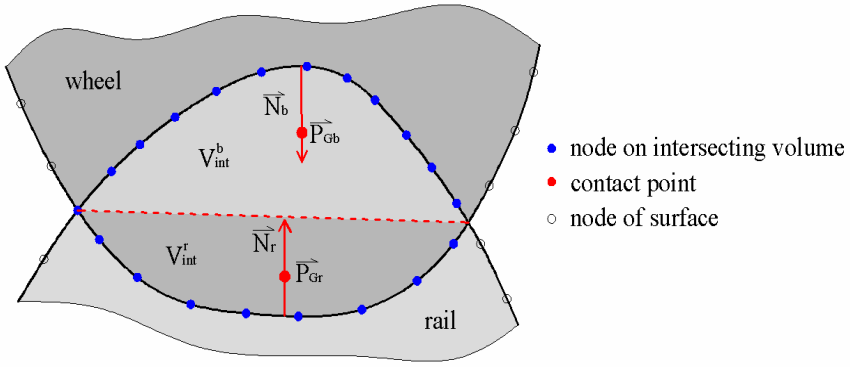

Figure 5.8
Wheel/rail intersecting volume in the method of barycentre.

5.4.3 - Normal contact forces

With reference to the geometry depicted in figure 5.7b, the normal contact forces $\vec{F}_{cs}$ and $\vec{F}_{cd}$, in the left and right wheel-rail interface respectively, are computed as follows :

$$\vec{F}_{cs} = -C^s_{\max} k_c \vec{N}_s$$
$$F_{cd} = -C^d_{\max} k_c \vec{N}_d$$

where:

k_c is the contact stiffness;

$C^s_{\max}$ and $C^d_{\max}$ are the maximum normal indentations of the left and right wheel respectively;

$\vec{N}_s$ and $\vec{N}_d$ are the outward normals of the left and right wheel, respectively.

The value of k_c is established through iteration. In particular, convergence is achieved when the variables x_G, y_G, z_G, θ_x, θ_y, θ_z simultaneously satisfy both the equilibrium equations (5.1) and the following inequalities:

$$C^s_{\max} \le C^{amm}_{\max}$$
$$C^d_{\max} \le C^{amm}_{\max} \qquad (5.3)$$

where $C_{\max}^{amm}$ is the maximum indentation allowed. In this investigation $C_{\max}^{amm}$=0.01 mm is assumed. This last value is broadly justified by some qualitative considerations. The value should be lower than the expected compression as suggested by the Hertz theory. Furthermore, the mesh refinement should be carried out in such a way that edge effects due to meshing are lower than the same value.

It should be observed that the values of contact stiffness, within a given range, do not influence the position of the contact points which depends on the surfaces geometry. The stiffness values adopted solving the system of equations (5.1) are those given in Table 5.2. It can be observed that changing the stiffness values for *n* times, with *n* spanning between 1 to 10, the maximum values of the contact point displacements achieved is 10^{-19} m.

$k_{el}^{x} = k_{el}^{z} = n \cdot 10^{7} \; N/m$

This result, showed in Figure 5.9, proves that the position of the contact point is almost independent on the initial preload of the external springs. This rests upon the convergence of the iterative method.

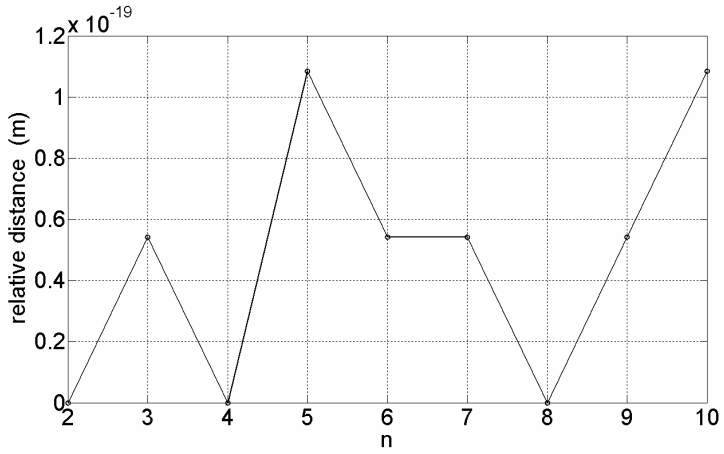

Figure 5.9
Relative distance from contact points as regard to *n*

The proposed algorithm for the detection of contact points can be summarized in the following steps:

1) Prescribe the values of the independent variables y_g e θ_z. Set to zero the dependent variables x_g, zg, θ_x, θ_y .

2) Prescribe an initial value to the stiffness k_c.

3) Define the intersecting volume V_{int} , the position of the provisory contact points, normals and maximum indentation between the wheels and the rails.

4) Compute the normal forces with equations (5.2).

5) Update the values of x_g, z_g, θ_x, θ_y making use of equilibrium equations (5.1).

6) Update the intersecting volume V_{int}, the position of the provisory contact points, normals and maximum indentation between the wheels and the rails.

7) If the maximum indentation is less than C_{max}^{amm} then store in a database the values of x_g, y_g, z_g, θ_x, θ_y, θ_z and the contact points;

8) If the previous condition is not satisfied then increase the value of k_c and go back to step 4).

The flow-chart of this algorithm is shown in figure 5.10.

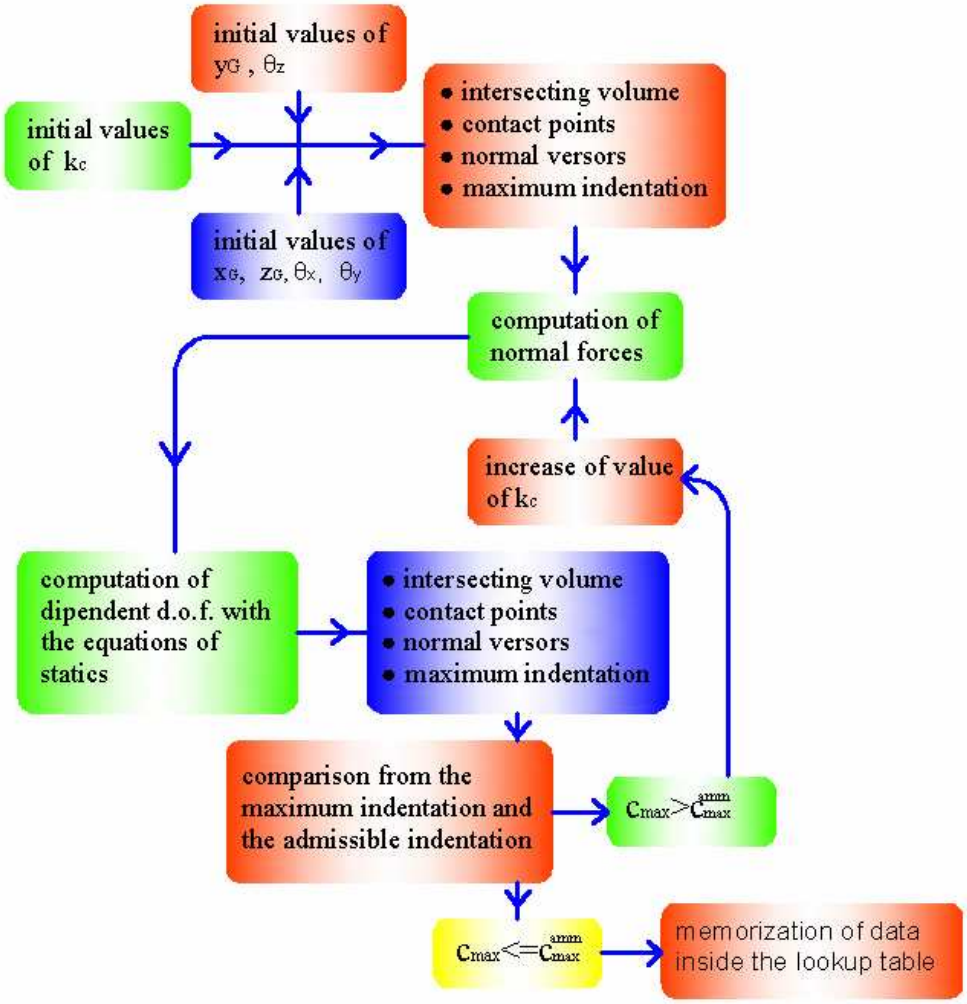

Figure 5.10
Iteration scheme for the detection of contact points

5.4.4 - The maximum indentation value

The limit $C_{\max}^{amm}$ = 0.01 mm, adopted as the maximum indentation value, has been established considering Hertz theory for the contact cylinder-plane (see Figure 5.11). The average vertical load estimated on each wheel is *P*=75000 N.

The width *L*=5mm of the cylinder has the same order of magnitude of the transverse dimension for the wheel-rail contact area.

The radius *R* of the cylinder is the same of the wheel. Cylinder and plane are both in steel with Young's modulus $E = 206 \cdot 10^9 \frac{N}{m^2}$ and Poisson's coefficient $\nu = 0.3$.

Hence, the maximum value of the indentation is

$$C_{\max}^{amm} = \frac{2PK}{L}\left(1 + \ln\left(\frac{4L^3}{2KPR}\right)\right) \approx 0.11\,mm \quad \text{where} \quad K = \frac{1-\nu^2}{\pi E}$$

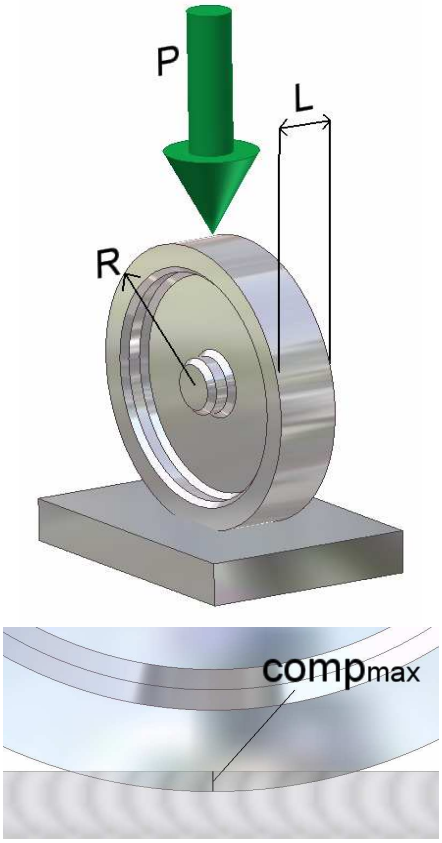

Figure 5.11
Indentation in the contact cylinder-plane

5.4.5 - The stiffness of the lateral flange

Because of the special shape of the wheel profile with the presence of a lateral flange, a linearly variable value of wheel-flange stiffness k_c is herein assumed. In particular k_c is linearly interpolated only on the flange between a maximum value K_{max} at the flange base and a minimum value K_{min} at the flange tip.

The value of K_{max} at the base of the flange is estimated considering the Hertz's type of deformation. The value of K_{min} is calculated considering two contributions: the first one is the Hertz's deformation, the second regards the flange bending as a cantilever beam. Figure 5.12 illustrates the two contributions to the overall displacement caused by an applied force at the tip of the flange.

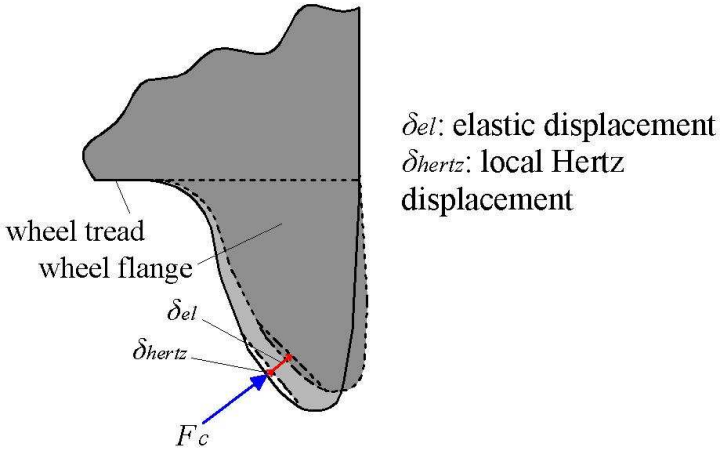

Figure 5.12
Contributions to the total displacement of the flange

The stiffnesses due to Hertz's type deformation is computed by means of the formula:

$$K_{hertz} = \frac{2\pi G}{3(1-\nu)} \frac{1}{\sqrt{D_{\max} + D_{\min}}} \frac{\sqrt{E(g)}}{gW(g)^{\frac{3}{2}}}$$

where:

G is the tangential module of elasticity;

ν is the Poisson coefficient;

$D_{\max}$ and $D_{\min}$ depend on the local curvatures of the two surfaces in contact, in particular;

$D_{\max} = \max(D_{long}, D_{trasv})$

$D_{\min} = \min(D_{long}, D_{trasv})$

with:

$$D_{long} = \frac{1}{2}\left(C_{long}^{r} + C_{oong}^{b}\right)$$

$$D_{trasv} = \frac{1}{2}\left(C_{trasv}^{r} + C_{trasv}^{b}\right)$$

C_{long}^{r} and C_{long}^{b} are the longitudinal curvatures at contact point of the wheel and the rail, respectively;

C_{trasv}^{r} e C_{trasv}^{b} are the transversal curvatures at contact point of the wheel and the rail respectively;

$$g = \min\left(\frac{a}{b}, \frac{b}{a}\right)$$

where *a* and *b* are the semi-axis lengths of the contact ellipse, *K (g)* and *W (g)* are elliptic integrals, defined as follows:

$$W(g) = \int_0^{\pi/2}\left[1-\left(1-g^2\right)\sin^2\psi\right]^{-1/2} d\psi$$

$$E\left(g\right) = \int_0^{\pi/2}\left[1-\left(1-g^2\right)\sin^2\psi\right]^{1/2} d\psi$$

Replacing the values of the curvatures for the contact on the base and the contact on the tip of the flange, the stiffness values follows:

$$k_{hertz}^{bf} = 7.87\cdot 10^{10}\,\frac{N}{m}$$

$$k_{hertz}^{pf} = 7.09\cdot 10^{9}\,\frac{N}{m}$$

where k_{hertz}^{bf} and k_{hertz}^{pf} are the values of the Hertz's stiffnesses at the base of the flange and at the tip, respectively. The second contribution k_{el}^{pf} is obtained considering the wheel flange as a cantilever beam having the dimensions of the base section equal to (see figure 5.13):

$$b = 0.32m$$

$$h = 0.045m$$

$$l = 0.0275m$$

$$k_{el}^{pf} = \frac{bh^3E}{4l^3} = 7.6\cdot 10^{10}\,\frac{N}{m}$$

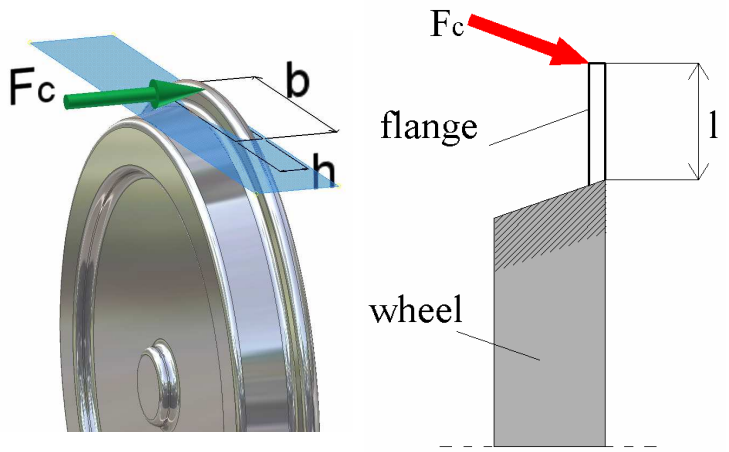

Figure 5.13
Model of the flange as a cantilever beam

The overall stiffness at the tip flange is:

$$k^{pf} = \frac{k_{hertz}^{pf} k_{el}^{pf}}{k_{hertzx}^{pf} + k_{el}^{pf}} = 6.48 \cdot 10^{9} \frac{N}{m}$$

while the ratio between the stiffnesses at the tip and the base of the flange is given by:

$$\chi = \frac{k^{pf}}{k_{ertz}^{bf}} = 0.082$$

Figure 5.14 shows the concept. The magnitude of this ratio, though significant, seems neglected in the models available in the current literature. The intermediate stiffnesses values within the base and the tip of the flange are calculated with a linear interpolation assuming as parameter the distance between the contact point and the axis of the wheel.

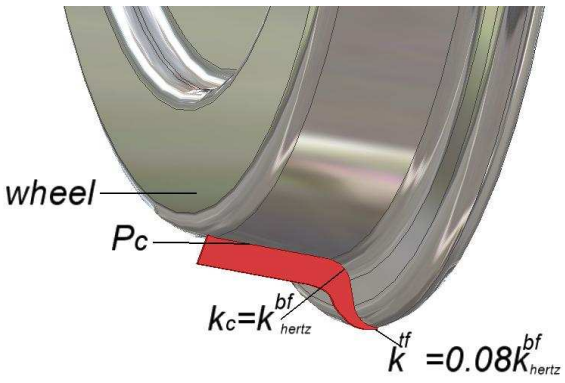

Figure 5.14
Variation of contact stiffness k_c according to the position of the point of contact P_c.

5.4.6 - The double contact

In most cases, our model finds only one point of contact between the wheel and rail surfaces. However, in some cases there are configurations with a double contact, *i.e.* flange-rail and tread-rail. In this case two separated volumes of intersection are created on the same wheel. With reference to figure 5.15, two different possibilities are considered:

- *split intersecting volumes*;
- *merged intersecting volumes*.

In order to establish if the intersecting volumes are split or merged, i.e. the contact is double or single, the following test is applied: if one or more rows of aligned nodes that do not belong to V_{int} exists in the group of nodes that form the surface of V_{int} then there are two contact points. As can be observed from figures 5.6a and 5.15, the presence of such rows implies split intersecting volumes and a double contact. Figure 5.16 shows the wheel and rail surfaces in two configurations: single and double contact.

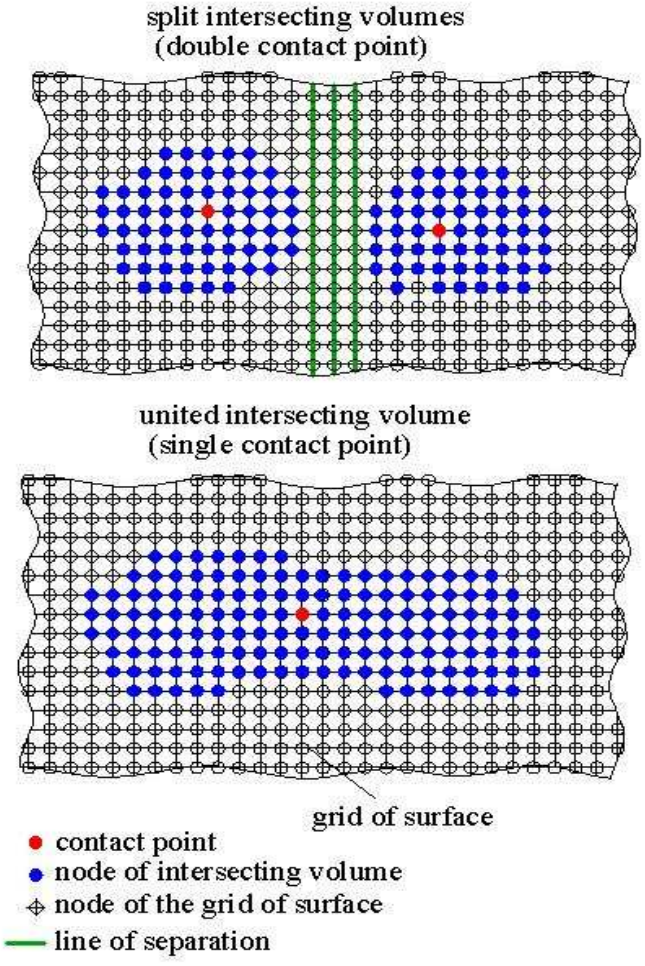

Figure 5.15
Example of united and split volume of intersection

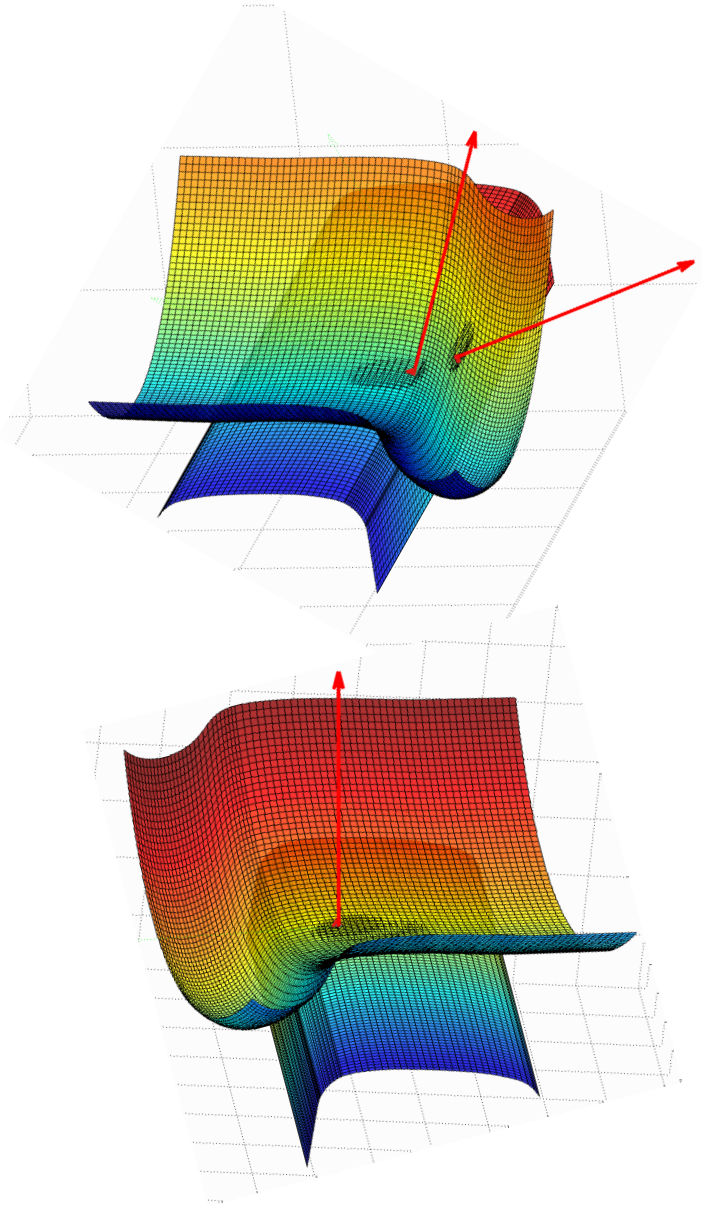

Figure 5.16
Wheel and rail surfaces in two configurations with normal versors: a) double contact; b) single contact.

5.5 - GENERATION OF THE LOOKUP TABLE

In order to reduce CPU time required, the points of contact and all the other contact characteristics - for a given configuration of the wheel-set - are obtained from a previously compiled lookup table. This consists of matrices in which the dependent variables are computed as a function of the two independent variables.

The values of the two independent coordinates are uniformly spaced within an interval extended to the obvious engineering range of interest:

$$-9\,mm \le y_G \le 9\,mm; \qquad -0.12\,rad \le \alpha_z \le 0.12\,rad.$$

The values of dependent coordinates are here stored in $37\times37\times100$ matrix, . The rows represent the values of y_G while the columns define the yaw angle ϑ_z.

The contact features stored in the lookup tables are:

- four dependent coordinates;
- coordinates of the contact points on the wheel;
- coordinates of the contact points on the rail;
- components of the longitudinal, transverse and normal versors on the wheel in correspondence to the contact point;
- components of the longitudinal, transverse and normal versors on the rail in correspondence to the contact point;
- principal curvatures and directions on the wheel surface in the contact point;
- principal curvatures and directions on the rail surface in the contact point;
- contact characteristics determined by means of the Hertz theory (e.g. the major and minor semi-axes of the contact ellipse).

Given two values of the independent variables the remaining four values of the dependent variables are readily obtained through linear interpolation. Furthermore, the position of the contact points between wheels and rails and the normal versors are computed making use of the interpolated data. All the stored quantities can be visualized by means of three-dimensional diagrams. The axes represent the coordinate y_G, the angle ϑ_z and vertical depth is the quantity to visualize. Figure 5.17 shows a simplified scheme of the lookup table while Figure 5.18 shows the surface of the coordinate *x* of the contact point on the left wheel, obtained with the three discussed methods.
The three methods are denoted as follows: 1 (*method of the centre of load*), 2 (*method of maximum distance*), 3 (*method of maximum normal distance*). We observe that:

- the results of method 1 are much more smoothed than the remaining methods, this is observed on both wheel-set positions and contact points;
- the results of method 1 are less affected by mesh refinement;
- method 2 supplies lightly irregular results, mainly caused by the location of the contact points within the grids points;
- method 3 supplies irregular surfaces again, although these are smoothed on the rail; this is due to the search contact algorithm that refers to wheel nodes

Figures 5.19-5.22 show the dependent coordinates versus the values of y_G and θ_z.

Figures 5.23-5.28 show the coordinates of the contact points on the left wheel and rail. Figures 5.29-5.31 show the three components of the normal versor to the left wheel in the contact point. Figures 5.32-5.37 show the coordinates of the contact points on the right wheel and rail. Figures 5.38-5.40 show the components of the normal versor to the right wheel in the contact point. Figures 5.41-5.48 show the longitudinal and transverse curvatures of the wheel and rail surfaces in correspondence of the contact point.

All the surfaces are very regular, not presenting any isolated peaks. In the cited figures all the lengths are expressed in meters, while the angles are given in radians.

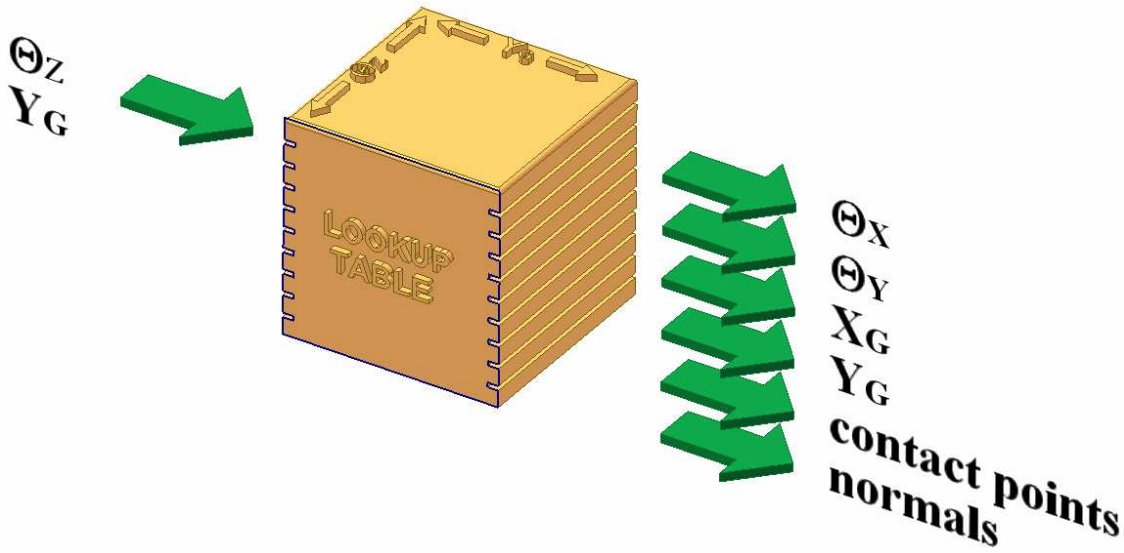

Figure 5.17
Scheme of lookup table

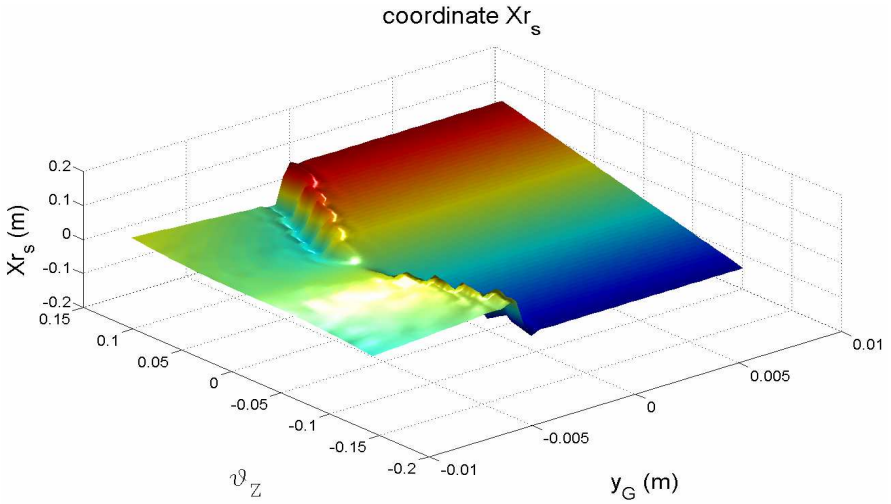

Coordinate x of the contact point on the left wheel with the method of center of load

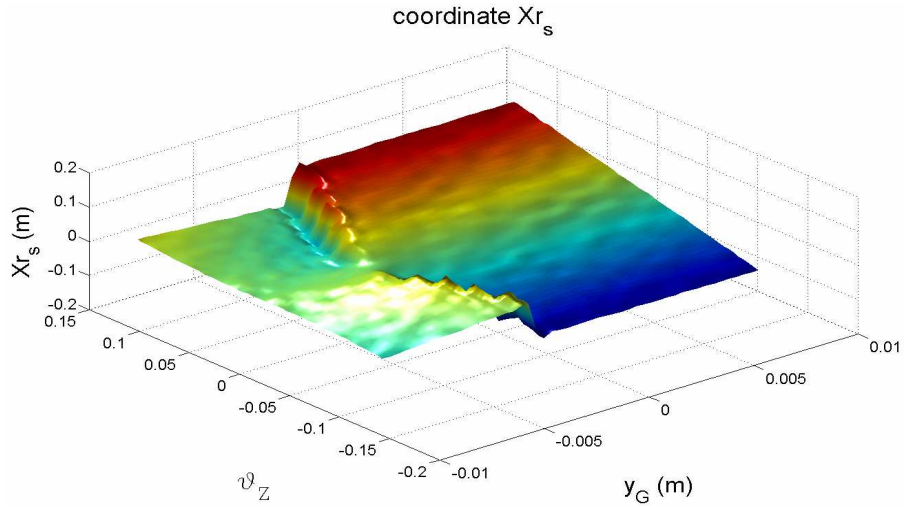

Coordinate x of the contact point on the left wheel with the method of the maximum distance

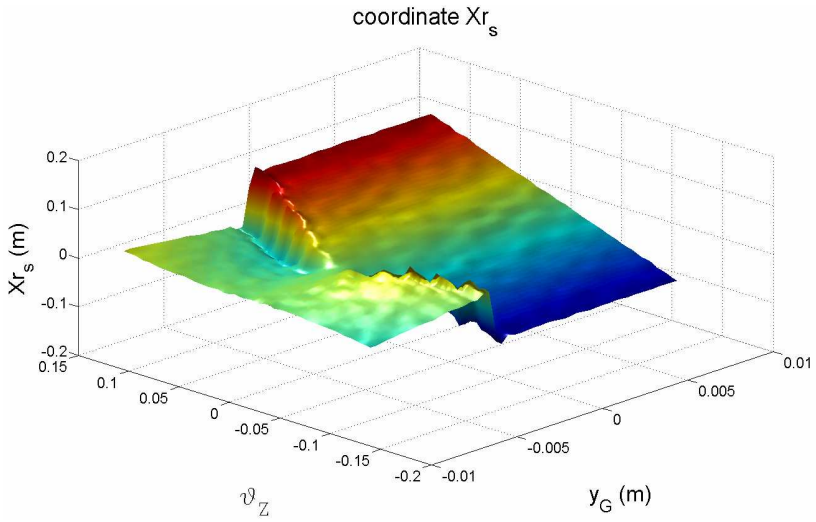

Coordinate x of the contact point on the left wheel with the method of the maximum normal distance

Figure 5.18
Graphic of coordinate x of the contact point on the left wheel regarding the two independent position variables

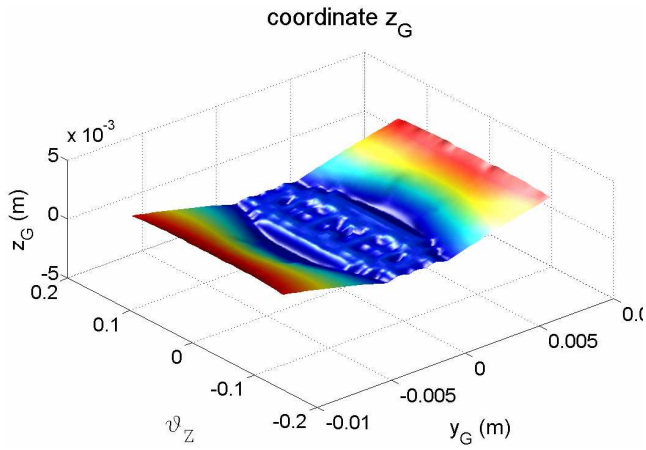

Figure 5.19
Coordinate Z_G of the wheel-set

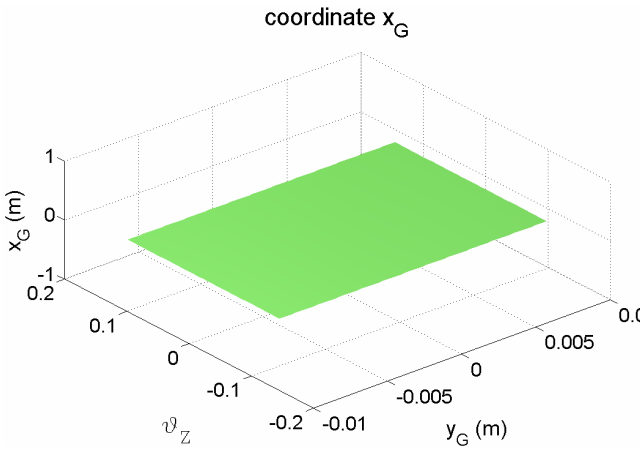

Figure 5.20
Coordinate X_G of the wheel-set

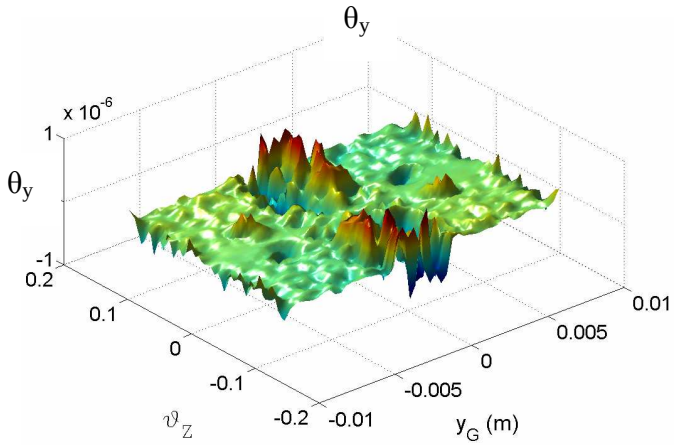

Figure 5.21
Angle θ_y of the wheel-set.

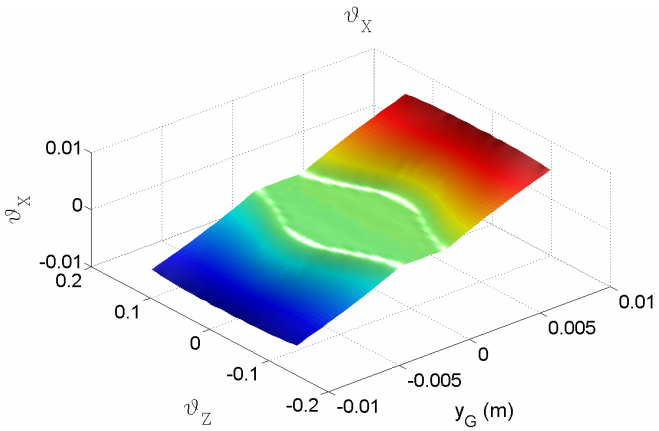

Figure 5.22
Angle θ_x of the wheel-set.

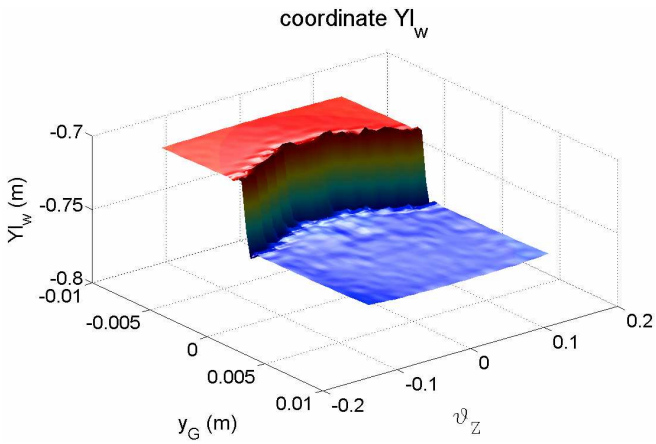

Figure 5.23
Coordinate y of the contact point on the left wheel.

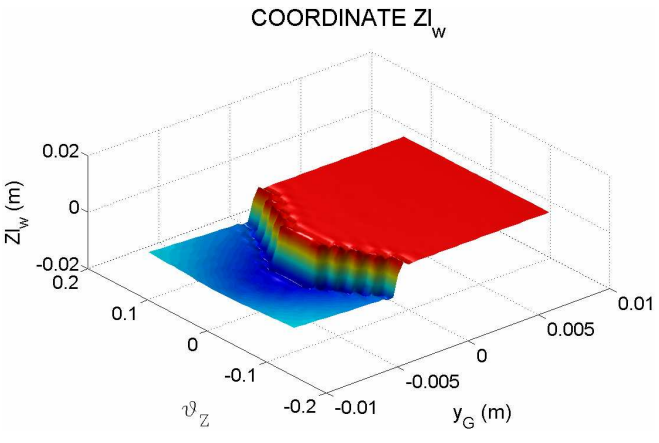

Figure 5.24
Coordinate z of the contact point on the left wheel.

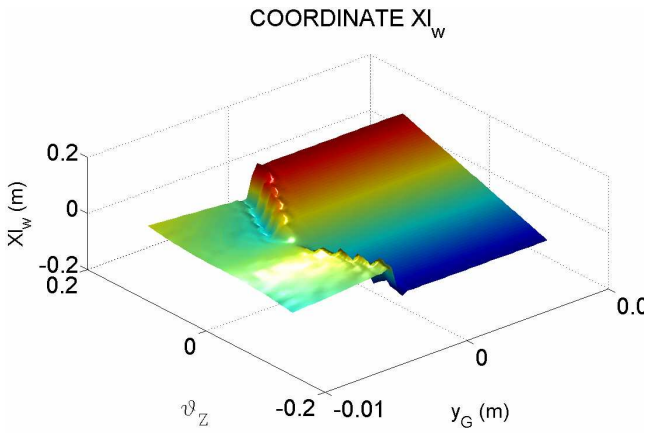

Figure 5.25
Coordinate x of the contact point on the left wheel

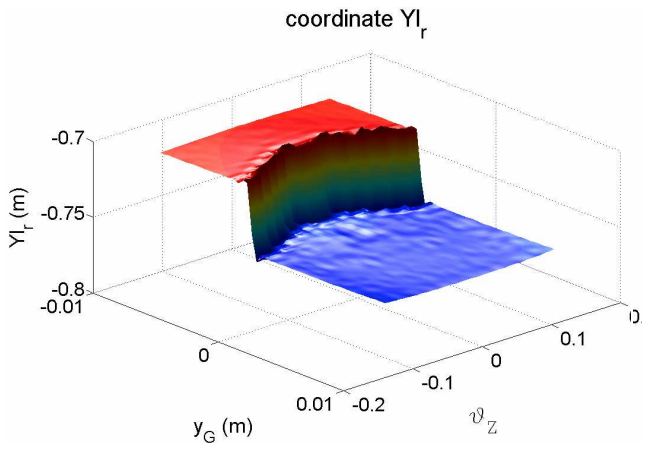

Figure 5.26
Coordinate y of the contact point on the left rail

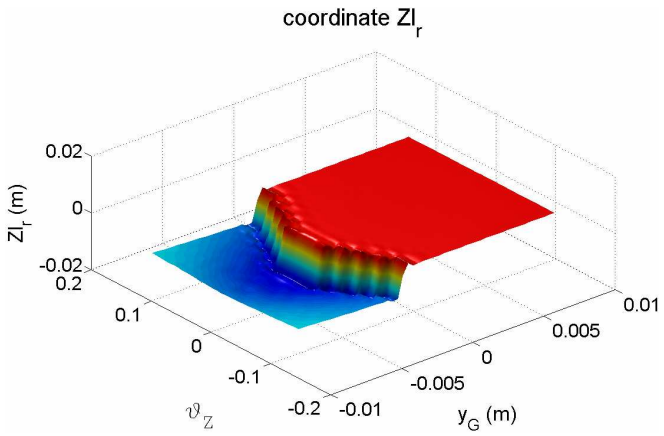

Figure 5.27
Coordinate z of the contact point on the left rail.

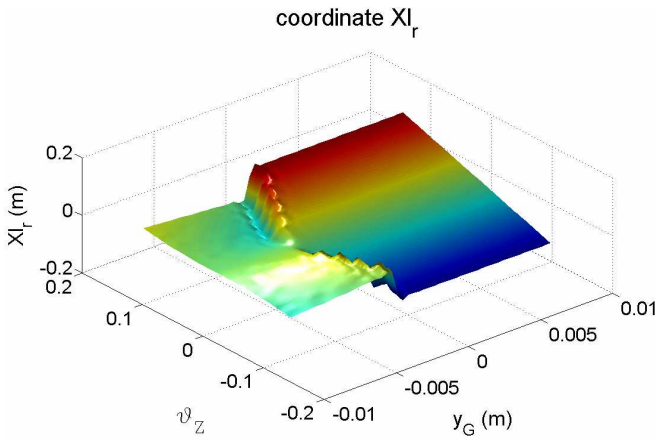

Figure 5.28
Coordinate x of the contact point on the left rail.

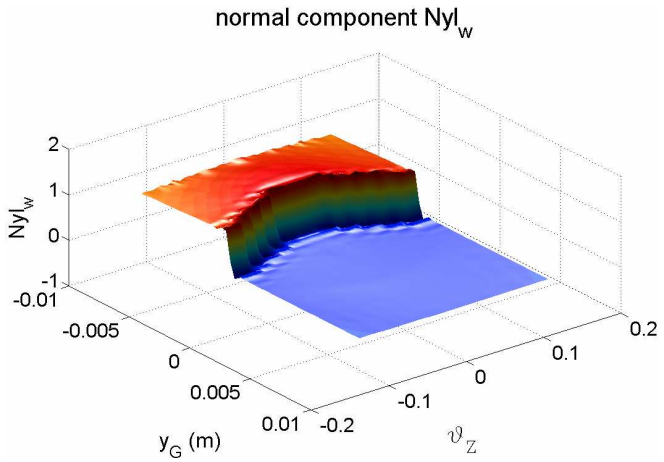

Figure 5.29
Component y of the normal versor on the left wheel.

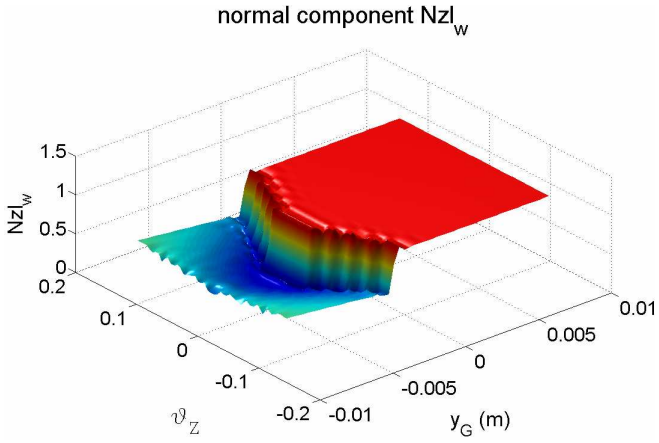

Figure 5.30
Component z of the normal versor on the left wheel.
.

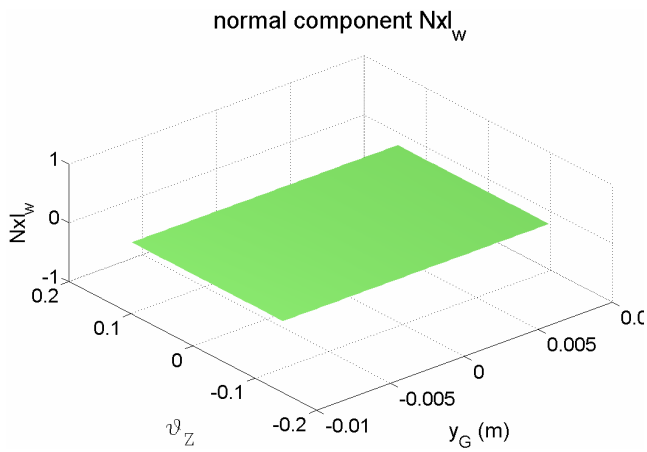

Figure 5.31
Component x of the normal versor on the left wheel.

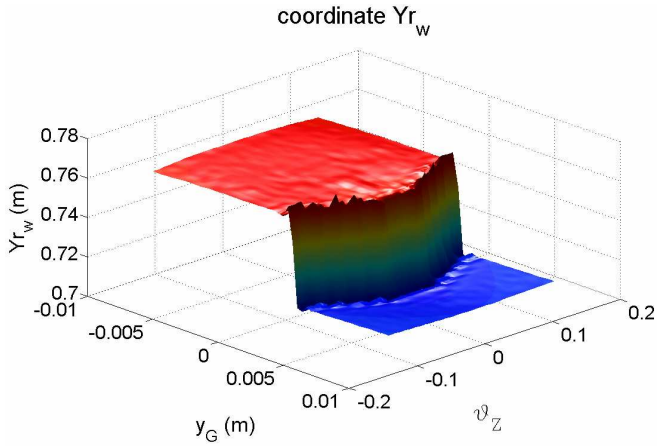

Figure 5.32
Coordinate y of the contact point on the right wheel

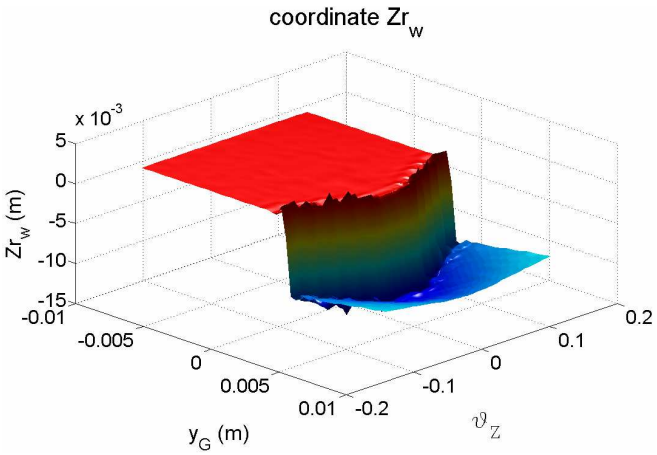

Figure 5.33
Coordinate z of the contact point on the right wheel.

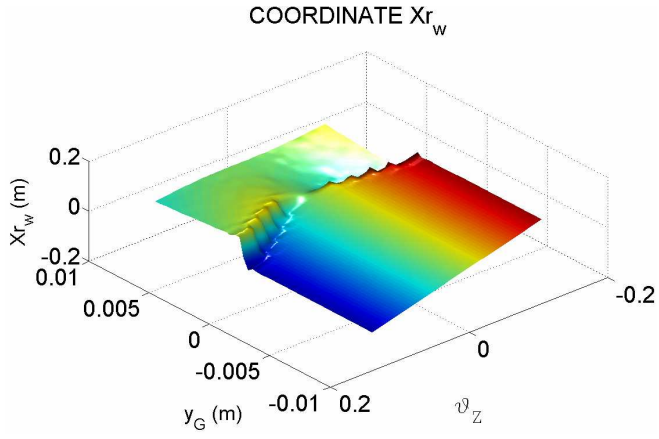

Figure 5.34
Coordinate x of the contact point on the right wheel.

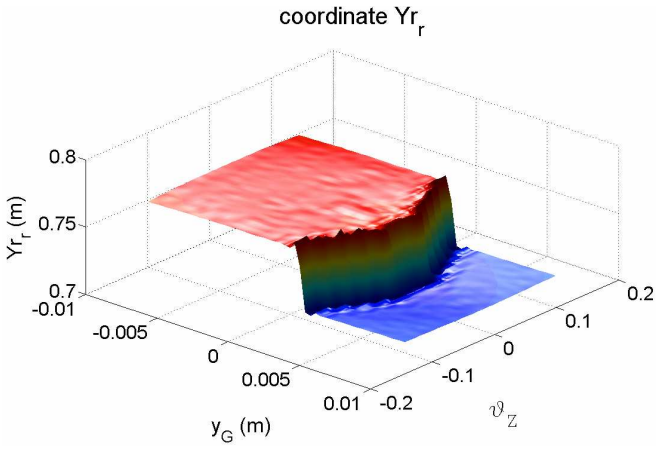

Figure 5.35
Coordinate y of the contact point on the right rail.

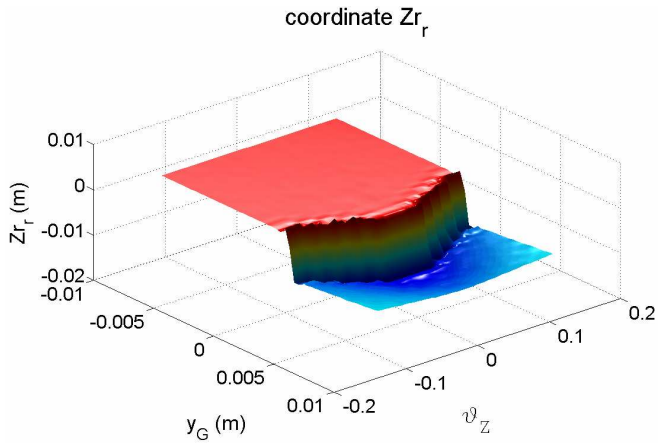

Figure 5.36
Coordinate z of the contact point on the right rail.

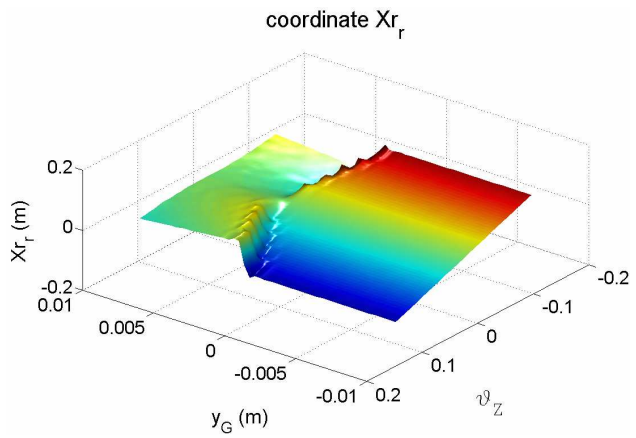

Figure 5.37
Coordinate x of the contact point on the right rail

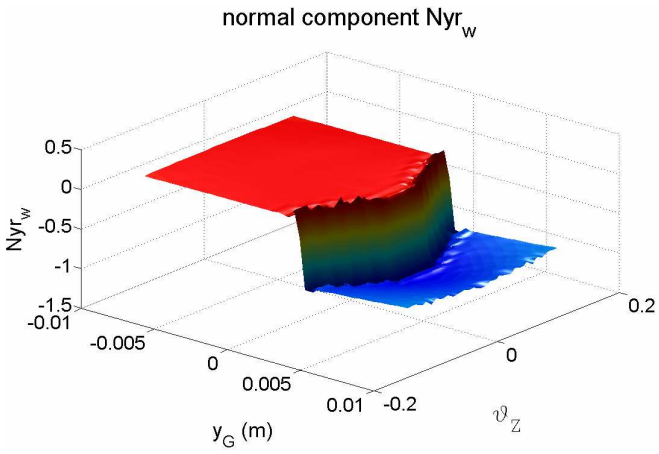

Figure 5.38
Component y of the normal versor on the right wheel.

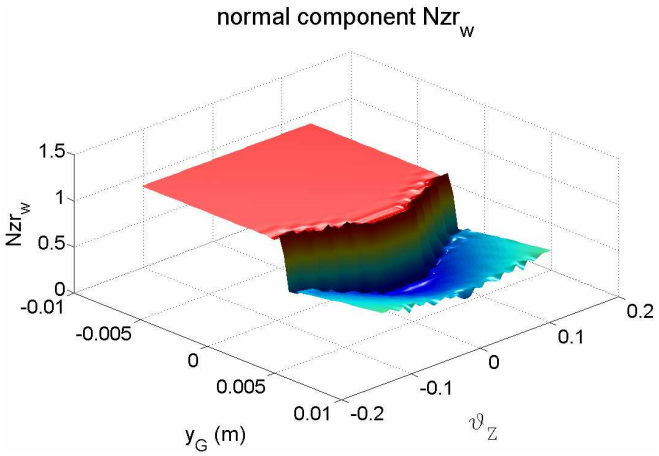

Figure 5.39
Component z of the normal versor on the right wheel.

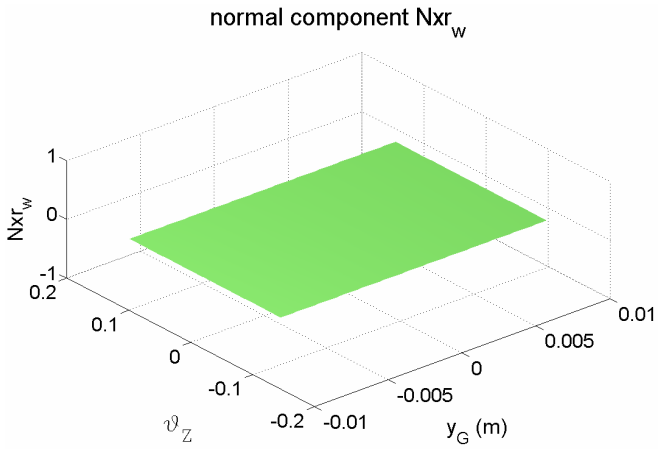

Figure 5.40
Component x of the normal versor on the right wheel.

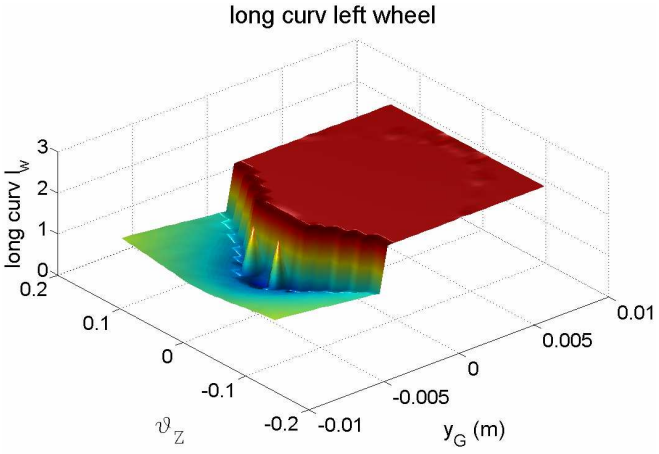

Figure 5.41
Longitudinal curvature of the left wheel in correspondence of the contact point.

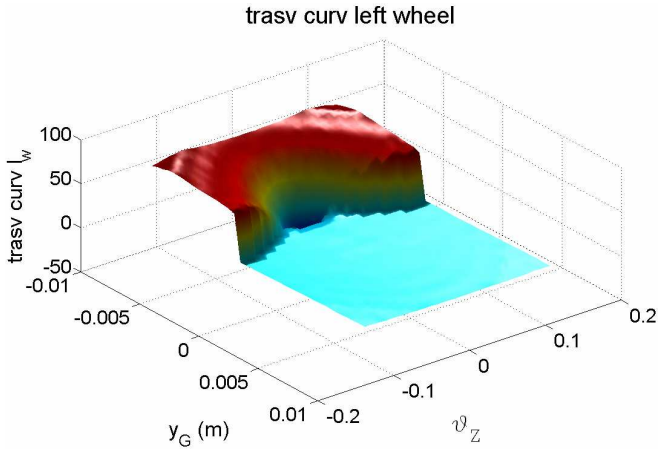

Figure 5.42
Transverse curvature of the left wheel in correspondence of the contact point.

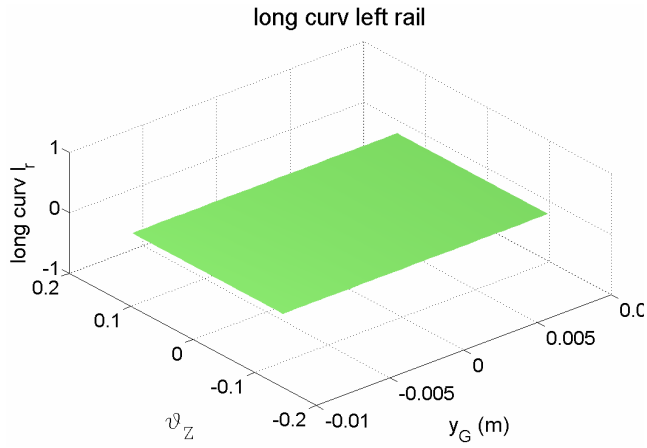

Figure 5.43
Longitudinal curvature of the left rail in correspondence of the contact point.

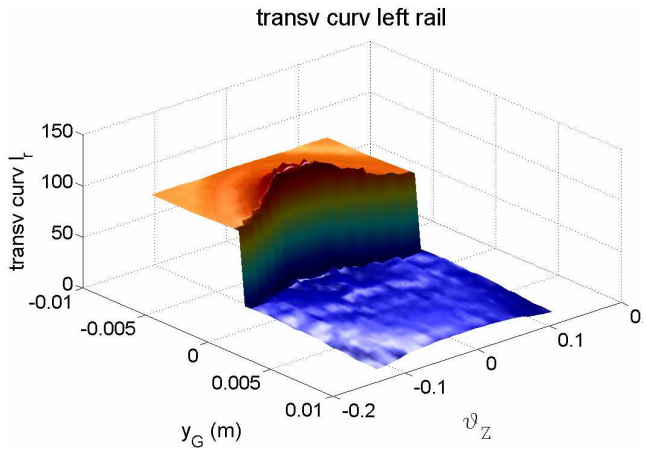

Figure 5.44
Transverse curvature of the left rail in correspondence of the contact point.

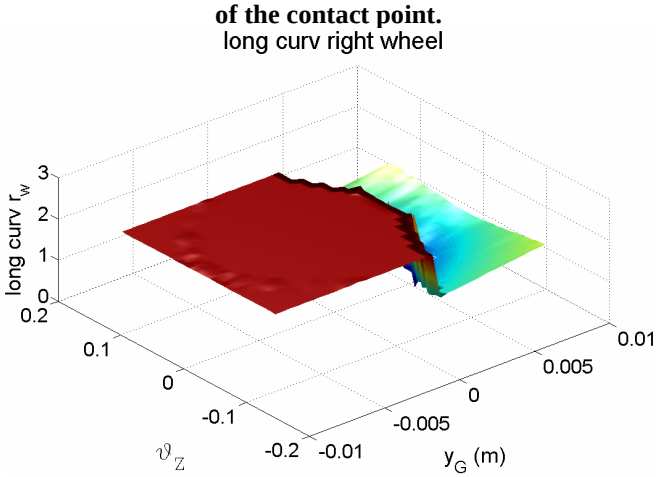

Figure 5.45
Longitudinal curvature of the right wheel in correspondence of the contact point.

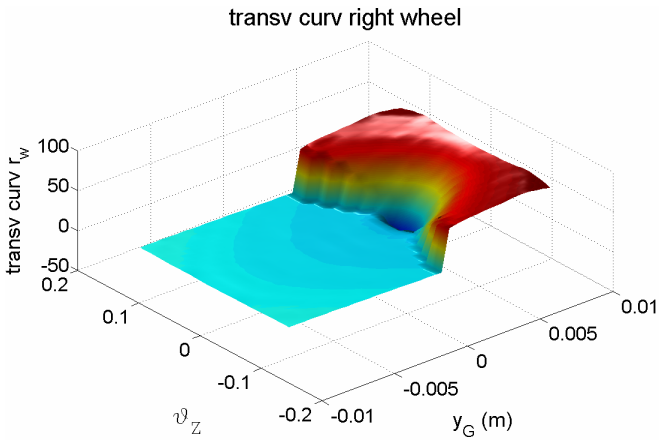

Figure 5.46
Transverse curvature of the right wheel in correspondence of the contact point.

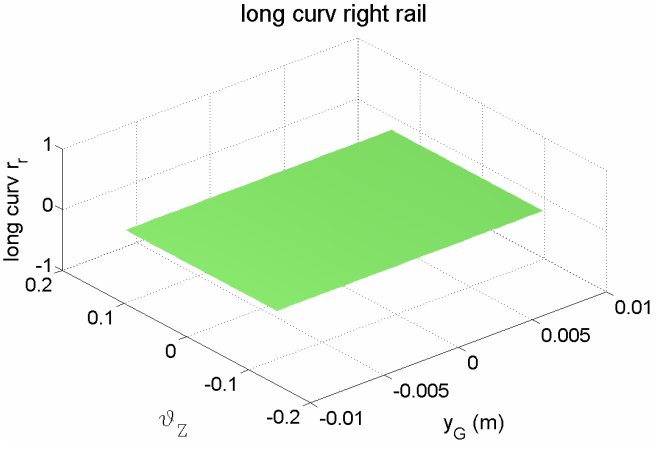

Figure 5.47
Longitudinal curvature of the right rail in correspondence of the contact point.

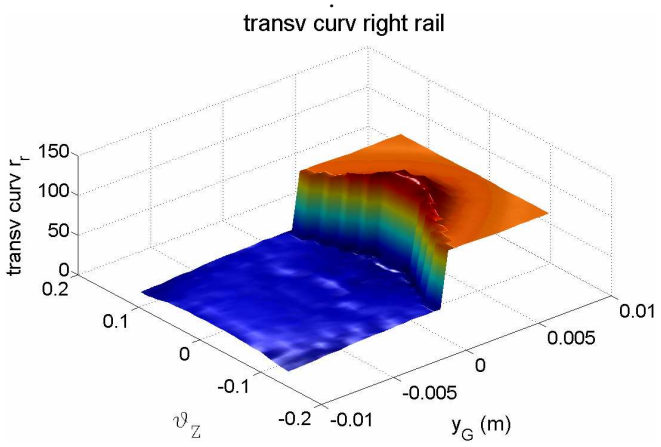

Figure 5.48
Transverse curvature of the right rail in correspondence of the contact point.

CHAPTER 6

THE BOGIE DYNAMIC

6.1 - INTRODUCTION

The dynamic analysis of a single wheel-set and an assembled bogie plays an important role for the monitoring the different events characterizing the motion. In particular [1-4, 8, 15, 24], the following analyses have a significant interest:

- wheel-set, bogie and convoy critical speed determination;
- study of the hunting motion, both in time and frequency domain;
- analysis of the behaviour while turning;
- analysis of the contact forces;
- analysis of the limit derailment conditions;
- study of the forces transferred by the suspension elements to the bogie frame;
- passenger comfort optimization;
- study of the acoustic emissions from the contact surfaces.

Rail defects, extraneous bodies on the rails, railroad switches, work imperfections cause sudden perturbations to the motion of a wheel-set or of a bogie. Under these conditions hunting motion occurs with transverse oscillations whose amplitudes, frequencies and eventual decay depend on perturbation itself and on the wheel-set velocity [4,6,8,9,15].

The oscillatory motion is caused by the changing of the curvature radii of the wheels in the contact points when the wheel-set is displaced from its centered position. In fact, when the barycenter of the wheel-set is moved from the middle of the rail, the tangent forces acting on the two wheels are different. This unbalance generates a yaw torque. The corresponding yaw motion is coupled with the transverse motion.

The oscillations may affect motion stability. In fact, when the bogie has a speed lower than the critical speed the amplitude of the oscillations decreases with time. On the contrary, when the speed is higher than the critical speed, instability occurs.
Because of its influence on contact forces, passenger comfort, noise and, in the extreme event of the derailment of the convoy, bogie travelling around unstable conditions must be avoided or at least controlled in transitory events.
The primary suspension system has a beneficial effect on the stability limits of the bogie. The system acts mainly towards the transverse and longitudinal directions. In this manner the spring-damper suspension elements reduce the hunting motion and, as a consequence, the working speed can be increased safely.

For these reasons, it is crucial to assess at which operating conditions instability occurs. In particular, an estimate of the critical speed is required to guarantee the system safety. Therefore in this investigation a software tool for the dynamic analysis of the main bogie components has been developed. A reliable computation of a railway vehicle dynamics needs an accurate wheel-rail contact model. This usually increases the computation time. To reduce the cpu-time required by the simulation the approach of the lookup tables [1] is adopted. In particular, precalculated tables have been compiled in order to evaluate in a very short time the actual wheel-rail contact characteristics, such as the location of contact points and the direction of normal versors to the surfaces.

The analysis herein described uses the *Kalker linear theory* explained in detail in paragraph 3.4.2 [2, 3]. Tangential forces are linearly dependent on local creepages between the contact surfaces.
The starting point has been the creation of the wheel and rail models and their programming in a Matlab environment. Wheel and rail surfaces are considered as a node grid. The compilation of the lookup tables was obtained by adopting the *load center method* explained in paragraph 5.4.2.3. The results of this method appear more uniform and less affected by mesh coarseness.
The classical *Hertz theory* has been adopted for the accounting of the actual contact surfaces.

In order to reduce cpu time, the standard Matlab function that is able to access and interpolate the numerical values stored in the lookup tables has been substituted with a new one. Moreover, two different strategies during the integration of differential equations have been tested; namely the "*macrostep method"* and "*variable step method*".

The main components of the bogie are the two wheel-sets and a bogie frame. These are connected through a suspension device. This last is modelled by means of spring-damper elements acting towards vertical, longitudinal and transverse directions. The literature records different bogie types and models. The main differences regard the accuracy in modelling the suspension system, the degrees of freedom of the moving masses and the models adopted to manage surfaces contact . Table 6.1 reports a concise and not exhaustive list of the assumption made for each model with the appropriate bibliographic references.

Ref	Analyzed system	Wheel-set d.o.f	Bogie frame d.o.f.	Wheel-set Independent coordinates	Wheel-set dependent coordinates	Bogie frame Independent coordinates	Contact model	Direction interested to suspensions
This	Bogie	6	6	$y_{G,}\vartheta_z$	$x_{G,}z_{G,}\vartheta_x,\vartheta_y$		Lookup table	All directions
[4]	Bogie	4	2	$y_{G,}z_{G,}\vartheta_z,\vartheta_x$		$y_{G,}\vartheta_z$	Equivalent conicity	All directions
[19]	Bogie							All directions
[20]	Wheel-set						Double cone	
[21]	Bogie							Lateral, longitudinal
[22]	Bogie	6	6	$y_{G,}\theta_z$	$x_{G,}z_{G,}\vartheta_x,\vartheta_y$		Equivalent conicity	All directions
[23]	Bogie							Lateral, longitudinal
[28]	Bogie						Non linear model	Active lateral and longitudinal

Table 6.1

Comparison among different bogie models found in literature.

6.2 - THE BOGIE MODELLING

The bogie here examined is composed of three masses: two wheel-sets, a bogie frame and a primary suspension system. The masses, main dimensions and features of the components are summarized in Table 6.2.

Wheel-set mass	1595 Kg	**Wheel-set distance**	2.5 m
Bogie frame mass	2469 Kg	**Wheel radius**	0.457 m
Wheel profile	S1002	**Rail gauge**	1.360 m
Rail profile	UIC60	**Inclination rail angle**	1/20

Table 6.2

Masses, main dimensions and features of the bogie components.

6.2.1 - The suspension system

As shown in Figure 6.2, for each wheel the primary suspension system has been modelled with three translational spring-damper elements: one for each principal direction. The stiffnesses and the damping of the suspension elements are reported in Table 6.3.

Longitudinal spring stiffness	$10^6\ N/m$	**Vertical damping coefficient**	$3.04 \cdot 10^3\ Ns/m$
Transverse spring stiffness	$2 \cdot 10^7\ N/m$	**Vertical length at rest**	0.5 m
Vertical spring stiffness	$1.5 \cdot 10^6\ N/m$	**Longitudinal length at rest**	0.75 m
Longitudinal damping coefficient	$2.49 \cdot 10^3\ Ns/m$	**Transverse length at rest**	0.3 m
Transverse damping coefficient	$1.11 \cdot 10^4\ Ns/m$		

Table 6.3

Stifnesses and damping coefficients of the suspension elements.

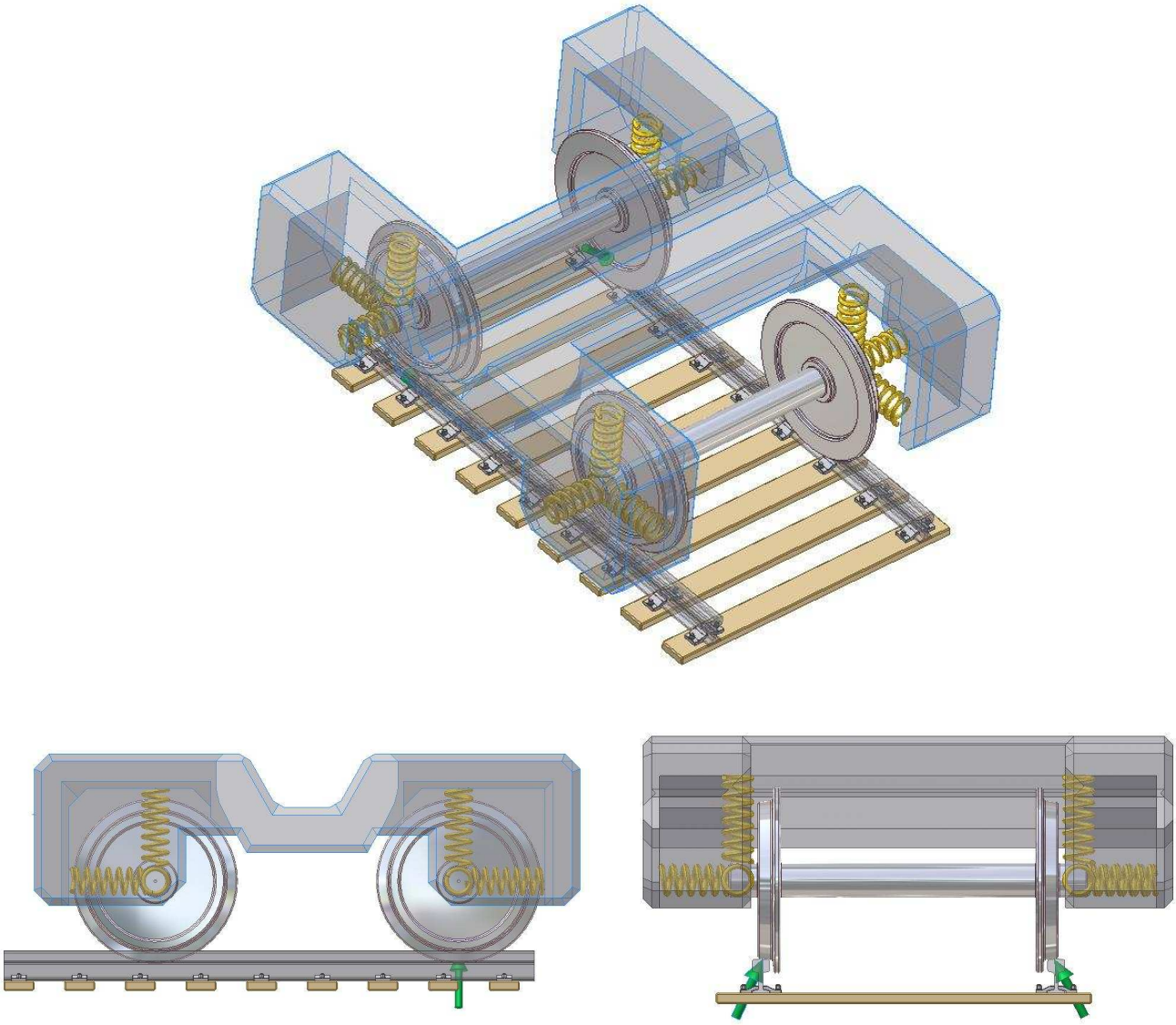

Figure 6.1

The bogie with the primary suspension system

6.3 – THE WHEEL-SET-RAIL MODEL

Due to symmetry we refer only to the front wheel-set. The first step in the model generation is the acquisition of wheel and rail profiles (see Figure 5.3) . The creation of the wheel and rail surfaces is carried out with the procedure described in paragraph 5.3.

6.4 – THE CARTESIAN COORDINATE SYSTEMS

The following right-hand Cartesian coordinate systems are introduced in the analysis:

- inertial fixed reference system SR_0;
- reference system fixed with the front wheel-set SR_{Gfront};
- reference system fixed with the back wheel-set SR_{Gback};
- reference system fixed with the bogie frame SR_{Gfr};
- reference system that follows the front wheel-set on the rail path SR_{1front};
- reference system that follows the back wheel-set on the rail path SR_{1back};

The fixed inertial reference system SR_0 has its origin on the rail longitudinal plane of symmetry and on the rolling plane, the axis x_o is tangent to the railway path. The axis z_o is vertical and directed upward.

The coordinate systems SR_{Gfront} and SR_{back} are framed with the front and back wheel-sets, respectively. Their origins are coincident with their centers of masses. The axes y_{Gfront} and y_{Gback} are coincident with the wheel-sets axes, whereas the axes z_{Gfront} and z_{Gback} are initially vertical and directed upwards.
The coordinate system SR_{Gfr} is fixed with the bogie frame mass. Its origin is coincident with the bogie frame center of mass. The axis x_{Gfr} is initially parallel to the rail direction, the axes z_{Gfr} is initially vertical and directed upwards.

The two reference systems attached to the wheel-sets – SR_{1front} and SR_{1back} for the front and back one respectively - have their origins belonging to the track longitudinal plane of symmetry and to the rolling plane. The origins of the two coordinate systems follow the path of the centers of mass of the wheel-sets (see Figure 6.2). Therefore, when the rail path is straight, the positions of the two frames have the same coordinates x of the wheel-set centers of mass.

The axes x_{1front} and x_{1back} are parallel to the rail direction. The axes z_{1front} and z_{1back} are orthogonal to the rolling plane and directed upward. Figure 6.2 locates all the coordinate systems introduced.

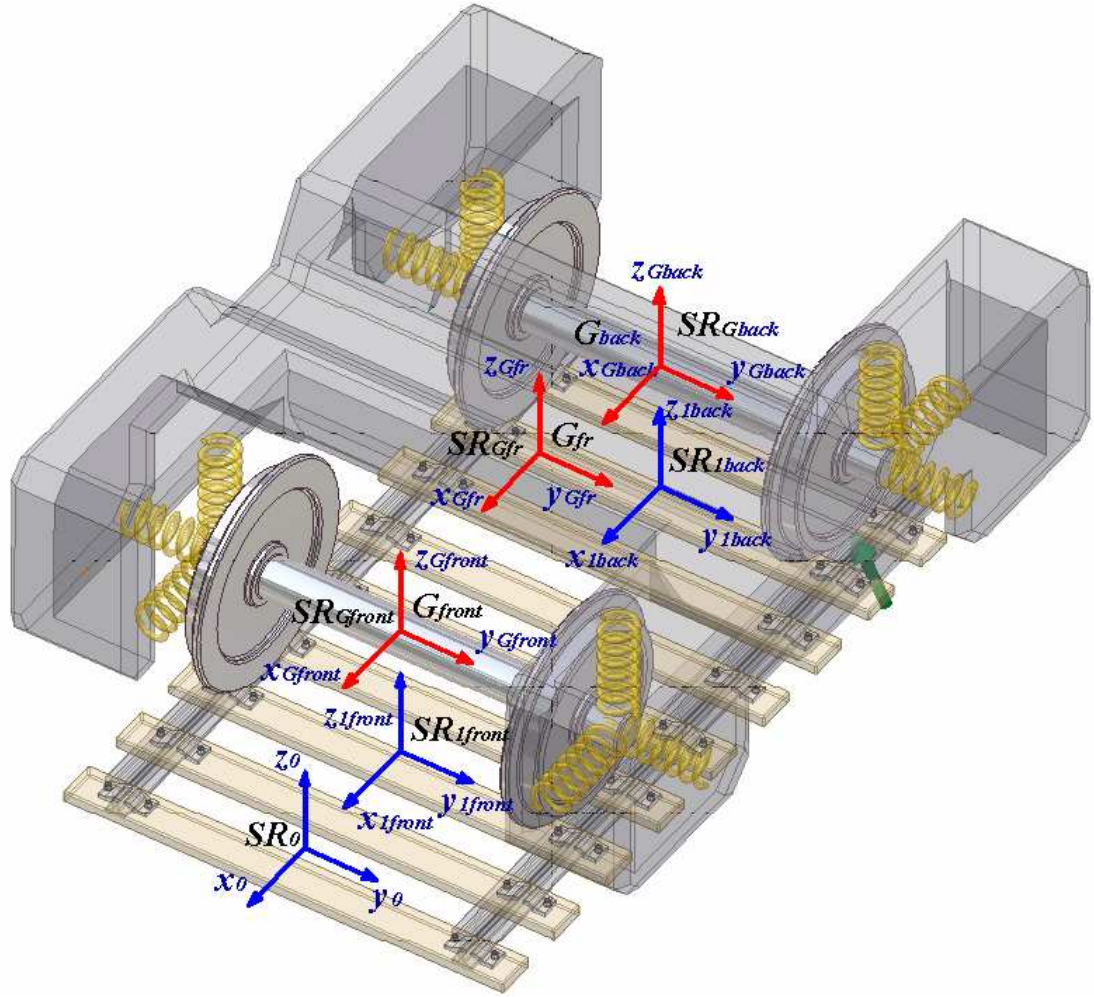

Figure 6.2

Reference systems used in the dynamic analysis of the bogie

6.4.1 - Transformation between coordinate systems

In order to obtain the transformation matrix between two generic coordinate systems, the following convention regarding the rotation angles has been adopted: given the two coordinate systems $\boldsymbol{S_a}$ and $\boldsymbol{S_b}$, $\boldsymbol{S_a}$ is assumed fixed while $\boldsymbol{S_b}$ is moving.

Let us denote with $\alpha_x, \alpha_y, \alpha_z$ the Bryant's angles which define the attitude of $\boldsymbol{S_b}$ with respect to $\boldsymbol{S_a}$.

The rotation order with which $\boldsymbol{S_a}$ must rotate in order to superimpose himself on $\boldsymbol{S_b}$ is the following:

- 1° rotation about axis $\boldsymbol{z_a}$ belonging to S_a. Under this rotation axes *x* and *y* move to ***x'*** and ***y'***, respectively.
- 2° rotation about axis ***x'*** belonging to the intermediate frame. Under this rotation axis ***y'*** moves to ***y''***;
- 3° rotation about axis ***y''*** coincident with $\boldsymbol{y_b}$.

In this manner the matrix which transforms the vector components from $\boldsymbol{S_b}$ to $\boldsymbol{S_a}$ has the following expression:

$$A_{rot}^{S_b \to S_a} = \begin{bmatrix} \cos\alpha_z \cos\alpha_x & -\cos\alpha_z \cos\alpha_y sen\alpha_x + sen\alpha_z sen\alpha_y & \cos\alpha_z sen\alpha_x sen\alpha_y + \cos\alpha_y sen\alpha_z \\ sen\alpha_x & \cos\alpha_x \cos\alpha_y & -sen\alpha_y \cos\alpha_x \\ -sen\alpha_z \cos\alpha_x & sen\alpha_z \cos\alpha_y sen\alpha_x + sen\alpha_y \cos\alpha_z & -sen\alpha_x sen\alpha_y sen\alpha_z + \cos\alpha_y \cos\alpha_z \end{bmatrix}$$

Hence, the relation between the vector components in the two reference systems is:

$\vec{V}_{S_a} = A_{rot}^{S_b \to S_a} \vec{V}_{S_b}$

where:

$\vec{V}_{S_a}$ is the vector $\vec{V}$ according to $\boldsymbol{S_a}$;

$\vec{V}_{S_b}$ is the vector $\vec{V}$ according to $\boldsymbol{S_b}$.

6.4.1.1 - The coordinate system transformations regarding the rail path

The analyses regard both straight and curved paths. In the first case, making reference to the motion of a single wheel-set, the frame SR_1 translates with respect to SR_0 (see Figure 6.3). When the track is curved, the motion of the frame *SR1* is characterized by a translational motion together with a rotational one, such that x_1 axis is tangent to the rail track centerline and y_1 axis points toward the center of curvature. In this case the reading of the lookup tables is done with reference to the relative attitude of the frame SR_G – fixed with the wheel-set - respect to the frame SR_1; then, the relative position and orientation of SR_G respect to SR_1 and all the data obtained from the lookup tables are transformed respect to SR_0 by means of the transformations reported in section 6.4.1.

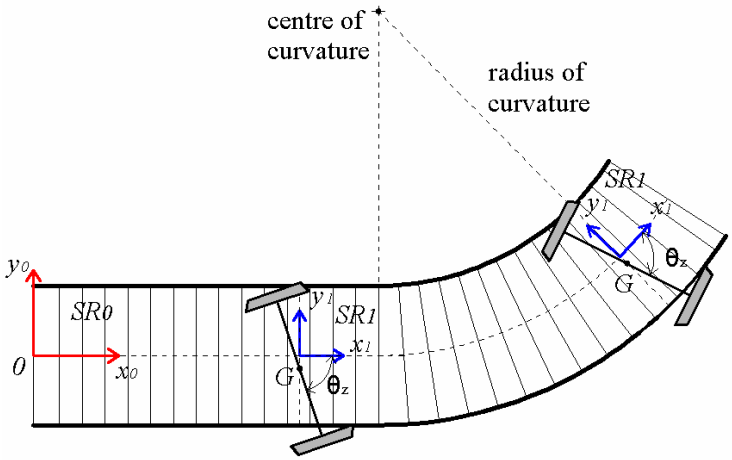

Figure 6.3

***SR*$_1$ attitude in the straight and curved rail path cases.**

6.5 – THE EQUATIONS OF MOTION OF THE BOGIE

6.5.1 – The cardinal equations

The equations of dynamics are written only for the main three moving masses. The inertia of the suspension deformable elements is neglected.

The equations are expressed in the inertial coordinate system SR_o and are given below:

$$\vec{F}_{ext}^{\,i} = m_i \vec{a}_G^{\,i}; \qquad {}_{ext}\vec{M}_G^{\,i} = \frac{d\vec{K}_G^{\,i}}{dt}; \qquad \vec{F}_{ext}^{\,fr} = m_{fr} \vec{a}_G^{\,fr}; \qquad {}_{ext}\vec{M}_G^{\,fr} = \frac{d\vec{K}_G^{\,fr}}{dt}. \qquad (6.1)$$

where:

subscript or upperscript i can assume the meaning of "*front*" or "*back*" when denoting the *front* or *back* wheel-set, respectively;

$\vec{F}_{ext}^{\,i}$ is the sum of all external forces acting on the i^{th} wheel-set;

$\vec{a}_G^{\,i}$ is the acceleration of the barycenter of the i^{th} wheel-set;

m_i is the mass of the i^{th} wheel-set;

${}_{ext}\vec{M}_G^{\,i}$ is the resultant external moment about the center of mass acting on the i^{th} wheel-set;

$\vec{K}_G^{\,i}$ is the angular momentum about the center of mass of the i^{th} wheel-set;

$\vec{F}_{ext}^{\,fr}$ is the sum of all the external forces acting on the bogie frame;

m_{fr} is the bogie frame mass;

$\vec{K}_G^{\,fr}$ is the angular momentum about the center of mass of the bogie frame;

${}_{ext}\vec{M}_G^{fr}$ is the resultant of all external forces moments about the center of mass and acting on the bogie frame;

6.5.2 – The external forces and moments

The external forces acting on the wheel-sets and on the bogie frame are obtained from the following sums:

$$\vec{F}_{ext}^{\,i} = \vec{P}_i + \sum_{h=1}^{Nl} {}_{cl}\vec{F}_i^{\,h} + \sum_{k=1}^{Nr} {}_{cr}\vec{F}_i^{\,k} + \vec{F}_i^{\,susp} + \vec{F}_i^{\,o}$$

$$\vec{F}_{ext}^{\,fr} = \vec{P}_{fr} + \vec{F}_{fr}^{\,susp} + \vec{F}_{fr}^{\,o}$$

where:

$\vec{P}_i$ is the weight of the i^{th} wheel-set;

${}_{cl}\vec{F}_i^{\,h}$ is the contact force acting on left wheel regarding the h^{th} contact point on the i^{th} wheel-set

${}_{cr}\vec{F}_i^{\,k}$ is the contact force acting on right wheel regarding the k^{th} contact point on the i^{th} wheel-set

$\vec{F}_i^{\,susp}$ is the sum of all forces acting on i^{th} wheel-set and transmitted by the suspension system;

$\vec{F}_i^{\,o}$ is the sum of all possible further external forces (pull force, load directly applied on the masses, etc..) acting on the i^{th} wheel-set;

$\vec{P}_{fr}$ is the weight of the bogie frame;

$\vec{F}_{fr}^{\,susp}$ is the sum of all forces acting on the bogie frame and transmitted through the suspension system;

$\vec{F}_{fr}^{\,o}$ is the sum of the remaining external forces (e.g. pull force, load directly applied on the bogie frame, etc..) acting on bogie frame;

N_l is the number of the contact points on the left wheel;

N_r is the number of the contact points on the right wheel.

The resultant bending moments acting on the wheel-sets and on the bogie frame are:

$${}_{ext}\vec{M}_G^{\,i} = \sum_{h=1}^{Nl}\left({}_{cl}G\vec{P}_i^{\,h} \times {}_{cl}\vec{F}_i^{\,h} + {}_i^{cl}\vec{M}_{spin}^{\,h}\right) + \sum_{k=1}^{Nr}\left({}_{cr}G\vec{P}_i^{\,k} \times {}_{cr}\vec{F}_i^{\,k} + {}_i^{cr}\vec{M}_{spin}^{\,k}\right) + {}_i\vec{M}_G^{\,susp} + {}_i\vec{M}_G^{\,o} + {}_i\vec{M}_G^{\,mot}$$

$${}_{ext}\vec{M}_G^{\,fr} = {}_{fr}\vec{M}_G^{\,susp} + {}_{fr}\vec{M}_G^{\,o}$$

where:

${}_{cl}\vec{GP}_i^h$ is the vector joining the barycenter of the i^{th} wheel-set with the h^{th} contact point on the left wheel of the i^{th} wheel-set;

${}_{cr}\vec{GP}_i^k$ is the vector joining the barycenter of the i^{th} wheel-set with the k^{th} contact point on the right wheel of the i^{th} wheel-set;

${}^{cl}_{i}\vec{M}^{h}_{spin}$ is the spin moment acting just on the h^{th} contact point on the left wheel of the i^{th} wheel-set;

${}^{cr}_{i}\vec{M}^{k}_{spin}$ is the spin moment acting just on the k^{th} contact point on the right wheel of the i^{th} wheel-set;

${}_{i}\vec{M}_G^{susp}$ is the resultant moment about the center of mass of the forces transmitted by the suspension system to the i^{th} wheel-set.

${}_{i}\vec{M}_G^{o}$ is the resultant moment about the center of mass of all possible further external forces acting on the i^{th} wheel-set;

${}_{i}\vec{M}_G^{mot}$ is the engine couple applied on the i^{th} wheel-set;

${}_{fr}\vec{M}_G^{susp}$ is the resultant moment about the center of mass of the forces transmitted by the suspension system to the bogie frame;

${}_{fr}\vec{M}_G^{o}$ is the resultant moment about the center of mass of the remaining external forces acting on the bogie frame;

Figure 6.4 shows the block-diagram used for the dynamic analysis of each wheel-set. Therefore, in this diagram the wheel-set is assumed as isolated from the rest.

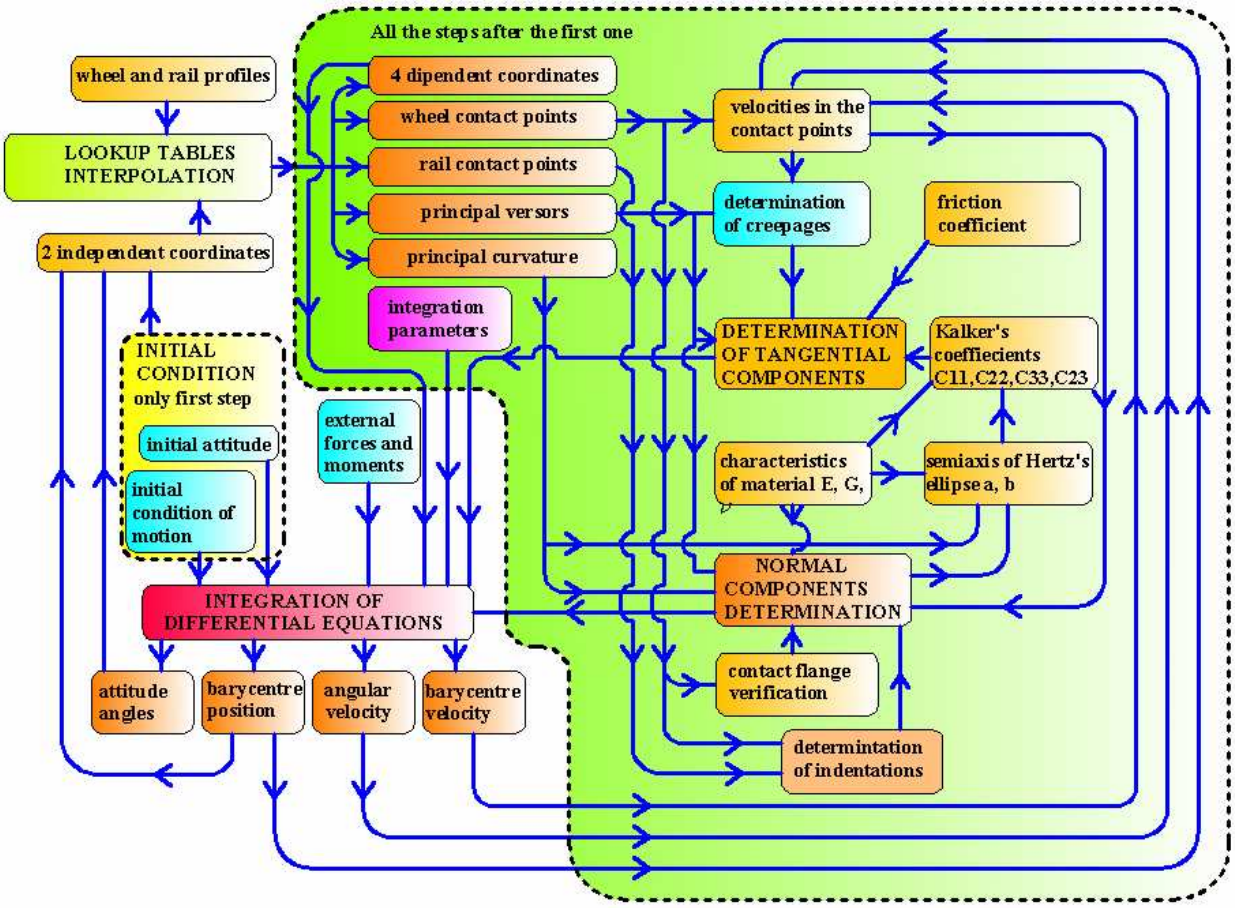

Figure 6.4

Flow chart of the wheel-set dynamic analysis.

6.6 – CONTACT POINTS DETECTION

The position of the contact points, the normal versors and the principal curvatures has been determined using the lookup table. The contact points has been determined with the *method of the barycentre* illustrated in paragraph 5.4.2.3.

6.6.1 – Use of lookup tables

Given the generic values y_G and α_z, the corresponding values of x_G, z_G, α_x, α_y are computed by means of linear interpolation of the values stored in the lookup tables.

The query of the values can be done through two different strategies:

- *method 1*: at each integration step
- *method 2*: at previously established steps (macrosteps

In the first method the query to the lookup table occurs every time the Matlab procedure, namely *ODE23t*, evaluates the differential equations. Alternatively with the method 2, a constant macrostep is introduced. Within the macrostep the dependent values are not updated.

When switching from one macrostep to the next one, the coordinates at the end of a macrostep are considered as initial conditions for the next time interval. The two different strategies are sketched in Figure 6.5.

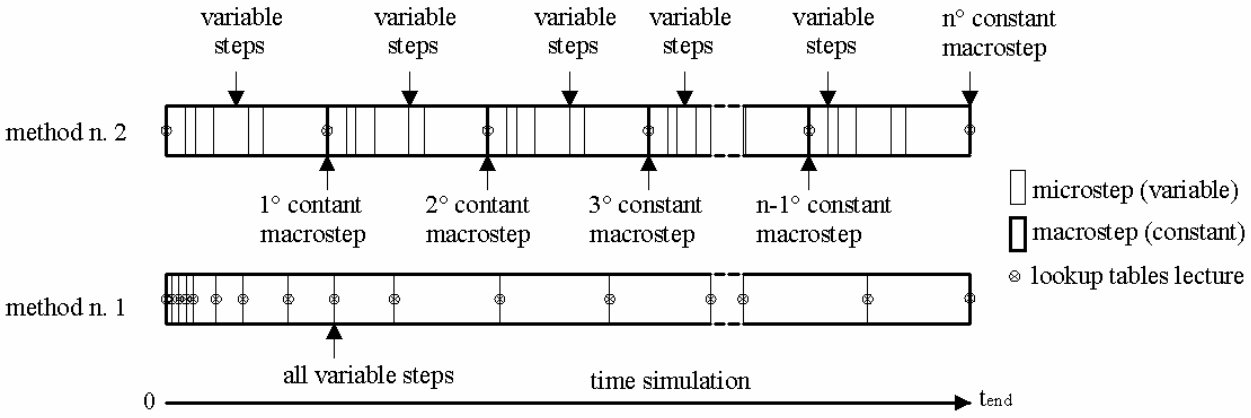

Figure 6.5

The two query methods of the lookup tables

With the aim to find the best method for both cpu time and data accuracy, the results of the two methods have been compared with these obtained a commercial multibody software. For the second method of query, we have adopted three different macrosteps, i.e. $10^{-4}\,s, 4\cdot10^{-4}\,s, 4.2\cdot10^{-4}$ s.

Figure 6.6a shows the transverse displacement of the wheel-set moving with a longitudinal speed equal to 12 m/s, initially perturbed through a transverse velocity of 0.1 m/s. The simulation lasts for 10 s. Figure 6.6b shows the absolute value of the relative error obtained by the comparison of the two method results and these given by the commercial multibody software.

The absolute value of the relative error at time *t* is calculated as follow:

$$err_{rel}^{abs}(t) = \left\| \frac{f(t) - g(t)}{g(t)} \right\|$$

While the mean of err_{rel}^{abs} on a interval $(t_1\text{-}t_0)$ is:

$$mean_{rel} = \frac{\int_{t_0}^{t_1} err_{rel}^{abs}(t)}{(t_1 - t_0)}$$

In the formula *f(t)* and *g(t)* are two given time functions to compare. It is natural that the lower is $mean_{rel}$ the higher is the result accuracy. Table 6.4 compares the two methods for different macrosteps length. It is evident that the first method is the most accurate and (this is unexpected at first glance) rapid. For this reason we have adopted the first method in all

simulations. As a matter of fact, even if the increasing number of queries should require a longer cpu-time, the abrupt change of contact condition encountered in the second method implies a significant reduction in the time step (more iterations are needed for the same analysis) that masks the benefits of lighter queries.

METHOD		CPU TIME (sec)	MEAN RELATIVE ERROR
Method 1		346	0.53
Method 2	**Macrostep (sec)**		
	$1 \cdot 10^{-4}$	8415	4.85
	$4 \cdot 10^{-4}$	1122	1.71
	$4.2 \cdot 10^{-4}$	1037	0.84

Table 6.4

Cpu time for 10 s simulation and mean relative error referred to the commercial multibody software results obtained by means of the two methods and with 3 macrostep values.

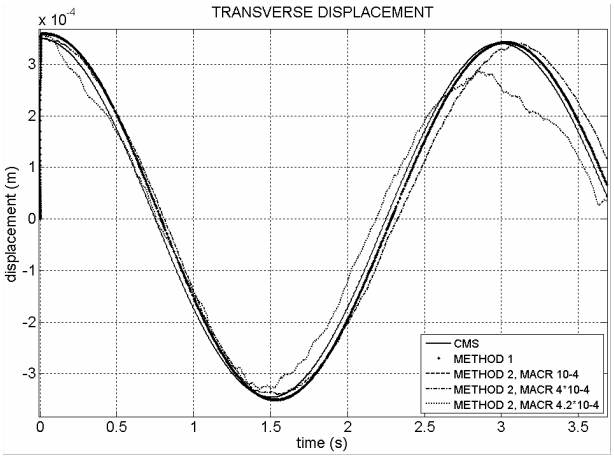

a)

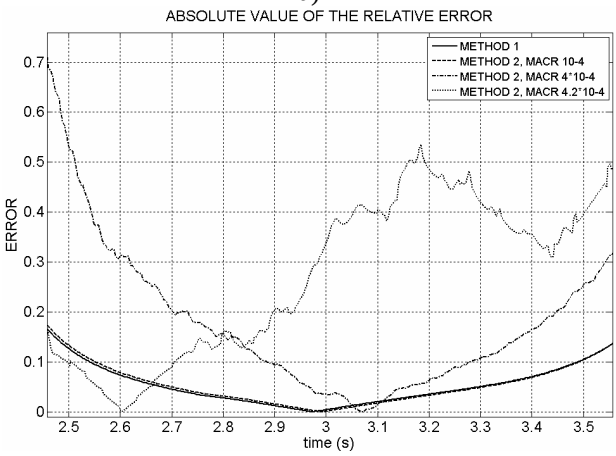

b)

Figure 6.6

Wheel-set barycenter motion calculated by means of the two query methods compared with the commercial multibody software (CMS) results; a) Transverse displacement; b) Mean relative error of the transverse displacement

6.6.2 – The interpolation of the lookup tables

In order to optimize the interpolation of the values stored in the lookup tables, a new function called *my_interp2.m* has been developed in replacement of the two functions *interp2.m* and *griddata.m* given in the standard Matlab library.

The interpolation is performed in two steps:

- query of the matrix stored in the lookup tables;
- apply linear interpolation.

The $37\times37\times100$ matrix is initially saved on the mass storage. Herein we refer for generality to a generic $r\times m\times p$ matrix, where *r* is the number of rows, *m* the number of columns and *p* the number of layers.

Let us denote by *x* and *y* the two coordinate axes related to the column and row directions respectively. The values of x_i and y_i, both monotonically varying, satisfy the following inequalities:

$$x_{\min} \le x_i \le x_{\max}$$
$$y_{\min} \le y_j \le y_{\max}$$

where:

x_i and y_j are the values of *x* and *y* in correspondence to the i^{th} column and j^{th} row;

$x_{\min}$ and $x_{\max}$ are the minimum and maximum values of the column values;

$y_{\min}$ and $y_{\max}$ are the minimum and maximum values of the row values.

$i\in[1,m]$ and $j\in[1,r]$ are integer subscripts.

In order to reduce cpu-time a block matrix [A] of dimensions $2\times2\times p$ is extracted from the whole matrix containing the lookup table. Let us denote by c_x and c_y the generic values of the independent coordinates. At the row and column boundaries of the block matrix there are the stored independent coordinates adjacent to c_x and c_y such that (see Figure 6.7)

$$x_n \le c_x \le x_{n+1}$$
$$y_h \le c_y \le y_{h+1}$$

Given [A], the linear interpolation is applied. The following procedure refers to a smaller block matrix with dimensions $2\times2\times1$.

Let us denote by:

- $z(y,x)$ the value of the matrix element in correspondence of the *y* and *x* values and related to the directions of the row and the column;
- $z_{rs} = A(r,s)$ the value of the block matrix [A] element in correspondence of the r^{th} row and s^{th} column.

Given the matrix of the whole lookup table and the values c_x and c_y, the linearly interpolated value $z_0 = z(c_y, c_x)$ is computed through the following steps.

1) Form the elements of the block matrix:

$z_{11} = A(h,n); \quad z_{12} = A(h,n+1); \quad z_{21} = A(h+1,n); \quad z_{22} = A(h+1,n+1);$

2) Let $\Delta_x = x_{i+1} - x_i$ the constant column spacing and $\Delta_y = y_{j+1} - y_j$ the constant row spacing.

3) Evaluate $z^{up} = z(y_h, c_x)$ and $z^{low} = z(y_{h+1}, c_x)$ in correspondence of the value c_x by means of the following expressions:

$$z^{up} = z_{11} + (c_x - x_n)\frac{z_{12} - z_{11}}{\Delta_x} \qquad z^{low} = z_{21} + (c_x - x_n)\frac{z_{22} - z_{21}}{\Delta_x}$$

4) Evaluate the column z_0 value, namely z_0^x, by means of the following expression:

$$z_0^x = z^{up} + (c_y - y_h)\frac{z^{low} - z^{up}}{\Delta_y}$$

5) Evaluate $z^{lft} = z(c_y, x_n)$ and $z^{rig} = z(c_y, x_{n+1})$ in correspondence of the value c_y by means of the following expressions:

$$z^{lft} = z_{11} + (c_y - y_h)\frac{z_{21} - z_{11}}{\Delta_y} \qquad z^{rig} = z_{12} + (c_y - y_h)\frac{z_{22} - z_{12}}{\Delta_y};$$

6) Evaluate the row z_0, namely z_0^y, by means of the following expression:

$$z_0^y = z^{lft} + (c_x - x_n)\frac{z^{rig} - z^{lft}}{\Delta_x}$$

7) Finally, the value of z_0 is given by:

$$z_0 = \frac{(z_0^x + z_0^y)}{2}.$$

The Figure 6.7 shows the diagram of the whole and the block matrix [A].

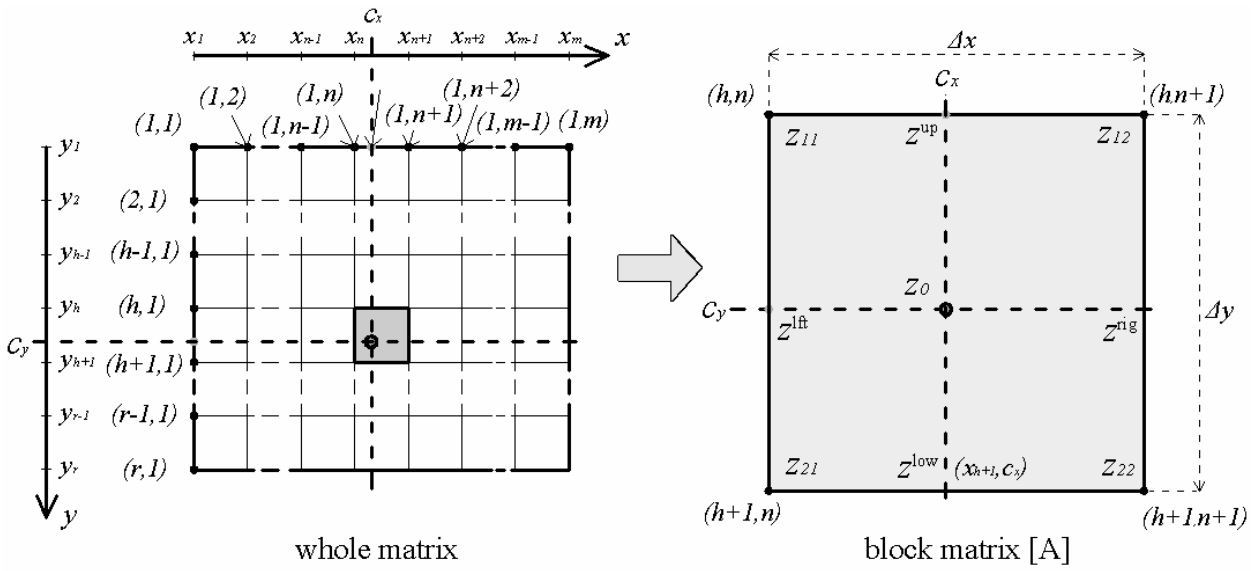

Figure 6.7

Diagram of the interpolation method used for the lookup table.

In order to test the speedup obtained by adopting the new function, the cpu time requested for the interpolation of the two standard Matlab functions *interp2.m* and *griddata.m* and the new function *my_interp2.m* is compared. The superiority of the proposed approach is demonstrated by the fact that using a 2x2 matrix the new function is almost 5.3 and 4.75 faster than *interp2.m* and *griddata.m*, respectively.

6.7 – THE CONTACT FORCES

6.7.1 – Classification of the contact forces

The contact force $\vec{F}_c$ between the wheel and rail are split in normal and tangent components. The normal component $\vec{N}_c$ has the direction of the normal versor at the contact point. The current normal components is obtained adding spring $\vec{N}_{el}$ and damper $\vec{N}_{visc}$ forces.. The tangent component lies in the tangent plane and is formed by two contributions: $\vec{F}_{long}$, directed along the longitudinal direction and $\vec{F}_{trans}$, parallel to the transverse versor. The tangent component is estimated by means of *Kalker* linear theory [2].
In conclusion the following relationships can be established:

$$\vec{F}_c = \vec{N}_c + \vec{F}_{tang}; \qquad \vec{N}_c = \vec{N}_{visc} + \vec{N}_{el}; \qquad \vec{F}_{tang} = \vec{F}_{long} + \vec{F}_{trans};$$

6.7.2 – Computation of the normal component $\vec{N}_c$

6.7.2.1 – The elastic contribution

The elastic contribution $\vec{N}_{el}$ is expressed in the form

$$\vec{N}_{el} = k_{el} C \vec{n}$$

where:

$\vec{n}$ is the normal versor to the surface in the contact point;

C is the indentation between the wheel and rail;

k_{el} is the elastic contact stiffnesses;

The value of k_{el} depends from the location of the area of contact and it is calculated according to the procedure illustrate in the paragraph 5.4.5.

6.7.2.2 – The damping contribution

The contribution to contact forces due to damping is proportional to the interpenetrating velocity v_{pen} of the wheel in the rail. One can use the following expressions:

$$\vec{N}_{visc} = c_v v_{pen} \vec{n} \quad \text{if} \quad v_{pen} > 0$$

$$\vec{N}_{visc} = 0 \qquad \text{if} \quad v_{pen} \le 0$$

where

$$v_{pen} = \vec{V}_P \cdot \vec{n}$$

$$\vec{V}_P = \vec{V}_G + \vec{\omega} \times G\vec{P} \qquad (6.2)$$

The previous symbols have the following meaning:

c_v damping coefficient;

$\vec{V}_P$ is the velocity of the wheel in correspondence of the contact point;

$\vec{n}$ is the normal versor in the contact point;

$\vec{V}_G$ is the velocity of the barycenter of the wheel-set;

$\vec{\omega}$ is the angular velocity of the wheel-set;

$G\vec{P}$ is the vector joining the barycenter of the wheel-set with the contact point P;

The damping coefficient c_v depends on the material of the solids in contact. A value usually reported in literature for similar analyses it is assumed as $c_v = 10^4$ Ns/m.

6.7.3 – Wheel-rail tangent component analysis

The tangent component of the contact force, $\vec{F}_{long}$ and $\vec{F}_{trans}$ and the moment of spin, $\vec{M}_{spin}$, is determined by means of the Kalker's linear theory according to the procedure reported in paragraph 3.4.2 [2]. This is based on a linear relationship between the tangent forces and the creepages, ζ, η and φ determined as showed in paragraph 3.3.

A creep force saturation coefficient ε is defined according to the modified Johnson-Vermeulen formulation [8], that permits to use a nonlinear model instead of a linear one:

$$\vec{F}_{long}^{nl} = \varepsilon \vec{F}_{long}; \qquad \vec{F}_{trans}^{nl} = \varepsilon \vec{F}_{trans}$$

with ε computed according to the following equations

$$if \quad F_{tan} \le 3\mu N \qquad \varepsilon = \frac{\mu N}{F_{tan}} \left[\left(\frac{F_{tan}}{\mu N} \right) - \frac{1}{3} \left(\frac{F_{tan}}{\mu N} \right)^2 + \frac{1}{27} \left(\frac{F_{tan}}{\mu N} \right)^3 \right]$$

$$if \quad F_{tan} > 3\mu N \qquad \varepsilon = \frac{\mu N}{F_{tan}}$$

The symbols have the following meaning:

$\vec{F}_{long}$ and $\vec{F}_{trans}$ are respectively the longitudinal and transverse component of the tangential force;

$\vec{F}_{long}^{nl}$ and $\vec{F}_{trans}^{nl}$ are respectively the longitudinal and transverse component of the tangential force calculated in the non linear model;

N is the normal force component;

$F_{tan} = \left\| \vec{F}_{tan} \right\| = \sqrt{F_{long}^2 + F_{trans}^2}$ is the Euclidean norm of the tangential force $\vec{F}_{\tan}$.

F_{long} and F_{trans} are respectively the longitudinal and transverse component of the tangential force;

μ is the friction coefficient equal to 0.2.

6.8 - FORCES GENERATED BY THE SUSPENSION SYSTEM

The forces generated by the suspension system are due to elastic and damping effects. These last are expressed by the following formulas

$$\vec{F}_{el}^{\,susp} = \left(l_o - AB\right) k_{el} \vec{n}_{AB}; \qquad \vec{F}_{v}^{\,susp} = c_v \left(\left(\vec{V}_A - \vec{V}_B \right) \cdot \vec{n}_{AB} \right) \vec{n}_{AB};$$

where the symbols have the following meaning:

$\vec{F}_{el}^{\,susp}$ is the elastic contribution to the suspension force;

$\vec{F}_{v}^{\,susp}$ is the viscous contribution to the suspension force;

AB is the length of the segment AB;

k_{el} is the elastic constant of the suspension;

c_v is the damping coefficient of the suspension;

$\vec{n}_{AB}$ is the versor along the line through attachment points A and B, oriented from A to B;

$\vec{V}_A$ is the velocity of point A;

$\vec{V}_B$ is the velocity of point B;

l_o is the length of the unloaded elastic element.

In Figure 6.8 is given a scheme of the spring-damper element modelling the suspension

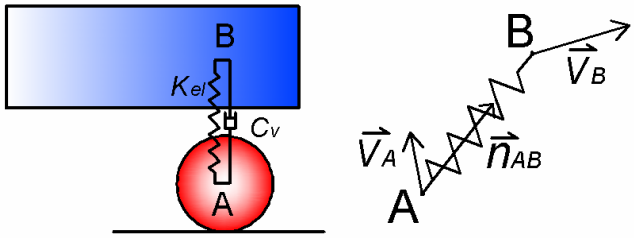

Figure 6.8

Spring-damper suspension element

6.9 - THE DIFFERENTIAL EQUATIONS

The dynamic equilibrium conditions (6.1) form a system of 18 second order differential equations. The unknowns are the following coordinates of the moving bodies:

$x_G^j(t), y_G^j(t), z_G^j(t)$, coordinates of the barycenter of the j^{th} body respect to a SR_o;

$\vartheta_x^j(t), \vartheta_y^j(t), \vartheta_z^j(t)$, attitude angles of the frame $SR_{Gj,}$ connected to j^{th} body, respect to a SR_o;

The subscript *j* is equal to "*front*", "*back*" or "*fr*" when the variable pertains to front, back wheel-set bogie frame, respectively.

The accelerations of the barycenters are given by the following relations:

$$\vec{a}_G^j = \frac{d^2 x_G^j}{dt^2}\vec{i}_o + \frac{d^2 y_G^j}{dt^2}\vec{j}_o + \frac{d^2 z_G^j}{dt^2}\vec{k}_o$$

where $\vec{i}_o, \vec{j}_o, \vec{k}_o$ denote the versors of SR_o.

The equilibrium at rotation is expressed by the differential equations

$$\begin{cases} I_{xx}^j \dfrac{dp_j}{dt} - \left(I_{yy}^j - I_{zz}^j\right) q_j r_j = {}_{ext}^{x}M_{G^*}^{j} \\ I_{yy}^j \dfrac{dq_j}{dt} - \left(I_{zz}^j - I_{xx}^j\right) r_j p_j = {}_{ext}^{y}M_{G^*}^{j} \\ I_{zz}^j \dfrac{dr_j}{dt} - \left(I_{xx}^j - I_{yy}^j\right) p_j q_j = {}_{ext}^{z}M_{G^*}^{j} \end{cases}$$

where:

$I_{xx}^j, I_{yy}^j, I_{zz}^j$ are the central moment of inertia of the j^{th} body;

p_j, q_j, r_j are the angular velocity components of the j^{th} body expressed in the local frame SR_{Gj};

${}_{ext}^{x}M_{G^*}^{j}$, ${}_{ext}^{y}M_{G^*}^{j}$, ${}_{ext}^{z}M_{G^*}^{j}$ are the Cartesian components of the external resultant moment about the barycenter of j^{th} body of the external forces expressed in the local frame SR_{Gj}.

The relations between the angular velocity components expressed in the local frames and the attitude angles and their derivatives are determined by means of the following transform

$$\begin{bmatrix} p_j \\ q_j \\ r_j \end{bmatrix} = \begin{bmatrix} \cos\alpha_x^j \cos\alpha_z^j & 0 & sen\alpha_z^j \\ sen\alpha_x^j & 1 & 0 \\ -\cos\alpha_x^j sen\alpha_z^j & 0 & \cos\alpha_z^j \end{bmatrix} \cdot \begin{bmatrix} \dot{\alpha}_x^j \\ \dot{\alpha}_y^j \\ \dot{\alpha}_z^j \end{bmatrix}$$

The j^{th} body angular velocity components expressed in the absolute frame SR_o follow from the transformation

CHAPTER 7

THE WAGON DYNAMIC

7.1 – INTRODUCTION

As for the bogie, the wagon analysis is very important for many reasons because it allows the definitions of the stability limits of the wagon on different tracks. Moreover the secondary suspension system makes the analysis more complex and variegated.
Beyond the list reported in the chapter 6 introduction, the following items have a significant interest in the analysis of the wagon motion:

- analysis of the interactions between the primary and secondary suspension system;
- analysis of the reciprocal motion of the two bogies;
- influence of the secondary suspension system characteristics on the critical limits of the wagon;
- investigation on the transmission of the vibrations through the suspension systems;
- analysis of the maximum attitude values of the car body during the curved and straight track;
- analysis of the transient period of the motion during the braking and acceleration phase.

These analysis can be carried out by means of a dynamic model of the wagon. The model presented herein has been developed in Matlab environment using the two bogie models described in chapter 6.

7.2 – THE WAGON MODEL

The wagon described in this chapter is formed by the following masses:

- the car body;
- the two bogies;
- the secondary suspension system.

The secondary suspension system acts on the three principal directions, that is the longitudinal, transverse and vertical ones; it is able to damp all the car body oscillations and to transmit the motion from the bogies to the car body.
The masses, main dimensions and features of the components are summarized in Table 2.2, while figure 7.1 shows a scheme of the wagon.
The motion can be analyzed in a straight or curved paths, with or without an initial perturbation. Some dynamic results are reported in chapter 8 where the graphics are compared with those obtained by means of a CMS software.

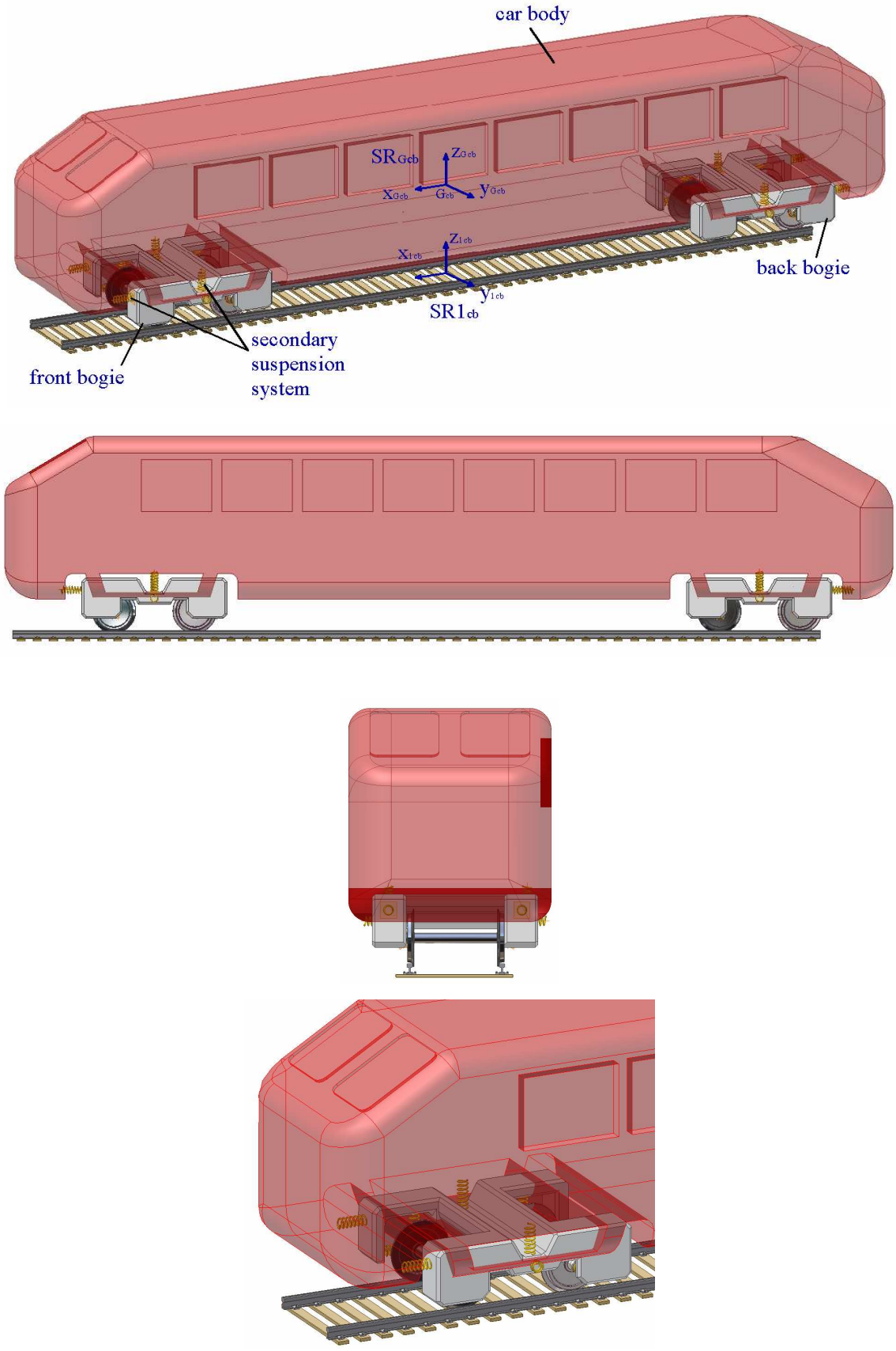

Figure 7.1

The wagon model developed in Matlab environment with the secondary suspension system and its reference systems.

7.3 – THE CARTESIAN COORDINATE SYSTEMS

The following right-hand Cartesian coordinate systems are introduced in the analysis:

- absolute reference system SR_0 ;
- reference systems inherent the front bogie, as described in paragraph 6.4;
- reference systems inherent the back bogie, as described in paragraph 6.4;
- reference system fixed with the car-body SR_{Gcb} ;
- reference system that follows the car-body on the rail path SR_{1cb} ;

The coordinate system SR_{Gcb} is fixed with the car-body mass. Its origin is coincident with the car-body center of mass. The axis x_{Gcb} is initially parallel to the rail direction, the axes z_{Gcb} is initially vertical and directed upwards.

The reference system SR_{1cb} has its origin belonging to the track longitudinal plane of symmetry and to the rolling plane. The origin of the coordinate system follows the path of the center of mass of the car-body (see Figure 7.1). Therefore, when the rail path is straight, the positions of the frame has the same coordinate *x* of the car-body center of mass.

The axes x_{1cb} is parallel to the rail direction. The axes z_{1cb} is orthogonal to the rolling plane and directed upward.

7.4 – THE EQUATIONS OF MOTION OF THE WAGON

7.4.1 – The cardinal equations

The equations of dynamics are written only for the main seven moving masses. The inertia of the suspension deformable elements is neglected.

The equations are expressed in the inertial coordinate system SR_o and are given below:

$$ {}^{j}\vec{F}_{ext}^{\,i} = {}^{j}m_i \, {}^{j}\vec{a}_G^{\,i}; \qquad {}_{ext}{}^{j}\vec{M}_G^{\,i} = \frac{d\,{}^{j}\vec{K}_G^{\,i}}{dt}; \qquad {}^{j}\vec{F}_{ext}^{\,fr} = {}^{j}m_{fr} \, {}^{j}\vec{a}_G^{\,fr}; \qquad {}_{ext}{}^{j}\vec{M}_G^{\,fr} = \frac{d\,{}^{j}\vec{K}_G^{\,fr}}{dt}. $$

$$ \vec{F}_{ext}^{\,wag} = m_{wag}\vec{a}_G^{\,wag}; \qquad {}_{ext}\vec{M}_G^{\,wag} = \frac{d\vec{K}_G^{\,wag}}{dt} $$

where:

subscript or upperscript i can assume the meaning of "*front*" or "*back*" when denoting the *front* or *back* wheel-set respectively while the upperscript j can assume the meaning of "*front*" or "*back*" when denoting the *front* or *back* bogie;

${}^{j}\vec{F}_{ext}^{\,i}$ is the sum of all external forces acting on the i^{th} wheel-set belonging to the j^{th} bogie;

${}^{j}\vec{a}_{G}^{\,i}$ is the acceleration of the barycenter of the i^{th} wheel-set belonging to the j^{th} bogie;

${}^{j}m_i$ is the mass of the i^{th} wheel-set belonging to the j^{th} bogie;

${}_{ext}{}^{j}\vec{M}_{G}^{\,i}$ is the resultant external moment about the center of mass acting on the i^{th} wheel-set belonging to the j^{th} bogie;

${}^{j}\vec{K}_{G}^{\,i}$ is the angular momentum about the center of mass of the i^{th} wheel-set belonging to the j^{th} bogie;

${}^{j}\vec{F}_{ext}^{\,fr}$ is the sum of all the external forces acting on the bogie frame belonging to the j^{th} bogie;

${}^{j}m_{fr}$ is the bogie frame mass belonging to the j^{th} bogie;

${}^{j}\vec{K}_{G}^{\,fr}$ is the angular momentum about the center of mass of the bogie frame belonging to the j^{th} bogie;

${}_{ext}{}^{j}\vec{M}_{G}^{\,fr}$ is the resultant of all external forces moments about the center of mass and acting on the bogie frame belonging to the j^{th} bogie;

$\vec{F}_{ext}^{\,wag}$ is the sum of all the external forces acting on the car body;

m_{wag} is the car body mass;

$\vec{K}_{G}^{\,wag}$ is the angular momentum about the center of mass of the car body;

${}_{ext}\vec{M}_{G}^{\,wag}$ is the resultant of all external force moments about the center of mass and acting on the car body;

7.4.2 – The external forces and moments

The external forces acting on the wheel-sets, on the bogie frame and on the car body are obtained from the following sums:

$${}^{j}\vec{F}_{ext}^{\,i} = {}^{j}\vec{P}_i + \sum_{h=1}^{{}^{j}Nl_i} {}_{cl}\,{}^{j}\vec{F}_i^{\,h} + \sum_{k=1}^{{}^{j}Nr_i} {}_{cr}\,{}^{j}\vec{F}_i^{\,k} + {}^{j}\vec{F}_i^{\,susp} + {}^{j}\vec{F}_i^{\,o}$$

$${}^{j}\vec{F}_{ext}^{\,fr} = {}^{j}\vec{P}_{fr} + {}^{j}\vec{F}_{fr}^{\,susp1} + {}^{j}\vec{F}_{fr}^{\,o} + {}^{j}\vec{F}_{fr}^{\,susp2}$$

$$\vec{F}_{ext}^{\,wag} = \vec{P}_{wag} + \vec{F}_{wag}^{\,o} + \vec{F}_{wag}^{\,susp2}$$

where:

${}^{j}\vec{P}_i$ is the weight of the i^{th} wheel-set belonging to the j^{th} bogie;

${}_{cl}{}^{j}\vec{F}_i^{h}$ is the contact force acting on left wheel regarding the h^{th} contact point on the i^{th} wheel-set belonging to the j^{th} bogie;

${}_{cr}{}^{j}\vec{F}_i^{k}$ is the contact force acting on right wheel regarding the k^{th} contact point on the i^{th} wheel-set belonging to the j^{th} bogie;

${}^{j}\vec{F}_i^{susp1}$ is the sum of all forces acting on i^{th} wheel-set belonging to the j^{th} bogie and transmitted by the primary suspension system;

${}^{j}\vec{F}_i^{o}$ is the sum of all possible further external forces (pull force, load directly applied on the masses, etc..) acting on the i^{th} wheel-set belonging to the j^{th} bogie;

${}^{j}\vec{P}_{fr}$ is the weight of the bogie frame belonging to the j^{th} bogie;

${}^{j}\vec{F}_{fr}^{susp1}$ is the sum of all forces acting on the bogie frame belonging to the j^{th} bogie and transmitted through the primary suspension system;

${}^{j}\vec{F}_{fr}^{o}$ is the sum of the remaining external forces (e.g. pull force, load directly applied on the bogie frame, etc..) acting on bogie frame belonging to the j^{th} bogie;

${}^{j}Nl_i$ is the number of the contact points on the left wheel of the i^{th} wheel-set belonging to the j^{th} bogie;

${}^{j}Nr_i$ is the number of the contact points on the right wheel of the i^{th} wheel-set belonging to the j^{th} bogie;

${}^{j}\vec{F}_{fr}^{susp2}$ is the sum of all forces acting on the bogie frame belonging to the j^{th} bogie and transmitted through the secondary suspension system;

The resultant bending moments acting on the i^{th} wheel-sets belonging to the j^{th} bogie, on the j^{th} bogie frame and on the car body are the following:

$$ {}_{ext}{}^{j}\vec{M}_G^{i} = \sum_{h=1}^{{}^{j}Nl_i}\left({}_{cl}{}^{j}G\vec{P}_i^{h} \times {}_{cl}{}^{j}\vec{F}_i^{h} + {}_{i}^{cl}\vec{M}_{j\ spin}^{h} \right) + \sum_{k=1}^{{}^{j}Nr_i}\left({}_{cr}{}^{j}G\vec{P}_i^{k} \times {}_{cr}{}^{j}\vec{F}_i^{k} + {}_{i}^{cr}\vec{M}_{j\ spin}^{k} \right) + {}_{i}{}^{j}\vec{M}_G^{susp1} + {}_{i}{}^{j}\vec{M}_G^{o} + {}_{i}{}^{j}\vec{M}_G^{mot} $$

$$ {}_{ext}{}^{j}\vec{M}_G^{fr} = {}_{fr}{}^{j}\vec{M}_G^{susp1} + {}_{fr}{}^{j}\vec{M}_G^{o} + {}_{fr}{}^{j}\vec{M}_G^{susp2} $$

$$ {}_{ext}\ \vec{M}_G^{wag} = {}_{wag}\vec{M}_G^{o} + {}_{wag}\vec{M}_G^{susp2} $$

where:

${}_{cl}{}^{j}G\vec{P}_i^{h}$ is the vector joining the barycenter of the i^{th} wheel-set belonging to the j^{th} bogie with the h^{th} contact point on its left wheel;

${}_{cr}{}^{j}G\vec{P}_i^{k}$ is the vector joining the barycenter of the i^{th} wheel-set belonging to the j^{th} bogie with the k^{th} contact point on its right wheel;

${}^{cl}_{i\ j}\vec{M}^{h}_{spin}$ is the spin moment acting just on the h^{th} contact point on the left wheel of the i^{th} wheel-set belonging to the j^{th} bogie;

${}^{cr}_{i\ j}\vec{M}^{k}_{spin}$ is the spin moment acting just on the k^{th} contact point on the right wheel of the i^{th} wheel-set belonging to the j^{th} bogie;

${}_{i}{}^{j}\vec{M}^{susp1}_{G}$ is the resultant moment about the center of mass of the forces transmitted by the primary suspension system to the i^{th} wheel-set belonging to the j^{th} bogie;

${}_{i}{}^{j}\vec{M}^{o}_{G}$ is the resultant moment about the center of mass of all possible further external forces acting on the i^{th} wheel-set belonging to the j^{th} bogie;

${}_{i}{}^{j}\vec{M}^{mot}_{G}$ is the engine couple applied on the i^{th} wheel-set belonging to the j^{th} bogie;

${}_{fr}{}^{j}\vec{M}^{susp1}_{G}$ is the resultant moment about the center of mass of the forces transmitted by the primary suspension system to the bogie frame belonging to the j^{th} bogie;

${}_{fr}{}^{j}\vec{M}^{o}_{G}$ is the resultant moment about the center of mass of the remaining external forces acting on the bogie frame belonging to the j^{th} bogie;

${}_{fr}{}^{j}\vec{M}^{susp2}_{G}$ is the resultant moment about the center of mass of the forces transmitted by the secondary suspension system to the bogie frame belonging to the j^{th} bogie;

${}_{wag}\vec{M}^{o}_{G}$ is the resultant moment about the center of mass of the remaining external forces acting on the car body;

${}_{wag}\vec{M}^{susp2}_{G}$ is the resultant moment about the center of mass of the forces transmitted by the secondary suspension system to the car body.

7.4.3 - FORCES GENERATED BY THE SECONDARY SUSPENSION SYSTEM

The forces generated by the secondary suspension system are due to elastic and damping effects. The force expressions are reported in paragraph 6.8 with reference to the secondary suspension system; point A of Figure 6.8 belongs to the bogie frame while point B belongs to the car body.

7.5 - THE WAGON DIFFERENTIAL EQUATIONS

The dynamic equilibrium conditions of the wagon form a system of 42 second order differential equations. The unknowns are the following coordinates of the moving bodies:

${}^{i}x_G^j(t),\ {}^{i}y_G^j(t),\ {}^{i}z_G^j(t)$, coordinates of the barycenter of the j^{th} body respect to a SR_o of the i^{th} bogie;

${}^{i}\vartheta_x^j(t),\ {}^{i}\vartheta_y^j(t),\ {}^{i}\vartheta_z^j(t)$, attitude angles of the frame $SR_{Gj,}$ connected to j^{th} body of the i^{th} bogie, respect to a SR_o;

$x_G^{wag}(t), y_G^{wag}(t), z_G^{wag}(t)$, coordinates of the barycenter of the car body respect to a SR_o;

$\vartheta_x^{wag}(t), \vartheta_y^{wag}(t), \vartheta_z^{wag}(t)$, attitude angles of the frame fixed with the car body, respect to a SR_o;

The subscript *j* is equal to "*front*", "*back*" or "*fr*" when the variable pertains to front, back wheel-set, bogie frame, respectively and the subscript *i* is equal to "*front*" or "*back*" when the variable pertains to front, back bogie.

The accelerations of the barycenters are given by the following relations:

$$ {}^{i}\vec{a}_G^j = \frac{d^2\,{}^{i}x_G^j}{dt^2}\vec{i}_o + \frac{d^2\,{}^{i}y_G^j}{dt^2}\vec{j}_o + \frac{d^2\,{}^{i}z_G^j}{dt^2}\vec{k}_o $$

$$ \vec{a}_G^{wag} = \frac{d^2 x_G^{wag}}{dt^2}\vec{i}_o + \frac{d^2 y_G^{wag}}{dt^2}\vec{j}_o + \frac{d^2 z_G^{wag}}{dt^2}\vec{k}_o $$

where $\vec{i}_o, \vec{j}_o, \vec{k}_o$ denote the versors of SR_o.

The equilibrium at rotation is expressed by the differential equations

$$ \begin{cases} I_{xx}^j \dfrac{dp_j}{dt} - \left(I_{yy}^j - I_{zz}^j\right) q_j r_j = {}_{ext}^{x}M_{G^*}^{j} \\ I_{yy}^j \dfrac{dq_j}{dt} - \left(I_{zz}^j - I_{xx}^j\right) r_j p_j = {}_{ext}^{y}M_{G^*}^{j} \\ I_{zz}^j \dfrac{dr_j}{dt} - \left(I_{xx}^j - I_{yy}^j\right) p_j q_j = {}_{ext}^{z}M_{G^*}^{j} \end{cases} $$

where:

$I_{xx}^j, I_{yy}^j, I_{zz}^j$ are the central moment of inertia of the j^{th} body;

p_j, q_j, r_j are the angular velocity components of the j^{th} body expressed in the local frame SR_{Gj};

${}^{x}_{ext}M^{j}_{G^*}$, ${}^{y}_{ext}M^{j}_{G^*}$, ${}^{z}_{ext}M^{j}_{G^*}$ are the Cartesian components of the external resultant moment about the barycenter of j^{th} body of the external forces expressed in the local frame SR_{Gj}.

CHAPTER 8

NUMERICAL RESULTS

8.1- INTRODUCTION

The numerical results discussed in this chapter regard:

- code and lookup table validation;
- monitoring the time-steps variation under strongly non stationary conditions;
- investigation of the wheel-set and bogie critical speed under different loads and configurations;
- analysis of the influence of the longitudinal stiffness of the primary suspension system on the bogie critical velocity;
- analysis of the contact forces between the bogie wheels and the rails in a curved track;
- investigation of the derailment conditions in function of the longitudinal characteristics of the primary suspension system in a curved track;
- analysis of the critical speed in function of the super-elevation in a curved track.

8.2 – CODE AND LOOKUP VALIDATIONS

In order to validate the lookup table and the developed code, a comparison is made with the results supplied by a commercial multibody software (CMS); in particular the analyses concerns with the behaviour of a single wheel-set and of a complete bogie behaviour under stable, critical and unstable conditions.

To obtain the critical speed of the wheel-set and the bogie - namely V_{cr}^{w} and V_{cr}^{b} - moving on a straight path, the two systems - the wheel-set and the bogie - running with a longitudinal

velocity V_{long} are initially perturbed with a transverse velocity component V_{trans}. In all simulations the V_{trans} is set equal to 0.1 m/s. For the wheel-set case let us assume that V_{long} is lower than the V_{cr}^{w}. For establishing the *critical speed* the hunting motion after the initial kinematic perturbation should be monitored. If the amplitudes of the oscillations decrease with time then $V_{long} < V_{cr}^{w}$ and it is necessary to increment V_{long}. Otherwise, if the amplitudes increase, then $V_{long} > V_{cr}^{w}$ and V_{long} must be decreased. When the amplitudes are almost constant in time the condition for which $V_{long} = V_{cr}^{w}$ is given.

The same procedure is applied to the computation of V_{cr}^{b}. In this case kinematic perturbations are initially applied to both wheel-sets.

Figures 8.1-8.4 show the transverse displacement, the yaw and roll angles of the wheel-set and the transverse tangent contribution of the tangent component acting on the two wheels in three different initial conditions, that is $V_{long} < V_{cr}^{w}$, $V_{long} = V_{cr}^{w}$ and $V_{long} > V_{cr}^{w}$.

Figures 8.5-8.10 show the transverse, vertical and longitudinal displacements and the rotation, yaw and roll angles of the three masses of the bogie that is the front and back wheel-sets and the bogie frame; Figures 8.11-8.13 show the two contributions of the tangent component and the normal one acting on the four wheels in the case of $V_{long} < V_{cr}^{w}$.

Figure 8.14 and 8.15 show the barycentre transverse displacement and the yaw angle of the unperturbed wheel-set in a curved track with radius of curvature equal to 900 m and with initial longitudinal velocity equal to 10 m/s.

Figure 8.16 shows the barycentre transverse displacement of all wagon masses - the four wheel-sets, the two bogie frames and the car body - moving with longitudinal velocity equal to 15 m/s and initially perturbed with a transverse velocity equal to 0.1 m/s. Figures 8.17 and 8.18 show the yaw and roll angle respectively of all wagon masses; Figures 8.19 and 8.20 report respectively the transverse component of the tangential force and the normal component of the contact force among all wagon wheels and rails.

The symbols in the figures have the following meaning: W=wheel, WS=wheel-set, CMS=commercial multibody software, BG=bogie, MAT=Matlab.

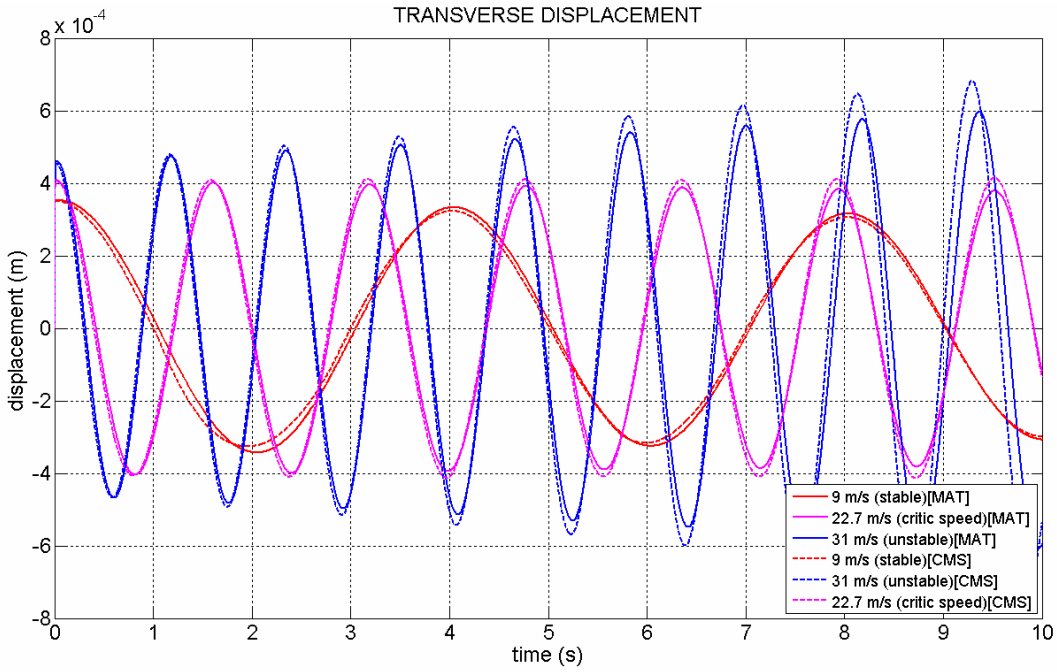

Figure 8.1

Plots of the transverse displacement of the wheel-sets obtained by means of the Matlab software and the commercial multibody software with three longitudinal velocity: stable, critical and unstable conditions.

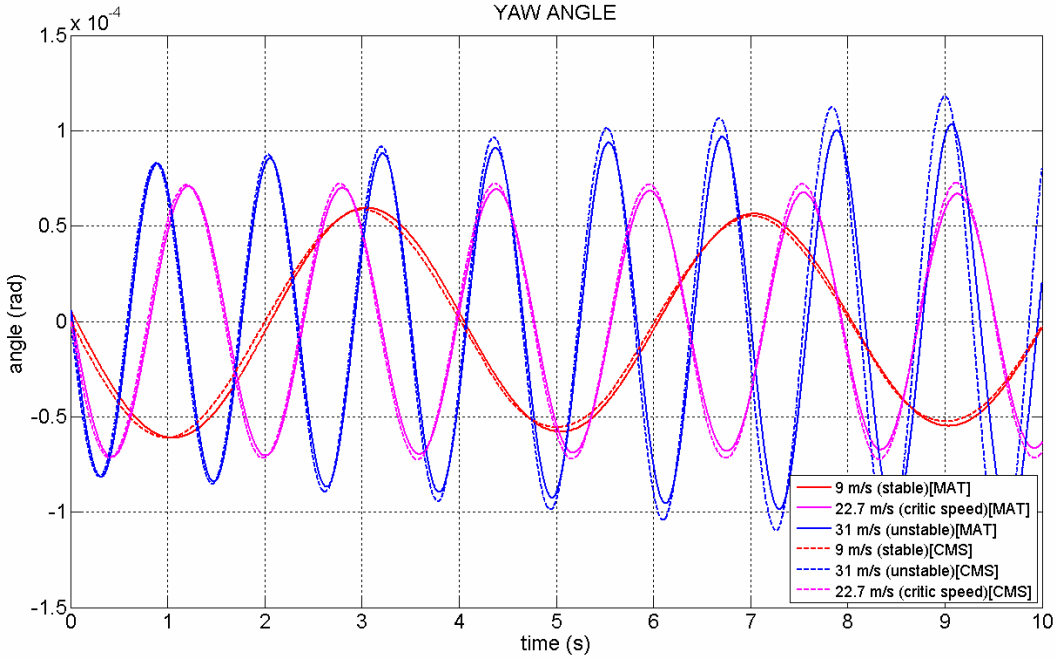

Figure 8.2

Plots of the yaw angle of the wheel-set obtained by means of the Matlab software and the commercial multibody software with three longitudinal velocities: stable, critical and unstable conditions.

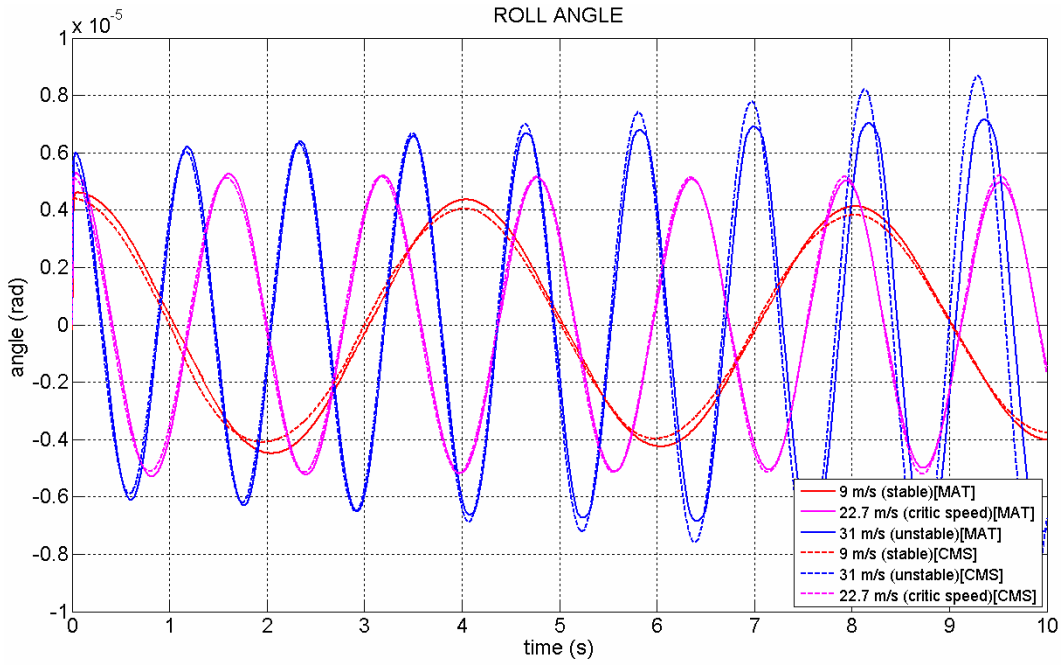

Figure 8.3

Plots of the roll angle of the wheel-set obtained by means of the Matlab software and the commercial multibody software with three longitudinal velocities: stable, critical and unstable conditions.

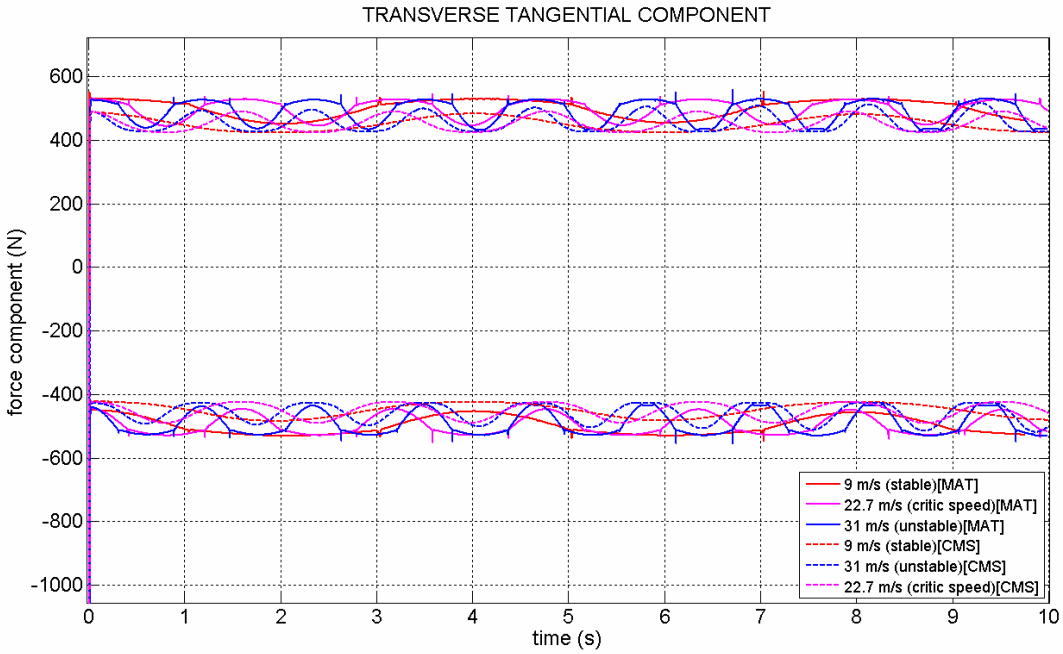

Figure 8.4

Plots of the transverse tangent component acting on the two wheels obtained by means of the Matlab software and the commercial multibody software with three longitudinal velocities: stable, critical and unstable conditions.

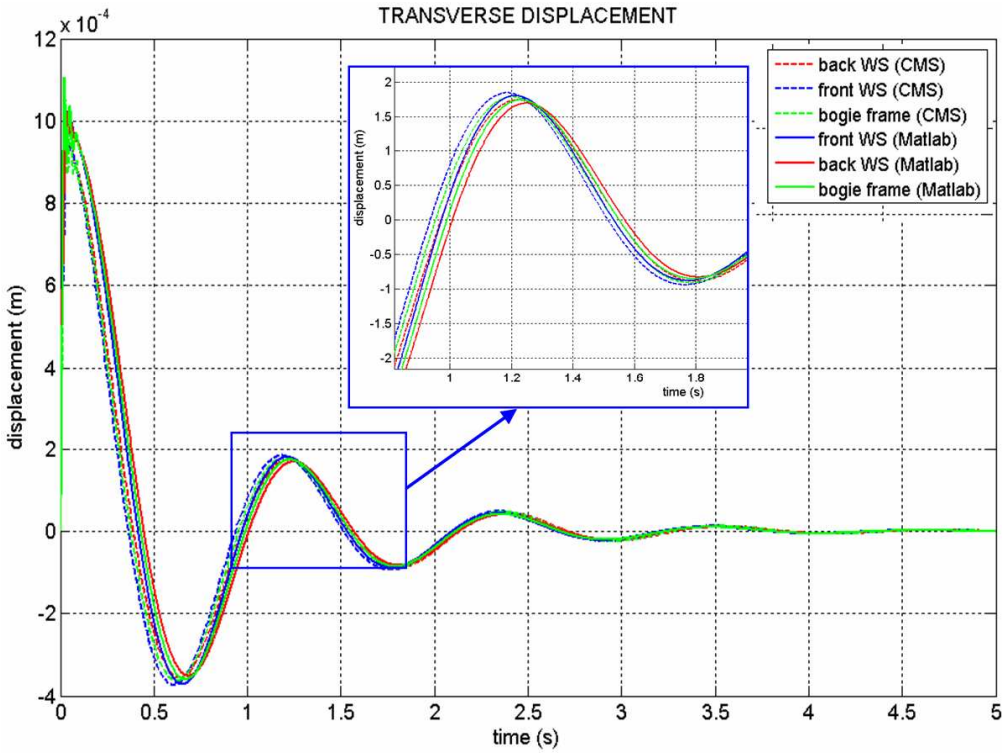

Figure 8.5

Plots of the transverse displacement of the two wheel-sets and the bogie frame obtained by means of the Matlab software and the commercial multibody software.

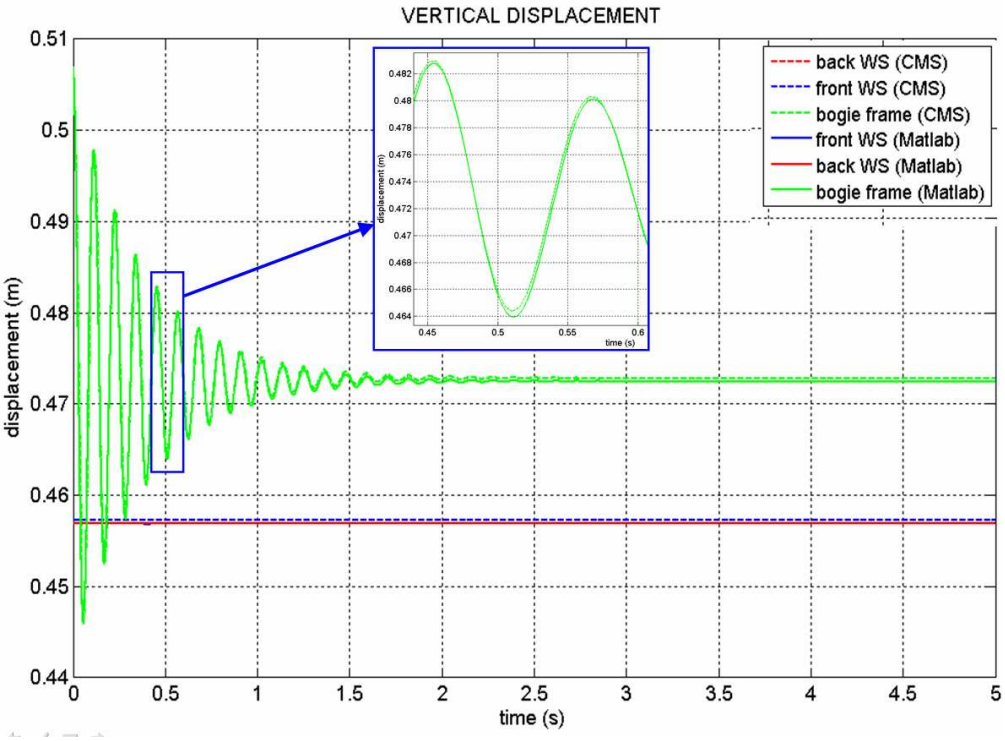

Figure 8.6

Plots of the vertical displacement of the two wheel-sets and the bogie frame obtained by means of the Matlab software and the commercial multibody software.

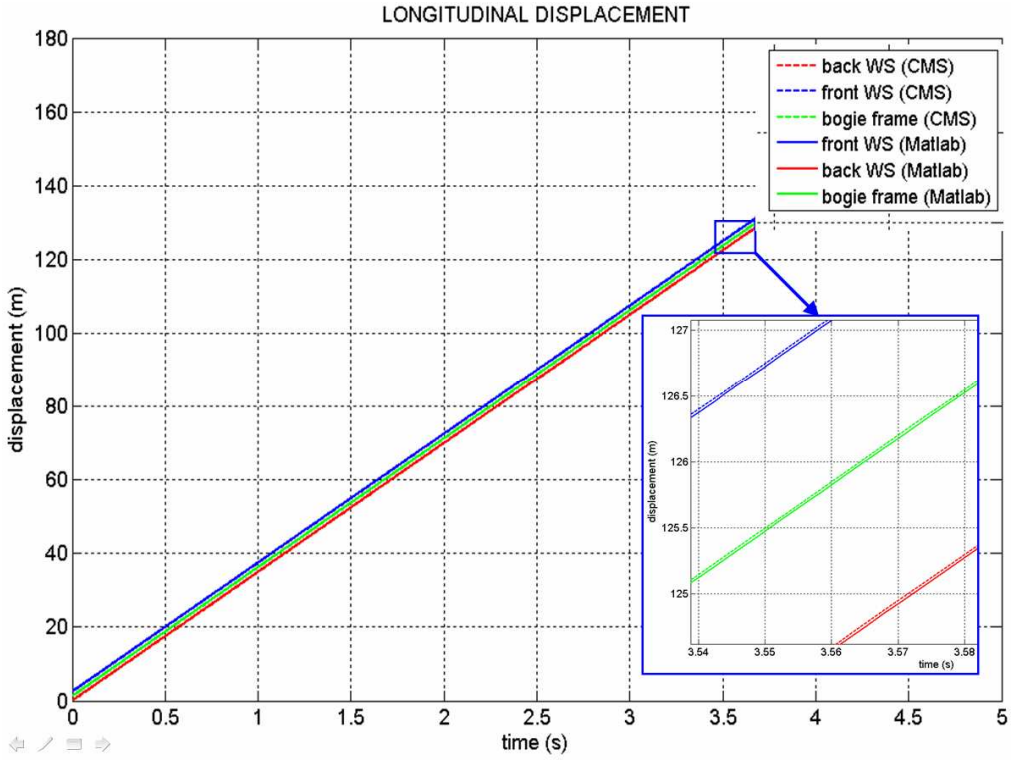

Figure 8.7

Plots of the longitudinal displacement of the two wheel-sets and the bogie frame obtained by means of the Matlab software and the commercial multibody software.

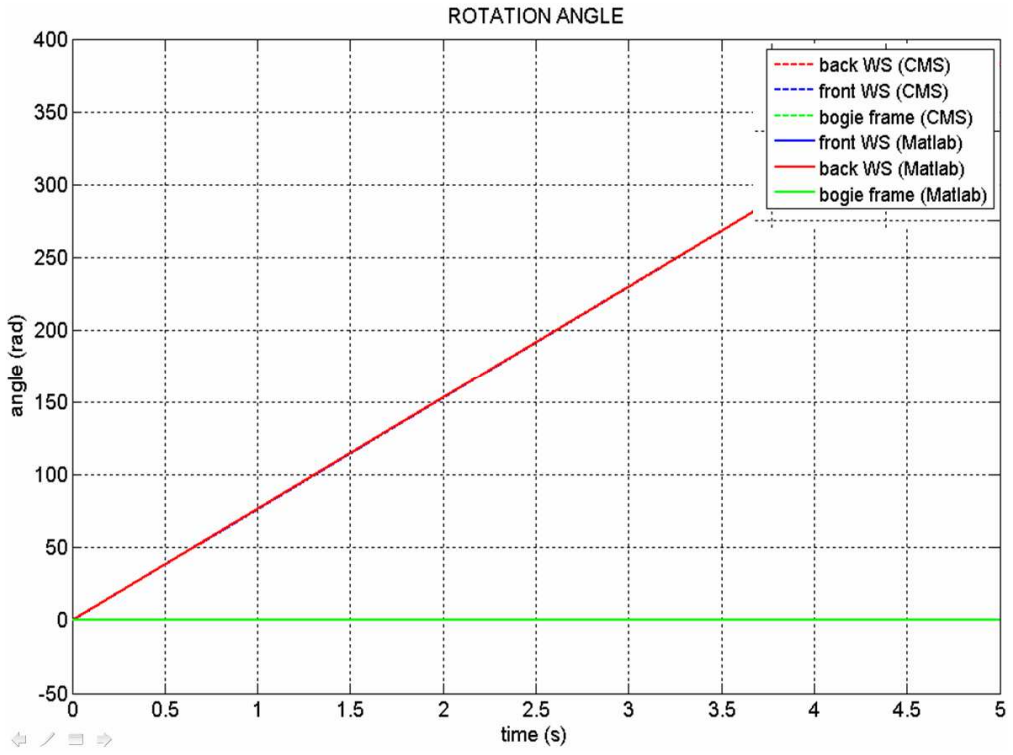

Figure 8.8

Plots of the rotation angle of the two wheel-sets and the bogie frame obtained by means of the Matlab software and the commercial multibody software.

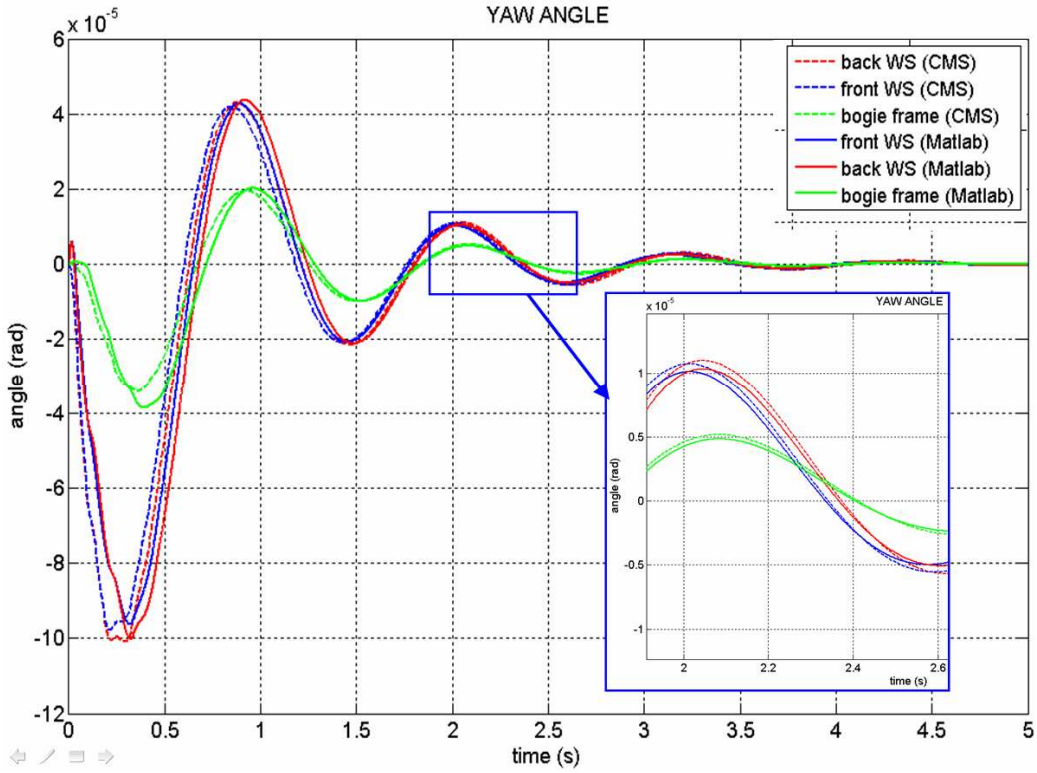

Figure 8.9

Plots of the yaw angle of the two wheel-sets and the bogie frame obtained by means of the Matlab software and the commercial multibody software.

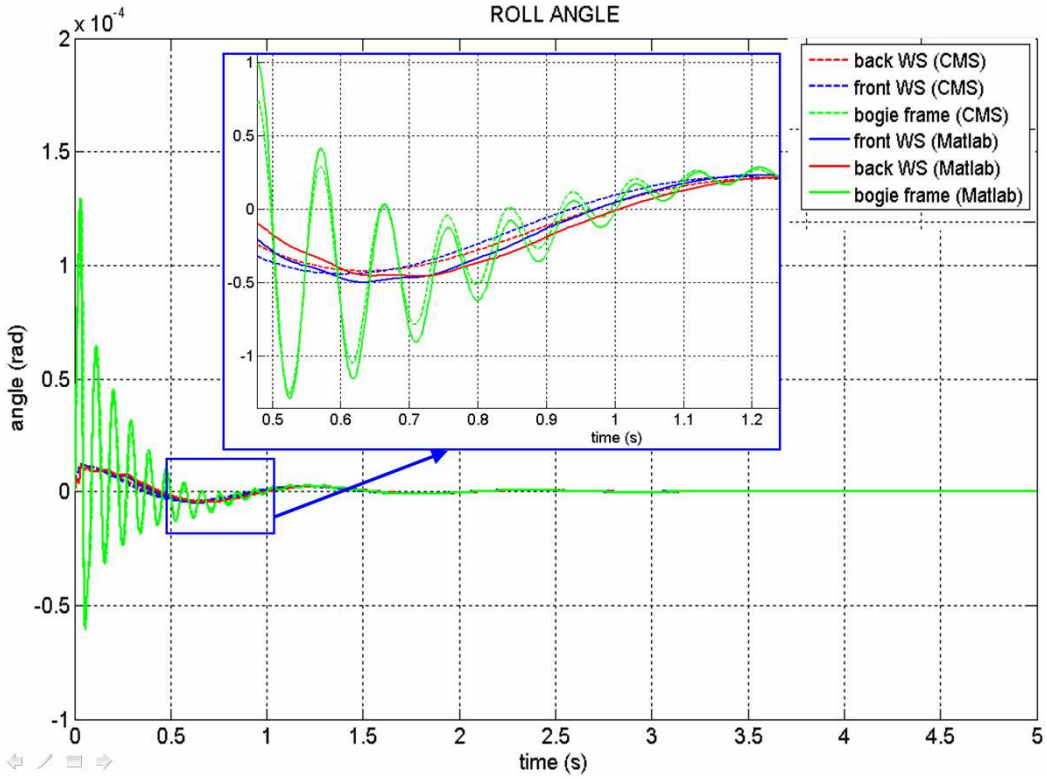

Figure 8.10

Plots of the roll angle of the two wheel-sets and the bogie frame obtained by means of the Matlab software and the commercial multibody software.

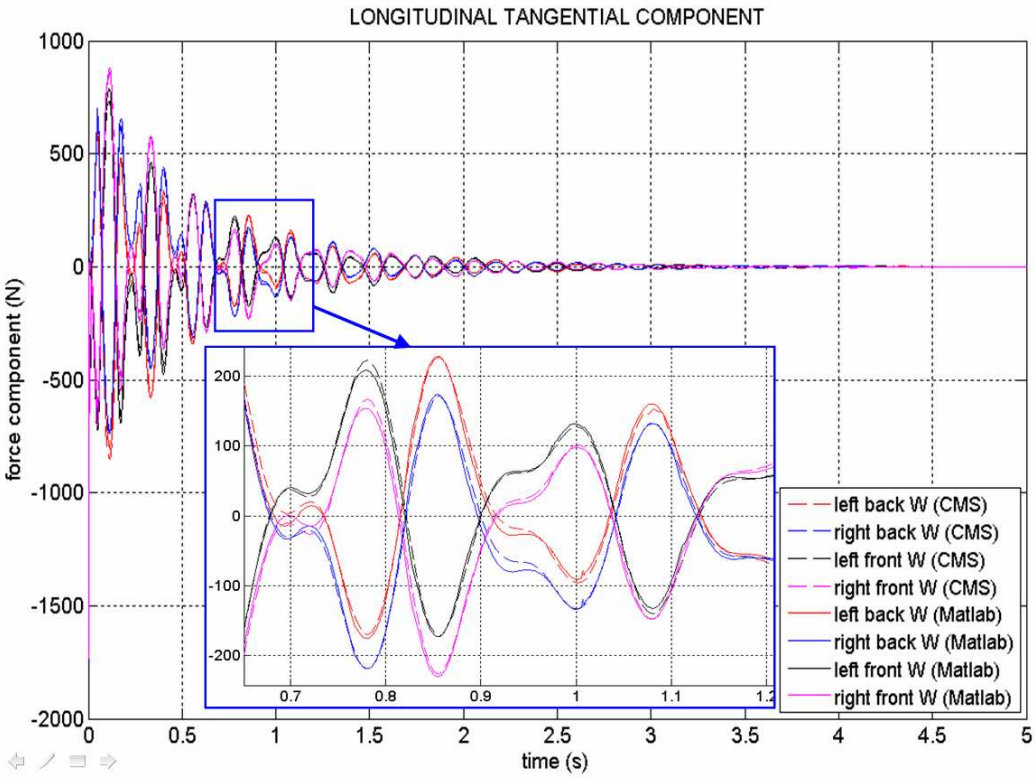

Figure 8.11

Plots of the longitudinal tangent components acting on the four wheels obtained by means of the Matlab software and the commercial multibody software.

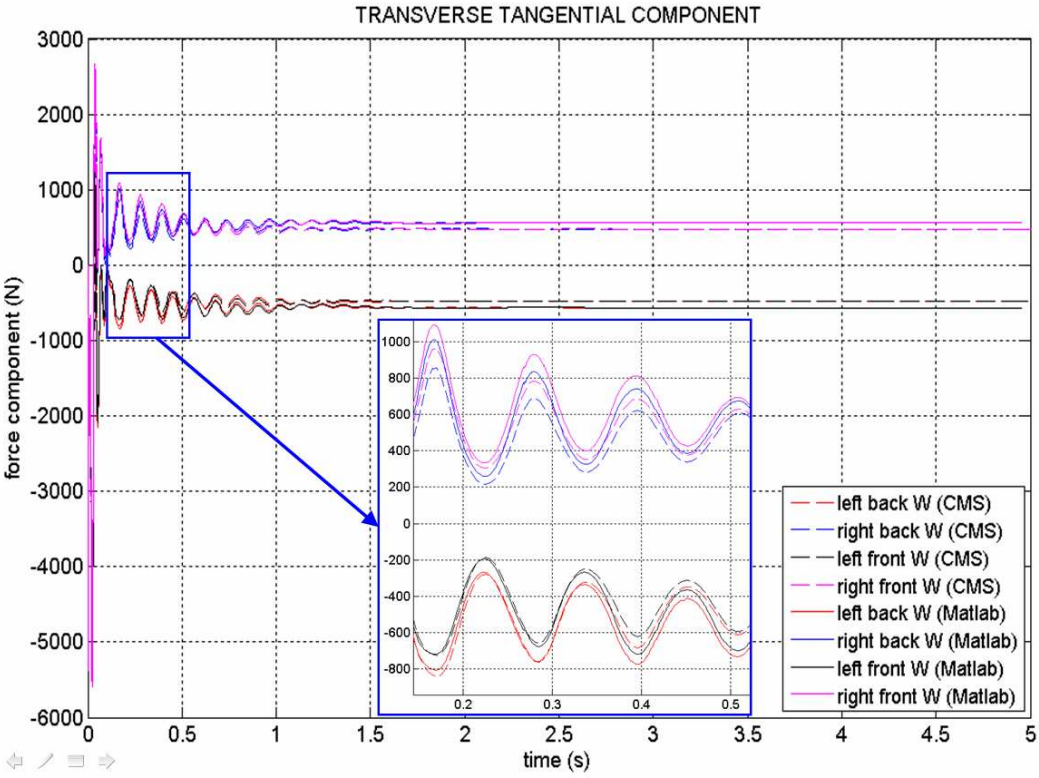

Figure 8.12

Plots of the transverse tangent component acting on the four wheels obtained by means of the Matlab software and the commercial multibody software.

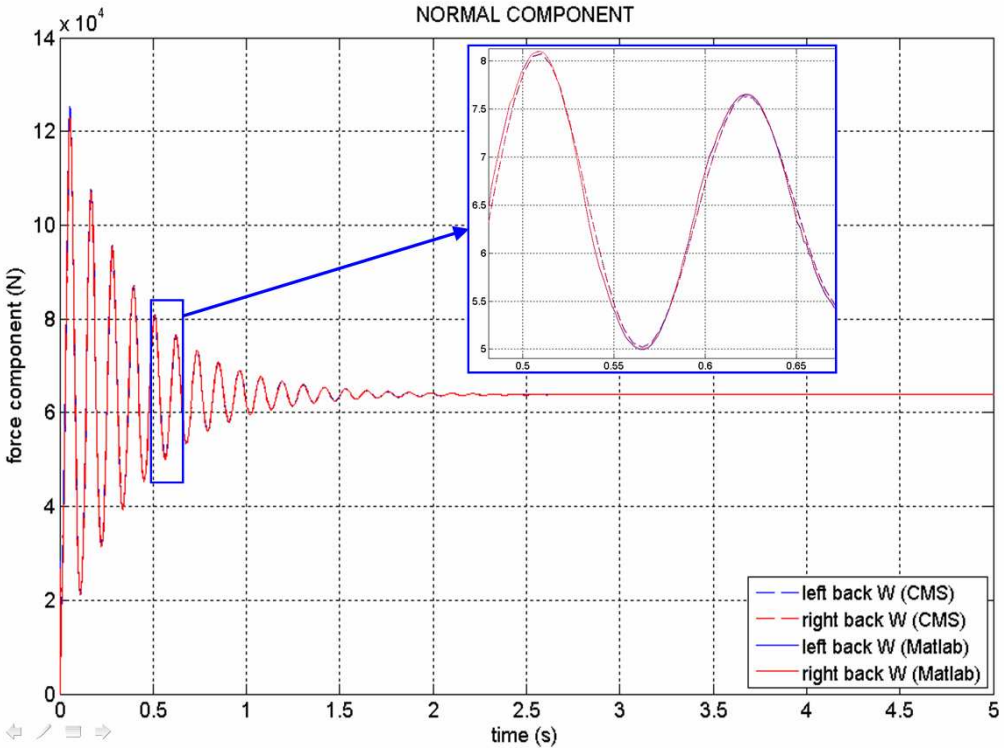

Figure 8.13

Plots of the normal components acting on the two back wheels obtained by means of the Matlab software and the commercial multibody software.

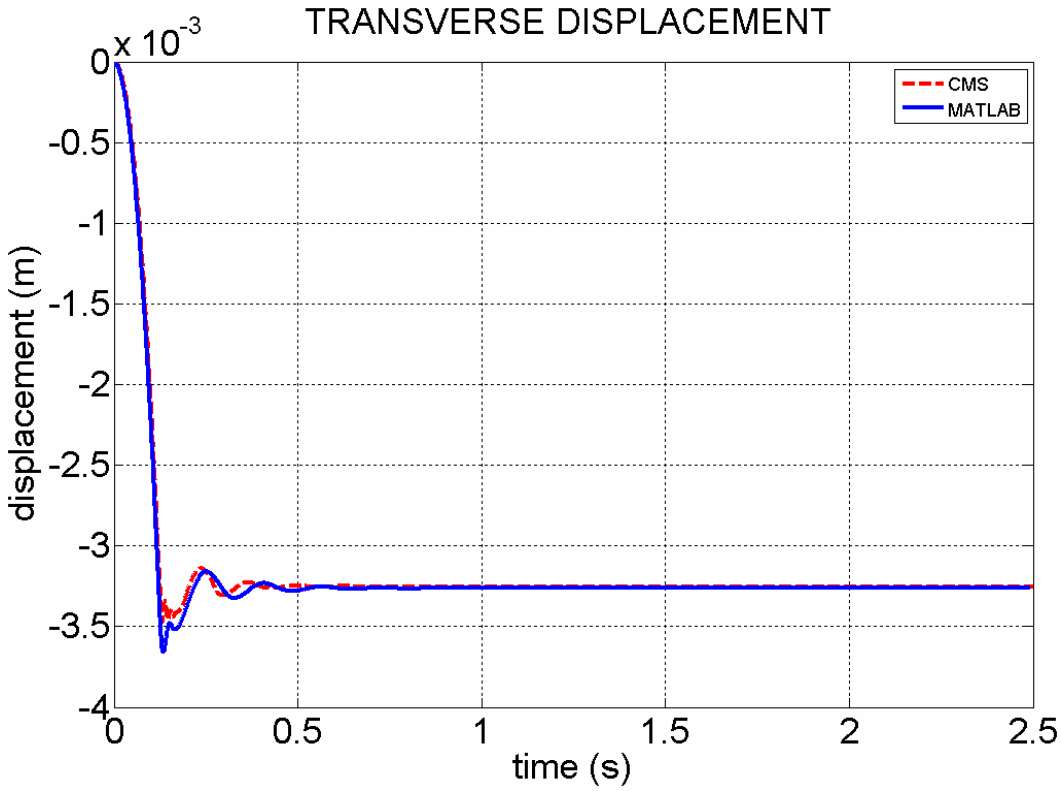

Figure 8.14

Plots of the transverse displacement of the unperturbed wheel-set obtained by means of the Matlab software and the commercial multibody software in a curved track with radius of curvature equal to 900 m and with initial longitudinal velocity equal to 10 m/s.

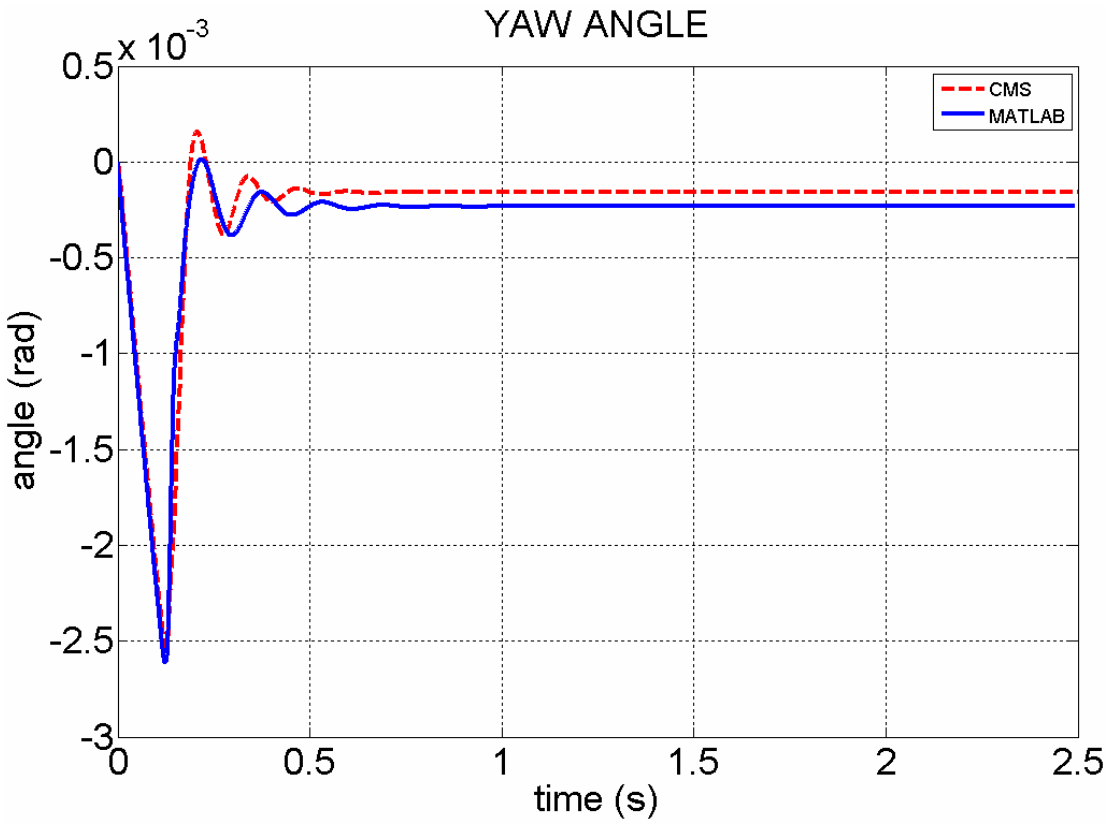

Figure 8.15

Plots of the yaw angle of the unperturbed wheel-sets obtained by means of the Matlab software and the commercial multibody software in a curved track with radius of curvature equal to 900 m and with initial longitudinal velocity equal to 10 m/s.

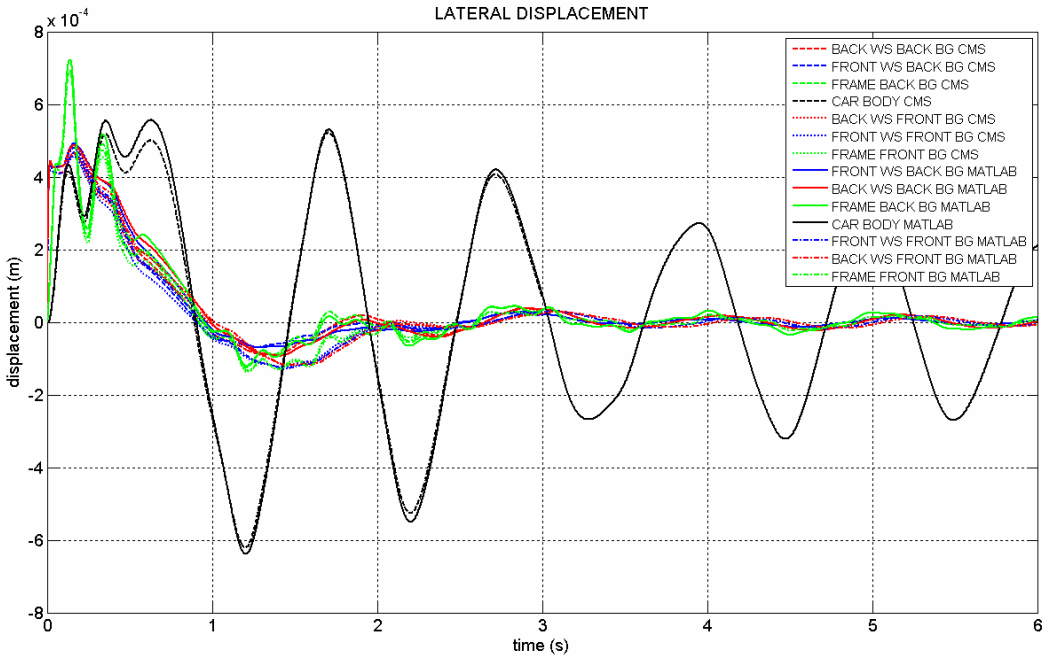

Figure 8.16

Plots of the transverse displacement of the wagon masses that is the four wheel-sets, the two bogie frames and the car body, obtained by means of the Matlab software and the commercial multibody software.

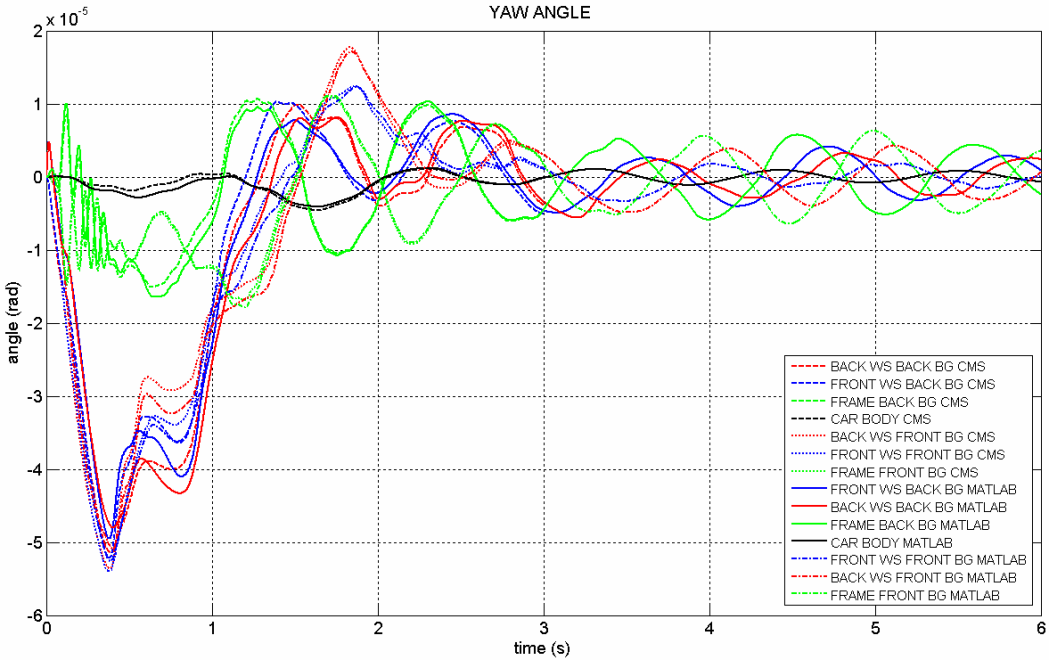

Figure 8.17

Plots of the yaw angle of the four wheel-sets, the two bogie frames and the car body, obtained by means of the Matlab software and the commercial multibody software.

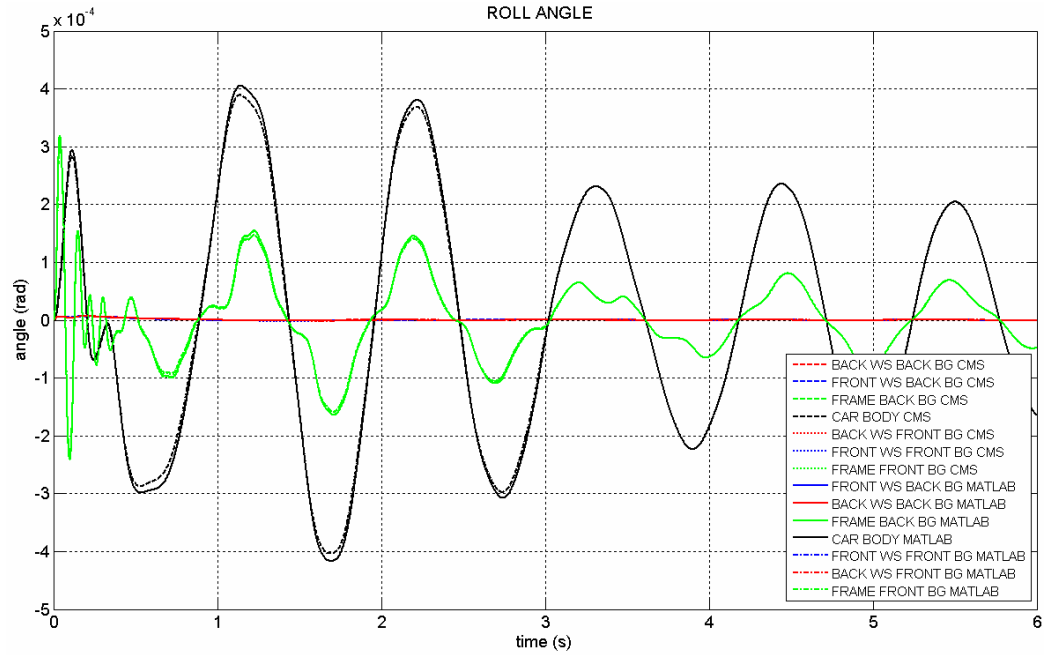

Figure 8.18

Plots of the roll angle of the wagon masses that is the four wheel-sets, the two bogie frames and the car body, obtained by means of the Matlab software and the commercial multibody software.

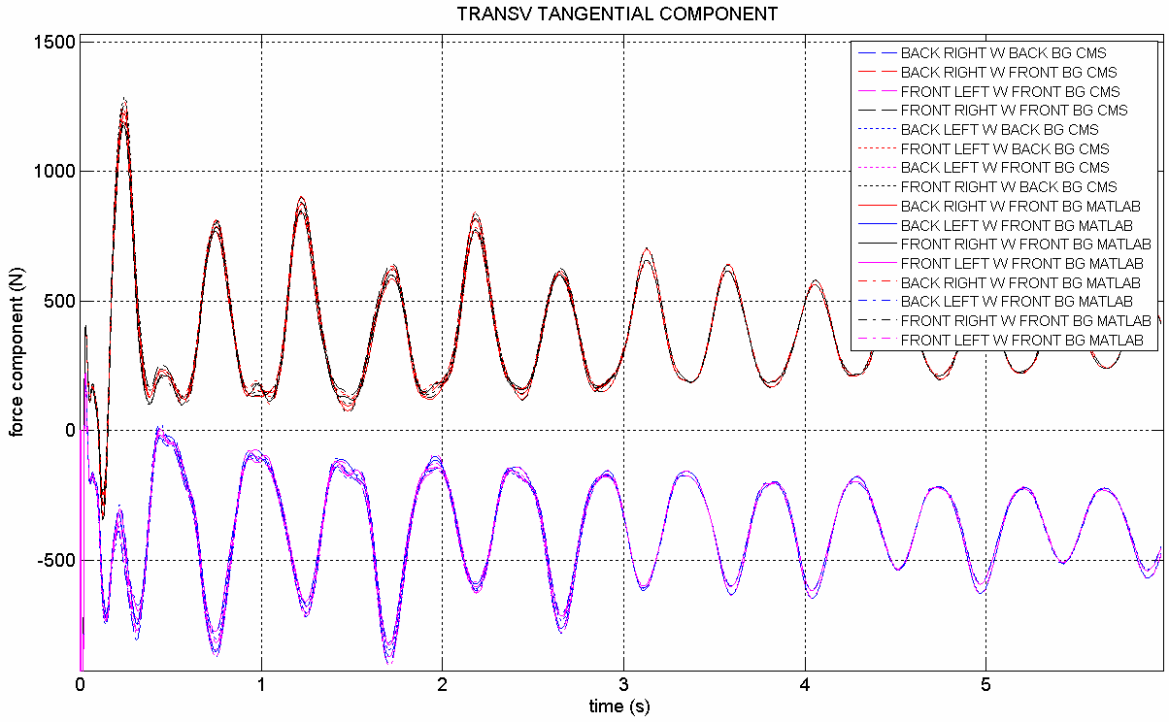

Figure 8.19

Plots of the transverse tangential components among the wagon wheels and the rails; obtained by means of the Matlab software and the commercial multibody software.

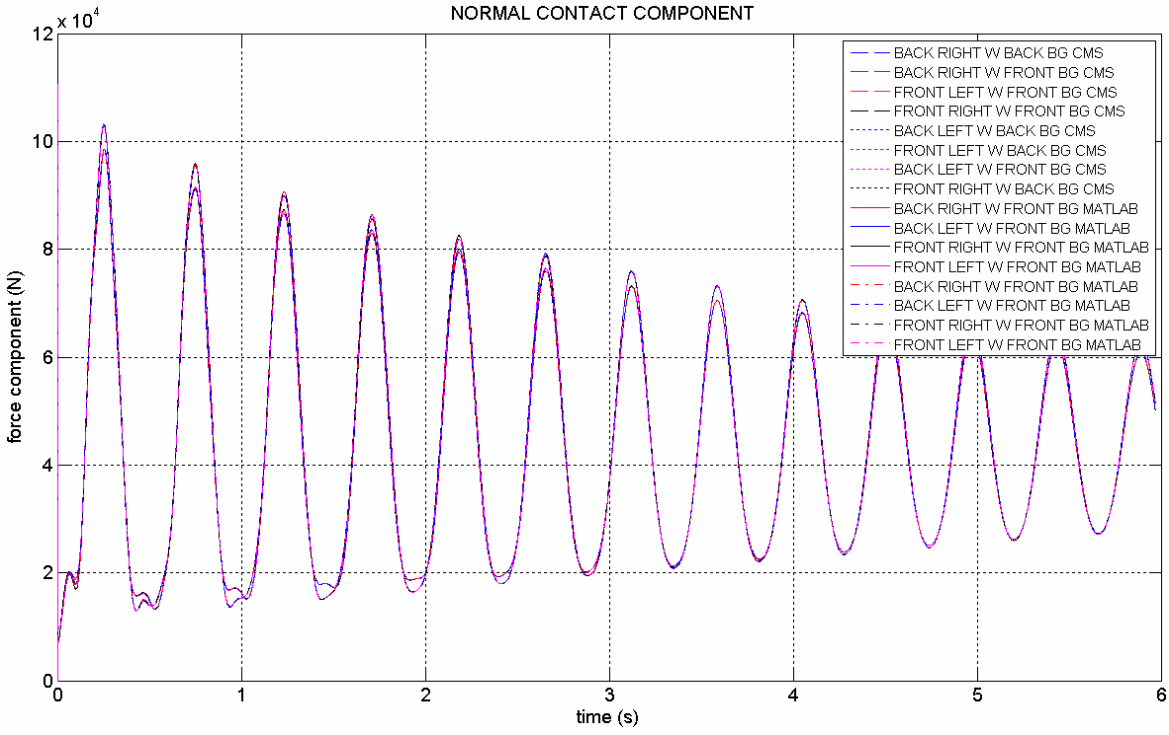

Figure 8.20

Plots of the normal contact components among the wagon wheels and the rails; obtained by means of the Matlab software and the commercial multibody software.

The mentioned figures demonstrate the agreement between the results obtained by means of the Matlab code and the commercial multibody software models described in chapter II. This is observed for both the displacements (kinematics) and the contact forces (dynamics). Moreover it can see that the displacement and the yaw angle present a very similar periodicity; this prove that the hunting motion is coupled and thus generated by the interaction of the transverse displacement and the yaw rotation. From the Figures 8.5, 8.9, 8.10 one observe that all the masses concerning the bogie oscillate in phase; this behaviour is characteristic of the rectilinear track when the perturbations are applied to the front and back wheel-sets at the same manner.

8.3 – THE TIME STEP MONITORING

With the aim to monitor the time-step variation during integration, so that the simulation duration, we have observed that the required step depends strongly on the degree of variation of the variables that control the motion of the system. When the variables are stationary the integration step increases continuously; on the contrary, when many perturbations occur, for example when the contact point crosses from the wheel tread to the flange, the step stays at its lower values.

Figure 8.21 compares in a semi-logarithmic scale three different simulations of the same system having equal time span but with the following initial conditions:

- absence of perturbation (Figure 8.21a);
- initial transverse perturbation set to 0.1 m/s, so that the contact points remain on the wheel tread (Figure 8.21b);
- initial transverse perturbation set to 0.35 m/s in such a way that the contact points concern both the tread and the flange wheel (Figure 8.21c);

One can observe that:

a) the step lengths increase with time up to 0.25 s in the case of unperturbed motion; the sharp decrease observed after the first peak is due to the vertical motion of the wheel-set in the transitory phase;
b) in the case of small initial perturbation, for instance 0.1 m/s, we have a hunting motion and the step length, after a first increasing phase, stabilizes on a value close to $1.2 \cdot 10^{-3}$ s. This behaviour can be justified considering the higher variation of the motion variables by respect to the unperturbed motion;
c) with a perturbation allowing the flange contact, Figure 8.21c, the variables rate of change is very high when the contact points moves between the tread and the flange; in the same

figure we can observe three consecutive and alternate (left-right) flange contacts. Hence due to the sharp discontinuities the integration step is reduced .

The step length influences the duration of the simulation and the global step number; in fact we pass from 125 steps in the first case to 320 in the second one and even to 4900 in the last one.

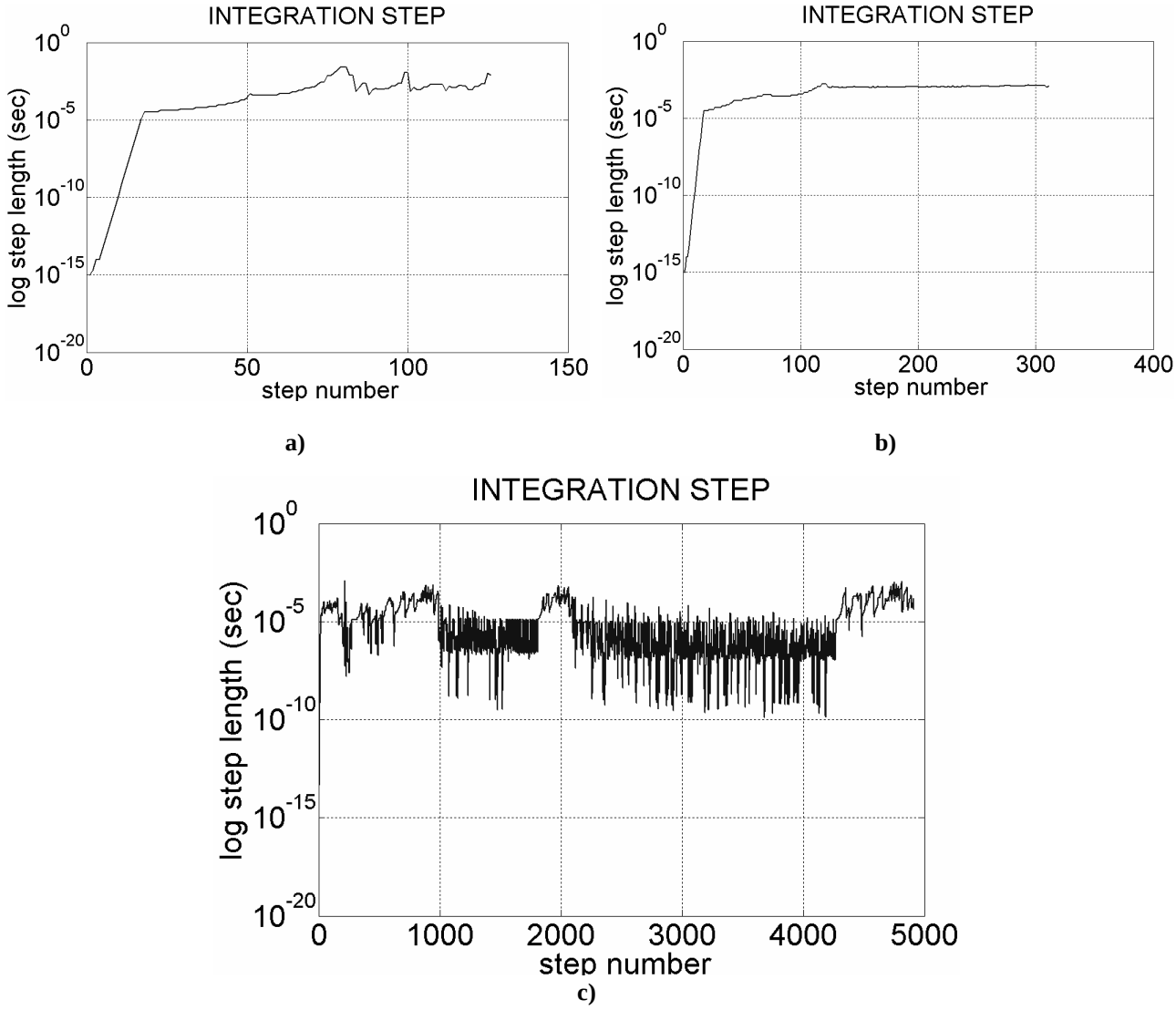

Figure 8.21

Step length in semi-logarithmic scale in three different cases: a) unperturbed motion; b) small initial perturbation without flange contact; c) relevant initial perturbation with flange contact.

8.4 – THE CRITICAL SPEED

It is well known that the critical speed of a wheel-set depends also from the external load applied on it. In fact one can report (see Figure 8.22a) the critical speed by respect to the *wheel-set load ratio*, defined as the ratio between the vertical load directly applied on the wheel-set

barycentre and the wheel-set weight. At the same time one can plot the curve of the critical hunting frequency obtained by means of a Fourier's analysis of the displacement oscillations by respect to the load ratio (see Figure 8.22b). Figure 8.23a shows the bogie critical speed vs. the *bogie load ratio* defined as the ratio between the vertical load directly applied on the frame bogie and its weight. Figure 8.23b reports the bogie hunting frequency vs. the bogie load ratio.

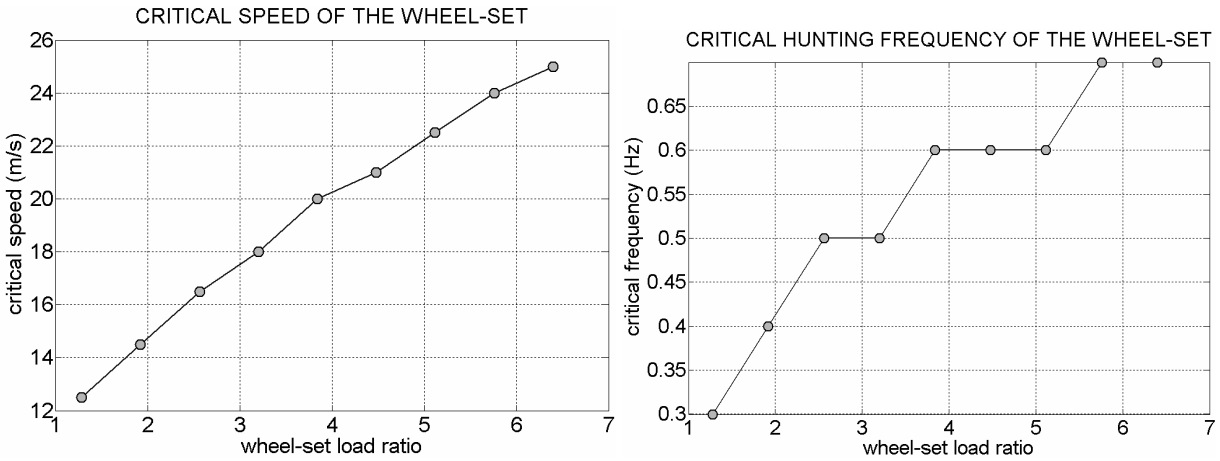

a) **b)**

Figure 8.22

Plots of the critical speed and hunting frequency of the wheel-set as regards the wheel-set load ratio.

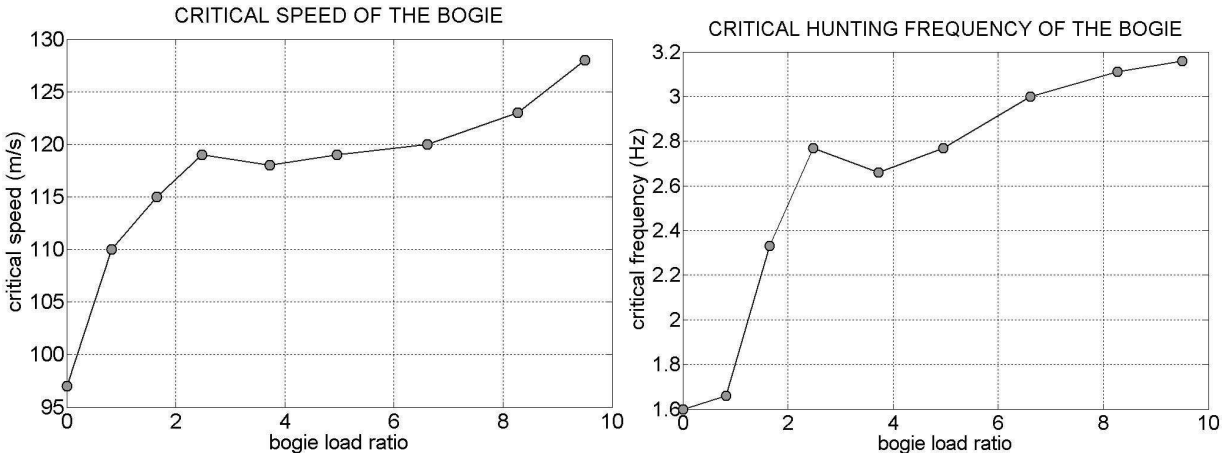

a) **b)**

Figure 8.23

Plots of the critical speed and hunting frequency of the bogie .vs. the bogie load ratio

As one can observe from the figures, the critical bogie speed is much higher when compared to the wheel-set one, having the same load ratio. This is mainly due:

- the presence of spaced wheel-sets on the bogie
- the presence of the primary suspension system.

The strongly perturbed wheel-set is not able, by means of the contact force actions, to generate a set of forces able to damp the motion. However, the stabilizing action generated by the bogie can reach very high values as it is promoted by the distance of the two wheel-set .

Also the primary suspension system contributes to the stabilizing action.
Another interesting evidence is the rise of the critical speed when the load ratio increases. This phenomenon reveals the importance of the contact forces on the stability of the system; in fact when the external load is increased also the normal and tangential components rise accordingly.
The system has better possibilities of reacting to the perturbations. In order to explain this concept we can imagine the limit case where all the external loads, included the weight, are null. The contact forces are null as well and the system cannot counter any perturbation.

8.5 – THE INFLUENCE OF THE BOGIE LONGITUDINAL STIFFNESS IN A STRAIGHT TRACK

The analysis of the influence of the longitudinal stiffness of the bogie primary suspension system on the bogie stability limits in the case of straight track is carried out by the hunting motion analysis with different value of the stiffness. In particular we consider the stiffness value:

$k_{long} = hk_0$

where h is a numerical coefficient and k_0 is the value reported in table 6.3 and it is equal to $10^6\ N/m$.

The critical speed is determined also with different load conditions, defined by means of the bogie load ratio. The used values for h are:

$h = 1.5;\ 1; 0.5; 0.1; 0.05;$

The critical velocity respect the load ratio and k_{long} is reported in figure 8.24 where the results obtained by means of the Matlab code and Simpack software are compared.

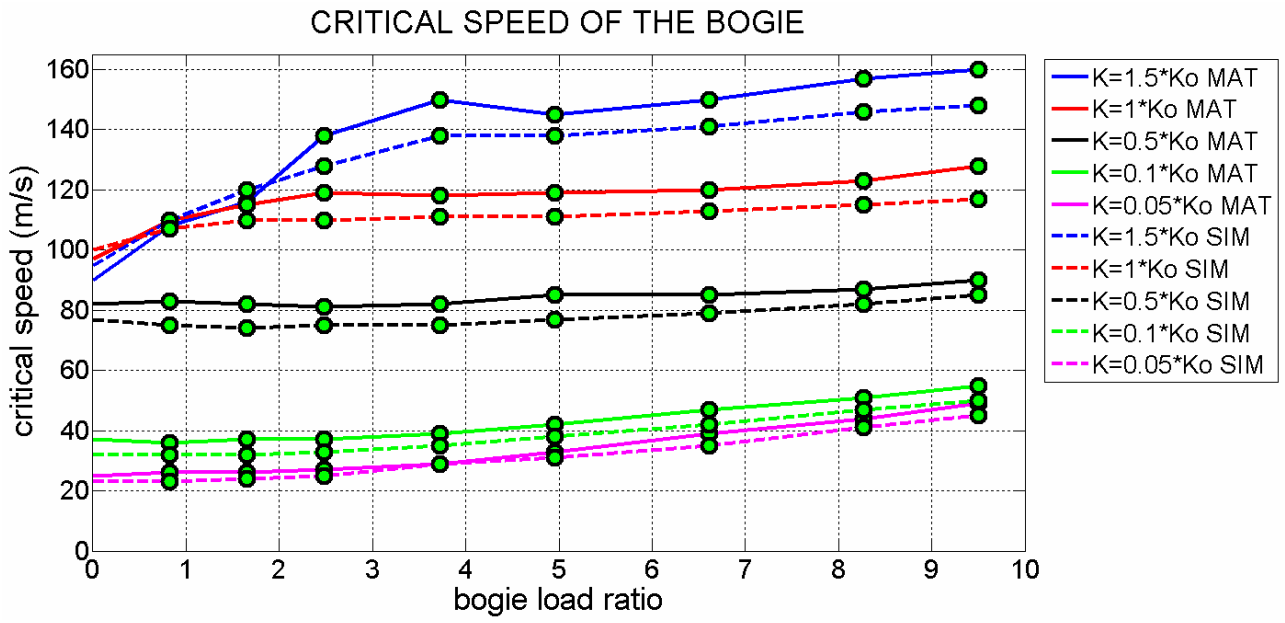

Figure 8.24
Critical bogie velocity respect to the load ratio and k_{long}

From the figure it is evident that the critical velocity strongly increases when k_{long} rises. In fact we pass from a value like 30 m/s to about 150 m/s with an increment of 30 times of k_{long}.

Observing Figure 8.24 one can notate two different behaviours of the critical speed especially for the intermediate values of k_{long}; the first one occurs for low values of the load ratio and reveals a rapid change of the critical speed respect to the load and in the second behaviour the stability characteristics are not very variable respect to the load.

This fact permits to define a stability limit after which it is possible to use the bogie with a load stability interval. From the figure one can observe that the limit and the interval change with k_{long}, that is the higher is k_{long}, the higher is the stability limit and the lower is the stability interval extension. In fact, considering h=1, we show that the stability limit is about 3 and the extension of the interval is from 3 (empty wagon) to 8 (full loaded wagon). Any change to the load ratio generate, at the external of the interval, a higher change in the critical speed than at the inner of the interval. It is interesting to observe that such critical conditions can be approached also when an emergency braking is necessary. As a matter of fact in an emergency braking of a long train some wagons can have their load-ratio reduced due to the friction forces transmitted by bumpers.

8.6 – THE INFLUENCE OF THE BOGIE LONGITUDINAL STIFFNESS IN A CURVED TRACK

The influence of k_{long} on the stability limits of the bogie in a curved track should account of the effective radius of curvature. The diagrams presented show the critical speed as a function of k_{long} having the track radius of curvature as a parameter. All computations are here conducted with a fixed load ratio equal to 8.26. The analysed radii of curvature are the following:

R_{curv} =1000 m, 1200 m, 2000 m, 2500 m, 3500 m, 4500, 6000 m.
The used values for *h* are:
$h = 1.5;\ 1;\ 0.5;\ 0.1.$

The values of the bogie critical speeds as a function of k_{long} and R_{curv} are reported respectively in Figure 8.25 and Figure 8.26. a comparition between the results obtained by means of the Matlab code and Simpack software are also showed.

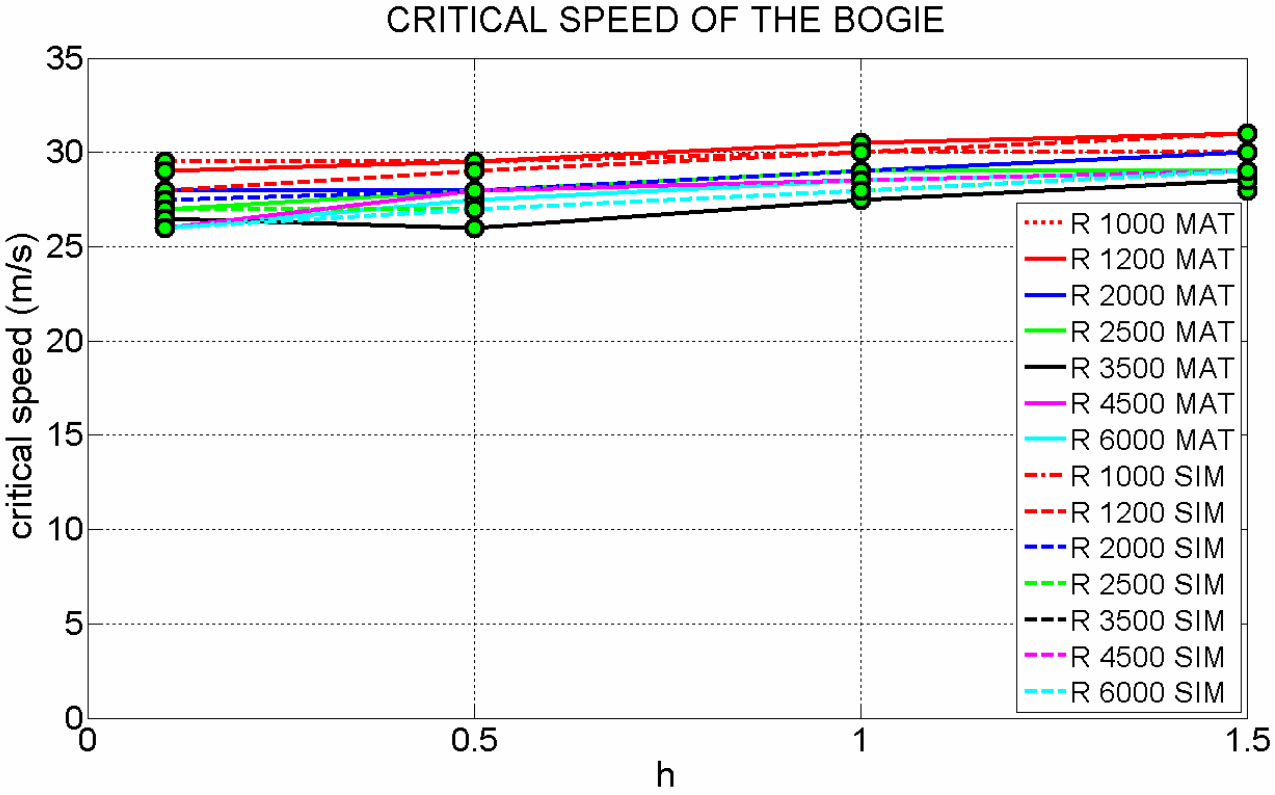

Figure 8.25
Critical bogie velocity in a curved track respect to k_{long} at different radius of curvature. The bogie load ratio is equal to 8.26.

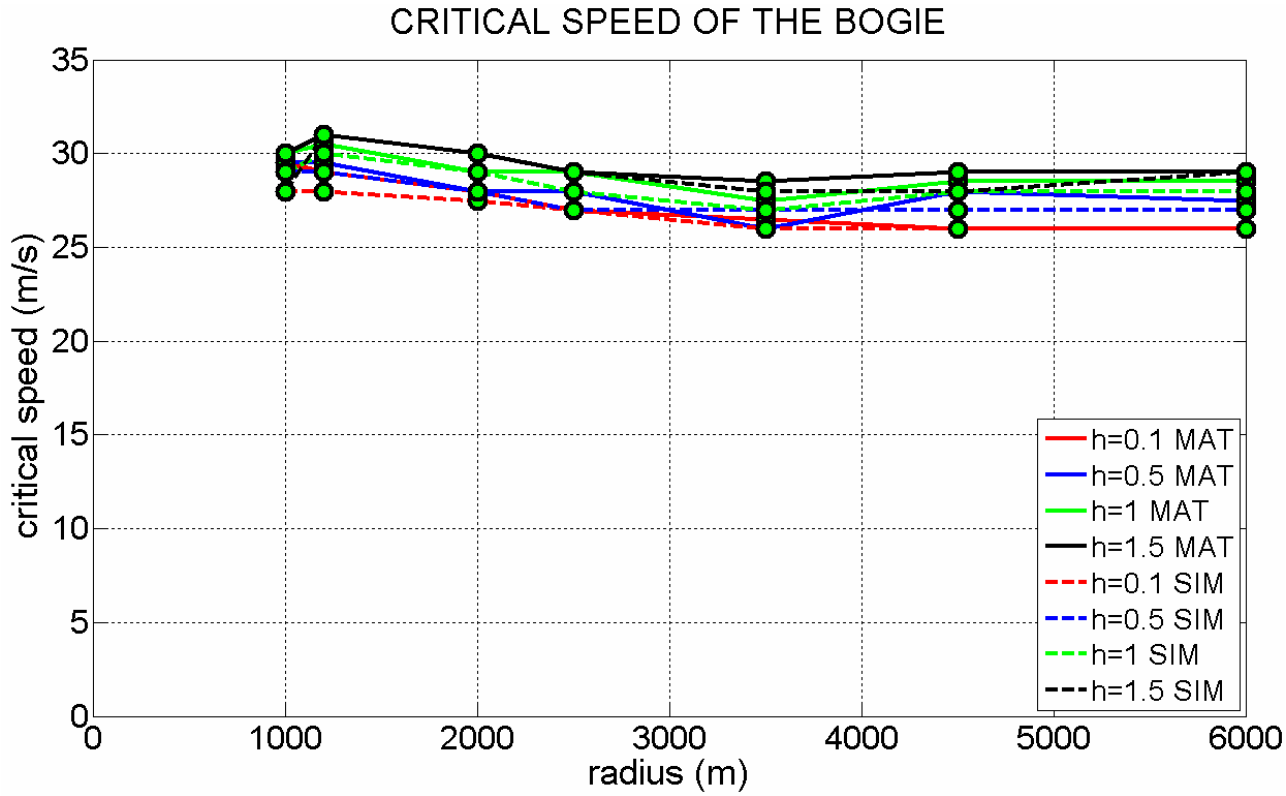

Figure 8.26

Critical bogie velocity in a curved track respect to the radius of curvature at different value of k_{long} . The bogie load ratio is equal to 8.26.

The figures show that for all the radii of curvature the critical speed increases with the rise of the longitudinal stiffness, thus reflecting the same behaviour of the rectilinear track case. However, the values obtained are much different. In fact in the curved track the critical speed does not exceed the value of 34 m/s, even when introducing a high stiffness. This apparently unexpected event is explained by the continuous interactions among the wheel flanges and the rails when running on a curved track, in particular among the outer wheels and rail. This occurrence doesn't happen in a straight track if the initial perturbation is sufficiently small. In fact the graphic reported in Figure 8.24 is obtained with an initial perturbation set to 0.1 m/s. This lateral displacement of the wheel-sets is not enough to guarantee the flange-rail contact condition. Considering a bogie having h=1 and load ratio equal to 8.26, when the initial perturbation is equal to 0.25 m/s, the contact among the wheel flanges and the rails does happen. The bogie critical speed strongly reduces passing from a value of 123 m/s in the small perturbation case to 43 m/s in the case of severe perturbation. This last value is now comparable with the one obtained along a curved track even at very large radius of curvature. The significant reduction of the critical speed is due to the sharp variations of the geometrical characteristics of the surfaces in contact when the contact region goes by the wheel tread to the

flange. This variations have a great influence on the tangential forces in particular on the spin components affecting the system dynamic.

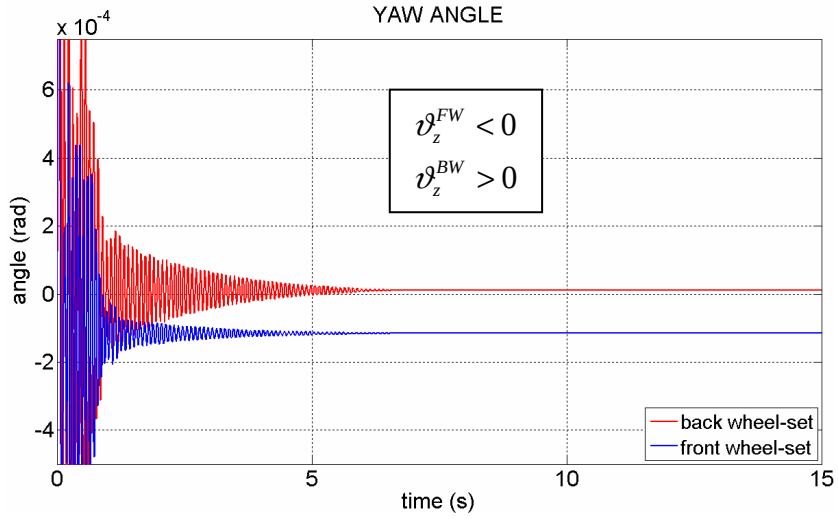

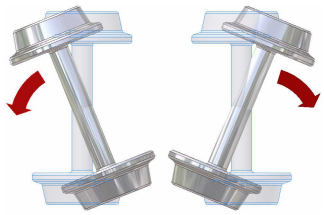

Bending mode

a) Yaw angle of the back and front wheel-sets with h=1.5 and radius equal to 1200 m.

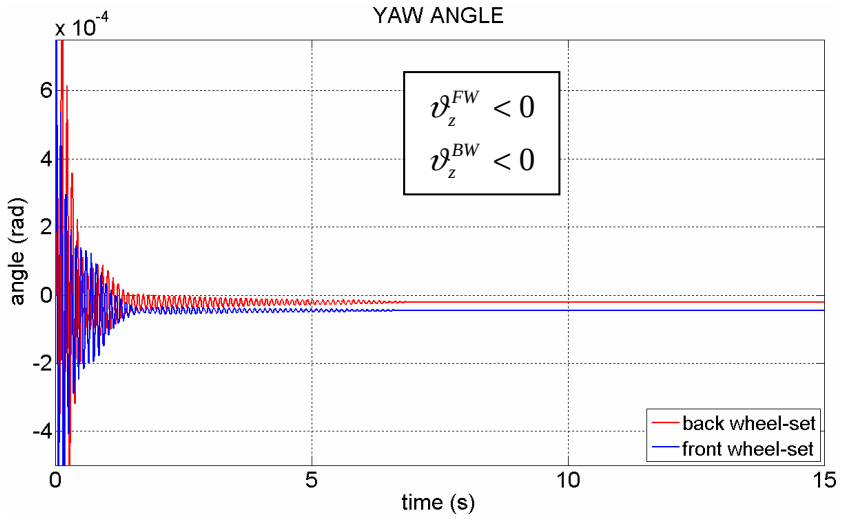

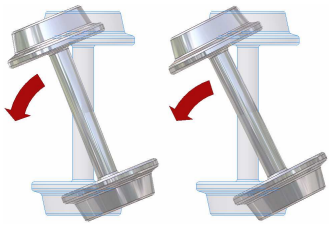

Shearing mode

b) Yaw angle of the back and front wheel-sets with h=1.5 and radius equal to 3500 m.

Figure 8.27
Yaw angle of the two wheel-sets in the two oscillatory modes, bending and shearing ones.

Figure 8.26 shows that with radius of curvature included between 1200 m and 3500 m, the critic speed slightly decreases with the rise of the radius while after 3500 m it increases again. This behaviour is explained with the two different oscillatory modes of the two wheel-sets. Figure 8.27 reports the two yaw angles at regime of the two wheel-sets, the front one (ϑ_z^{FW}) and the back one (ϑ_z^{BW}) considering the radius equal to 1200 m and 3500 m; h is assumed equal to 1.5; the critic velocities are respectively 31 m/s and 28.5 m/s. We can notate that the two signs of the

wheel-set yaw angles are different: in the case of 1200 m the two angles have opposite signs, while in the case of 3500 m the angles have the same sign that is they are negative. This fact demonstrate that in the first case the wheel-sets oscillate in *bending mode* while in the second one they oscillate in the *shearing mode* (see figures 4.1 and 8.27) . It is well known that the best condition for a bogie moving in a curved track is realized when the two wheel-sets are positioned in a symmetric configuration respect to the radial direction of the track and this condition is realized when the two yaw angles have opposite signs, that is they assume a bending configuration. This condition influences also the bogie critic velocity that tends to be slightly higher in the bending mode than in the shearing one also in presence of a lower radius.

The plots in the straight and curved tracks suggest that the optimum value of k_{long} is toward the highest values, but this is only apparently true. A complete and more realistic stability investigation must consider the wheel-set or bogie not as an isolated systems but as coupled with the rails. In other words, in order to predict the stability limits of a railway systems the rails layout and their geometric and resistance characteristics must be considered as well.
It is the case for example of the lateral displacement of the rails generated by the lateral force transmitted from the wheel-flange in the contact point. The rail displacement can produce the following effects [29]:

- the *gage widening*, that can lead to a wheel-rail separation as shown in Figure 8.28;
- the *rail rollover* , that is a rotation of the rail about its corner, as shown in Figure 8.29.

In many cases one of these effects can cause the entire system to be unstable.

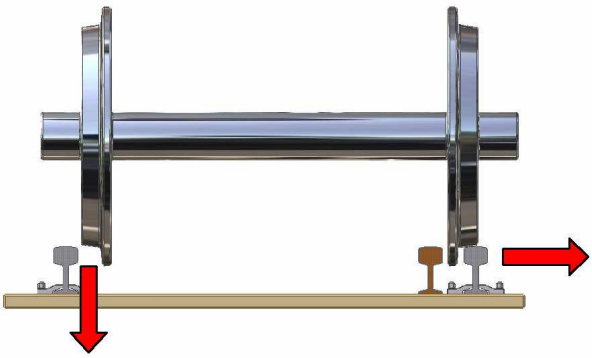

Figure 8.28
The gage widening

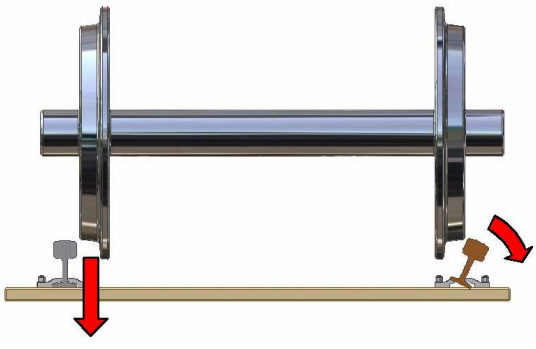

Figure 8.29
The rail rollover

For these reasons, in order to analyze these two last critical phenomena, it is necessary to evaluate the contact forces between the wheels and the rails as a function of the geometrical and dynamical

characteristics of the system. The lateral component of the contact force is the one that strongly stresses the rail in the horizontal plane. Figure 8.30 shows the lateral components of the four wheels of the bogie in a curved track; they are considered positive when directed outward the rails.

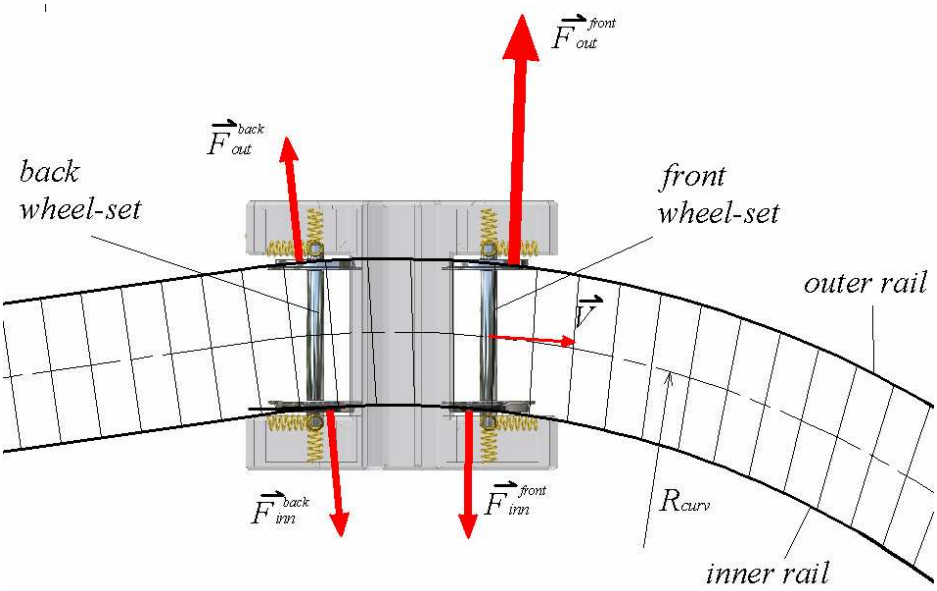

Figure 8.30
The lateral components of the contact forces acting on the inner and outer rails in a curved track.

The lateral component of the contact force depends on the following characteristics:

- *vertical load acting on the bogie;*
- *track radius of curvature;*
- *bogie velocity;*
- *characteristics of the primary suspension system;*
- *wheel-rail geometry.*

Figure 8.31 reports the plots of lateral components of the contact forces, transmitted from the four wheels of the bogie to the inner and outer rails, versus the track radius and the longitudinal stiffness parameter *h* of the primary suspension system. The velocity of the bogie is the critical one showed in Figure 8.25. The load ratio is equal to 8.26. The results are compared with which obtained by means of Simpack software.

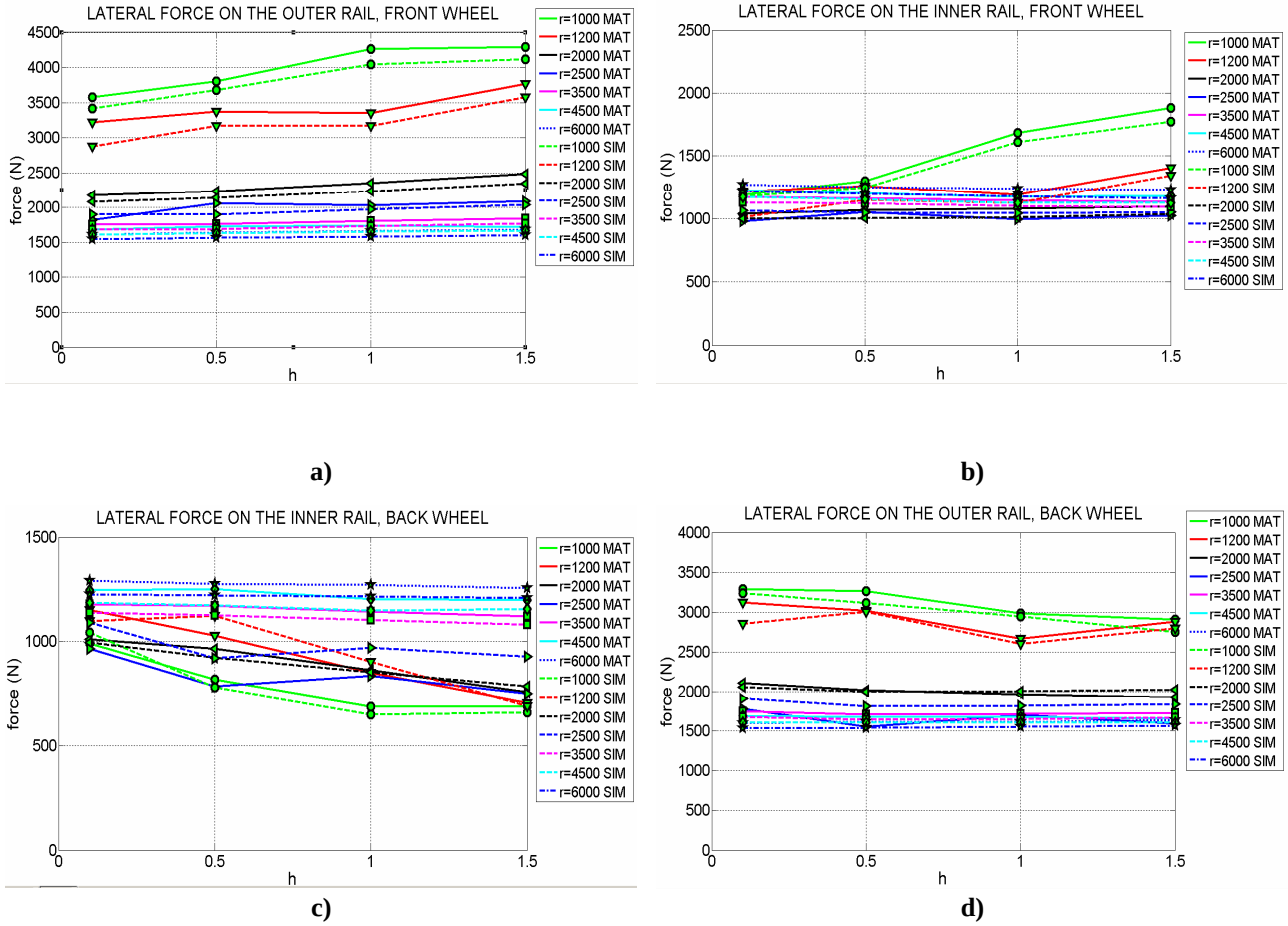

Figure 8.31
Lateral component of the contact forces acting on the outer and inner rails respect to the longitudinal stiffness parameter *h* and the track radius of curvature.

The figures show how the lateral component is differently distributed on the four wheels; the wheel that strongly stresses the rail is the one belonging to the front wheel-set in contact with the outer rail. This wheel is the first one that experiences the rail curvature in the transition from the rectilinear to the curved track. For this reason this wheel will be accounted for in all following considerations. With reference to the Figure 8.31a, we observe that the lateral component increases when the longitudinal stiffness rises at any curvature radii.

Hence, the use of very stiff longitudinal suspensions from one side increases the critical speed, both in a rectilinear and curved tracks, but from another side increases the stress on the rails and exposes the system to a dangerous phenomena. We can also observe that the lateral component increases when the track radius decreases. In fact, the lower is the track radius, the higher will be the constraint force.

A significant parameter used for the critical conditions analysis is the ratio L/V, between the lateral and vertical components of the contact force acting on the rail, as shown in Figure 8.32. The two components L and V follow from a different decomposition of the contact force that traditionally is

decomposed in the normal and tangential components. The ratio L/V is the most important criterion for predicting derailment of locomotives or bogies due both to the wheel flange climbing and to the rail rollover. The studies about this parameter were initiated by Nadal in 1908. Figure 8.33 reports the plots of L/V of the outer wheel of the front wheel-set of a bogie in a curved track moving at critical velocity, as shown in Figure 8.25, under the stationary conditions.

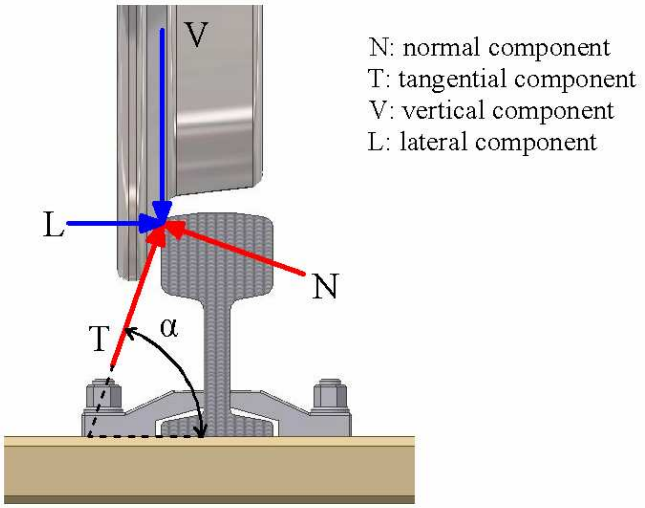

Figure 8.32
The L and V components of the contact force between wheel and rail.

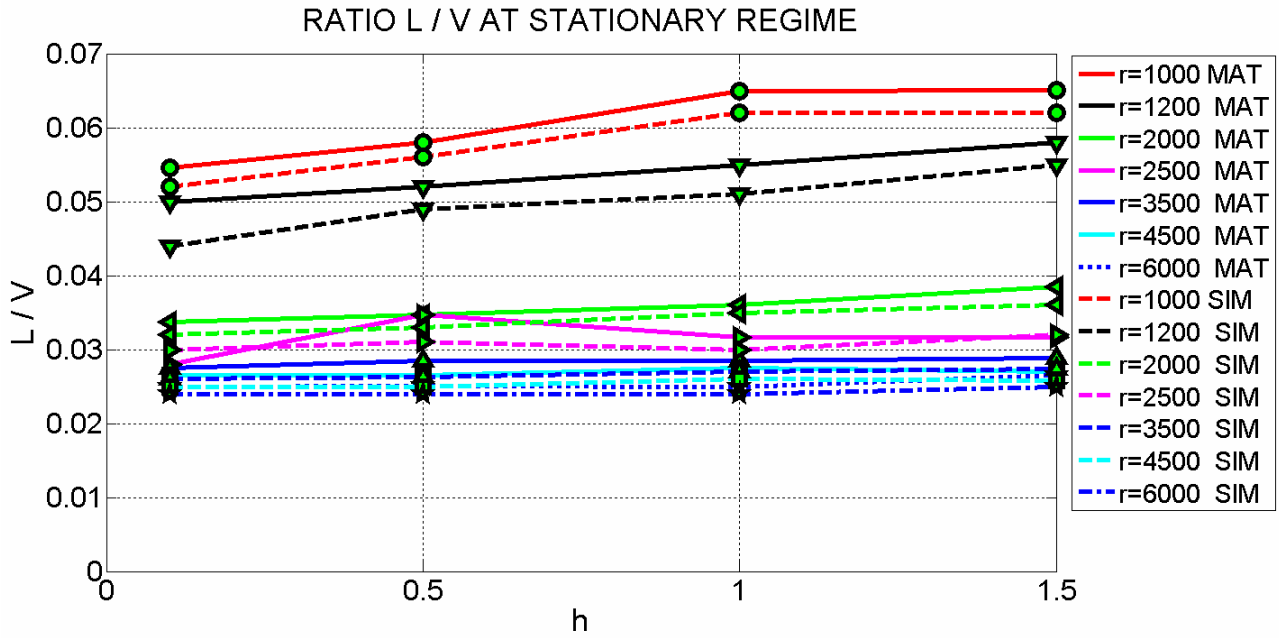

Figure 8.33
Ratio L/V of the outer wheel of the bogie front wheel-set in a curved track moving at critical velocity and at stationary regime

From Figure 8.33 one can infer that the ratio L/V increases with the rise of the longitudinal stiffness and with the decreasing of the track radius. The values reported in the figure are not too high because they are the values obtained at stationary running, few seconds of motion after the passage from a rectilinear to a curved track, when all lateral displacements and force oscillations are damped.

It is interesting to visualize the plot of the maximum ratio $(L/V)_{\max}$, shown in Figure 8.34, concerning the same wheel and obtained when the bogie enter the curved part of the track from the straight one. The values are higher than the ones obtained at regime; $(L/V)_{\max}$ increases when the radius of curvature decreases. We also see that the dependence of $(L/V)_{\max}$ from the longitudinal stiffness is low. The maximum value of L/V is obtained at the first interaction between the wheel flange and the rail, after the passage from straight to curved track. Since the interaction is very short, the suspension system has almost no time to influence the dynamics of the system.

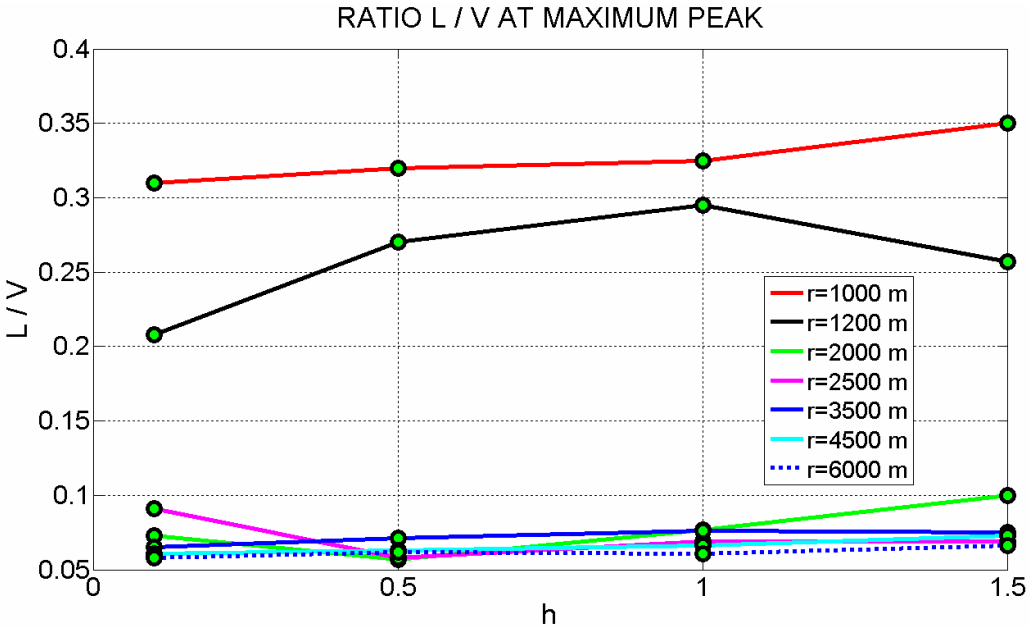

Figure 8.34
Peak of the ratio L/V of the outer wheel of the front wheel-set of a bogie in a curved track moving at critical velocity.

The limit values of the ratio $(L/V)_{der}$ that predict the derailment of the system are not precisely defined in literature because they depend on many parameters such as:

- the system analyzed: wheel, wheel-set or bogie;
- the *gage widening* or *rail rollover* phenomena;
- the models or standards adopted.

Let us denote by α the wheel flange angle (see Figure 8.32), by μ the friction coefficient between wheel and rail. The $(L/V)_{der}$ is given by the following simple formula valid for a positive angle of attack of the wheel-set:

$$\left(\frac{L}{V}\right)_{der} = \frac{\tan\alpha - \mu}{1 + \mu\tan\alpha} \qquad (8.1)$$

Replacing the value α = 75° and μ =0.2 we obtain:

$$\left(\frac{L}{V}\right)_{der} = 2.02$$

that is extremely conservative for most practical cases. This is due to the simplification of the *Nadal's* model that consider the tangential force acting only on the plane perpendicular to the track axis. Other accurate methods that predict the derailment conditions of a vehicle are available. *Blader* (1989) [29, 32] showed that if the contact point on the rail is near the gage point, the ratio L/V must be between the limits 0.66 and 0.73 depending from the shape of the rail. Obviously if the contact point moves toward the corner of the rail, the ratio $(L/V)_{der}$ is reduced. The AAR (Association of American Railroads) standard distinguishes the systems wheel, wheel-set and bogie and adopts the following limits:

- $(L/V)^{W}_{der}$ =1 for wheel;
- $(L/V)^{WS}_{der}$ = 1.5 for wheel-set;
- $(L/V)^{TS}_{der}$ = 0.6 for truckside.

In the case of a wheel-set a Weinstock criterion is adopted. The ratio $(L/V)^{WS}$ of the wheel-set is calculated as the sum of the absolute values of the ratios $(L/V)^{W}$ of the two wheels as follows:

$$\left(\frac{L}{V}\right)^{WS} = \left|\frac{L}{V}\right|^{W}_{L} + \left|\frac{L}{V}\right|^{W}_{R} \qquad (8.2)$$

The advantage of using this criterion is that it has a reduced dependence from the coefficient of friction. This coefficient being difficult to measure in an experimental test.

The third derailment measure is the truckside L/V ratio. This is the ratio between the sum of the lateral forces to the sum of the vertical forces for the wheels on one side of a truck:

$$(L/V)^{TS} = \sum_{i=1}^{n}\left(\frac{L}{V}\right)_i \qquad (8.3)$$

Where *n* is the number of wheels on one side of the truck. This criterion is devoted to rail rollover.

8.7 – THE INFLUENCE OF THE SUPER-ELEVATION

In order to reduce in a curved track the contact forces between wheels and rails and to improve the stability characteristics of the system, the rolling plane is inclined at an angle α named *super-elevation angle*. In this manner the two rails lies on different horizontal planes, spaced by a distance *s* named super-elevation. One can establish that:

$$\tan\alpha = \frac{s}{G}$$

where *G* is the horizontal cross distance between the rails. Since α is very small, *G* is generally approximated with the gauge. With reference to Figure 8.33, the super-elevation *s* is calculated imposing the equilibrium conditions with the centrifugal force as follow:

$$s = \frac{mV^2 G}{R(mg + F)} \qquad (8.4)$$

obtained supposing that the centrifugal force, the weight and the force F acting on the bogie frame are applied on the centre of mass of the system. In the expression (8.4) *m* is the mass of the system, *V* the bogie longitudinal velocity, *g* the gravity acceleration, *R* the radius of curvature of the track and *F* is the external vertical force applied on the bogie.

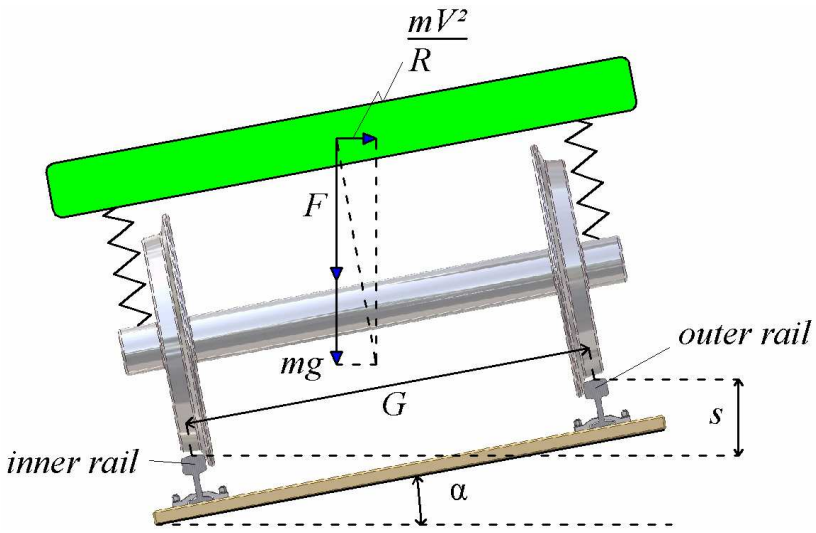

Figure 8.35
The mass and external forces acting on the bogie and the super-elevation in a curved track.

In order to verify the influence of *s* on the bogie critical velocity, the motion of a bogie on a curved track having super-elevation *s* and radius equal to 800 m has been studied; the longitudinal stiffness is set equal to $10^6 \ N/m$. The results are plotted in Figure 8.36.

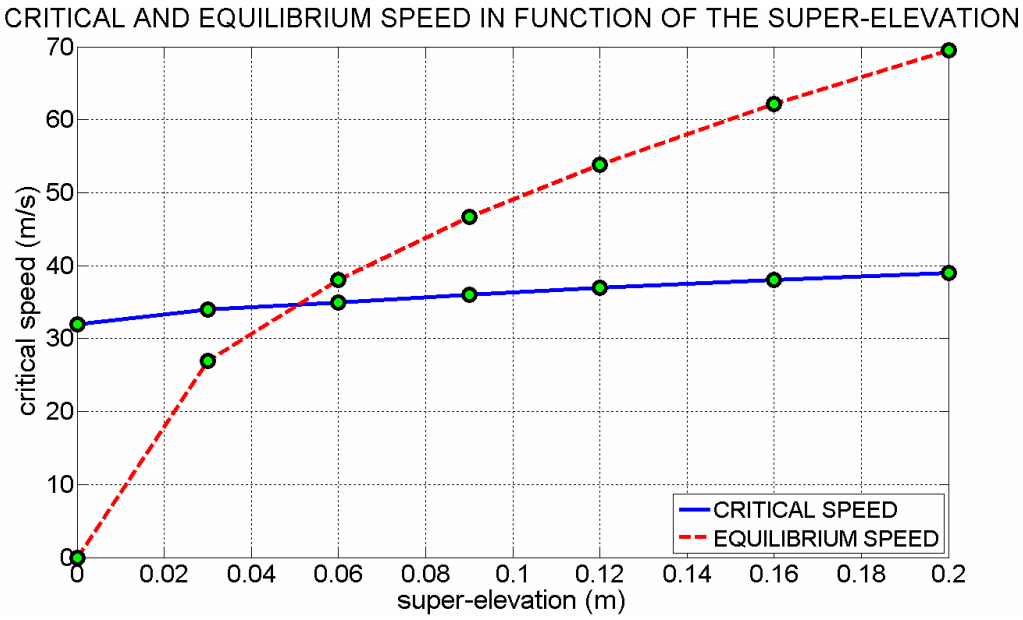

Figure 8.36
The bogie critical and equilibrium velocities as regards the track super-elevation with a bogie load ratio equal to 8.26 and track radius equal to 800 m .

The Figure 8.36 shows that the critical velocity V_{cr} increases with the super-elevation in a nearly linear pattern from a value of 32 m/s, with a planar track, to 39 m/s in the case of 0.2 m of super-elevation. This behaviour is strongly influenced by the intensity of the wheel-rail forces.

Let us denote by V_{eq} the velocity at which the resultant of the external and mass forces acting on the system has only an orthogonal component to the rolling plane. Its value is determined from equation (8.4). Figure 8.36 reports the plot of V_{eq}. There exists a critic super-elevation s_{cr} beyond which $V_{eq} > V_{cr}$. Since V_{eq} is the optimum velocity for a bogie moving in a curved track, the preferred super-elevation values are those for which $V = V_{eq}$ and $V < V_{cr}$ where V is the bogie longitudinal velocity. These conditions are satisfied when $s < s_{cr}$. On the contrary, if $s > s_{cr}$ then it is not possible to find an equilibrium configuration. s_{cr} may be obtained also by means of the analysis of the lateral components of the contact forces acting on the rails. Figure 8.37 shows the plots of two lateral components of the contact forces transmitted from the two wheels of the front bogie wheel-set on the inner and outer rails. The bogie moves with the critical velocity reported in Figure 8.36.

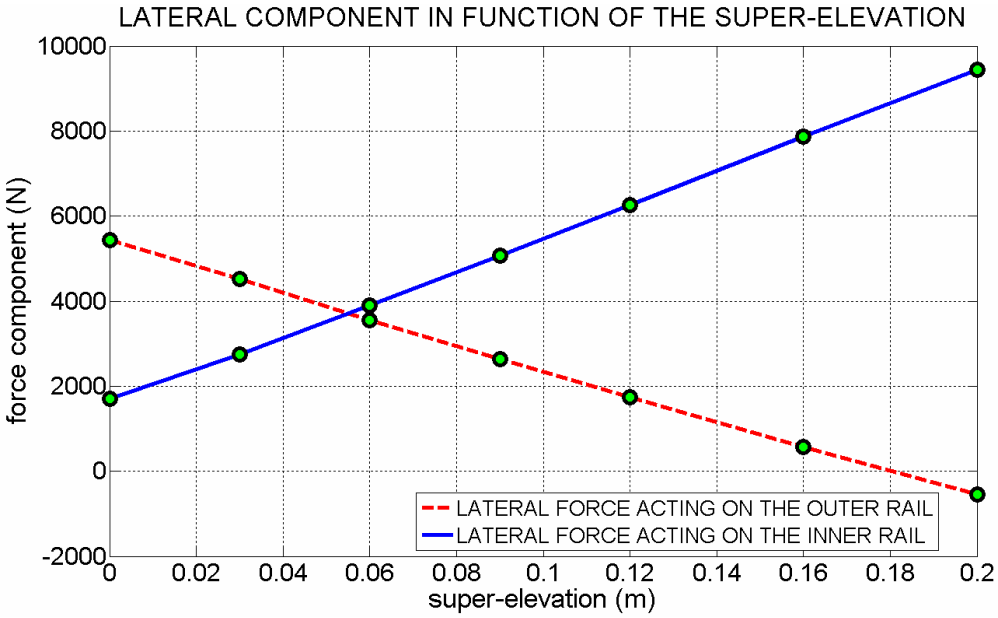

Figure 8.37
Lateral components of the contact forces transmitted from the bogie front wheel-set to the inner and outer rails in a curved track with radius equal to 800 m.

Figure 8.37 shows that when the super-elevation increases, the lateral component acting on the outer rail decreases while the one acting on the inner rail increases. The plots in both cases are nearly linear. s_{cr} is determined from the equivalence of the lateral components acting on the rails. For $s > s_{cr}$ the lateral component acting on the inner rail is predominant on the one acting on the outer rail, otherwise when $s < s_{cr}$ the component acting on the outer rail prevails.

We can also observe that the lateral component acting on the outer rail assumes negative values beyond a second-critic super-elevation s_{cr2}, that is directed along the inner direction of the curvature. In this case there is a super-elevation excess. To overcome this condition it is necessary to increment the centrifugal force and then the bogie velocity beyond the critical one, forcing the system to move in an unstable condition. A similar behaviour is noticed in the plot of the ratio L/V for what concerns the super-elevation. Figure 8.38 shows the ratios at stationary regime of the two wheels of the front wheel-set of the bogie moving at critical speed as a function of s in a curved track with radius equal to 800 m and bogie load ratio equal to 8.26.

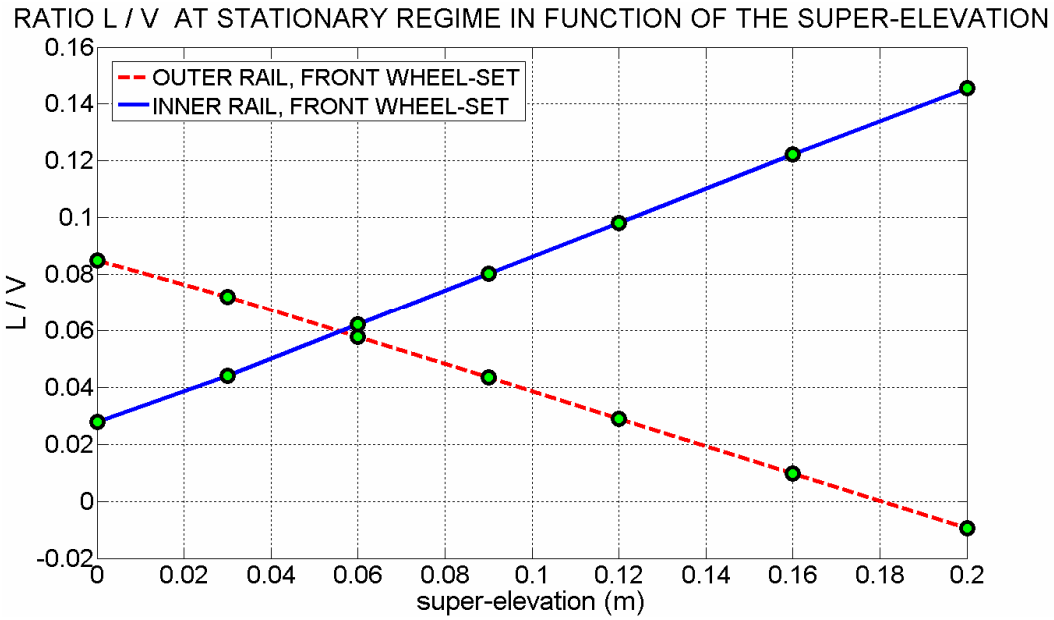

Figure 8.38
Ratio L/V at stationary regime of the inner and outer wheels of the front wheel-set in a curved track with radius equal to 800 m.

8.8 – THE INFLUENCE OF THE WAGON LONGITUDINAL STIFFNESS IN A STRAIGHT TRACK

The analysis of the influence of the longitudinal stiffness k_{long}^{W} of the wagon secondary suspension system on the wagon stability limits in the case of straight track is carried out by the hunting motion analysis with different values of the stiffness and the load wagon ratio. In particular we consider the stiffness value:

$$k_{long}^{W} = h_w k_o^{W}$$

where h_w is a numerical coefficient and k_o^{W} is equal to $8 \cdot 10^6 \; N/m$.

The used values for h_w are:

$$h_W = 1.5;\ 1;\ 0.5;\ 0.1;$$

The load conditions are defined by means of the *wagon load ratio* defined as the ratio between the car-body and the bogie frame weights. Three wagon ratios are considered, that is 12.5, 16.2 and 20.25.

The wagon critical velocity respect the load ratio and k_{long}^{W} is reported in figure 8.39 where the results obtained by means of the Matlab code and Simpack software are compared. The h bogie value is assumed equal to 1.

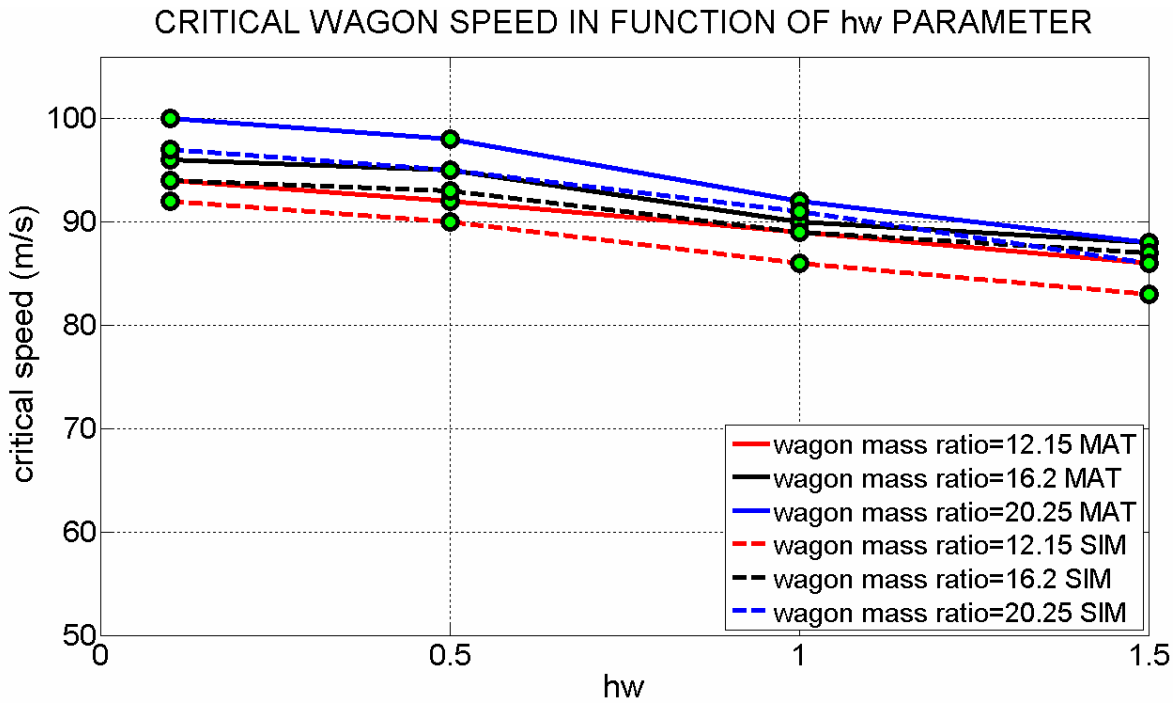

Figure 8.39

Critic wagon speed in function of the wagon load ratio and the longitudinal stiffness of the secondary suspension system

From the figure it is evident that the wagon critical velocity decreases when k_{long}^{W} rises and it increases when the wagon load ratio rises. We may observe also that the wagon critical speed values are lower than the bogie ones loaded with the same vertical cargo; this fact is due to the mutual influence of the two bogies through the secondary suspension system that reduces the critical speed of the entire wagon.

CONCLUSIONS AND FUTURE WORK

In the thesis the models and dynamic behaviours of a railway systems, as a wheel-set, bogie and wagon are presented. The bogie is composed by two wheel-sets, a frame and by the primary suspension system while the wagon by two bogies, a car-body and by the secondary suspension system.

The computer simulation includes a new wheel-rail contact model that accounts a different local stiffness of tread and flange wheel. Thanks to an optimized use of a a preliminary compiled look-up table the computation time is reduced considerably. In particular, all data that define the complex contact between wheel and the rail are stored as a function of two independent coordinates.

Both straight and curved tracks could be analysed for the monitoring of the hunting phenomenon and critic conditions.

Because of its influence on overall cpu-time, the interpolation procedure of the look-up table has been optimized.

A particular interest is given by the results concerning hunting instability when varying the load on each axes and the track radius of curvature . It has been recorded a different influence of the load ratio on the critical speed of the wheel-set and of the bogie assembly. For the wheel-set the load ratio has an almost linearly proportional influence. For the bogie, this influence is much more limited in the range of practical interest.

In order to reduce the danger caused by critical speed, the influence of the longitudinal stiffness of the primary suspension system and the super-elevation angle are analysed. Super-elevation changes the stability motion condition but a careful analysis should be carried out in order not to increase dangerously lateral loads.

The software developed in Matlab environment has been validated through the comparison with Simpack-rail, a widely tested multibody software for the dynamic analysis of railway systems.

As regard the future developments, a different wheel-rail profiles may be analysed, in particular a worn out ones to study the influence of the wear on the critic limits and on the contact forces between the wheel and rail.

As regard the stability analysis field the influence of the other suspension characteristics that is the lateral and vertical ones and its geometric configurations may be studied in order to optimize the design of the primary and secondary suspension systems.

R E F E R E N C E S

[1] Bozzone M., Salvini P., Pennestrì E., A computationally efficient method for whell-rail contact analysis, Contact Mechanic Conference, Florence 2009.

[2] Kalker J.J., Three-dimensional elastic bodies in rolling contact, Dordrecht, Kluwer Academic Publishers, 1990.

[3] Kalker J.J., Rolling contact phenomena, Delft University of Technology, The Netherlands, 2003.

[4] Lee S.Y., Cheng Y C., Hunting stability analysis of high-speed railway vehicle bogies on tangent tracks, Journal of Sound and Vibration, Vol. 282, pp. 881-898, 2005.

[5] Knothe K., Böhm F., History of stability of railway and road vehicles, Technical University of Berlin, 16th Symposium on Vehicle System Dynamics, Pretoria, 1999.

[6] Parena D., Kuka N., Vivalda P., Kik W., Stability investigation and narrow curving analysis of a streetcar model, 4th Adams/rail users' Conference, Uthrect, 1999.

[7] Banerjee N., Karmakar R., Bond Graph Modelling of Rail Wheel-set on Curved Track, Vol. 83, pp. 695-706, 2007.

[8] Meli E., Auciello J., Malvezzi M., Papini S., Pugi L., Rindi A., Determination of wheel rail contact points with semi analytic methods, Multibody System Dynamics, Vol. 20, pp. 327-358, 2008.

[9] Bosso N., Gugliotta A., Somà A., Realizzazione di un modulo di contatto a ruote indipendenti, XXXI Aias, settembre, Parma, 2002 (in Italian).

[10] Tullio Levi Civita, Ugo Amaldi, Lezioni di meccanica razionale, ed. Zanichelli, 1991 (in Italian).

[11] Vladimir Ivanovic Smirnov, Corso di matematica superiore, Editori riuniti, Vol.. II, pp. 417-463, 1999 (in Italian).

[12] Pombo J., Ambrosio J. A. C.,General spatial curve joint for rail guided vehicles: kinematics and dynamics, Multibody system dynamics, Vol. 9, pp. 237-264, 2003.

[13] Pombo J., Ambrosio J. A. C., Application of a wheel–rail contact model dynamics to railway in small radius curved tracks, Multibody system dynamics, Vol. 19, pp. 91-114, 2008.

[14] Pombo, J. Ambrosio, Dynamics analysis of a railway vehicle in real operation conditions using a new wheel-rail contact detection model, Int. J. of Vehicle Systems Modelling and Testing, Vol. 1, pp. 79-105, 2005.

[15] Shabana A.A., Zaazaa K. E., Escalona J. L., Sany J. R., Development of elastic force model for wheel-rail contact problems, Journal of Sound and Vibration, Vol. 269. pp. 295-325, 2004.

[16] Shabana A.A., Sany J. R., A Survey of Rail Vehicle Track Simulations and Flexible Multibody Dynamics, Nonlinear Dynamics, Vol. 26, pp. 179-210, 2001.

[17] Shabana A. A., Tobaa M., Sugiyama H., Zaazaa K. E., On the Computer Formulation of the Wheel/Rail Contact Problem, Nonlinear Dynamics, Vol. 40, pp. 169-193, 2005.

[18] Shabana A.A., Sany J.R., An augmented formulation for mechanical systems with non-generalized coordinates: application to rigid body contact problems, Nonlinear Dynamics, Vol. 24, pp. 183-204, 2001.

[19] Hans True, Recent advances in the fundamental understanding of railway vehicle dynamics, Int. J. Vehicle Design, Vol. 40, Num. 1/2/3, 2006.

[20] Bond graph modelling of rail wheel-set on curved track, N. Banerjee, R. Karmakar, Simulation, Vol. 83, Num. 10, pp. 695-706, 2007.

[21] G. Golash, G. Gungor, R. Meisinger, C. W. Gong, S. G. Wei, Simulation of railway-bogie, ISSN 1616-0726 Sonderdruck Schriftenreihe der Georg-Simon-Ohm-Fachhochschule Nürnberg Num. 3, Nürnberg 2001.

[22] Y. M. Huang, K. L. Chen, Tsung-Shou Wang, Running stability simulation and field testing of two axle-bogie design, Int. J. of Vehicle Design 2001, Vol. 26, Num. 2/3, pp.131-145.

[23] W. Kortum, R.M.Goodall, Mechatronic developments for railway vehicles of the future, Control Engineering and Practice, 10 (2002), pp. 887-898.

[24] O. Polach, On non-linear methods of bogie stability assessment using computer simulations, IMechE Vol. 220 Part F: J. Rail and Rapid Transit.

[25] O. Polach, Bogie design for better dynamic performance, European Railway Review, Num. 1/2003, pp. 69-77.

[26] O. Polach, Influence of wheel/rail contact geometry on the behaviour of a railway vehicle at stability limit, ENOC 2005, Eindhoven, Netherlands, 7-12 August 2005.

[27] O. Polach, Influence of locomotive tractive effort on the forces between wheel and rail, Vehicle system dynamics supplement 35 (2001), pp. 7-22.

[28] J.T.Pearson, R.M.Goodall, T.X.Mei, S.Shen, C. Kossmann, O.Polach, G.Himmelstein, Design and experimental implementation of an active stability system for a high speed bogie, Extensive

summaries of the 18th IAVSD symposium dynamics of vehicle on roads and tracks, Atsugi, Kanagawa, Japan, August 24-30, 2003.

[29] A.A.Shabana, K.E.Zaazaa, H. Sugiyama, Railroad vehicle dynamics, CRC Press 2008.

[30] P. Herring, Il libro complete dei treni, Istituto Geografico DeAgostini, 2000.

[31] R. Pocaterra, Treni, Istituto Geografico DeAgostini, 2003.

[32] Blader F.B., Assessing Proximity to Derailment from Wheel/Rail Forces: a Review of the State of the Art, ASME Rail Transportation, Vol. 3, pp. 179-188, 1989.

[33] Eds., Finnish National Publisher, Lappeenranta, 1974.

[34] K.L. Johnson, Contact Mechanics, Cambridge University Press, Cambridge, England, 1985.

[35] N. Kikuchi and J.T. Oden, Contact Problems in Elasticity, SIAM Studies in Applied Mathematics, Philadelphia, Pennsylvania, 1988.

[36] C. Esveld, Modern Railway Track, Delf University of Technology, Delft, Netherlands, 2001.

[37] Dukkipati, R.V., Parametric Sensitivity of the Hunting of a Freight Car Truck on the NRC Curved Track Simulator, Trans. CSME, V18, N2, pp. 147-164, 199.

[38] Weinstock, H., Wheel Climb Derailment Criteria for Evaluation of Rail Vehicle Safety, ASME Paper #84-WA/RT-1, 1984 ASME Winter Annual Mtg.

[39] Shabana A.A., Zaazaa K. E., Escalona J. M. Gonzales, A technique for validating a multibody wheel/rail contact algorithm, ASME 2003 Design Engineering Technical Conferences and Computers and Information in Engineering Conference, Chicago, Illinois USA, September 2-6, 2003.